Title
Microfluidics for the analysis and synthesis of radiopharmaceuticals

Author
Ha, Noel

Publication Date
2018

UNIVERSITY OF CALIFORNIA

Los Angeles

Microfluidics for the analysis and synthesis of radiopharmaceuticals

A dissertation submitted in partial satisfaction
of the requirements for the degree Doctor of Philosophy
in Bioengineering

by

Noel Ha

2018

ABSTRACT OF THE DISSERTATION

Microfluidics for the analysis and synthesis of radiopharmaceuticals

by

Noel Ha
Doctor of Philosophy in Bioengineering
University of California, Los Angeles, 2018
Professor Robert Michael van Dam, Chair

Radiopharmaceuticals labeled with short-lived positron-emitting or gamma-emitting isotopes are injected into patients just prior to performing a positron emission tomography (PET) or single photon emission computed tomography (SPECT) scan. These imaging modalities are widely used in clinical care, as well as in the development and evaluation of new therapies via clinical trials. Unlike ordinary pharmaceuticals, the short lifetime of radiopharmaceuticals requires that they be produced in relatively small batches close to the geographical location where the patient is scanned.

Since PET tracers are classified as drugs by regulatory agencies, they must pass stringent quality control (QC) tests after their production to ensure patient safety prior to injection. Performing and documenting these tests is cumbersome and time-consuming, and requires an array of expensive analytical chemistry equipment and significant

dedicated lab space, and there is considerable interest in the development of automated and lower-cost approaches.

By replacing conventional techniques with lab-on-a-chip technologies, it may be possible to achieve further reductions in the size, cost, and complexity of automated QC testing platforms. While some advances have been made for some of the many QC tests, high-resolution miniaturized methods suitable for assessment of chemical or radiochemical identity and purity are notably missing. We have been exploring microchip capillary electrophoresis (MCE) as a potential means to fill this gap. We have shown the potential to perform chemical identity and purity analysis by successful separation of the PET tracer [^{18}F]FLT from all of its side products, with comparable limit of detection as HPLC. More recently, we demonstrated first-in-field work to add radiation detection to the MCE system, using a high-resolution positron detector to perform the radiochemical identity analysis of PET tracers.

Microfluidic systems are also useful for the synthesis of radiopharmaceuticals such as radiolabeled peptides and antibody fragments, which provide a means to image disease-specific targets with extremely high specificity. To substantially reduce the high cost of radiolabeling, we have explored the feasibility of using a microdroplet reactor approach. As an example, a thiol-containing RGD peptide was labeled with fluorine-18 in a site-specific manner via the maleimide-based prosthetic group, [^{18}F]FBEM on a microfluidic chip. We have also explored the site-specific radiofluorination of engineered antibody fragments (diabody) for ImmunoPET imaging via this microfluidic approach.

These studies, and other work on small-molecule synthesis, have shown that there are advantages in performing radiochemistry in microdroplets. Active means of

manipulating microdroplets, such as electrowetting-on-dielectric (EWOD) provides more flexibility of reaction implementation than passive methods, but EWOD devices are well known to suffer from a charging effect and the dielectric and hydrophobic layers have been found to suffer defects during harsh chemical reactions. Therefore, a novel droplet actuation mechanism, electro-dewetting, has been developed to address these challenges. Electro-dewetting uses an electric field formed inside a droplet to manipulate the adsorption of ionic surfactant molecules on the solid surface to change the contact angle. The underlying mechanism of this pheromone has been elucidated.

We believe that all the work described here shows the potential for dramatic miniaturization of the complete PET tracer production process, and ultimately increasing the availability of diverse PET tracers for research use, further development, and clinical translation via lowering the cost and complexity of tracer production.

The dissertation of Noel Ha is approved.

Pei-Yu Chiou

Thomas G. Graeber

Seyed Sam Sadeghi Hosseini

Robert Michael van Dam, Chair

University of California, Los Angeles

2018

Table of Contents

1. LIST OF FIGURES

2. LIST OF TABLES

3. ACKNOWLEGEMENTS

I would like to express the deepest appreciation to my research advisor, Professor R. Michael van Dam: Mike continually and patiently conveyed a spirit of adventure regarding research and scholarship. He has shown me, by his example, what a good scientist and person should be. Without his guidance and persistent support this dissertation would not have been possible. I am very fortunate to have Mike as a mentor.

I want to thank all my fellow lab members in van Dam group, whether past or present: Dr. Jimmy Ly, Jason Jones, and Alec Barajas for their devotion, effort, and contribution to our CE projects; Jeffrey Collins and Maxim Sergeev for help with radiochemistry; our brilliant fellow graduate students Philip Chao, Jia Wang, Ksenia Lisova, Alejandra Rios, Travis Holloway for their warm friendship.

I want to thank other members of my doctoral committee, with whom I have been able to establish a dissertation worthy of coming from both the Bioengineering and Pharmacology departments of UCLA and to obtain my doctoral degree.

I would like to thank the administrative team: Sandy Ma, Karen Lum, Stacey Chiong, Emily Fitch, and Erika Corrin for all their help with behind-the-scene issues.

I would like to thank all my friends who have stood by me through this doctoral journey. I will not forget the great times we spent together.

Nobody has been more important to me in the pursuit of this project than the members of my family. I want to thank my godly parents, Suna Hwang and Taewan Ha, for showing me unconditional love and support with prayer. You are always there for me. I am truly grateful for your wise counsel and sympathetic ear. My sister Marinae, has been there for me as well through every crisis, and is an endless source of great love.

Finally, all praise, honor and glory to my Lord Jesus Christ for His richest love and grace for the accomplishment of this journey. He is truly the Road, the Truth, and the Life.

Portions of Chapter 1: Introduction are taken from:

- Noel S. Ha, Saman Sadeghi, R. Michael van Dam. “Recent Progress Toward Microfluidic Quality Control Testing of Radiopharmaceuticals”. Micromachines 8(11): 337, 2017.
- Noel S. Ha, Jimmy Ly, Jason Jones, Shilin Cheung, R. Michael van Dam. “Novel volumetric method for highly repeatable injection in microchip electrophoresis”. Analytica Chimica Acta 985: 129-140, 2017.

Chapter 2: Microfluidic Quality Control Testing of Radiopharmaceuticals is a modified version of:

- **Noel S. Ha**, Saman Sadeghi, R. Michael van Dam. “Recent Progress Toward Microfluidic Quality Control Testing of Radiopharmaceuticals”. Micromachines 8(11): 337, 2017.

Chapter 3: Development of microchip electrophoresis for analysis of radiopharmaceuticals is a modified version of:

- Jimmy Ly*, **Noel S. Ha***, Shilin Cheung, R. Michael van Dam. “Toward miniaturized analysis of chemical identity and purity of radiopharmaceuticals via microchip electrophoresis”. Analytical and Bioanalytical Chemistry. DOI: 10.1007/s00216-018-0924-y, **2018**. **(*Co-first authors**)

Chapter 4: Novel volumetric method for highly repeatable injection in microchip electrophoresis is a modified version of:

- **Noel S. Ha**, Jimmy Ly, Jason Jones, Shilin Cheung, R. Michael van Dam. “Novel volumetric method for highly repeatable injection in microchip electrophoresis”. Analytica Chimica Acta 985: 129-140, 2017.

Chapter 5: Integration of high-resolution radiation detector for microchip electrophoresis is a modified version of a manuscript in progress.

- Jason Jones*, **Noel S. Ha***, Alec Barajas, R. Michael van Dam. “Integration of high-resolution radiation detector for microchip electrophoresis”. **2018** (***Co-first authors**, in preparation)

Portions of Chapter 6: Microscale radiolabeling of Biomolecules are taken from:

- Jeffrey Collins, Christopher M. Waldmann, Christopher Drake, Roger Slavik, Noel S. Ha, Maxim Sergeev, Mark Lazari, Bin Shen, Frederick T. Chin, Melissa Moore, Saman Sadeghi, Michael E. Phelps, Jennifer M. Murphy, R. Michael van Dam. “Producing diverse probes for positron emission tomography with limited resources: Synthesis of 24 ^{18}F-labeled compounds with a single radiosynthesizer”. Proceedings of the National Academy of Sciences (PNAS) 114(43): 11309-11314, 2017.
- Kirstin A. Zettlitz, Richard Tavaré, Jeffrey Collins, **Noel S. Ha**, Wen-Ting K. Tsai, Reiko E. Yamada, R. Michael van Dam, John M. Timmerman and Anna M. Wu. “^{18}F-labeled anti-human CD20 cys-diabody for same-day immunoPETin a model of aggressive B-cell lymphoma in human CD20 transgenic mice”. European Journal of Nuclear Medicine and Molecular Imaging (EJNMMI), **2018,** (Accepted)

Chapter 7: Electrodewetting microfluidic droplet manipulation is a modified version of:

- Jia Li, Noel S. Ha, Tingyi “Leo” Liu, R. Michael van Dam, and Chang-Jin “CJ” Kim. “Electro-dewetting for digital microfluidics”. 2018 (Submitted to Nature, in revision)

4. VITA

EDUCATION

11/2018 (expected)	Ph.D. candidate in Bioengineering (Biomedical Engineering), University of California, Los Angeles, CA. Advisor: R. Michael van Dam (PhD)
05/2016	M.S. Bioengineering, University of California, Los Angeles, CA.
06/2013	M.S. Biomedical Engineering, University of California, Irvine, CA. Advisors: Wendy Liu (PhD), Tigran Khalapyan (MD)
06/2011	B.S. in Materials Science and Engineering (Semiconductor), Sung Kyun Kwan University (SKKU), Seoul, Korea. Advisor: Hoo Jeong Lee (PhD)

ACADAMIC RESEARCH EXPERIECE

2014-2018	Graduate Student Researcher in Crump Institute for Molecular imaging, Dept. of Molecular & Medical Pharmacology, David Geffen School of Medicine, UCLA.
2011-2013	Graduate Research Assistant, Edwards Lifesciences Center for Advanced Cardiovascular Technology, UC Irvine

INDUSTRIAL RESEARCH EXPERIECE

03/2013-08/2013	R&D Engineer at medical device company, Microvention (Terumo USA), Tustin, CA

PUBLICATIONS (PEER-REVIEWED)

- Kirstin A. Zettlitz, Richard Tavaré, Jeffrey Collins, **Noel S. Ha**, Wen-Ting K. Tsai, Reiko E. Yamada, R. Michael van Dam, John M. Timmerman and Anna M. Wu. "^{18}F-labeled anti-human CD20 cys-diabody for same-day immunoPETin a model of aggressive B-cell lymphoma in human CD20 transgenic mice". European Journal of Nuclear Medicine and Molecular Imaging (EJNMMI), **2018 (**Accepted)
- Jimmy Ly*, **Noel S. Ha***, Shilin Cheung, R. Michael van Dam. "Toward miniaturized analysis of chemical identity and purity of radiopharmaceuticals via microchip electrophoresis". Analytical and Bioanalytical Chemistry. DOI: 10.1007/s00216-018-0924-y, **2018**. **(*Co-first authors**)
- **Noel S. Ha**, Saman Sadeghi, R. Michael van Dam. "Recent Progress Toward Microfluidic Quality Control Testing of Radiopharmaceuticals". Micromachines 8(11): 337, **2017**.
- **Noel S. Ha**, Jimmy Ly, Jason Jones, Shilin Cheung, R. Michael van Dam. "Novel volumetric method for highly repeatable injection in microchip electrophoresis". Analytica Chimica Acta 985: 129-140, **2017**.
- Jeffrey Collins, Christopher M. Waldmann, Christopher Drake, Roger Slavik, **Noel S. Ha**, Maxim Sergeev, Mark Lazari, Bin Shen, Frederick T. Chin, Melissa Moore, Saman Sadeghi, Michael E. Phelps, Jennifer M. Murphy, R. Michael van Dam. "Producing diverse probes for positron emission tomography with limited resources: Synthesis of 24 18F-labeled compounds with a single radiosynthesizer". Proceedings of the National Academy of Sciences (PNAS) 114(43): 11309-11314, **2017**.

MANUSCRIPTS IN REVIEW

- Jia Li, **Noel S. Ha,** Tingyi "Leo" Liu, R. Michael van Dam, and Chang-Jin "CJ" Kim. "Electro-dewetting for digital microfluidics". **2018** (Submitted to Nature, in revision).
- Jason Jones*, **Noel S. Ha***, Alec Barajas, R. Michael van Dam. "Integration of high-

resolution radiation detector for microchip electrophoresis". 2018 (*Co-first authors, in preparation)

PATENT APPLICATIONS

- R. Michael van Dam, **Noel S. Ha**, Jason Jones, Jimmy Ly, Stephen Liu and Shilin Cheung. Microscale device and method for purification of radiopharmaceuticals. Patent Application PCT/US17/61611, filed Nov 14, 2017 [Priority data: 62/423,963, filed Nov 18, 2016], International publication WO 2018/093794 A2 on May 24, 2018.
- **Noel S. Ha**, Jimmy Ly, R. Michael van Dam. Volumetric micro-injector for capillary electrophoresis. Patent Application PCT/US17/55607, filed Oct 6, 2017 [Priority data: 62/405,158, filed Oct 6, 2016], International publication WO 2018/067976 A1 on April 12, 2018.
- **Noel S. Ha**, R. Michael van Dam. Method for efficient radiolabeling of biomolecules. PCT/US17/50214, filed Sept 6, 2017 [Priority data: 62/384079, filed Sept 6, 2016], International publication WO 2018/048856 A1 on March 15, 2018.

SELECTED CONFERENCE ABSTRACTS

- Jason Jones*, **Noel S. Ha***, Jeffrey Collins and R. Michael van Dam. "Toward microscale testing of radiochemical purity: development of a microchip capillary electrophoresis system with integrated radiation detector" The World Molecular Imaging Congress (WMIC). September **2018**; Seattle, WA, USA (*Co-first author)
- **Noel S. Ha**, Jimmy Ly, Jason Jones, Shilin Cheung and R. Michael van Dam. "Toward miniaturized QC testing of PET tracers: Chemical and radiochemical purity analysis via microchip electrophoresis". International Symposium on Radiopharmaceutical Sciences (ISRS). May **2017**; Dresden, Germany
- **Noel S. Ha**, Jimmy Ly, Shilin Cheung, R. M. van Dam. "Novel volumetric micro-injector for highly reproducible capillary electrophoresis". The 20th International Conference on Miniaturized Systems for Chemistry and Life Sciences (MicroTAS). October **2016**; Dublin, Ireland
- **Noel S. Ha**, Jeffrey Collins, R. Michael van Dam. "On-chip Microscale Radiolabeling Reduces Precursor Consumption in the Production of Biomolecule-based PET tracers". The World Molecular Imaging Congress (WMIC). September **2016**; New York, NY, USA
- Jeff Collins, **Noel S. Ha**, Mark Lazari, Roger Slavik, Saman Sadeghi, Ken Herrmann, Jennifer M. Murphy, and R. Michael van Dam. "Routine production of >20 ^{18}F-labeled PET Tracers in a single hot cell using the fully automated ELIXYS FLEX/CHEM radiosynthesizer". The World Molecular Imaging Congress (WMIC). September **2016**; New York, NY, USA
- Kirstin A. Zettlitz, **Noel S. Ha**, Wenting K. Tsai, Jeffrey Collins, R. Michael van Dam and Anna M. Wu. "Site-specific ^{18}F-labeling of an anti-CD20 cys-diabody ([^{18}F]FBEM-GAcDb) for in vivo monitoring of B cells by immunoPET". The World Molecular Imaging Congress (WMIC). September **2016**; New York, NY, USA

HONORS AND AWARDS

2009-2010	Departmental scholarship, Advanced Materials Science & Engineering Dept., SKKU
2008-2009	Reciprocal exchange student scholarship, University of Oklahoma (One of three students campus-side)
2007-2008	Honors student scholarship, School of Engineering, SKKU (Selected by university president)
2006-2007	Departmental scholarship, Advanced Materials Science and Engineering Dept., SKKU

1. Chapter 1: Introduction

1.1 Positron emission tomography (PET)

Positron emission tomography (PET) and single photon emission tomography (SPECT) are real-time, 3D imaging techniques that have unparalleled specificity and sensitivity for visualizing biochemical processes in living subjects [1], [2]. The information from a PET or SPECT scan is used clinically in disease diagnosis, prediction of response to therapy, and monitoring of response to therapy [1], [3]–[7]. PET is also an indispensable research tool for uncovering mechanisms of disease initiation and progression, developing new therapies, measuring and optimizing the pharmacokinetic properties of new therapeutic compounds, and evaluating new therapies in clinical trials [8]. PET and SPECT both rely on the injection of a radioisotope-labelled compound, known as a radiotracer or radiopharmaceutical, into the patient that targets specific receptors, enzymes, or proteins and allows their location and density/activity to be measured via radiation detectors during a PET or SPECT scan. PET employs radiotracers labelled with positron ($\beta+$)-emitting isotopes (e.g. F-18, C-11, O-15, N-13, Ga-68, Cu-64, Zr-89, etc.), which release positrons upon decay. These positrons rapidly annihilate with nearby electrons to form two anti-parallel gamma (γ) rays (511 keV each) that are detected by a ring of detectors [2]. SPECT typically utilizes radioisotopes that directly emit γ rays (e.g. Tc-99m, I-123, In-111, etc.) which are detected using a collimator and gamma camera [9]. In both cases, many decay events are detected to enable reconstruction of the three-dimensional radiotracer distribution in the body. Due to the short half-life of PET and SPECT radioisotopes, labeled tracers must be manufactured just prior to imaging (**Figure 1-1**).

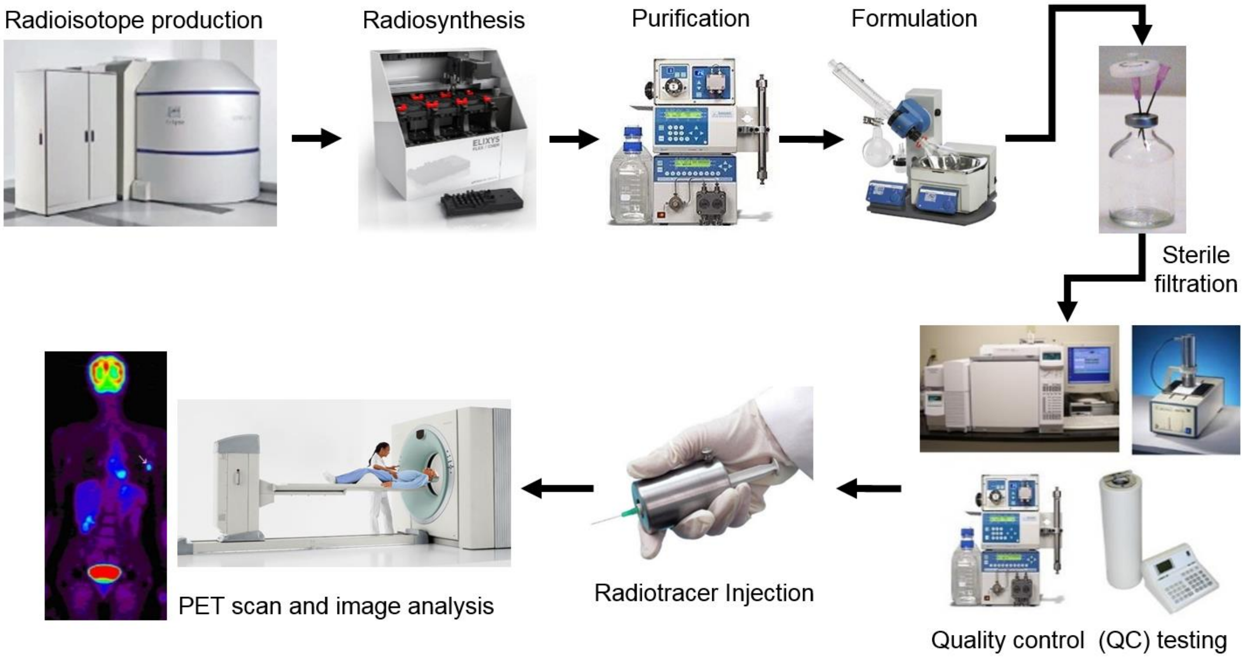

Figure 1-1. Workflow of PET and SPECT tracer production
Production of positron emission tomography (PET)/single photon emission tomography (SPECT) radiotracers for clinical imaging involves generation of the radioisotope (via cyclotron or generator), radiosynthesis, purification (via HPLC or solid-phase extraction), formulation (via evaporative or solid-phase extraction methods), followed by quality control (QC) testing to ensure safety of the formulated radiotracer prior to injection.

1.2 PET tracer production; Radiochemistry

Among many radioisotopes, fluorine-18 (F-18) is the most commonly used radioisotope in clinical PET. This is in part due to its relatively low positron emission energy (maximum 635 keV) and thus short positron linear range in the tissue, resulting in higher resolution than other isotopes. Its half-life (109.8 min) is long enough to allow production, purification, testing, and delivery of radiolabeled tracers, as well as to give access to relatively extended imaging protocols [10], [11]. In addition, the strong covalent bond it forms with carbon atoms results in tracers with good in vivo stability [13].

Numerous methods have been developed for efficient incorporation of F-18 into a variety of structurally diverse compounds. Most methods rely on nucleophilic aliphatic or nucleophilic aromatic substitution reactions starting from [^{18}F]fluoride [14]. In the case of PET, the majority of scans are currently performed using the glucose analog 2-[^{18}F]fluoro-2-deoxy-D-glucose ([^{18}F]FDG) as a wide range of conditions can be detected via altered metabolism [5], [11], [15], but there is a growing interest in visualizing more diverse biological processes and biomarkers using other tracers [16], [17]. Not all tumors show high [^{18}F]FDG uptake. Also, tumors near brain or heart can be difficult to see due to high uptake of [^{18}F]FDG. In addition, inflammatory processes can cause false-positive FDG-PET scans [18]. On top of that, [^{18}F]FDG uptake reveals little about the molecular phenotype of the tumor requiring additional approaches [19].

In combination with other tracers, PET can provide even more specific diagnoses based on the detection of specific underlying molecular alterations associated with many health conditions. PET also provides tremendous benefit in the process of developing new targeted drugs and companion diagnostics for precision medicine, as well as in the development of novel gene- and cell-based therapies [20]. Routine access to tracers other than [^{18}F]FDG could accelerate progress in all of these areas.

1.3 Microfluidics in PET tracer production

PET tracer production requires specialized equipment, infrastructure, technology, and expert personnel, resulting in the high cost and complexity of the production [21]. Currently, PET tracers for clinical PET service are produced in a centralized manner by commercial PET radiopharmacies. Most universities operate in a similar, centralized manner with a core radiochemistry facility to produce PET tracers for research laboratories [21]. By spreading the significant costs over many customers in the production of one tracer, commercial radiopharmacies have significantly lower the cost of [^{18}F]FDG for clinical and research use.

Although many other PET tracers are being used in preclinical settings and some in clinical trials, the cost of these tracers compared to [^{18}F]FDG is prohibitive, especially for non-clinical studies, and cannot be provided at a reasonable price due to relatively low demand and thus inability to coordinate schedules for shared production [22], [23].

To increase the diversity of PET tracers available at low cost will require a fundamental reduction in the production cost, and this requires new technologies.

One approach is miniaturized radiosynthesizers, which have the potential to dramatically reduce the cost of the synthesizer itself, as well as the amount of radiation shielding infrastructure needed for operation. Other emerging technologies, such as automated and microscale quality control testing, will further reduce equipment, personnel, and documentation costs and simplify production.

A key technology driving miniaturization is the use of microfluidics. It has been well established that microfluidic devices offers many advantages for the synthesis of radiopharmaceuticals [24]–[26]. In particular, the small dimensions enable improved control of reaction conditions that can lead to faster and higher yield production, and reduce the reagent consumption and overall cost of the system.

The emerging technology of digital microfluidics is opening the possibility of performing radiochemistry and analyzing radiopharmaceuticals at the microliter scale. In digital microfluidic devices, reagent droplets are controlled electronically, providing high reliability, a compact control system, and flexibility for diverse syntheses with a single-chip design. Keng et al. has demonstrated the successful synthesis of several PET tracers using a digital microfluidic device based on the digital manipulation of droplets between two parallel plates (electrowetting-on-dielectric device) [27].

More recently, a large number of microfluidic systems have been introduced for various steps in PET tracer production including radiosynthesis [23],[28]–[30], radioisotope concentration [31], tracer formulation and concentration [32], and quality control of tracers [33].

2. Chapter 2: Microfluidic Quality Control Testing of Radiopharmaceuticals

2.1 Quality control testing of PET tracers

Since PET tracer is injected into humans and defined as drug, there are strict regulatory requirements for performing quality control (QC) testing of the purified, formulated product of each batch that is produced, to ensure safety before they can be released for clinical use [34], [35]. Specific procedures and requirements for these tests are described in regulatory documents published in each country or region (e.g. U.S. Pharmacopeia (USP) General Chapter <823> [36, p. 823] and U.S. Food and Drug Administration (FDA) 21 CFR Part 212 [37]; European Pharmacopoeia (EP) [38]). Procedures specific to the PET tracer [^{18}F]FDG have been discussed in detail in several review articles [39], [40]. In general, pharmaceutical tests (e.g., pH, color and clarity, chemical purity, residual solvents, pyrogenicity, sterility) are required to ensure physiological compatibility of the final preparation and the absence of microbiological, pyrogenic, chemical or particulate contamination. In addition, radioactive tests (e.g., radiochemical identity, radiochemical purity, radioisotope identity, radioisotope purity, and radioactivity concentration) are required to ensure there are no radioactive or radionuclidic impurities that could interfere with the biodistribution or imaging protocol and to ensure the proper patient dose [41].

Performing and documenting these required QC tests is cumbersome and time-consuming, and requires an array of expensive analytical chemistry equipment and significant dedicated lab space. In addition, for most tests, manual handling, loading, and/or visual assessment of samples leads to significant radiation exposure to personnel and operator-induced variability in the results. In particular Ferguson *et al.*

found that QC personnel received significant radiation exposure, especially due to performing sterility (filter integrity), pH, and chemical/radiochemical purity and identity testing [42]. Furthermore, in contrast to ordinary pharmaceuticals, each batch of short-lived PET radiopharmaceuticals has to be manufactured and tested within a short period of time to prevent significant losses due to radioactive decay [41].

Several companies, including QC-1 (Munster, Germany) [43], Trace-ability (Culver City, CA USA) [44], and ABT Molecular Imaging Inc. (Louisville, TN USA) [45], [46], have been developing QC systems that automatically perform the tests and also handle the majority of the needed equipment calibrations, performance testing, and report generation. After further development and appropriate validation, such automated QC testing systems have the potential to significantly alleviate the labor burden and decrease radiation exposure.

More recently, there have been efforts to miniaturize the instrumentation for QC testing by using microfluidics, much like the efforts to miniaturize other stages of radiotracer production (radioisotope concentration, radiosynthesis, purification, and formulation) [20], [24], [32], [47], [48]. Microfluidic QC systems could lead to significantly lower instrumentation cost and reduction of needed laboratory space. Microfluidic techniques in general also offer many other important advantages over their conventional counterparts, including vastly reduced sample and reagent consumption, shorter analysis times, higher detection sensitivity, and increased multiplexing or parallelism [20], [49]. Furthermore, the fabrication and material cost of many techniques used in microfluidic QC systems can be very low, potentially enabling tests to be implemented with a disposable fluid path. These advantages could be especially helpful in conjunction with emerging technologies that produce smaller batches of PET/SPECT tracers at a time (each requiring QC testing), including dose-on-demand approaches [28].

While the field is still far from achieving a fully-integrated microscale QC testing platform, we highlight in this review the significant progress that has been made in developing microscale implementations suitable for several of the required QC tests for radiopharmaceuticals and pharmaceuticals.

2.2 Miniaturization of quality control (QC) tests

Testing of PET and SPECT radiopharmaceuticals involves several specific measurements to ensure product purity, identity, and biological safety for human subjects [36], [38]. The detailed criteria for passing each test depend on the particular radiopharmaceutical and method of preparation, but in many cases the tests are similar or identical across a broad range of radiotracers. Below, we describe each of the required tests and the conventional method(s) for performing them, and then describe current efforts to directly miniaturize each test or discuss examples from the field of microfluidics that could be implemented to miniaturize the test.

2.3 pH test

pH must be controlled to ensure both the stability of the formulated radiopharmaceutical (to ensure it does not degrade between manufacturing and injection) and its physiological compatibility with the patient. Due to the high buffer capacity of the blood and the relatively small injection volume (typically 1-10 mL), a relatively wide pH range (typically 4.5 – 8.5) is considered to be acceptable from a physiological point of view [41]. The requirement for stability often shrinks the acceptable range. The pH of the formulated radiotracer is most commonly measured using a calibrated electronic pH meter or pH indicator strips.

While there are a myriad of approaches and technologies developed for the measurement of pH, to the best of our knowledge, there is only one report (aside from a brief mention in a patent [50]) on application of a microscale approach to pH measurement of radiopharmaceuticals. Tarn *et al.* described a simple, 3-layer, glass microfluidic device, in which the sample is first combined with a universal pH indicator in an on-chip mixer, and the optical absorbance of the mixture is measured with a spectrometer connected via optical fibers to an extended flow-cell in the chip (**Figure 2-1A**) [51]. The absorption spectrum of the indicator shifts as a function of pH, and a calibration was created using reference standards to relate the pH value to the absorbance at that wavelength. With this device, the pH of small samples (<2 µL) of [^{18}F]FDG solutions could be determined (in the pH range 1 – 13) within a few minutes. A second analysis method was also reported, where the absorbance was monitored at multiple wavelengths to obtain a “fingerprint” of the sample, which could be “matched” with fingerprints of standards. The flow cell is an important part of the implementation as the small dimensions of microchannels can lead to low optical path lengths (OPL) and thus low absorbance values and low detection sensitivity. A variety of detection cell designs have been reported in the literature that incorporate (i) an extended optical path to increase absorbance by the sample, (ii) multiple passes of the illumination light through the sample to increase absorbance, or (iii) or an optical resonator that is filled with the sample. These approaches were reviewed by Rushworth *et al.* [52].

A wide variety of other microfluidic methods for measuring sample pH have been reported [53]. These include miniaturized approaches based on traditional pH indicators or electrochemical cells, as well as approaches based on detection of physical or optical changes in pH-responsive coatings. Many of these approaches could presumably be applied to pH analysis of radiopharmaceuticals, provided they have a sufficiently wide working pH range and fast analysis time. A few examples of these approaches are discussed below.

Maruyama *et al.* used gel microbeads impregnated with pH indicator to measure local pH in the sample immediately surrounding the bead (**Figure 2-1B**) [54]. The gel microbeads, positioned with optical tweezers, changed color within a few seconds when in contact with sample solution indicating the local pH over the range 5.8 – 9.0. Maclin *et al.* reported a similar approach in which the indicator was contained in nanocapsules immobilized in high-porosity polyvinyl alcohol matrix [55], and demonstrated analysis of 30 µL sample volumes within 2 min spanning a pH range of 2.7 to 12.6. An advantage of these approaches is more accurate measurements (since they avoid adding the indicator into solution, which, in high quantities, can affect the pH being measured). Furthermore, because mixing is not required, the implementation can be simpler.

Other approaches for pH measurement are based on detectable changes in a pH-sensitive coating. For example, Mela *et al.* reported the detection of pH by modifying the internal surface of a microfluidic channel with the pH-sensitive fluorescent dye Oregon Green 514 (**Figure 2-1C**) [56]. By monitoring fluorescent emission intensity, pH in the range 2-10 could be measured in real time as an aqueous sample flowed through a 20 x 2 µm channel inside a PDMS/glass chip. Florea *et al.* described a device in which the surface of a microchannel was coated with polyanaline [57]. pH of the sample flowing through the device affects the optical properties of the polymer coating resulting from a reversible protonation/deprotonation reaction. Response could be detected over the pH range 2 – 12 in real time (**Figure 2-1D**).

In addition to optical changes, pH can induce changes in density, volume, and stiffness of coatings such as hydrogels that can be detected as changes in refractive index, electrical resistance, natural frequency of mechanical oscillation, etc. These approaches have been described in a comprehensive review [58]. In one example of these approaches, Trinh *et al.* reported a hydrogel-based piezoresistive pH sensor, in which a hydrogel was placed between a stiff, porous grate and a piezoresistive bending plate transducer [59]. pH-induced swelling of the hydrogel deflected the plate and caused a detectable resistance change, allowing detection of pH values in the range 5.5 – 11 within 12 min.

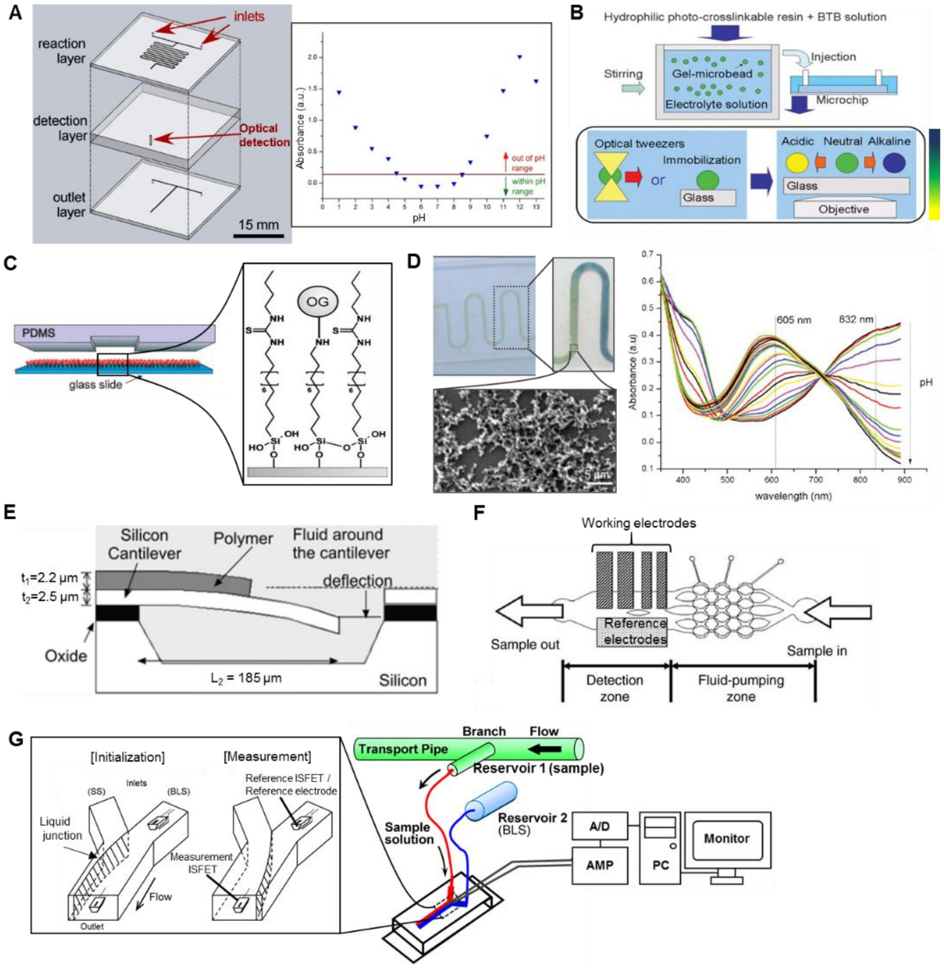

Figure 2-1. Examples of microfluidic pH measurement systems.

Examples of microfluidic pH measurement systems. (**A**) (**Left**) Microfluidic device to mix a sample with a universal pH indicator and then measure optical absorbance in a 3.1 mm long detection cell. (**Right**) Representative absorbance measurements at 551 nm as a function of sample pH. Adapted with permission from [51] Copyright © 2014 The Chemical and Biological Microsystems Society. (**B**) (**Top**) pH-sensing polymer microbeads are prepared by introducing the pH indicator during the cross-linking process. (**Bottom**) The beads are immobilized using optical tweezers or tethered to the surface, and the color of each bead reflects the pH of the local environment. Adapted from [54] with permission of The Royal Society of Chemistry. (**C**) Microfluidic device with internal channel surface coated with pH-sensitive fluorescent molecules (Oregon Green 514). The fluorescence intensity is correlated with pH. Adapted from [56] with permission of The Royal Society of Chemistry. (**D**) (**Left**) PDMS microfluidic channel with polyaniline coating that changes color in response to pH. The zoomed in image shows the response to a pH gradient along the channel. Inset SEM image shows the structure of the coating layer. (**Right**) Absorbance spectra of the polyaniline coating when exposed to solutions of different pH. Adapted from [57] with permission of The Royal Society of Chemistry. **(E)** Micro-cantilever undergoes deflection in response to pH-dependent swelling of a hydrogel polymer coating. Deflection is monitored with a laser beam. Adapted with permission from [60] Copyright © 2003 Springer. **(F)** Thin-film electrodes integrated into a PDMS chip allow pH to be measured based on potential between working and reference electrodes. Adapted with permission from [61] Copyright © 2006 Elsevier. (**G**) Flow-based microfluidic pH measurement system using ion-sensitive field-effect transistor (ISFET) sensors, one acting as a reference and one as a working electrode. Modulation of flow rates moves the liquid junction and allows measurement of the sample solution (SS) after an initialization process using a baseline solution (BLS). Adapted from [62] with permission from MDPI AG.

In a similar approach, Hilt *et al.* [60] reported the use of a hydrogel coating on a micro-cantilever that could respond to changes in environmental pH resulting in a surface stress that deflected the cantilever (**Figure 2-1E**). By measuring the deflection with a laser beam reflecting from the cantilever surface, pH measurements in the range 2.8 – 6.8 were reported.

pH can also be detected via electrochemical reactions, in which the electrical potential is sensitive to the pH of the sample solution in the electrochemical cell. A wide variety of implementations of electrochemical cells have been reviewed [33,40] and a few examples of microscale cells reported for pH measurement are given below. Lin *et al.* developed a microfluidic continuous-flow pH measurement chip by integrating thin-film pH-sensing electrochemical electrodes into in a PDMS chip (**Figure 2-1F**) [61]. The free hydrogen atoms of the sample react with the sensing electrodes (fabricated by sputtering layers of SiO_2–Li O_2–BaO–Ti O_2–La_2O_3 (SLBTLO) on platinum (Pt) electrodes) inducing a detectable change in potential with respect to the reference electrode (Ag electrode with thin coating of AgCl). pH measurements in the range pH 2 to 10 could be made using only ~0.5 µL sample volume and 200 s duration. Yamada and Suzuki developed a flow-based microfluidic pH measurement system using ion-sensitive field-effect transistor (ISFET) sensors for measurement of the proton concentration (**Figure 2-1G**) [62]. Two ISFET sensors and an Ag/AgCl pseudo reference electrode are fitted into a microfluidic Y-junction such that the reference ISFET and reference electrode are always immersed in a stream of baseline solution and the measurement ISFET is immersed in baseline solution or the sample, depending on a switchable flow. Under a continuous flow, sample solution could be measured in <120 s with a wide detection range (pH 1.68–10.0). Though the authors reported 2.0 mL sample consumption per measurement due to filling and flushing the external tubing and syringe pumps, the dimensions of the microfluidic chip suggest the detection volume was < 14 µL, a value that can be compared with other papers.

2.3.1 **Appearance test (Optical clarity test)**

In general, only a clear and colorless, particulate-free solution should be used for injection. Formulated PET and SPECT tracers are generally colorless due to the lack of appreciable absorbance by the tiny amounts of tracer used (e.g. pmol to nmol for a ~370 MBq (10 mCi) single patient dose of a ^{18}F-labeled PET tracer, or nmol to µmol for a >37GBq (>1 Ci) multi-dose batch). Any coloration would indicate a significant quantity of an impurity. Generally, the test is performed manually, via qualitative visual inspection, resulting in variability in the readout.

Using the same microfluidic device as described above for pH testing, Tarn *et al.* reported automation of a *quantitative* optical clarity test for [^{18}F]FDG [51]. A non-clear sample could be detected when the absorbance exceeded that of a reference solution (water). Though this appears to be the only microfluidic implementation of the appearance test applied specifically to the analysis of radiopharmaceuticals, it is likely that any of the other strategies described above based on optical absorbance could also be used to implement a miniature optical clarity test based on the same principle.

2.3.2 Sterility test

According to the FDA document “current good manufacturing practice for PET drugs” [63], even if care is taken to minimize microbiological contamination during synthesis, a drug is considered to be nonsterile until it is passed through a sterilizing grade filter. Generally, radiopharmaceutical production can use commercially available, pre-sterilized filters, provided that the vendor has been shown to be reliable and the filter meets certain specifications. Conventionally, sterility is assessed by inoculating the filtered sample into two types of culture media (soybean-casein digest medium (SCDM) to culture aerobic bacteria and fungi, and fluid thioglycollate medium (FTM) to culture anaerobic bacteria), incubating for ≥14 days, and then looking for formation of colonies [64]. However, because this timeframe is much longer than the half-life of SPECT and PET radioisotopes, the FDA allows a quick, short-term test to be used to enable early release of the radiotracer (though the culture test must still be completed). In the short-term test, the integrity of the filter membrane is assessed (typically via a bubble point test) after completing sterile filtration. In this test, compressed gas is applied to the inlet of the wetted filter and pressure is increased until bubbling appears at the outlet (i.e., the bubble point). If the bubble point exceeds a threshold pressure, then it can be assured that the membrane is intact and pores do not exceed the specified size. A drawback of this test is that the operator has to manually handle the filter membrane and it has been reported that this test results in the largest radiation dose to QC personnel [42].

Although not yet demonstrated specifically for the analysis of radiopharmaceuticals, microfluidics may provide a way to directly assess sterility in a much shorter time than 14 days, and potentially obviate the need for the bubble point test. In the conventional culture test, the long duration is essentially needed for amplification, i.e. to allow many cycles of growth, such that any bacterial colonies could be detected visually. This growth amplification step could be omitted for high-sensitivity microfluidic approaches that enable direct detection of individual microorganisms in liquids [65].

A large number of reports (reviewed in [65]–[68]) have demonstrated the detection of small numbers of bacteria (even single cells). Some strategies rely on PCR amplification of specific DNA sequences, or sensitive assays of specific surface antigens or metabolites. In one example, Jung *et al.* reported an integrated microfluidic device capable of detection and identification of as few as 1 colony-forming unit (CFU) in a 10 µL sample via a sandwich-type assay within 30 min [69]. In the assay, bacteria are bound by two types of particles functionalized with antibodies that target the bacteria. The magnetic particles allow the bacteria to be immobilized using a magnetic field while unbound particles were washed away, and then “barcode” DNA was released from the other particle for analysis by an electrophoretic separation and detection unit. Despite impressive sensitivity and operation speed, such methods may not be suitable for QC testing of radiopharmaceuticals because they detect only the specifically-targeted pathogens rather than *all* pathogens.

This can be partially addressed by incorporating certain types of “universal” PCR primers or bacterial stains that target broad classes of pathogens. For example, Lantz *et al.* reported a high-sensitivity microfluidic device capable of detecting diverse bacteria and fungi down to the single cell level [70]. The sample was stained with the dye

BacLight Green, then a series of plugs (sample, buffer, and “blocking agent”) were injected into a capillary/channel causing aggregation of cells when electrophoretic potential was applied (**Figure 2-2A**). The concentration process, combined with fluorescence measurement over a 10 min integration time resulted in high detection sensitivity.

Rather than relying on specific biochemical markers, other rapid approaches for bacterial detection have been reported that are based on detection of physical properties such as electrical impedance of single cells (reviewed in [71], [72]). In impedance-based flow cytometry, the sample solution is focused down into a narrow channel containing a detector such that at most only one cell at a time flows over a region with detection electrodes. When there is a cell within the detection region, the impedance differs from that of the buffer due to capacitance of the cell membrane and possibly differing resistance of the cell contents. Haandbæk *et al.* reported a resonance-enhanced microfluidic impedance cytometer for detection of single bacteria (**Figure 2-2B**) [73]. After focusing cells to the center of the channel via DEP, bacterial cells passing over downstream electrodes were detected and characterized by frequency and phase shifts an electrical resonator. With the sample flowing at a speed of 0.5 µL/min, the system was able to detect single particles as small as 0.9 µm in diameter, as well as distinguishing different sizes and types (bacteria or polymer bead) of particles.

Though extensive validation and other work would be needed, it seems that microfluidic approaches like impedance cytometry might be capable of performing a rapid sterility test by counting the number of bacterial cells in a sample if throughput can be increased to measure a sufficiently large representative sample (e.g., 100 µL) of the radiopharmaceutical formulation without compromising detection sensitivity. If such a technique could be realized, there would potentially be no need for the filter integrity test.

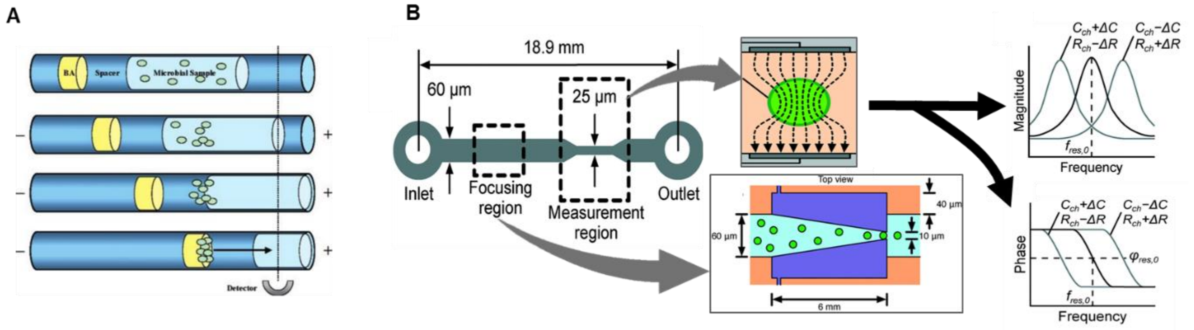

Figure 2-2. Microfluidic methods for detection of bacteria.
(**A**) A microbial sample with “universal” fluorescent stain is concentrated by capillary electrophoresis to improve detection sensitivity. (BA = “blocking agent”). Adapted with permission from [50] Copyright © 2007 American Chemical Society (**B**) Impedance-based bacterial detection chip. Cells are first focused via dielectrophoresis (DEP) to the center of channel for downstream detection. A detectable shift in resonant frequency and phase occur when a single cell or particle passes through the measurement area due to a change in the channel impedance. Adapted from [53] with permission of The Royal Society of Chemistry.

2.3.3 Bacterial Endotoxin test

Bacterial endotoxins, lipopolysaccharides (LPS), are toxic components of the outer membrane of gram-negative bacteria that can cause fever and possibly leukopenia in immunosuppressed patients [41]. Because endotoxins can contaminate a solution even if the bacteria have been thoroughly removed via sterile filtration, it is necessary to test radiopharmaceutical formulations for their presence. According to the USP Bacterial Endotoxins Test (General Chapter <85>) [74], the maximum allowable endotoxin level in radiopharmaceutical injections is 175 EU/V, where V is the maximum volume (mL) of drug administered at the time of expiration (1 EU = 100 pg of Escherichia coli LPS). The conventional test for bacterial endotoxins is based on a multi-step biochemical pathway leading to activation of a clotting enzyme that occurs when bacterial endotoxins are mixed with Limulus amebocyte lysate (LAL) derived from blood cells of horseshoe crabs (Limulus polyphemus or Tachypleus tridentatus) [75]. The enzyme acts on a coagulogen to create a “clot” in the test sample (“gel clot method”) or to increase its turbidity which can be optically detected (“turbidimetric method”). Alternatively, if a chromogenic substrate is added, a color change can be detected (“chromogenic method”). The timescale of clotting, turbidity increase, or color change is related to the endotoxin concentration. Several commercial reagent kits and test instruments are currently available and are routinely used in QC testing of radiopharmaceuticals [75].

One of these commercial systems (EndoSafe, Charles River Laboratories, Wilmington, MA, USA), already in widespread use in testing of radiopharmaceutical formulations, performs a small-scale version of the chromogenic assay in 15 min using disposable ~25 mm x 75 mm microfluidic cartridges pre-loaded with reagents (**Figure 2-3A**) [76]. In this system, a 25 µL sample is loaded on the cartridge, mixed with the LAL reagent and then combined with the chromogenic substrate, incubated, and finally the color intensity is measured over time via a small handheld spectrophotometer-based reader. This system can detect down to 0.005 – 10 EU/mL. Though not specifically applied to radiopharmaceutical analysis, one group demonstrated a similar assay in a microfluidic chip (18 mm W x 62 mm L) made of PDMS (**Figure 2-3B)** [77]. After mixing the sample with reagents outside the chip, a 4 µL sample was injected and result could be obtained after 10 min. To match the capabilities of the EndoSafe device, the PDMS chip would have to be modified to include analysis of a replicate as well as positive controls.

Miao *et al.* reported an electrochemical approach that replaced the optical readout of the standard gel clot assay with an electrical readout [78]. Millimeter-sized screen-printed electrodes were inserted in a small volume of a mixture of the sample and LAL reagent (270 µL) at 37 °C and the electrical current was monitored over time (**Figure 2-3C**). Onset of gel clotting resulted in a rapid drop in current, the timing of which could be correlated with endoxtoxin concentration. Response time was fast (< 100 s) and a detection limit of 0.03 EU/mL was reported.

In addition to miniaturized versions of the standard LAL assay, there has been considerable development of new approaches, including modifications to the standard assay to improve sensitivity, as well as miniature biosensors that detect endotoxins based on binding with surface-immobilized biomolecules (recently reviewed in [75]).

For example, Noda *et al*. a reported a modified LAL assay in which the coagulogen was replaced with a luciferin-modified peptide (benzoyl-Leu-Gly-Arg-aminoluciferin) [79]. When this substrate becomes activated by the LAL cascade (i.e. in the presence of endotoxin), the reaction with luciferase produces luminescence, allowing very sensitive detection. A detection limit of 0.0005 EU/mL was reported in an assay time of 15 min. Though such high sensitivity is not strictly necessary, it may provide the capability to use a smaller sample volume.

Sensor-based methods rely on detection of endotoxin binding, and can produce a signal via fluorescence or luminescence assays, electrical impedance, electrochemical reactions, or mechanical resonators. Though many of the approaches require lengthy procedures to modify/derivatize the LPS prior to detection or have poor sensitivity, there are a few approaches that appear sufficiently fast and sensitive for QC testing of radiopharmacuticals. For example, Su *et al.* demonstrated an impedance-based readout with a detection limit of 0.05 EU/mL within 10 min [80]. The electrochemical biosensor comprised a gold electrode functionalized with an LPS-specific single stranded DNA (ssDNA) aptamer as a probe (**Figure 2-3D**). A good linear relationship between charge-transfer resistance and logarithm of LPS concentration was demonstrated over a wide dynamic range (0.01 – 10 EU/mL). As surface binding sensors are often prone to fouling, non-specific binding, or sensitivity to sample matrix, a thorough characterization of these factors and validation of the testing method would be required.

Finally, detection of endotoxins has also been reported using miniaturized chromatography methods. Makszin *et al.* used microchip electrophoresis (MCE) to separate and detect S-and R-type endotoxin components conjugated with fluorescence dyes. Separation took ~1 min and the limits of detection were 2.6 and 6.9 ng for the S- and R-type endotoxins [81]. Despite sensitive quantitation, the method required significant off-chip processing to perform the conjugation step.

To summarize, there already exist miniaturized methods validated for performing endotoxin testing of radiopharmaceutical formulations. Many other approaches have also been developed for endotoxin testing in other applications, which may offer advantages of speed, reagent cost, or convenience of readout if applied to radiopharmaceutical samples.

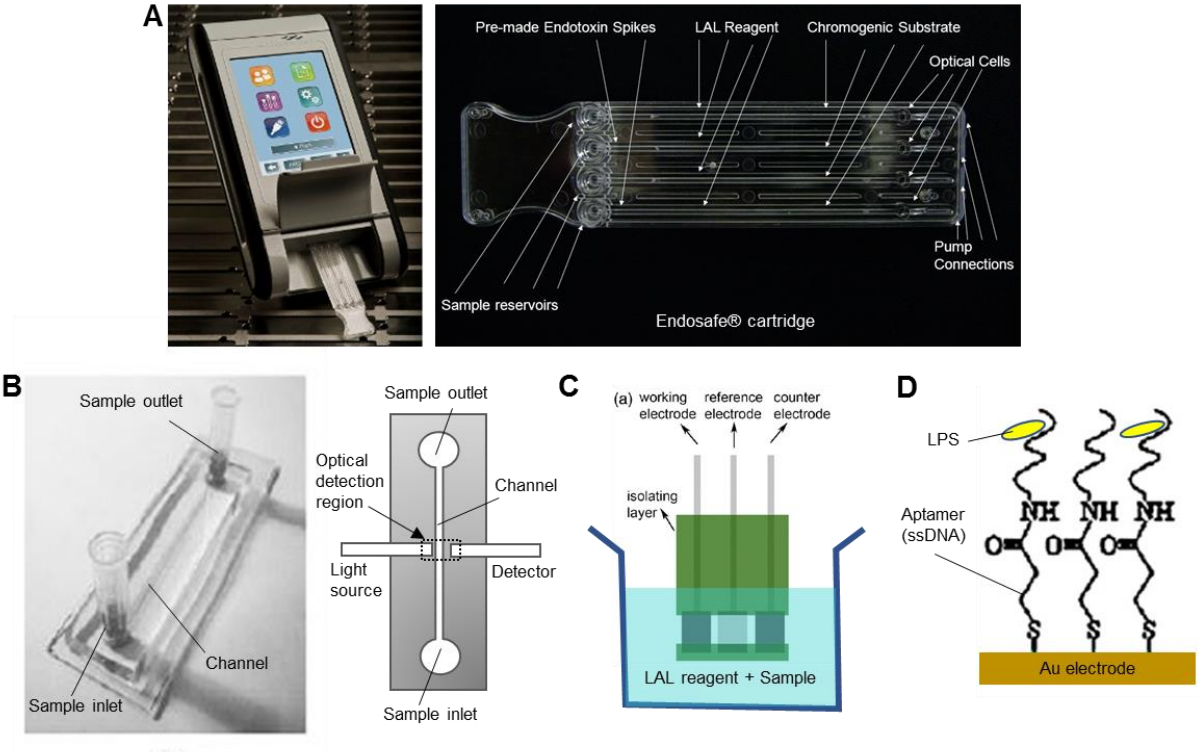

Figure 2-3. Examples of microfluidic devices for bacterial endotoxin test.
(**A**) Commercial LAL assay system (Endosafe®, Charles River Laboratories, Inc.) comprising a portable, hand-held spectrometer (**left**) and ~25 mm x 75 mm disposable microfluidic cartridge (**right**). Adapted from [56]. (**B**) Photograph of microfluidic LAL test chip (**left**) and block diagram illustrating detection method (**right**). Sample mixed with chromogenic substrate is loaded into the microchannel and optical detection is performed in the middle of channel. Photograph adapted with permission from [57] Copyright © 2004 Springer. (**C**) Screen-printed electrodes for electrical-impedance monitoring of standard gel clot LAL assay. Adapted with permission from [58] Copyright © 2013 Elsevier (**D**) Biosensor comprising a gold electrode functionalized with endotoxin-specific aptamer. Binding of endotoxin is detected via impedance spectroscopy. Adapted with permission from [60] Copyright © 2012 Elsevier.

2.3.4 Chemical purity and identity

Chemical purity refers to absence of non-radioactive impurities in the formulated PET or SPECT tracer, including side products as well as residues of other components used in the production process.-The purpose of testing is to ensure that the purification process has reduced residual amounts of impurities to safe levels (i.e. below allowed limits). The required chemical purity tests for radiopharmaceuticals depends on particular synthesis method and only needs to assess reagents added and byproducts expected for the particular synthesis route and conditions.

Though, in rare cases, a specific impurity can be determined via a simplified test (e.g., see Kryptofix test, Section 2.6), impurities are typically determined by chromatographic techniques, i.e. by performing chemical separation prior to detection. For some SPECT and PET radiopharmaceuticals that are labeled by a chelation reaction, the most significant impurity is unlabeled radioisotope, which can be detected via radio-TLC to determine (see Section 2.10). In other cases, impurities are typically quantified using HPLC combined with UV absorbance detection (HPLC/UV) or sometimes other modalities such as pulsed amperometric detection. Recently, analysis of radio-pharmaceuticals has also been performed using ultra-high performance liquid chromatography (UHPLC or UPLC), offering the advantages of faster separation times and more compact separation columns [82], [83]. The identity of each peak in the detected chromatogram is determined by comparison of retention time with reference standards, and the quantity is generally determined from the peak area. For known impurities, the amount present in the sample is compared with allowed regulatory limits. For unknown impurities, so long as the impurities are below the limit of observed adverse effects in preclinical toxicology studies, they may be safe for injection. More specifically, it is not required to identify all impurities if microdosing criteria are met, i.e. their total mass is <100 µg and if the injected dose contains <1% of the pharmacologically active dose (determined using the same formulation as used in preclinical studies).

Miniaturization of HPLC is one approach that could potentially be used for microscale implementation of the chemical purity test, though it has not yet been demonstrated for radiopharmaceuticals. In “microchip HPLC”, the HPLC column, and often elements of the injection valve, are integrated into a microfluidic chip. One implementation uses trapped cylindrical plugs of polymer monolith (formed by *in situ* polymerization) that slide within cylindrical glass microchannels to inject samples into the on-chip polymer monolith column [84] (**Figure 2-4A**). Another implementation that has been commercialized (HPLC-chip, Agilent, Santa Clarita, CA, USA) includes an integrated micro-rotary injection valve with sample enrichment column serving as the injection loop. In this setup samples are injected into an integrated column, flowing to a downstream electrospray emitter to nebulize and transfer the sample to a mass spectrometric detector [85] (**Figure 2-4B**). A recent review discusses the wide range of available microchip HPLC systems [86]. With chip-based HPLC, sample volume and separation time are significantly reduced (usually nL to µL), as is the physical size of the separation medium. However, chip-based HPLC systems still rely on bulky instruments that house the high-pressure pumping system, injection valve actuator, and detection modules, though efforts are underway to shrink these other components as well [86], [87]

Capillary electrophoresis (CE) is another separation method in which a sample is driven through a separation medium by application of an electric field. Species are separated based on electrophoretic mobility in the separation buffer, and sometimes based on additional interactions with functionalized particles within the capillary (capillary electrochromatography, CEC) or by partitioning of analytes between micelles and surrounding buffer (micellar electrokinetic chromatography, MEKC). Unlike HPLC, CE can readily be miniaturized into microfluidic chips that are simple to fabricate and operate without the need for high-pressure pumps [68–70]. Additionally, CE exhibits high separation resolution and can achieve high detection sensitivity, and has been employed in diverse applications such as protein separation and pharmaceutical analysis [91]–[93]. By replacing conventional HPLC methods with microchip electrophoresis (MCE), there is much potential to significantly reduce the size, cost, and complexity of chemical purity testing systems in the future. Furthermore, sample volume is generally reduced by orders of magnitude, and very short analysis times (seconds) have been reported [88], [94], [95].

While there are numerous examples of MCE employed for pharmaceutical analysis [93], [96], there have been very few examples of CE methods, and no examples of MCE methods, applied to the analysis of radiopharmaceuticals. Separation and detection of ^{99m}Tc-labeled SPECT compounds has been performed with capillary zone electrophoresis and isotachophoresis [97]–[101], and use of CE has been suggested for analysis of PET tracers in a patent application [50]. Recently, using the PET tracers [^{18}F]FLT and [^{18}F]FAC as model systems, our group explored the feasibility of using micellar electrokinetic chromatography (MEKC) to separate neutral tracers from neutral impurities, and showed comparable separation and limit of detection as HPLC/UV [102]. We further showed that the system could be implemented as a hybrid MCE device (unpublished work), and that baseline separation of FLT from its known impurities and very repeatable injections could be achieved using only 4 nL of sample (**Figure 2-4C**) [94].

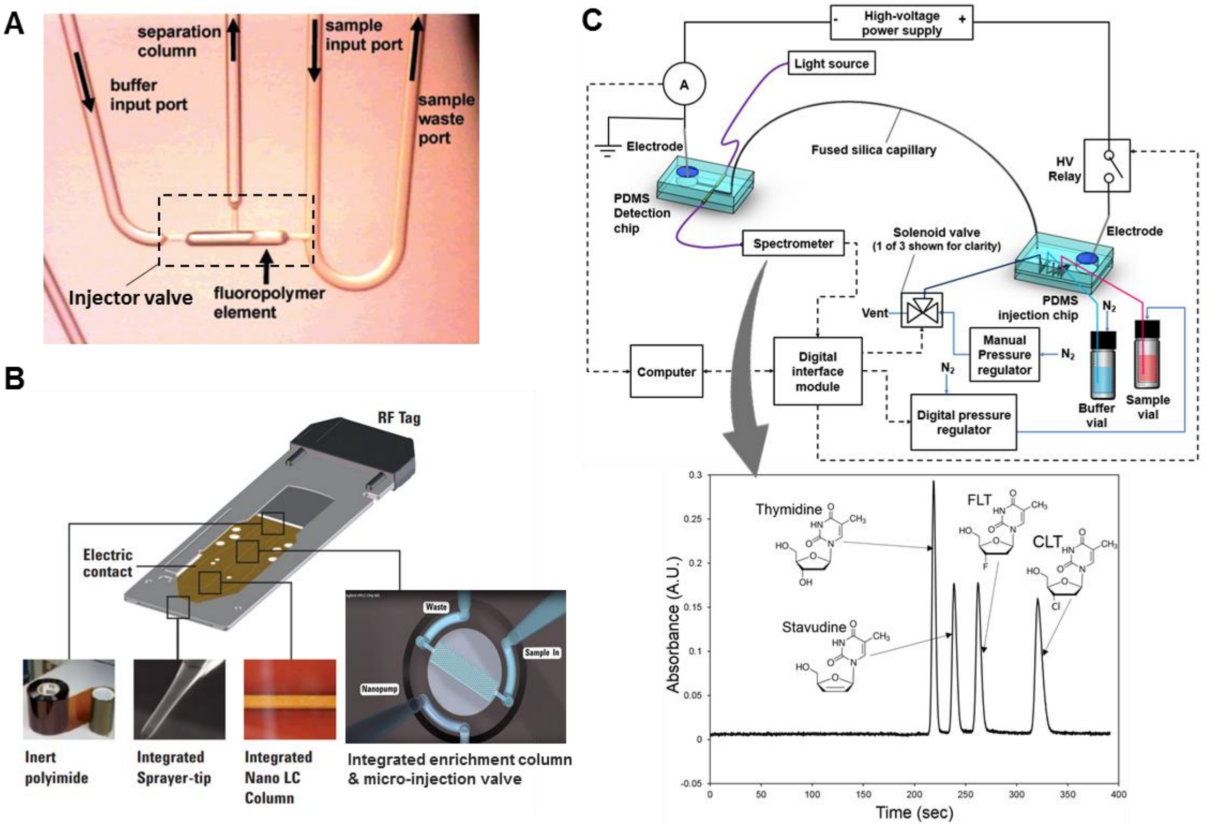

Figure 2-4 Examples of miniature chromatography systems.
(**A**) Microfluidic HPLC system. A sliding fluoropolymer element is used to create a high-pressure valve for sample injection. When the element is in the left position, sample can be loaded via the sample input port. When the HPLC pump is activated, the flowing buffer closes the valve (slides the element to the right) and sweeps the injected sample through the integrated monolith column for separation. Adapted with permission from [64] Copyright © 2005 American Chemical Society. (**B**) Commercial HPLC-chip (Agilent)) includes an integrated micro-rotary injection valve with sample enrichment column serving as the injection loop, for injecting samples into the integrated LC column and downstream electrospray emitter to nebulize and transfer the sample to a mass spectrometric detector. Adapted from [65]. (**C**) Microchip electrophoresis setup with a volumetric sample injection chip, a separation capillary, and an optical detection chip. Inset shows representative electropherogram showing baseline separation of a mixture of 4 compounds. Adapted with permission from [74] Copyright © 2017 Elsevier.

While our work has focused on detection via UV absorbance as a proof of concept, additional modes of detection can be implemented using techniques reported in the literature for pulsed amperometric detection [103], capacitively coupled contactless conductivity detection (C4D) [104]–[106] , refractive index detection [107], or mass spectrometry [108], [109]. For analysis of certain radiopharmaceuticals or impurities (e.g. with low UV absorbance), such alternative detection modes may be essential.

Efforts to miniaturize chemical purity testing for radiopharmaceuticals are just beginning, but chip-HPLC or MCE could provide a means to analyze a wide variety of PET and SPECT tracers with high sensitivity and separation resolution.

2.3.5 **Kryptofix 2.2.2 (K222)**

2,2,2-Cryptand or 4,7,13,16,21,24-hexaoxa-1,10-diazabicyclo [8.8.8]hexacosane, also known by its commercial name Kryptofix 2.2.2 (K222), is frequently used as a phase transfer catalyst in the manufacture of ^{18}F-labeled PET tracers. Radiopharmaceutical formulations must be analyzed for residual amounts of K222 before human application due to its toxicity. The limit specified in the US Pharmacopoeia (USP) is <50 µg/mL and EP limit is 2.2 mg/V (i.e. per patient). Most commonly, residual K222 is assessed qualitatively via a TLC method in which the size and intensity of spot of K222 from the sample solution should not exceed (by visual observation) that of a spotted reference solution [110]. Another method uses a spot test in conjunction with iodoplatinate indicator, and can be completed in 5 min (compared to 30 min for the TLC test) [111]. As with any colorimetric test, there is some risk of non-specific interactions that could interfere with the test result. For example, the spot test is sensitive to tertiary amines, which may be present in the radiotracer itself or impurities, potentially leading to false positives. To avoid such issues, K222 is sometimes analyzed after chromatographic separation. Reports have shown that K222 can be detected via gas chromatography (GC) with a nitrogen detector [112], liquid chromatography with mass spectrometric (MS) detector (LC/MS [113], [114] or UPLC/MS [115]) or HPLC with a UV detector (HPLC/UV) with post-column and pre-column derivatization [116].

Efforts to miniaturize indicator-based tests for radiopharmaceuticals in microfluidic chips have been reported. For example, Charles reported the on-chip optical absorbance-based detection of K222 by first mixing the sample with iodoplatinate reagent then loading the sample into a microchannel [117]. The limit of detection was within range of the allowed limits of K222, though the reported data suggest that further optimization of the test is warranted. Presumably this approach could be combined with an on-chip mixer, and could leverage approaches for high-sensitivity optical detection systems (see Section 2.1) to further improve sensitivity.

Other colorimetric K222 indicator chemistries can likely be used in microfluidic devices as well. Anzellotti *et al.* reported an evaluation of the I_2/I^- indicator for testing PET radiopharmaceuticals and suggested that it could be used to test sample volumes as low as 2 – 25 µL [118]. Experiments showed that the color change occurred within 1-2 s, and that the indicator was unaffected by the presence of several salts or amine-containing PET tracers in the formulation.

Alternatively, the K222 test could potentially be implemented in miniaturized form using microscale chromatographic approaches. For example, we have shown, using capillary electrophoresis, that K222 could be separated from FLT and several impurities and identified and quantified in <2 min [102], though miniaturized detection in an MCE device has not yet been demonstrated.

Although initial efforts have been made to miniaturize the K222 test for radiopharmaceuticals, further development is needed to demonstrate reliability and ease of use for implementation in a radiopharmaceutical QC facility.

2.3.6 Residual organic solvents

Residual solvents in the final formulation could exhibit a variety of toxic effects and the remaining amounts of all solvents used during the synthesis and purification process must be monitored to ensure residual amounts are below safe limits. Typically this test is needed for PET tracers, but often can be omitted for SPECT tracers when produced under aqueous reaction conditions. There is clear guidance on the limits for many possible solvents [119]. For the commonly used class 2 solvents acetonitrile (MeCN), dichloromethane (DCM), and N,N-dimethylformamide (DMF), the allowed limits are 4.1 mg/day (410 ppm), 6 mg/day (600 ppm) and 8.8 mg/day (880 ppm), respectively. Class 3 solvents such as ethanol (EtOH) and dimethylsulfoxide (DMSO) have much lower toxicity, and up to 50 mg/day (5000 ppm, 50mg/V) is allowed for each. Typically, residual solvents are assessed using gas chromatography (GC) in conjunction with a flame ionization detector. Testing can also be performed via HPLC in conjunction with a refractive index detector [45], [120]

For the particular application of radiopharmaceutical analysis, a recent preliminary study suggests that residual solvent impurities might be quantified via raman spectroscopy in a glass microfluidic flow cell [29], though details of the method and its performance have not yet been published. A patent application also mentions the possibility to detect solvents in radiopharmaceuticals via a gas sensor microarray (“electronic nose”) [121] MEMS device, though details are not described [122]. While, in principle, it seems possible that residual solvents could also be assessed via chip-HPLC systems [86], [87] (e.g. with RI detection) or microscale GC systems [123], [124], these approaches have not yet been demonstrated.

Further development is therefore needed to implement a reliable microfluidic detection method for organic solvents with the required performance for testing of radiopharmaceuticals.

2.3.7 **Radioactivity measurement (Radioactivity concentration)**

The concentration of radioactivity in every batch of the final drug preparation at the end of synthesis (EOS) must be measured [34]. This value is needed to determine how much volume to dispense for each individual patient dose (decay-corrected to the expected time of injection). The total amount of radioactivity in the vial containing the final drug preparation is usually measured using a calibrated dose calibrator. In order to determine the concentration, a known volume of the final drug preparation is withdrawn into a syringe, the activity of the syringe is measured, and the concentration then calculated.

To miniaturize this test, the sample can be loaded into a microfluidic channel placed in close proximity to a compact radiation detector. Taggart *et al.* have shown that a small array of silicon photomultipliers (SiPMs) could measure the radioactivity in a sample of PET or SPECT radiotracers ([^{18}F]FDG, [^{68}Ga]gallium citrate, [^{99m}Tc]pertechnetate) contained in an adjacent 40 µL serpentine microchannel after stopping the flow (**Figure 2-5A**) [125]. The effect of different microfluidic chip materials and substrate thicknesses were investigated. In their optimized device, good linearity was observed for the PET tracers over a range of ~0.01 to 100 MBq total activity, though upper and lower limits were not reported. The signal for the SPECT tracer required longer integration time to obtain a reliable reading. Convert *et al.* have demonstrated a miniaturized device for a slightly different application: measuring the radioactivity concentration in the blood of a rodent model for pharmacokinetic analysis of PET and SPECT radiotracers [126]. To maximize detection efficiency, a polymeric microfluidic device with a 0.7 µL microchannel was bonded directly on top of a commercial unpackaged 300 µm thick silicon PIN photodiode, with only 9 µm separation between the sample and detector (**Figure 2-5B**). Limits of detection were not reported, but absolute detection efficiency of the microfluidic geometry was significantly higher compared to a capillary-based setup, and detection efficiencies were close to the theoretical maximum for ^{11}C- and ^{18}F-decay events (47% and 39%, respectively, compared to 50% theoretical maximum), due to the high efficiency of direct positron detection. Dooraghi *et al.* reported radiation measurement of [^{18}F]fluoride and [^{18}F]FDG solutions in capillary tubing or a microchannel to calibrate an automated aliquoting / dose-dispensing system [127]. The detector comprised two 3 mm x 30 mm silicon PIN diodes at different distances from the sample such that the closest detector was sensitive primarily to positron interactions, while the further detector allowed measurement and subtraction of background gamma interactions (**Figure 2-5C**). The dynamic range of detectable activity was measured to be 0.74 – 4400 kBq/µL (0.02 – 120 µCi/µL) and 0.01 – 105 MBq/µL (0.3 – 2830 µCi/µL) for the high- and low-gain electronics configurations, respectively.

Additional compact radiation detection methods have been reported for applications that require a higher degree of spatial information about the radioactivity distribution of positron-emitting samples, but presumably these could be adapted to measure the radioactivity concentration in sample of a formulated PET radiopharmaceutical.

Cho *et al.* reported a system in which a scintillator was placed in close proximity to a PDMS microfluidic chip and scintillation light from positron interactions was detected with a CCD camera [128], [129] (**Figure 2-5D**) Preliminary studies showed that this imaging device is capable of discerning line pairs of printed [^{18}F]FDG solution with separation as low as 300 - 500 µm and quantifying the activity concentration reliably down to 1.48 Bq/mm^2 (40 pCi/mm^2) or 13.32 Bq/mm^2 (360 pCi/mm^2) in 5 min with the use of CsI or plastic scintillators, respectively. Pratx *et al.* reported a different scintillation-based approach known as radioluminescence microscopy [130] in which the sample was placed on a thin scintillator plate, and light produced by positron decay events was measured using a high-sensitivity microscope (**Figure 2-5E**). The spatial resolution, measured using a dried droplet of [^{18}F]FDG (370MBq), was estimated to be 5 µm FWHM, and the minimum detectable activity density was 150 Bq/mm^2 (4 nCi/mm^2). The high sensitivity allowed detection of [^{18}F]FDG uptake in single cells. The maximum detectable activity was not specified.

Cho *et al.* demonstrated an additional measurement technique in collaboration with our group: a sensitive CCD camera was used to detect the Cerenkov radiation emitted as energetic positrons from the sample travel through the surrounding medium [131], [132] (**Figure 2-5F**). Using solutions of [^{18}F]fluoride and [^{18}F]FDG, the system dynamic range was found to be 7.03 – 2740 kBq/mm^2 (0.19 -742 µCi/mm^2) for 5 min acquisitions , though the upper end of the dynamic range could be further improved by using a shorter camera acquisition time and a smaller lens aperture setting, if necessary. The spatial resolution of Cerenkov image was found to be ~200 µm.

Dooraghi *et al.* developed a system based on direct positron detection using a position-sensitive avalanche photodiode (PSAPD) (**Figure 2-5G**) [133]. In a PSAPD, the interaction of a positron creates an electron-hole pair that is amplified by an avalanche affect due to an applied bias across the device, allowing positron interactions to be easily distinguished from thermal noise. Furthermore, a 4-point detector allows localization of the detection event across the substrate. The sample is contained in a chamber on a PDMS microfluidic chip with 50 µm thick PDMS substrate separating the fluid from the detector. For ^{18}F-containing solutions, the lower detection limit was measured to be 0.5 Bq/mm^2 (~14 pCi/mm^2) for a 1 min acquisition and 62 × 62 µm pixel size. The same device has been used to quantify activity in single cells [134] The upper count rate limit was 21 ,000cps (~46 kBq). The spatial resolution ranged from 0.4 mm FWHM at the center of the field of view (FOV), and 1 mm at a distance of 5 mm away from center.

Tarn *et al.* have demonstrated the use of the commercially available miniaturized positron sensor array (Medipix2, Medipix Collaboration) with a pixel size of 55 µm x 55 µm and overall detector size of 14 mm x 14 mm (65k pixels) to measure activity of [^{68}Ga]Ga-citrate solutions in Tygon tubing (709 nL detection volume, 254 µm sample to detector distance). Upper and lower detection limits were not reported but a linear response was observed over the range tested (0.05 – 100 MBq/mL). The detector was also used to measure the activity passing through a silica monolith **(Figure 2-5H**) [135] as described in Section 2.10. Maneuski *et al.* reported the use of a similar detector

(Timepix) for measurement of activity in an adjacent tubing designed to measure the output of a UPLC system [136]. Though complete details of geometry were not provided, if the tubing is assumed to have a standard 1.6 mm (1/16”) outer diameter, then the distance from sample to detector is ~400 µm. Injected samples with concentration as low as 1 kBq/mL could be detected. Sensitivity was found to be much greater than several scintillation-based detetors.

Mapelli *et al.* have reported an interesting detector comprising a serpentine microfluidic channel filled with liquid scintillation material [137], [138] (**Figure 2-5I)**. Each path of the serpentine channel acts as an independent detector to convert radiation into light in one portion of the channel (via the liquid scintillator), and also as a liquid waveguide to guide this light to a distant photodetector in a non-irradiated portion of the device. The idea was to provide improved detector resolution and increased radiation resistance, while achieving efficient optical coupling throughout the system and potentially enable fabrication of low-cost, high-resolution detectors. The photoelectric yield of the chip was measured by exciting the liquid scintillator with electrons from an external collimated ^{90}Sr source and found to be in the order of 1.65 photoelectrons per minimum ionizing particles (MIP) for 200 µm deep microchannels. Presumably this device could be used to measure the activity of radiopharmaceutical samples loaded into an adjacent microfluidic chip.

Another technique that has been used to analyze compounds labeled with C-11, Ga-68, or F-18 in microfluidic channels is autoradiography (**Figure 2-5J**) [139], [140]. Laven *et al.* did not report the detection limit but reported good linearity in the range of ~10 – 180 Bq. The need to first expose then image the phosphorimaging plates could make this approach too slow and impractical for an automated QC testing system, and too bulky for microscale implementation.

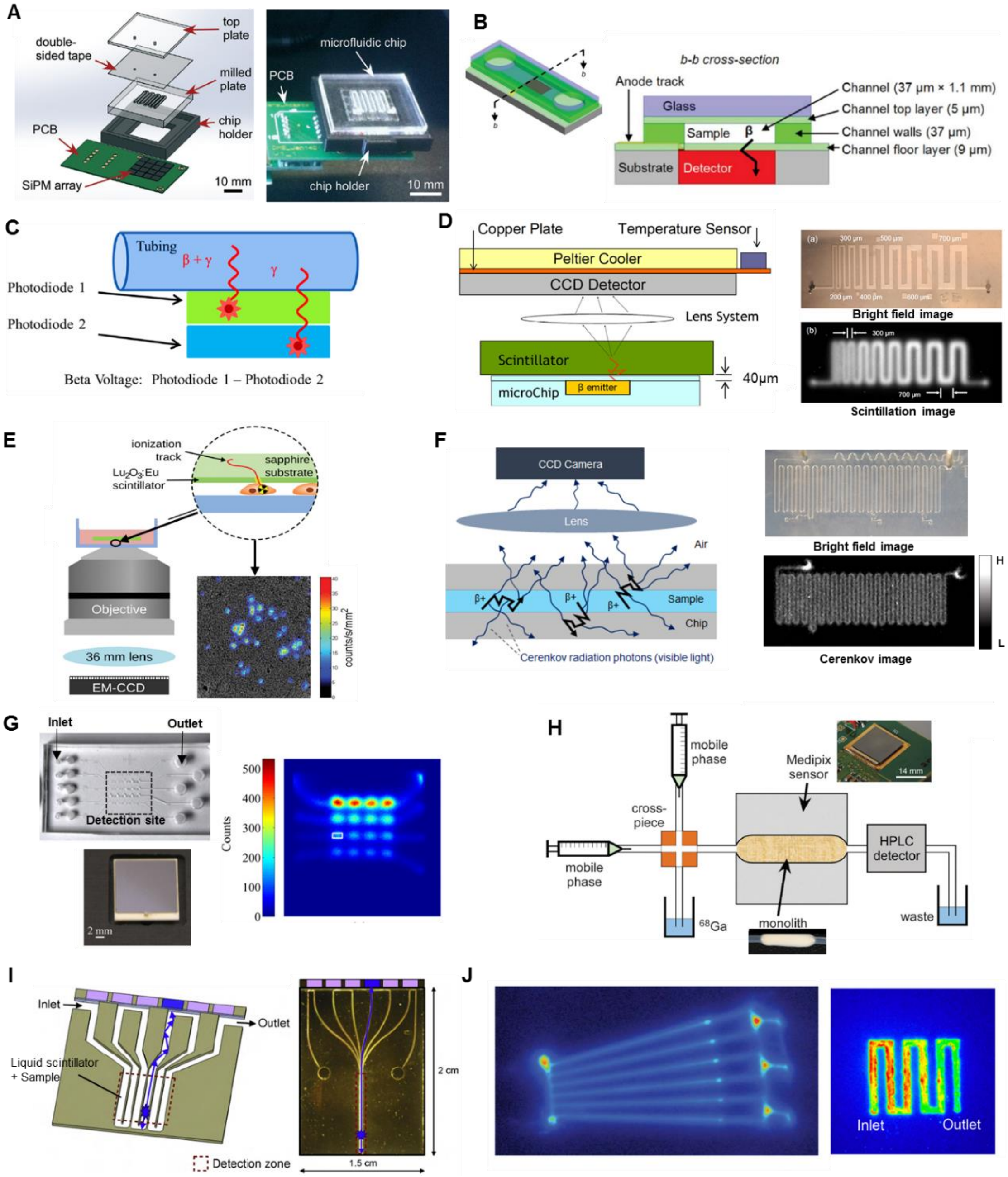

Figure 2-5. Examples of radiation detection methods

(A) (**Left**) Setup of microfluidic chip and silicon photomultiplier (SiPM) array for measurement of radioactivity and half-life of a sample. (**Right**) Photograph of the final chip setup on the SiPM array. Adapted from [125] with permission of the Royal Society of Chemistry. (**B**) Device for positron detection from blood samples in a microchannel bonded to a silicon PIN photodiode. Adapted from [126] with permission of the Royal Society of Chemistry. (**C**) Dual silicon PIN photodiode detection of a sample in a channel or tubing. Photodiode 1 responds to both positrons and gamma rays, while photodiode 2 responds only to gamma radiation, allowing subtraction of the background gamma signal. Adapted with permission from [127]. Copyright © 2016 Springer. (**D**) Scintillator based detection. A scintillator was placed in close proximity to a PDMS microfluidic chip and scintillation light from positron interactions was detected with a CCD camera. Adapted with permission from [128] Copyright © 2007 IEEE. (**E**) Radioluminescence imaging. Scintillator light output is observed via sensitive microscope as radioactive decays occur in sample. Adapted with permission from [141] Copyright © 2015 John Wiley & Sons, Inc. (**F**) Cerenkov imaging. (Left) Cerenkov radiation is emitted as energetic particles travel through the liquid or chip material. (Right) Bright-field and Cerenkov images of 200 µm-wide microchannel filled with [^{18}F]FDG solution. Adapted from [131] with permission of IOP PUBLISHING, Ltd. (**G**) Beta-box imaging. (Top left) Microfluidic chip containing multiple sample chambers is placed on the detector; (Bottom left) Photograph of position sensitive avalanche photodiode (PSAPD) detector; (Right) Resulting image when sample chambers are filled with varying concentrations of [^{18}F]fluoride. Adapted from [133] with permission of IOP PUBLISHING, Ltd. (**H**) System for measuring radioactivity in a silica-based monolith column placed above a Medipix sensor. Adapted from [135] with permission of the Royal Society of Chemistry. (**I**) Microfluidic channel filled with liquid scintillator that acts an array of scintillation detectors connected by liquid waveguides to photodetectors. Adapted with permission from [137] Copyright © 2010 Elsevier. (**J**) Autoradiography (phosphor imaging system). (Left) Autoradiography image of adsorbed radiolabeled peptide on the channel surfaces of a plastic microfluidic chip. Adapted from [139] with permission of The Royal Society of Chemistry. (Right) Autoradiography image of [^{18}F]fluoride trapped in the serpentine channel of an electrochemical cell. Adapted with permission from [140] Copyright © 2013 Elsevier.

The examples described here represent a wide variety of detection approaches that may be suitable for measuring radioactivity in microchannels. With further development, it is likely that several of these approaches could provide a compact means to perform radioactivity measurements for the radioactivity test (as well as some of the tests below).

2.3.8 **Radionuclidic purity and identity**

The radionuclidic purity is the ratio of the desired radionuclide activity to the total activity. The purpose of testing is to ensure that the radiopharmaceutical is not contaminated with other radionuclides, that could make the resulting PET/SPECT images difficult to interpret, or, in the case of long-lived isotopes, could cause harm to the patient. For example, SPECT and PET tracers labeled with generator-produced radionuclides can contain contamination by radioactive parent compounds. In general, the radionuclidic identity can be confirmed by measuring the half-life of the product, and the radionuclidic purity can be measured by a gamma spectrometer with a multichannel analyzer (e.g. based on sodium iodide scintillation detector or high-purity germanium detector). The half-life is determined by taking at least 3 radioactivity measurements of a sample using a dose calibrator (with the same geometry for each measurement), and then calculating half-life via a non-linear fit to the radioactivity decay equation [41]. For highest accuracy, the measurements should be carried out as far apart in time as practical. The radionuclidic purity is determined by obtaining a gamma spectrum of the sample, and matching this spectrum (after background spectrum is subtracted) to the expected energy spectrum. Each radionuclide has a characteristic gamma spectrum; for example, positron-emitting isotopes in PET tracers have a peak at 0.511 MeV due to positron annihilation, plus additional peaks corresponding to other decay modes, if applicable. Since some positron emitters have a very short half-life, the USP and EP allow PET radiopharmaceuticals to be released before the radionuclidic identity test is completed on each batch, in which case periodic tests of samples prepared in the same way would be necessary.

The half-life test can be miniaturized using an integrated radiation detector to measure the radioactivity of a sample in a microchannel in a consistent geometry multiple times. Taggart *et al.* used their SiPM array platform to measure not only the radioactivity concentration as described above but also the half-life of microfluidic samples [125]. Accurate half-life measurements were achieved for [^{18}F]fluoride and [^{18}F]FDG solutions based on 5 min measurements taken over a time period of several hours, but reliable values could not be obtained for calculations based on shorter measurements (e.g. 30-60 s) taken over a more realistic 20 min timespan without constraining the exponential fit. It is possible that performance could be improved with further optimization. In addition, any of the microscale radiation detection approaches described in Section 2.8, depending on activity level and geometry of the sample, could be considered for microscale implementation of the half-life test.

To the best of our knowledge, a microscale implementation of the radiouclidic purity test has not yet been demonstrated, though perhaps a microscale gamma spectrometer could be implemented using similar technologies to those discussed in Section 2.8, provided the radiation detector has adequate energy resolution.

2.3.9 **Radiochemical purity and identity**

The radiochemical identity of a positron-emitting radiopharmaceutical is generally determined after chromatographic separation by determining the retention time (radio-HPLC), retardation factor (radio-TLC), or migration time (radio-CE) of the main radioactivity peak (corresponding to the radioactive product), and comparing to that of a reference standard to confirm structural identity of the radiopharmaceutical.

In addition to confirming the identity of the product, it is also necessary to ensure the absence of radioactive impurities. Radiochemical purity is defined as the ratio of the activity of the radionuclide concerned, which is present in the desired chemical form, to the total activity of that radionuclide present in the radiopharmaceutical preparation. Any radiochemical impurity can potentially affect the biodistribution of the radiopharmaceutical giving a misleading imaging result. In general, the radiochemical purity should be >95%, though in the case of [^{18}F]FDG, USP specifies >90% as acceptable.

Typically, radiochemical identity and purity are determined via HPLC with a radiation detector positioned at the end of the column (radio-HPLC). While the same instrumentation can be used for the chemical purity test, the radiochemical identity and purity tests are often run on a sample that is spiked with a non-radioactive reference standard, while the chemical purity test is carried out on an unadulterated sample. The standard is used to confirm the radiochemical identity by matching retention times of the radiation and UV absorbance peaks in the chromatogram. In addition to radio-HPLC, analysis by radio-TLC may also be necessary for accurate determination of radiochemical purity since certain radioactive species such as [^{18}F]fluoride can be under-represented in HPLC [142]. In the case of some PET and SPECT tracers labeled via chelation reactions, where only the product and non-chelated radionuclide are expected in the final formulation, radio-TLC may be sufficient (without radio-HPLC) for determination of purity.

Similar to the corresponding non-radioactive tests, there is interest in developing miniaturized versions of the radiochemical identity and purity tests due to the bulkiness of radio-HPLC, radio-TLC, and radio-CE systems. As discussed in Section 2.5, HPLC and CE can be miniaturized into chip-HPLC or MCE format, and potentially these techniques could be integrated with one of the compact radiation detection approaches described in Section 2.8 to measure the output of the separation column or separation channel, respectively. To the best of our knowledge, such integration has not yet been reported.

Some efforts have been made to replace traditional HPLC/UPLC radiation detectors with more compact detectors, which could be a step in this direction. For example, the Timepix detector reported by Maneuski *et al.* [136] was suitable for measurements at the output of a UPLC system and showed a wider dynamic range and improved sensitivity compared to a PMT detector with either CsF or BGO scintillator.

Tarn *et al.* have used a Medipix detector to detect radioactivity within a porous silica monolith embedded in tubing with the goal of real-time imaging of separation processes. The detected signal was higher for a sample of [^{68}Ga]Ga-citrate passing through the monolith than the signal observed with a traditional radio-HPLC detector (NaI scintillator / PMT) positioned downstream in the tubing. In addition, the accumulation of activity could be measured as [^{68}Ga]Ga^{3+} was trapped on the monolith, as could the reduction in activity when the monolith was eluted. Maneuski *et al.* also demonstrated the spatial imaging capabilities of the Timepix detector in the context of radiochemical separations. The radioactivity distribution along a conventional radio-TLC plate containing an unspecified ^{18}F-labeled sample was measured with sub-mm resolution by placing it adjacent the detector [136]. Imaging of three parallel ^{18}F-solution-containing tubes was also demonstrated, perhaps in anticipation of performing chromatographic separations in channels in the future. Spatially-resolved radiation detection was also mentioned in a patent by Hansteen *et al*. [50] to monitor separation of radiopharmaceuticals in a capillary to determine radiochemical purity, though details were not provided.

While some steps have been taken toward miniaturized implementation of radiochemical identity and purity tests, much development is still needed in this regard.

2.3.10 Molar activity

Molar activity (often called “specific activity”) is a measure of the amount of radioactivity per molar amount of the radiopharmaceutical [3]. For certain radiopharmaceuticals, such as [^{18}F]FDG, radiolabeled amino acids, or fatty acids that visualize metabolic processes, molar activity determination is not crucial since these radiotracers have natural physiologically abundant levels of nonradioactive counterparts in vivo, especially in circulation. However, for receptor-binding radiotracers, radiolabeled mAbs, and peptide hormone analogs, a relatively high molar activity is crucial. Conventionally, for most organic radiopharmaceuticals, the concentration (total number of moles per volume) is determined based on analytical HPLC after creating a calibration curve using known concentrations of an ultra-pure reference standard. If radioactivity concentration is also known, then molar activity can easily be calculated.

Though it has not been demonstrated, molar activity measurement can likely be miniaturized by combining aforementioned techniques for measuring concentration (chemical purity test, Section 2.5) and radioactivity concentration (radioactivity test, Section 2.8). High-sensitivity and accuracy will be needed to measure the concentration, as the molar amounts can be very small (e.g. pmol to nmol for ^{18}F-labeled PET tracers).

2.4 Outlook

We have reviewed various microfluidic implementations of the QC tests for PET and SPECT radiopharmaceuticals, or techniques that could potentially be implemented to perform these tests (summarized in **Table 2-1**). It is encouraging that viable approaches for ultra-compact implementation of many of the required tests have been demonstrated at least as a proof of concept. In some cases, the desired performance has already been demonstrated, and/or significant reductions in sample consumption have been reported.

However, in most cases, considerable development and optimization efforts will be needed to increase reliability, speed, sensitivity or other measures of performance up to the rigorous requirements of clinical testing. In addition, in cases where the method of detection is fundamentally changed (e.g. sterility testing based on counting of individual bacterial, assessment of chemical/radiochemical purity via new chromatographic approaches such as MCE, and detection of residual solvents via Raman spectroscopy or an “electronic nose”), extra efforts may be required to demonstrate equivalence (or superiority) to currently-accepted test methods.

Once individual tests have been perfected, efforts will be needed to integrate them into a unified system that performs all tests, data collection, and report generation in a fully-automated manner. Integrated systems with some degree of microfluidic elements have been suggested in patents and patent applications [50], [122]. One approach would be to integrate all sample channels and detectors into a single lab-on-a-chip device, and develop a means to aliquot the original sample and distribute portions to each testing area. A challenge in splitting the sample and delivering aliquots to various detection systems via fixed fluid pathways is the possibility of cross-contamination from one sample to the next, which may require extensive cleaning protocols and cleaning validation. One advantage of microfluidics is that many of the fabrication methods and materials used can be very low cost, enabling tests to be implemented in disposable fluid paths. Leveraging such features could eliminate the need for cleaning, and could reduce the required maintenance, further simplifying the testing process and overall QC testing platform.

If realized, integration of microscale QC tests on an automated platform would allow for unified QC system validation, eliminate operator-induced variation, significantly reduce radiation exposure to personnel, and streamline the overall workflow. As increasing numbers of the thousands of known tracers [16], [17] move into the clinic, and as new technologies such as microfluidic systems enable more widespread production of tracers on demand [21], [23], [48], [143], it will become increasingly important to have an integrate QC testing platform that simplifies and reduces the cost of QC testing.

Though we have focused on the special needs of radiopharmaceutical analysis, where sample volume and total duration are extremely limited, the methods described here could likely also be applied to the analysis of non-radioactive pharmaceuticals, and may offer significant advantages in terms of speed and cost.

Table 2-1. Summary of required QC tests, the conventional method(s) used, and typical specifications.

In addition, examples of microfluidic approaches to perform each test are listed. Note we have indicated in italics approaches that have not been demonstrated/proven, but may be possible in principle. Abbreviations: HPLC/UV = HPLC with UV absorbance detector, HPLC/RI = HPLC with refractive index detector, etc.

QC Test	Conventional method(s)	Typical acceptance criteria	Examples of microfluidic suitable approaches
pH	pH indicator strips; electronic pH meter	4.5 < pH < 8.5	UV absorbance of sample + indicator [51], [54], [55] UV absorbance of pH-sensitive surface [57] Fluorescence emission from pH-sensitive dye/surface [56] Hydrogel-based pH sensing (physical or electrical change) [58]–[60] Electrochemical cell [61], [62]

Appearance (color / clarity)	Visual	Clear, colorless, particulate-free	UV absorbance of sample [51]
Sterility	Short term: filter integrity test (e.g. bubble point test); Long term: Bacterial culture	Long term: no bacterial growth observed	Fluorescent detection of “universal” dye that binds to bacteria [70] Electrical impedance detection of individual bacteria [71]–[73]
Bacterial endotoxin	LAL test	175 EU/V	Variations of LAL assay (UV absorbance detection [76], [77], electrical impedance detection [78], bioluminescence detection [79]) Detection of endotoxin binding to surface [75], [80] MCE/fluorescence [81]
Chemical identity/ purity	HPLC/UV	Varies	MCE/UV [94] *Chip-HPLC/UV*
Kryptofix 2.2.2	Color spot test	<50 µg/mL (USP); 2.2 mg/V(EP)	UV absorbance of sample + indicator [117], [118] *MCE/UV* *Chip-HPLC/UV*
Residual organic solvents	Gas chromatography ; HPLC/RI	Varies (e.g., MeCN 4.1 mg/day, EtOH 50 mg/day, DMSO 50 mg/day, DCM 6 mg/day, DMF8.8 mg/day)	*MCE/RI* *Micro-GC* *Electronic nose* [121]
Radioactivity concentration	Dose calibrator	Varies	Solid-state detectors (SiPM [125], PIN diode [126], [127], PSAPD-based detector [133], [144], Medipix/Timepix detector [135], [136]) Cerenkov imaging [131], [132] Scintillator-based detectors (CCD imaging [128], [129], radioluminescence microscopy [130], [141], liquid scintillator with photodetector [137])
Radionuclidic identity	Half-life measurement with dose calibrator	Varies (e.g. 105-115 min for ^{18}F-labled tracers)	Radiation detector (half-life measurement) [125] *Potentially some of radiation detectors listed under “Radioactivity concentration” can be used*
Radionuclidic purity	Gamma spectrometer	Match expected energy spectrum	*Potentially some of radiation detectors listed under “Radioactivity concentration” can be used*
Radiochemical identity and purity	Radio-HPLC; radio-TLC	>95%; (>90% for [^{18}F]FDG)	Porous silica monolith with Medipix positron detector array [135] TLC plate with Timepix positron detector array [136] *MCE / positron detector Chip-HPLC / positron detector*
Specific activity	Radio-HPLC and dose calibrator	Varies	*MCE/UV and radioactivity measurement* *Chip-HPLC/UV and radioactivity measurement*

3. Chapter 3: Development of microchip electrophoresis for analysis of radiopharmaceuticals

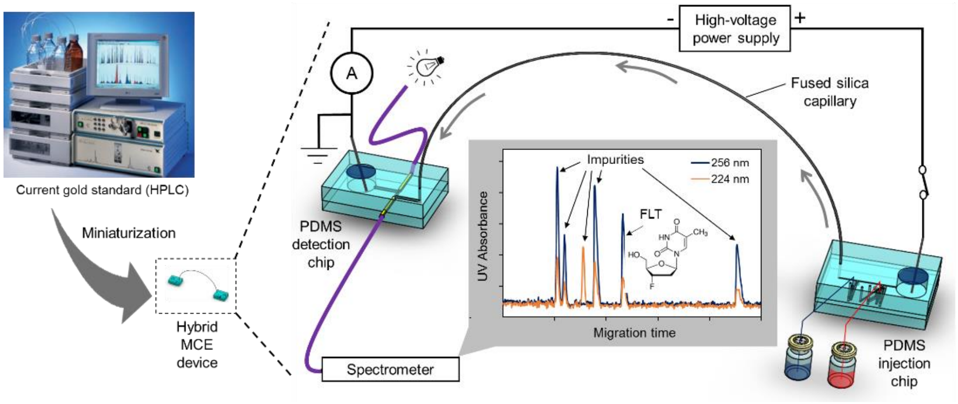

Background: Capillary electrophoresis (CE)

3.1 Capillary electrophoresis

Capillary electrophoresis (CE) is a powerful separation technique with high separation efficiency, flexibility in separation mechanism, low consumption of sample and reagents, and simple instrumentation [145], [146]. CE is employed in diverse applications including DNA and protein separation [92], [93], [147], detection of disease biomarkers [148], [149], environment monitoring on earth and other planets [150], [151], food (e.g. wine) analysis [152], and pharmaceutical analysis [153]–[155]. Unlike other separation methods such as high-performance liquid chromatography (HPLC), CE can more readily be miniaturized using microfluidic chip technology, microchip electrophoresis (MCE) [88]–[90], [156]. This is especially important for applications where compactness, portability, and/or low cost are needed. Miniaturization confers even further advantages, including lower sample consumption, improved resolution, shorter separation times, improved reproducibility (e.g. from improved temperature control), and increased sensitivity and diversity of detection methods [157]–[159].

3.2 Introduction: MCE for analysis of PET tracers

Microscale capillary-electrophoresis (CE)-based devices are increasingly being used for high-resolution separations where portability, ease of integration, or small sample size are of particular importance. Recent examples include environmental analysis [160], biomolecular separations [161], [162], and mobile heath diagnostics [163].

Another field that can benefit from the advantages of MCE devices is nuclear medicine, particularly in assessing patient safety of freshly-prepared batches of short-lived radiolabeled imaging tracers for positron-emission tomography (PET) or single photon emission computed tomography (SPECT). PET and SPECT are real-time, 3D medical imaging techniques with exquisite specificity and sensitivity for visualizing particular biological/biochemical processes depending on the tracer used.

Since PET tracers are classified as drug products by regulatory agencies, they must pass stringent quality control (QC) tests after their production for safety of the patient prior to injection (see 2.2 Miniaturization of quality control (QC) tests). Performing and documenting the tests is cumbersome and time-consuming, and requires an array of expensive analytical chemistry equipment and significant dedicated lab space, and there is considerable interest in the development of automated and lower-cost approaches.

By replacing conventional analysis techniques with lab-on-a-chip technologies, it may be possible to achieve significant reductions in the size, cost, and complexity of automated QC testing platforms, and potentially to increase sensitivity [161], [164]. Commercial microscale devices already exist for testing of endotoxins [76], and there have been recent efforts to miniaturize some of the other tests, including radioactivity measurement [125], radioisotope identity (half-life) test [125], pH test [51], color and clarity test [51], and Kryptofix 2.2.2 test [117]. While these results represent an impressive step forward, high-resolution miniaturized chromatographic methods, suitable for assessment of chemical or radiochemical identity and purity across a wide range of tracers, are notably missing. Due to the potential presence of several impurities in each batch of PET tracer, and due to the wide variety of tracers and synthesis methods, performing these tests will likely require some kind of chromatographic separation followed by a radiation detector (e.g. gamma rays or positrons) and additional detectors for non-radioactive species (e.g. UV absorbance, refractive index, or pulsed amperometric detectors) to quantify each compound and ensure it is below permitted limits. The identity of each peak can be determined by matching the retention time to a reference standard (or by co-injection of the standard), or, in rare cases, via a mass detector.

Here we focus on the development of a microscale CE-based device to replace the gold standard approach of high-performance liquid chromatography (HPLC) for this critical and challenging component of QC testing. We have been exploring CE methods due to the possibility of microchip implementation and corresponding reductions in size, cost, and complexity of the overall QC system. Microchip electrophoresis (MCE) has been shown capable of separating a vast range of analytes including large biomolecules (e.g. nucleic acids, proteins), peptides, and inorganic ions and chiral molecules [157], [165] simply by tuning the separation conditions. The versatility and separation power of CE have been noted to be equal to HPLC, or even better in some applications [96]. CE also avoids the use of high pressures, which simplifies the interface with other system components and eliminates the need for bulky and expensive high-pressure valves, pumps and fittings. Additional advantages of CE are the ability to miniaturize the QC system into a microfluidic chip measuring 25 mm x 75 mm or smaller that is operated via a compact electronic control system and power supply, and the extremely tiny sample consumption (typically nanoliters).

Conventional-scale CE separation of several ^{99m}Tc-labeled SPECT species from impurities has been reported [101], and we recently showed that two ^{18}F-labeled PET tracers, namely 3'-deoxy-3'-[^{18}F]fluorothymidine ([^{18}F]FLT) and 1-(2’-deoxy-2’-[^{18}F]fluoro-β-D-arabinofuranosyl) cytosine ([^{18}F]FAC) can be readily separated from impurities, including Kryptofix 2.2.2 (K222), using MEKC [166]. Compared to traditional HPLC/UV, we observed similar separation resolution and limits of detection (LOD), but reduction in analysis time in some cases, and several orders of magnitude reduction in buffer and sample consumption. (In typical HPLC analysis of radiopharmaceuticals, sample volume is on the order of 10-100 μL, the flow rate is 1-2 mL/min, and the analysis time may be 5-30 min, consuming 5 – 60 mL of mobile phase. On the other hand, in MCE, the buffer consumption can be as low as 100 μL and sample injection volume is typically in the nL range or lower.) However, to the best of our knowledge, there have been no reports on the miniaturization of these approaches to analyze chemical species relevant to the testing of radiopharmaceuticals. Here we describe a proof-of-concept hybrid microfluidic CE device consisting of a hydrodynamic injection chip, a separation capillary, and a microfluidic optical absorbance detection chip to perform chemical identity and purity analysis of FLT and its known impurities.

Potentially, with integration of a radiation detector in the future, this approach could also be used for radiochemical identity and purity tests. In addition, this approach could enable the fluid path to be inexpensive and disposable, reducing maintenance and eliminating the need for cleaning, further simplifying the testing process.

3.3 Materials and Methods

3.3.1 Miniaturized Capillary Electrophoresis system

We combined the three key components (injection, separation, and detection) into a hybrid MCE system (**Figure 3-1**). One microfluidic chip, used for sample injection and containing the anode, was connected to the upstream side of a 60 cm long, Teflon-coated fused silica capillary (75 µm I.D., 375 µm O.D; Polymicro, Phoenix, AZ, USA). A second microfluidic chip, used for sample detection and containing the cathode, was connected to the downstream side of the separation capillary. The capillary was connected to each chip via a port perpendicular to the channels within the chip.

All electronic components were connected to a digital acquisition (DAQ) module (USB 6211, National Instruments Corporation, Austin, TX, USA). A custom-written LabVIEW program (National Instruments Corporation, Austin, TX, USA) was used to coordinate the timing of all functions.

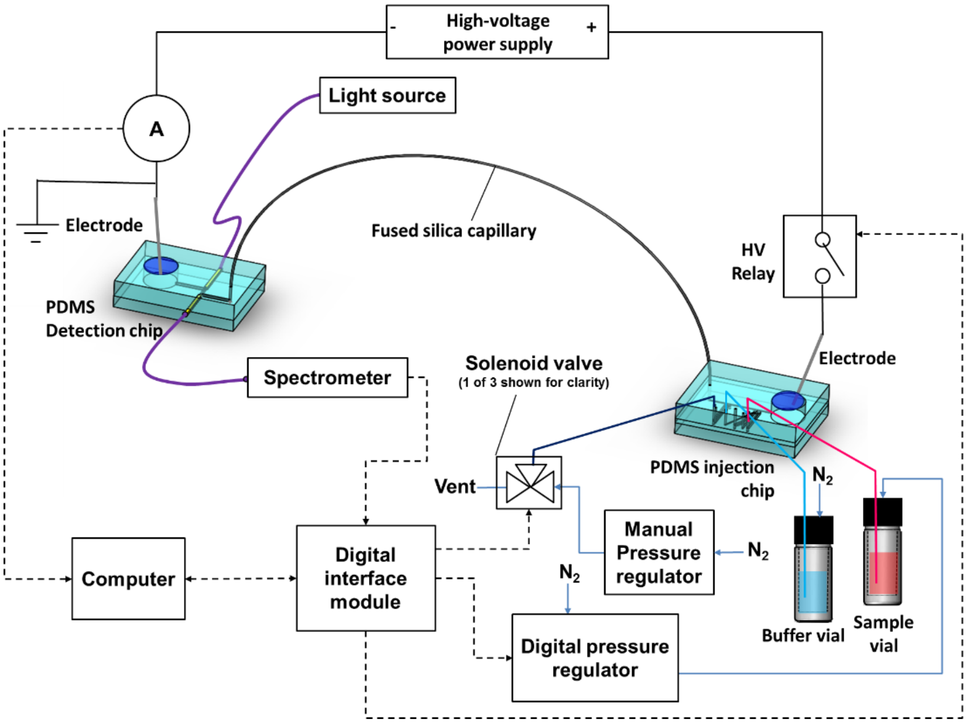

Figure 3-1. Schematic of complete hybrid MCE device setup.
The system includes PDMS optical detection chip, PDMS injection chip, and glass capillary separation channel. The solenoid valves are used to control the on-chip microvalves.

3.3.2 **Injection chip**

Though the commonly used technique of electrokinetic injection provides a very convenient means to inject samples in CE and MCE, this technique suffers from injection bias, i.e. solutes with higher electrophoretic mobilities are preferentially introduced, resulting in a difference between the composition of the original sample and that injected into the separation channel, as well as changing of the sample composition over time which interferes with repeat measurements [167], [168]. This bias, and other sensitivities of this technique (to voltage, sample conductivity, sample pH, electrolysis, and the possibility of complex formation) [168] could prevent accurate assessment of diverse impurities in PET tracer samples. Thus, pressure-driven injection [168], which avoids the above injection bias was used.

The design of the microfluidic injection chip, shown in **Figure 3-2A**, was adapted from the report of Li *et al.* [169]. The chip was fabricated from poly(dimethylsiloxane) (PDMS) using multilayer soft lithography [170]. The chip enables a controlled amount of sample to be loaded from the sample inlet port into the separation channel by momentarily opening a microvalve (v3) for a fixed time. An additional microvalve (v2) enables priming of the sample inlet to eliminate air. The sample was contained in a septum-sealed vial (Fisherbrand™ 2 mL screw thread autosampler vial, Thermo Fisher Scientific, Waltham, MA, USA). Pressurized nitrogen gas was supplied to the vial through an electronic pressure regulator (ITV0010-3BL, SMC Corporation of America, Noblesville, IN, USA). The vial also contained an outlet tubing (#30 PTFE tubing, Cole-Parmer, IL, USA) connected to the sample inlet port of the injector chip. In addition to the sample inlet, the chip also contained an inlet for buffer solution, which was similarly connected to a pressurized vial of the separation buffer (SDS-PB) and controlled via microvalve v1.

The detailed steps to perform sample injection are illustrated in **Figure 3-2B**. Before use, the chip was first primed with buffer by closing v3, opening v1, and pressurizing the buffer vial (6.0 psi) until buffer started flow out of all the buffer wells (and also out the buffer waste well of the detection chip connected to the other end of the capillary). Next, the sample vial was pressurized (1.5 psi) and the sample inlet was primed by closing v1 and v3 and then opening v2 until sample was seen entering the sample waste vial. To load the sample, valve v3 was then opened for a fixed time to allow sample to fill part of the main channel in the chip. After the sample is loaded all valves were closed and electrophoretic potential was applied to separate the sample.

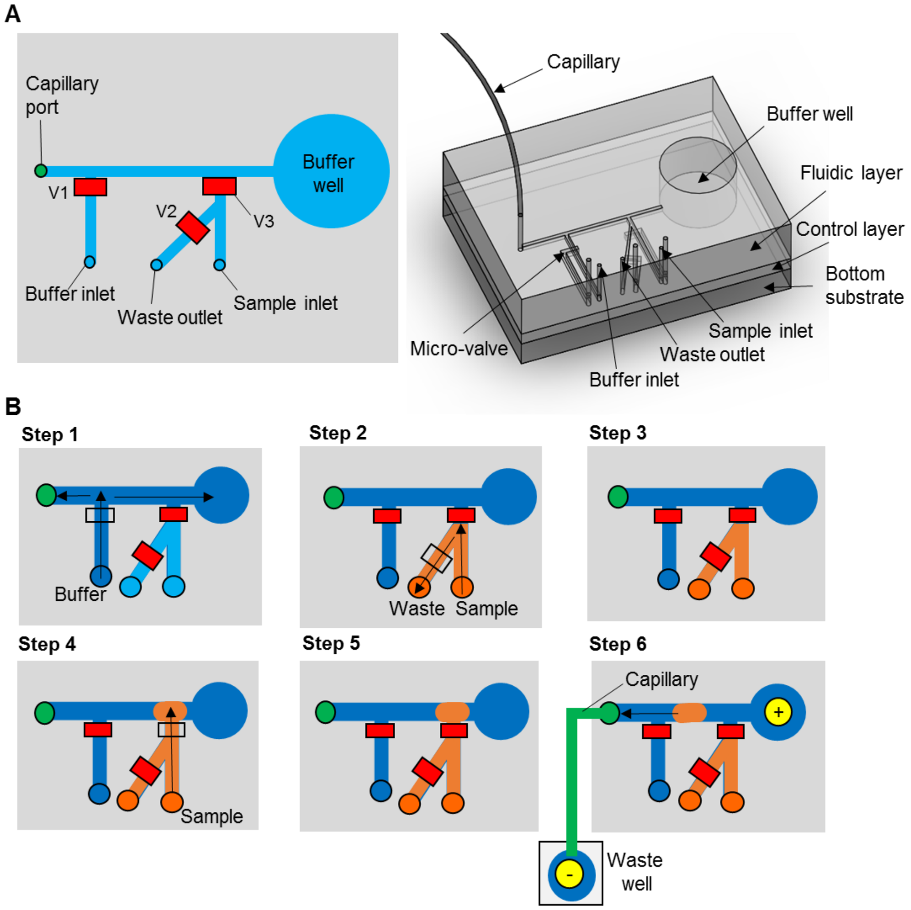

Figure 3-2. Design of PDMS injection chip and sample injection method. (**A**) Design of multi-layer PDMS chip for timed hydrodynamic sample injection. (Left) Schematic; (Right) 3D representation. (**B**) Schematic view of steps involved in injection process. First, the channel is primed with buffer (step 1). Next, the sample is loaded and primed (steps 2-3). The sample is then injected (steps 4-5), and the separation potential is applied along the separation channel (step 6). Solid red boxes indicate closed microvalves and hollow black boxes indicate open microvalves. Arrows indicate direction of fluid flow. Channels filled with buffer are shown in blue while those filled with sample are shown in orange. The capillary and waste well are connected for all steps but for clarity are only depicted in the final step when the separation voltage is applied. Diagrams not to scale.

On-chip microvalves were each controlled by the common port of an electronic solenoid valve (S070B-5DG, SMC Corporation), connected to the chip via #30 PTFE tubing. The solenoid valves switched between two states: (i) supplying pressurized nitrogen (35 psi) to close the on-chip microvalve, and (ii) venting to atmosphere to allow the on-chip microvalve to open via elastic restoration of the PDMS. To avoid the generation of air bubbles inside the sample-containing channels of the chip, the valve control channels were filled with water prior to use as previously described [94].

3.3.2.1 Fabrication details of microfluidic injector

The injection chip was fabricated from two patterned layers of poly(dimethylsiloxane) (PDMS) and a PDMS substrate using multilayer soft lithography. When the layers are aligned and bonded together two planar networks of sealed channels are formed: an upper layer in which the sample and buffer flow (flow layer), and a lower layer that contains microvalve control channels (control layer). The control layer channel is 15 µm deep and 75 µm wide and were rectangular in cross section. The flow layer channels were 20 µm deep and 75 µm wide and were rounded in cross section to enable complete channel sealing using the on-chip pneumatic valves [170].

The control layer mold was fabricated from a 4” silicon wafer (Silicon Valley Microelectronics, Santa Clara, CA USA). The wafer was first cleaned with oxygen plasma using a Matrix 105 – Downstream Asher (Allwin21, Morgan Hill, CA, USA), and baked at 150°C for 10 min. ~4 mL of SU-8 2010 negative photoresist (MicroChem, Newton, MA USA) was poured onto the wafer and spun at the following 3 step spin setting: 500:200:5, 1500:500:30, 0:500:0 (speed:acceleration:duration; units are RPM:RPM:s). After soft baking at 95°C for 3 min, the wafer was exposed to 140 mJ/cm^2 of UV light through the control layer transparency mask using a Karl Suss MA150 Mask Aligner (Karl Suss American Inc., Williston, Vermont, USA), followed by post-baking at 95°C for 4 min. Next, the wafer was developed by immersion in SU-8 Developer

(MicroChem, Newton, MA USA) for 3 min, followed by cleaning with methanol and drying with compressed nitrogen gas. Finally, the mold was hard baked at 175°C for 15 min and then 100°C for 5 min. The height of the inverse channel was measured using a Veeco Dektak 150 Surface Profilometer (Bruker, Tustin, AZ, USA) to be 15 μm.

The flow layer mold was made from a 4" silicon wafer, cleaned as described above. ~6 mL of the adhesion promoter hexamethydisilazane (HMDS) (Sigma-Aldrich, St. Louis, MO USA) was poured onto the wafer and spun at the following setting 3 step spin setting: 400:200:18, 1000:500:45, 0:500:0. Next, ~6 mL of SPR 220-7.0 positive photoresist (MicroChem, Newton, MA USA) was spun onto the wafer using the following setting 3 step spin setting: 400:200:30, 1000:500:80, 0:500:0. The coated wafer was then soft baked at 105°C for 6 min, and then exposed with 720 mJ/cm^2 through the flow layer transparency mask. After exposure, the coated wafer was set aside for rehydration for 3 h, post-baked at 110°C for 5 min, and again rehydrated at room temperature for 45 min. The wafer was then developed by immersing in CD-26 (MicroChem, Newton, MA USA) for 30 min, rinsed with DI water, and dried with compressed nitrogen gas. Once developed, a reflow process (to achieved rounded channel profile) was performed. This was accomplished by placing the wafer on a 65°C hot plate, ramping up to 140°C and holding for 40 min. Finally, a hard bake step was performed by placing the wafer on a 135°C hot plate, ramping up to 190°C, and holding for 3 h (channel features become blackened). The height of the inverse channel feature was then measured to be 20 μm using a profilometer.

Each microfluidic chip was made as follows. ~45 g of a 20:1 mass ratio of RTV615 A:B (Momentive, New Smyrna Beach, FL, USA) was prepared, thoroughly mixed, and then placed into a vacuum desiccator for 2 h to remove air bubbles. The degassed mixture was poured onto the control mold and spun at 2500 RPM (acceleration: 1000 RPM/s) for 1 min. ~50 g of a 5:1 mass ratio of RTV615 A:B was also prepared in a similar fashion. This mixture was poured to ~5mm thickness on the flow layer mold, which had been placed in a foil lined Pyrex petri dish (140 mm ID) (Product#3160101BO, Corning Inc., Corning, NY, USA). Both layers were then baked in an oven at 80°C for 20 min. The flow layer was then removed from the wafer mold, trimmed to the size of the chip, and aligned onto the control layer with the assistance of alignment marks and a stereo zoom microscope. Scotch tape was used to keep the surface of the chip clean before alignment (810 Scotch Tape, 3M, Saint Paul, MN, USA). The layers were placed in contact so that there were no air bubbles between them, and then baked at 80°C oven for at least 2 h to facilitate bonding. The bonded chip was then removed from the control wafer mold. A Schmidt manual press (Press Type 3/6, Schmidt, Cranberry Twp., PA, USA) equipped with metal punches was used to create a buffer well, ports for fluidic and control lines, and a port for a fused silica capillary. The buffer well was formed using a 4.75 mm ID catheter punch (HS1871730P1183S, Syneo, West Palm Beach, FL). A 720 µm ID catheter punch (CR0350255N20R4, Syneo) was used for all other ports except the capillary port, which used a 330 µm ID punch ID punch (CR0180115N26R4, Syneo). A 60 cm long, 75 µm I.D., 375 µm O.D. Teflon coated fused-silica capillary (Polymicro, Phoenix, AZ, USA) was then inserted into the capillary port with one end of the capillary end not quite flush with the bottom surface (i.e. ~1 mm retracted from the surface) of the PDMS chip. The combined chip (fluid and control layers) was then bonded to a flat PDMS substrate using a Corona Discharge bonder (LM4816-11MS-MSA, Enercon Industries). (To create this PDMS substrate, ~50 g of a 10:1 mass ratio of RTV615 A:B was prepared, degassed, and poured to a ~5 mm thickness on a blank silicon wafer, and then cured at 80°C for 2 h.) The completed chip was then baked at 80°C for at least 2 h. The thickness of the valve membrane between the control and flow channels was determined via profilometry to be ~15 µm (total thickness of PDMS control layer of 30 µm minus the 15 µm height of the channel feature on the mold).

3.3.3 **Detection chip**

In typical radio-HPLC systems used in the field of radiochemistry, the flow cell has a path length of ~10 mm (10,000 µm). In the case of capillary electrophoresis in capillaries or microchannels, the optical path length (OPL) is much shorter (e.g. 30-100 µm) if light is directed, via a window, perpendicular to the flow through the capillary of microchannel. Because this short optical path reduces the absorbance ‘signal’, it typically results in a relatively poor LOD in CE systems compared to HPLC. This problem can be addressed by leveraging the ability to precisely control fluid geometry in microfluidic devices and implementing an increased optical path length. An in-plane Z-shaped detection cell design [171] was selected, due to the simplicity of chip fabrication and interfacing of the illumination and detection optical fibers.

The chip was fabricated from a single patterned layer of PDMS bonded to a PDMS substrate. The design (**Figure 3-3**) includes fiber alignment channels to ensure accurate collinear alignment of both the optical fibers (i.e. to provide illumination via the external light source and detection via the external spectrometer) with a ‘jog’ in the sample channel representing the extended optical path within the chip [172]. Due to the elastic property of PDMS, the 125 µm OD optical fibers (ThorLabs, Newton, New Jersey, USA) are held stably in these channels by friction forces. The flat ends of the fibers sit flush against the flat end of the fiber channels, providing efficient optical coupling to the sample channel. Since PDMS absorbs strongly in the UV range [173], it was desirable to minimize the thickness of PDMS membrane between the end of the fiber and the sample within the channel. A thickness of 100 µm was chosen as it provides good optical transmission (>85% transmission for wavelengths > 220 nm), sufficient mechanical resistance to deformation, and high electrical breakdown voltage (~2000V [174], sufficient to sustain the CE potential at this point in the separation channel). In addition to the portion of each fiber alignment channel that is collinear with the optical path, there is a continuation that allows the air initially in the channel to be vented. All channels were 125 µm deep and 125 µm wide. Using the same depth for the fiber-aligning channels as for the fluid-containing channels simplifies the chip fabrication, requiring a single thickness of photoresist.

The performance of the detection chip was compared with two combinations of light sources and detectors, one with lower performance and one with higher performance. Detector 1 comprised a PX-2 pulsed xenon light source (Ocean Optics, Dunedun, FL, USA) and USB-4000 spectrometer (Ocean Optics) and Detector 2 consisted of a DH-2000-BAL continuous deuterium light source (Ocean Optics) and QE-Pro spectrometer (Ocean Optics). The PX-2 is ~5x cheaper than the DH-2000-BAL; however, it has significant noise, which adversely affects LOD. The pulse-to-pulse variation in light intensity is in the range 3-12% depending on pulse frequency [175], compared to an intensity drift of <0.01% per hour [176] for the DH-20000-BAL. Similarly, the USB4000 is ~20x cheaper than the QE-Pro, but has a lower signal-to-noise ratio (275:1 compared to 1000:1) and lower dynamic range.

While the current work serves as proof of concept for miniaturized analysis of PET radiopharmaceuticals, ultimately it will be necessary to incorporate a radiation detector with good spatial resolution to enable assessment of radiochemical identity and purity in addition to chemical purity. We are currently in the process of developing such an integrated detector for the detection chip and will publish these findings in the future.

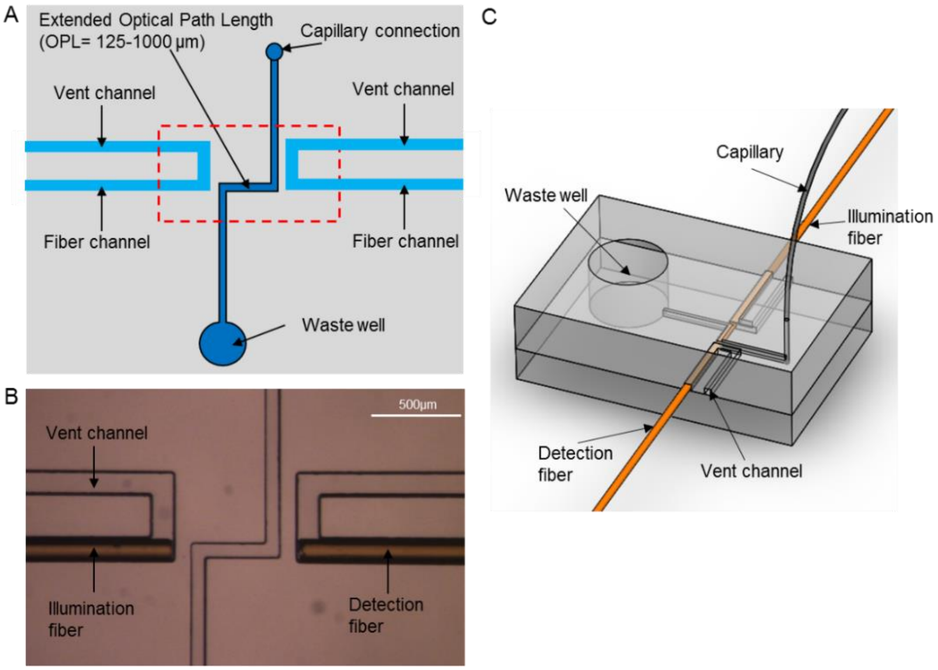

Figure 3-3. PDMS detection chip.
(**A**) Schematic of the PDMS detection chip with the extended optical path. (**B**) Micrograph of the region of the chip outlined by the dotted red line in A. (**C**) 3D representation of the PDMS detection chip with connected capillary and optical fibers for absorbance measurement.

3.3.3.1 Fabrication details of PDMS detection chip

The detection chip was fabricated from a single layer of patterned PDMS bonded to a PDMS substrate. The channel mold was created from a cleaned 4” silicon wafer. ~4 mL of SU-8 2150 negative photoresist (MicroChem) was poured and spun at the following 3 step spin setting: 500:200:5, 1500:500:30, 0:500:0. After soft-baking at 65°C for 5 min and then 95°C for 25 min, the wafer was exposed to 240 mJ/cm2 of UV light through the transparency mask. The exposed wafer was then post baked at 65°C for 5 min and 95°C for 11 min. The wafer was developed in SU-8 Developer for 15 min, cleaned with methanol, and dried with compressed nitrogen gas. Finally, the mold was hard baked at 175°C for 15 min and at 100°C for 5 min. The height of the inverse channel features was determined to be 125 µm using a profilometer. To prepare the chip, a ~50 g amount of 10:1 mass ratio RTV615 A:B was mixed and degassed and then poured onto the mold (~5 mm thickness) and baked at 80°C overnight. Once completely cured, the PDMS chips were peeled away from the mold and a 4.75 mm inlet well and 330 µm capillary port were made with metal punches. Next, the other end of the capillary (connected to the injection chip) was inserted in a similar fashion through the capillary port of the detection chip. Finally, the chip was bonded to a PDMS substrate using corona discharge bonding and baked at 80°C for at least 2 hr conditioning.

After fabrication and assembly of the hybrid chip, it was conditioned prior to use. First, the chips and capillary were filled with water via the buffer inlet port at 10 psi for 30 min to ensure all air was purged from the system. The both ends of the chips were placed in a Petri dish containing a damp Kimwipe and wrapped with parafilm. Next, this procedure was repeated with 1M NaOH to form hydroxyl groups [177] on the inner surfaces of the capillary and PDMS microchannels. The NaOH was removed during the buffer priming step of the sample injection process.

3.3.4 Separation and detection of analytes

The separation voltage was provided by a 0-30 kV high voltage DC power supply (HV350, Information Unlimited, Amherst, NH, USA). The tip of the high voltage electrode wire was submerged in the separation buffer well of the injection chip and that of the ground electrode wire was submerged in the waste well of the detection chip. Electrodes were held in place by electrically-insulated clamps mounted on a retort stand. 12 kV was supplied to achieve a field of ~200 V/cm along the separation channel. The total length of the separation path from the buffer well to the waste well was 62 cm. The effective separation length, i.e. injection point to the detector, was 61 cm. CE voltage was turned on or off using a solid-state relay in series with the high-voltage side of the circuit. During operation, DC current was monitored in real-time via a digital multimeter (Model 2831E, BK precision, Yorba Linda, CA, USA) to detect any abnormal behavior of the chip. For example, any air/gas bubble formation can lead to interruption of the current with intermittent electrical arcing; if this occurred, the high voltage was immediately interrupted, and the fluidic system was reconditioned for ~2 min to purge any bubbles and to re-equilibrate the inner surfaces.

3.3.5 Micellar Electrokinetic Capillary chromatography (MEKC)

In CE, the migration of analyte depends on the electroosmotic flow (EOF), bulk flow, and on the charge of analytes. If all analytes are neutral, they cannot be separated.

Micellar electrokinetic capillary electrophoresis (MECE) is a type of capillary electrophoresis where a surfactant (e.g., sodium dodecyl sulfate, SDS) is added to the running buffer to form micelles to assist with separation of neutral analytes [178]. Micelles are formed when surfactants with long hydrophobic tails and polar heads self-organize into spherical aggregates, which occurs above a specific surfactant concentration known as the critical micelle concentration (CMC; 8mM for SDS). Anionic (negatively charged) surfactants, such as SDS used in our study, form micelles with net negative charge and migrate towards the anode, which is the opposite direction of EOF. Since the EOF is typically faster than the migration velocity of the micelles, the net movement will still occur in the same direction of the EOF. When micelles are formed, neutral analytes with differing hydrophobicity distribute differently between the hydrophobic inner core of the micelles and the hydrophilic exterior. Thus, the species that are more hydrophobic will be slowed down due to more interaction with the micelles compared to those that are less hydrophobic and have less interaction with the micelles. This variation in analyte/micelle affinity produces different migration velocities for neutral analytes, resulting in separation.

3.3.6 **Reagents**

Sodium phosphate monobasic (NaH_2PO_4), sodium phosphate dibasic dihydrate (Na_2HPO_4), boric acid, sodium dodecyl sulfate (SDS), ammonium acetate, ethanol, sodium chloride (NaCl), sodium hydroxide (NaOH), thymine, thymidine, furfuryl alcohol (FA), 2',3'-didehydro-3'-deoxythymidine (stavudine), and 3' deoxy-3'-fluorothymidine (FLT) were purchased from Sigma–Aldrich (Milwaukee, WI, USA). Zidovudine impurity B (chlorothymidine, CLT) was purchased from LGC Standards (Wesel, Germany).

Kryptofix2.2.2 (K222), 3-N-Boc-5'-Odimethoxytrityl-3'-O-nosyl-thymidine (Boc-FLT) were purchased from ABX (Radeberg, Germany).

All samples were prepared with 18 MΩ deionized water using a Milli-Q® Integral Water Purification system (EMD Millipore, Billerica, MA, USA). 30 mM phosphate buffer (PB) was prepared via titration 100 mM solutions of NaH_2PO_4 and Na_2HPO_4 and monitored with a pH meter (Mettler, Toledo, Easy five, Columbus, OH, USA). 100 mM SDS in 30 mM phosphate buffer (SDS-PB) was prepared by dissolving SDS in 30 mM PB. All buffers were degassed prior to use.

3.3.7 **UV absorbance measurements**

Before the light source was turned on, the detector reading (i.e. dark noise) was recorded. Next, the optical path was filled with the buffer solution (SDS-PB), a blank (reference) signal was recorded as a function of wavelength, to enable removal of effects of the capillary wall / flow cell, buffer solution, etc. on the measurement.

The light transmission percentage (%T) at a given wavelength is equal to the intensity of light that passed through the sample, I, divided by the initial light intensity I_0. This can be calculated by taking the ratio of the sample signal (S) minus dark noise (D) over the reference signal (R) minus the dark noise:

$$\%T = \frac{I}{I_0} * 100 = \frac{S - D}{R - D} * 100 \qquad \text{(Equation S1)}$$

The absorbance, A, is then computed as follows:

$$A = 2 - \log_{10} \%T \qquad \text{(Equation S2)}$$

To create an electropherogram, spectrometer output was measured at a rate of 10 samples/s and converted to absorbance, starting at the time of injection.

Each electropherogram was analyzed using OriginPro 8.5 (OriginLab, Northampton, MA, USA) to determine peak migration times (t_m, taken at peak center), peak widths ($w_{1/2}$, full width at half maximum), as well as other values such as peak areas based on a Gaussian fit to each peak. Peaks were identified based on retention times determined by injecting standard compounds individually.

3.4 CE System characterization

3.4.1 Characterization of injection chip

For the purposes of characterizing the injector, the detection chip was not used; rather, detection of analytes was performed directly in the capillary using a 4-way junction (PEEK Cross, P-729, Idex Health & Science, Oak Harbor, WA, USA) positioned 7 cm away from the downstream end of capillary. A small portion of capillary was covered with a 1/16" OD tubing sleeve (Idex Health & Science, Oak Harbor, WA, USA) and secured via two opposite ports of the junction. The illumination and detection optical fibers were secured in the two perpendicular ports. Note that the effective separation length in this case was 54 cm. The total separation length between the buffer well of the injection chip and the waste vial was 61 cm and the separation voltage applied was +12 kV.

To assess the sample injection repeatibility, successive injections of 5mM thymidine were performed with a valve opening time of 800 ms.

3.4.2 Characterization of detection chip

Chemical purity tests are performed on radiopharmaceutical preparations to confirm the absence of impurities after the purification and formulation processes. For some impurities (e.g. Kryptofix K222, etc.), there are well-established limits based on toxicity studies that can safely be injected into patients. Unstudied impurities, provided they pose negligible risk of carcinogenicity, are typically limited to 1.5 µg per patient per day (5 nmol for a compound with molar mass of 300 g/mol). A typical radiopharmaceutical preparation has a volume of 1-10 mL (or larger) and contains sufficient material for 1 or more patient scans. In the conservative case (1 mL volume, 1 patient), this gives an upper permitted limit of 5 µM. To establish whether these levels can be detected in our setup, we have characterized the sensitivity of detection chip by measuring the limit of detection (LOD) and limit of quantitation (LOQ) for varying conditions, including varying optical detection path length and varying optical systems).

To characterize the detection chip, the capillary was connected but the injection chip was not used. Instead, UV absorbance was measured when the detection chip was fully filled with several concentrations of each analyte. The absorbance was measured for each sample at the desired wavelength(s) for ~ 1 min, and then averaged to obtain one data point. This procedure was repeated 3 times while flushing the optical path length with blank solution between each measurement. The three data points were then averaged to obtain an overall absorbance value for the particular concentration of the particular analyte. To minimize the impact of cross-contamination, the most dilute samples were measured prior to more concentrated samples. After performing a linear fit of absorbance versus concentration (i.e. Beer's Law), the LOD and LOQ were determined by calculating the concentration that corresponds to 3x and 10x, respectively, the standard deviation in background absorbance noise. UV absorbance was measured at 256 nm or 224 nm, corresponding to the wavelengths of maximum absorbance for the model compounds used.

3.4.3 **Evaluating separation efficiency**

To evaluate separation efficiency, we chose as a model system the PET tracer [^{18}F]3'-fluoro-3'-deoxythimidine ([^{18}F]FLT), for which the impurity profile is well known [179]. The synthesis scheme and the structurally-similar side-products are shown in **Figure 3-4**. A mixture of FLT and by-products (5 mM thymidine, 2 mM thymine, 2.5 mM furfuryl alcohol, 5 mM stavudine, 2.6 mM FLT, and 1.4 mM CLT) was injected to assess separation efficiency. Separation was performed with micellar electrokinetic chromatography (MEKC) since the compounds are all neutral.

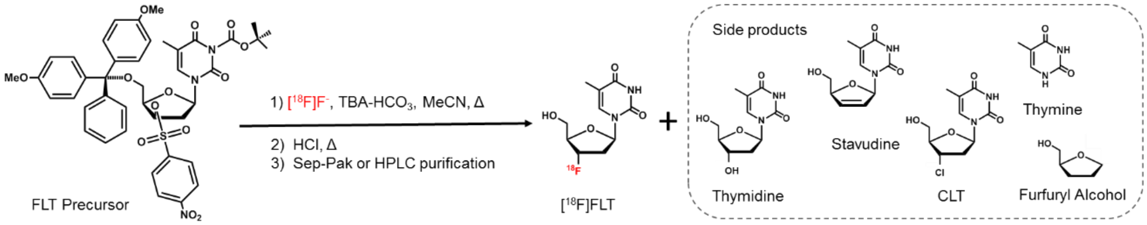

Figure 3-4. Radiosynthesis of [^{18}F]FLT showing side-product formation. A mixture of FLT and side-products was used as a model system in this work. Figure adapted from [45], copyright © 2012, with permission of Elsevier.

Samples were injected via injection chip using a valve opening time of 400 ms. For each peak in the resulting electropherogram, the number of theoretical plates, *N*, was calculated as follows [180], [181]:

$$N = 5.54\left(\frac{t_m}{w_{1/2}}\right)^2 \quad (1).$$

3.4.4 **Benchmark comparisons to conventional method**

Performance was compared to separations on an analytical HPLC system as previously described [166]: Knauer Smartline HPLC system using a C18 Luna reverse phase column (4.6 mm × 250 mm, 5 µm; Phenomenex, Torrance, CA, USA). Detection was performed at 224 and 254 nm with an inline UV detector (model 2500, Knauer, Berlin, Germany). The HPLC mobile phase for FLT separations was 10% ethanol in water (v/v), at flow rate of 1 mL/min. All chromatograms were collected by a GinaStar analog to digital converter (Raytest USA Inc., Wilmington, NC, USA) and GinaStar software (Raytest USA Inc., Wilmington, NC, USA). Comparisons were also made to previously reported results using a commercial (macroscale) CE system (PA800, Beckman Coulter, CA, USA) [166].

3.5 Results and Discussion

3.5.1 Sample injection

Injection repeatability of the PDMS injection chip was assessed by determining the consistency of peak area resulting from successive injections of single compound. The relative standard deviation (RSD) of peak area of successive injections of thymidine was 3.9% (n=8). Since this performance was sufficient for remaining experiments to assess the feasibility of the hybrid MCE for chemical purity analysis, further optimization was not performed at the time, and remaining results are performed with this injector.

However, peak area RSD <2% is generally desired for quantitative analysis [182]. Li *et al.* reported a peak area RSD as low as 1.77% (n=15) [169], using a similar PDMS injection chip, but with an integrated separation channel rather than external capillary as used here. We suspect that dead volume at the chip to capillary junction in our MCE setup (see discussion below) may be causing the variability.

Another way to improve performance may be to switch injection methods since the method can have a large impact on the peak area RSD. In HPLC, the amount of sample is measured volumetrically (by the injection loop), resulting in very high injection repeatability. Recently, we explored a novel volumetric injection technique for MCE and showed that a peak area RSD as low as 1.04% (n=4) [94] could be achieved (see Chapter 4: Novel volumetric method for highly repeatable injection in microchip electrophoresis), even using an external capillary for separation. We are thus confident that a next-generation device incorporating a PDMS-based injector will achieve sufficient repeatability for radiopharmaceutical analysis.

3.5.2 Sample detection in MCE device

Initially, we attempted UV detection directly in the capillary. The LOD and LOQ for several analytes, using both combinations of light source and detector are shown in **Table 3-1**. Even when the higher performance setup (Detector 2) was used for the in-capillary detection, LODs were all higher than 20 µM, and significantly worse than values previously measured for HPLC [166]. This is likely due to the much shorter optical path through the sample in the capillary (i.e. ~75 µm, the inner diameter of the capillary) compared to the 10000 µm flow cell in the HPLC system. The values were also significantly worse than those previously measured in a commercial CE system (5 – 11 µM; Beckman Coulter PA800) [166], likely due to differences in the optical system, capillary environment (i.e. temperature-controlled in the commercial CE system), and signal processing.

To improve the LOD, a PDMS detection chip with a Z-shaped extended optical path (500 µm) was implemented. In combination with the higher performance light source and detector pair (Detector 2), LODs ranged from 2 - 3 µM for the set of compounds with similar chromophore (thymidine, thymine, stavudine, FLT, and CLT), and 7 µM for furfuryl alcohol. Thus, the LOD values of the MCE setup are comparable to the performance of HPLC (i.e., 2 µM for stavudine and FLT, 35 µM for furfuryl alcohol) [166], and are below the typical permitted limit of impurities found in radiopharmaceuticals. Detection performance is summarized in **Table 3-1** for all system configurations. Since the desired performance was achieved, the 500 µm OPL was used in subsequent experiments. For a 500 µm OPL detection chip and Detector Configuration 2, we found the linear range of the various species to be: 2 µM – 5 mM (thymidine), 2 µM – 5 mM (thymine), 7 µM – 3 mM (furfuryl alcohol), 3 µM - 5mM (stavudine), 3 µM – 5 mM (CLT), and 2 µM – 5 mM (FLT).

Table 3-1. Limits of detection (LODs) and quantitation (LOQs) for all setups for FLT and its impurities.

Blank entries indicate conditions that were not measured. By combining a higher performance light source and detector with 500 µm OPL (bold entries), the sensitivity of the MCE setup was comparable to HPLC (bold entries).

Experimental Setup			**Compound**							
			Thymidine	**Thymine**	**FA**	**Stavudine**	**FLT**	**CLT**	**K222**	
MCE detection chip (with 500µm OPL)		Wavelength (nm)	256	256	224	256	256	256		
	Detector 1 (lower performance)	LOD	8		30					
		LOQ	30		96					
	Detector 2 (higher performance)	LOD	**2**	**3**	**7**	**3**	**2**	**3**		
		LOQ	8	10	23	10	8	9		
In-capillary detection		Wavelength (nm)	256	256	224	256	256	256		
	Detector 1 (lower performance)	LOD (µM)	210	260	790	310	300	1100		
		LOQ (µM)	750	850	2600	1000	1000	3500		
	Detector 2 (higher performance)	LOD (µM)	22	21	54	27	25	75		
		LOQ (µM)	72	69	180	91	84	250		
HPLC		Wavelength (nm)			224	254	254		*	*
		LOD (µM)			**35**	**2**	**2**		Not detected	

	LOQ (μM)			116	4	5		Not detected	
Commercial CE	Wavelength (nm)	254	254	218	254	254	254	218	205
	LOD (μM)	5	5	11	7	6	6	180	120
	LOQ (μM)	13	14	36	15	20	15	570	390

*Measurements were attempted at various wavelengths (205, 218, 224, 236, 254, and 267 nm) but K222 could not be detecteda

We also explored the possibility to achieve similar performance with the lower-performance (and lower cost) light source and detector (Detector 1) by fabricating additional detection chips with different OPL. The LOD and LOQ values for thymidine and furfuryl alcohol in detection chips with different OPL are summarized in **Table 3-2**. To more clearly see the effect of OPL, we note that LOD is defined as the concentration of analyte where the absorbance equals 3x the standard deviation of noise (N). Substituting into Beer's law, we can write LOD = 3N/ε/OPL, where ε is the molar absorbtivity. Thus, LOD is inversely proportional to the OPL and the data in **Figure 3-5** were thus fit to this function to extrapolate the OPL necessary to match the performance of HPLC. To achieve LOD = 2 μM for thymidine (and FLT and stavudine, which have an identical chromophore and thus similar absorbance), an OPL of 2500 μm would be required. Similarly, to achieve LOD = 35 μM for furfuryl alcohol, an OPL of 420 μm would be required. Thus, the PDMS detection chip with Detector 1 could match/surpass the detection sensitivity of HPLC by extending the optical path length to 2500 µm.

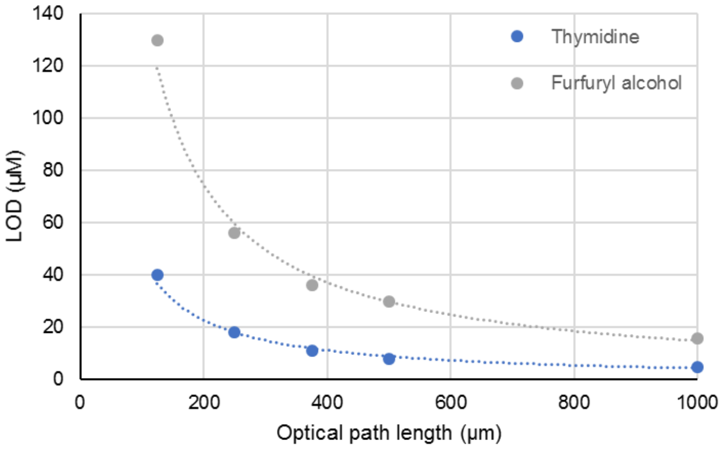

Figure 3-5. Dependence of LOD on the OPL of the PDMS detection chip.

Table 3-2. Performance of PDMS detection chip with varying optical path lengths. Limit of detection (LOD) and quantitation (LOQ) are indicated for thymidine (256 nm) and furfuryl alcohol (224 nm). Measurements were performed with the lower performance light source and detector (Detector 1).

	Thymidine (256 nm)		**Furfuryl alcohol (224 nm)**	
OPL (µm)	**LOD (µM)**	**LOQ (µM)**	**LOD (µM)**	**LOQ (µM)**
125	40	130	130	430
250	18	56	56	190
375	11	36	36	120
500	8	30	30	96
1000	5	16	16	54

3.5.3 **Separation of samples**

Previously we showed that mixtures of FLT and its structurally-similar byproducts (thymidine, thymine, furfuryl alcohol, stavudine, and CLT) could be separated by HPLC and by a conventional CE instrument with baseline resolution [102]. We analyzed similar samples to demonstrate the feasibility of injecting, separating, and detecting samples in the hybrid microfluidic system.

First, we started with the simplest geometry that resembles the commercial CE instrument, i.e., a capillary-only (“0-junction”) system without any microchips connected (**Figure 3-6A**). For this method, the injection was performed electrokinetically, by inserting the upstream side of the capillary in the sample vial (2 mL, C4013-15A, Thermo Scientific), applying +12 kV for 5 s, then moving the capillary back to the buffer vial prior to separation. Successful baseline separation of the sample mixture (FLT and five impurities) was achieved (**Figure 3-7A**).

Next, the injection microchip was added to the capillary to form a “1-junction” system (**Figure 3-6B**). Even though baseline separation was observed for most peaks, the first two peaks were not completely resolved (**Figure 3-7B**). Finally, we tested an integrated microfluidic system with injection chip, silica capillary and detection chip (**Figure 3-6C**). An electropherogram is shown in **Figure 3-7C.** While all expected peaks are discernable, baseline separation was not achieved among the three fastest eluting compounds (thymidine, thymine, and furfuryl alcohol). Qualitatively, it is clear that the peak width using the hybrid MCE device was greater than that for the 0-junction setup, leading to the reduced separation efficiency. This was confirmed by computing the number of theoretical plates, *N*, for each setup (**Table 3-3**): it was found that *N* is significantly lower for the hybrid MCE device compared to the 0-junction setup.

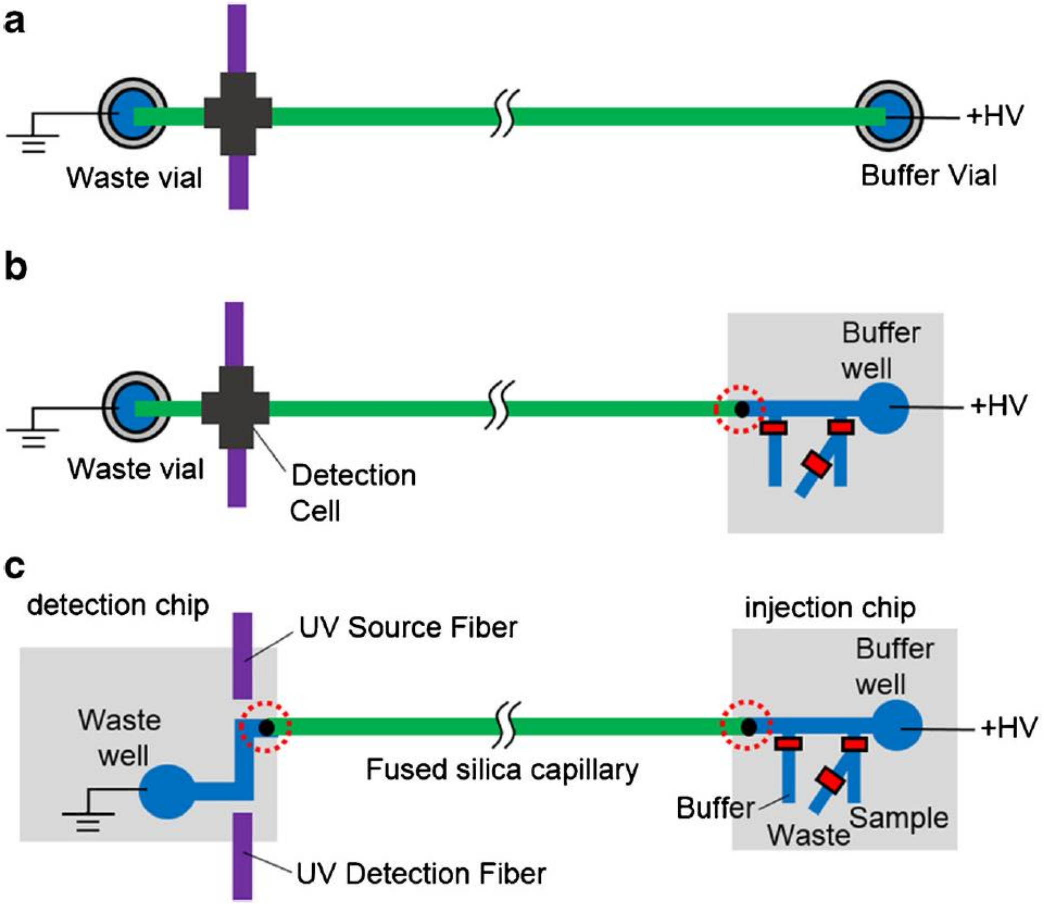

Figure 3-6. Schematic of system configurations with different numbers of capillary-chip junctions.

(**A**) Setup with the capillary only (0-junction configuration). Sample was introduced via electrokinetic injection, and detection occurred in a capillary detection cell. (**B**) Setup with the PDMS injection chip and capillary (1-junction configuration). Detection occurred in a capillary detection cell. This setup was used for evaluation of the injection performance. (**C**) Hybrid MCE device with PDMS injection chip, capillary, and PDMS detection chip. Red dotted circles highlight capillary junctions. Diagrams not to scale.

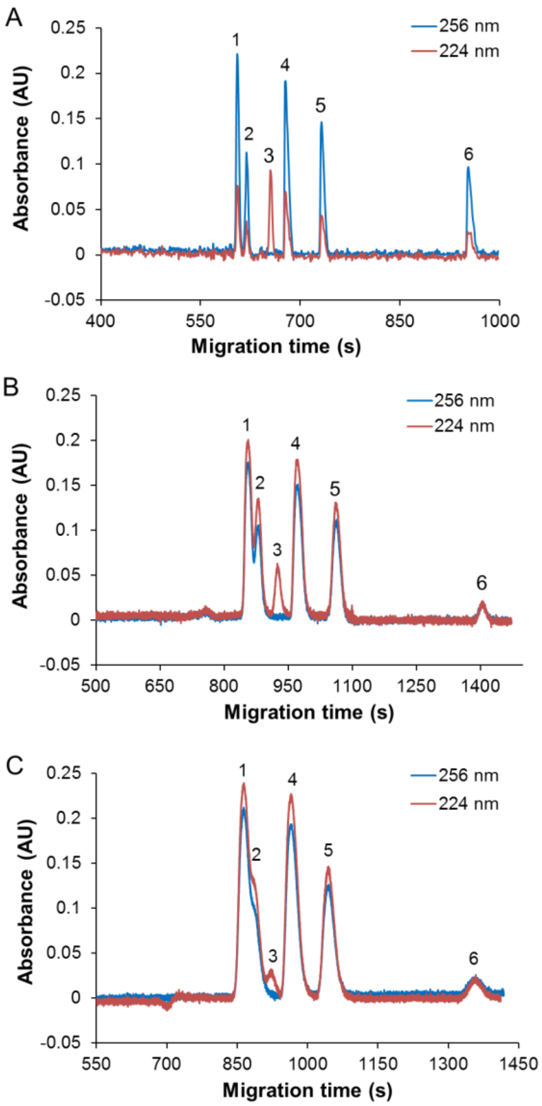

Figure 3-7. Separation performance of 3 different system configurations.
(**A**) Electropherogram from separation in a capillary-only (0-junction) setup. Peaks: 6 mM thymidine (peak 1), 3 mM thymine (peak 2), 5 mM furfuryl alcohol (peak 3), 6 mM stavudine (peak 4), 3 mM FLT (peak 5), 3 mM CLT (peak 6). (**B**) Electropherogram from separation in a 1-junction setup (i.e., injection chip with a capillary). Peaks: 5 mM thymidine (peak 1), 2 mM thymine (peak 2), 2.5 mM furfuryl alcohol (peak 3), 5 mM stavudine (peak 4), 2.6 mM FLT (peak 5), and 1.4 mM CLT (peak 6). (**C**) Electropherogram of sample mixture injected, separated, and detected with the hybrid MCE device (i.e. with 2 capillary-chip junctions). Peaks: 5 mM thymidine (peak 1), 2 mM thymine (peak 2), 2.5 mM furfuryl alcohol (peak 3), 5 mM stavudine (peak 4), 2.6 mM FLT (peak 5), and 1.4 mM CLT (peak 6).

To determine where improvements can be made, we analyzed another measure of efficiency: the plate height, $H=L/N$, where L is the effective separation length. Lower H values indicate more theoretical plates within the separation length meaning a higher separation efficiency. Conveniently, *H* can be expressed as a sum of contributing factors (injection, detection, diffusion, and geometry) [183]:

$$H = \frac{L}{N} = H_{inj} + H_{det} + H_{diff} + H_{geo} \quad (2)$$

The injection and detection components are determined from the length of the injection plug (l_{inj}) and the length of the detection cell (i.e. OPL) (l_{det}), respectively [183]:

$$H_{inj} = \frac{l_{inj}^2}{12L} \quad (3)$$

$$H_{det} = \frac{l_{det}^2}{12L} \quad (4)$$

where *L* is the effective separation length.

The contribution of axial diffusion [181], [183] is given by:

$$H_{diff} = \frac{2D_a}{v} \quad (5)$$

where D_a is the diffusion coefficient of the analyte and *v* is the linear velocity of the analyte.

The contribution due to the geometry is the most complex [183], [184]:

$$H_{geo} = n\frac{(\omega\theta)^2}{12L} + \frac{\sigma_{ni}^2}{L} + \frac{\sigma_{dv}^2}{L} \quad (6)$$

The first term can be ignored since our system does not currently use a separation channel with a serpentine pattern (n is the number of turns, ω is the width at the top of the channel (peak of the turn), θ is the turn angle). σ_{ni} represents band broadening from non-ideal behavior of injected sample and Joule heating, and σ_{dv} represents the broadening due to dead volume. Both σ_{ni} and σ_{dv} are of unknown form that depends of geometric shape of the channel, channel material, and electric field gradients [184].

Based on electropherograms, values of N, H, H_{inj}, and H_{det} were computed and are summarized in **Table 3-3**. These results show that the contribution to peak broadening due to the detector (H_{det}) in the hybrid MCE (2-junction) device is negligible and broadening due to the injector (H_{inj}) is ~1% for stavudine and <1% for CLT. Thus, the major contributors to the broadening of peak width are H_{diff} or H_{geo}.

For the 0-junction CE system, H (total) was low, i.e. 6.41 µm and 6.38 µm for thymidine and CLT, respectively. Based on the well-defined computed values of H_{inj} and H_{det}, and ignoring H_{geo} for the moment, maximum upper bounds on H_{diff} for the 0-junction system can be estimated as ~3.5 µm and ~5.2 µm for thymidine and CLT, respectively. It is expected that broadening due to diffusion (H_{diff}) would have a similar value for the 1- and 2-junction (hybrid MCE) systems. This is because the analytes, buffer, and temperature were consistent across these systems and thus D_a was constant. In addition, the elution velocities were very similar (e.g. for CLT, 0-junction velocity was 0.054 cm/s, 1-junction velocity was 0.038 cm/s, and 2-junction velocity was 0.045 cm/s). Thus, we expect H_{diff} to have an upper bound of only a few µm for the 1- and 2-junction cases, and we can deduce that H_{geo} must be the dominant factor for both.

Comparing the CLT peak from the 0- and 1-junction cases, there was a large increase in *H* (i.e. from 6.4 to 39), and comparing the 1- and 2-junction cases, there was another large increase (i.e. from 39 to 121). Since there are only minor expected differences in the injection, detection, or diffusion components of plate height, these increases must be due to geometric factors. Because of the strong increase in *H* as the number of junctions increases, the band broadening is likely occurring due to the geometry (e.g. dead volume) at each capillary-to-chip junction.

Table 3-3. Separation performance for the CE setups with different numbers capillary-chip junctions.
Migration time (tm), peak full width at half maximum (w1/2), number of theoretical plates (N), plate height (H), injection component of plate height (Hinj), and detection component of plate height (Hdet) are shown for each. Values were calculated for the fastest and slowest eluting analytes, i.e. stavudine and CLT for 1- and 2-junction cases and for thymidine and CLT for the 0-junction case.

Analytical Method	**MCE**												
No. Cap junction	**0**						**1**				**2**		
Compounds	**Thymidine**	**Thymine**	**FA**	**Stavudine**	**FLT**	**CLT**	**FA**	**Stavudine**	**FLT**	**CLT**	**Stavudine**	**FLT**	**CLT**
tm(s)	610	630	670	690	750	980	920	970	1070	1400	970	1050	1360
W1/2(s)	5	5	5	7	7	8	15	17	21	28	22	30	45
N	82400	88100	99200	54200	63600	82800	21000	18100	14300	13900	10700	6780	5060
H (µm)	6.43	6.01	5.34	9.78	8.33	6.40	26	30	38	39	57	90	121
Hinj (µm)	2.96	2.78	2.47	2.30	1.96	1.15	0.65	0.58	0.48	0.28	0.67	0.42	0.25
Hdet (µm)	9.01E-04	9.01E-04	9.01E-04	9.01E-04	9.01E-04	9.01E-04	2.93E-03	2.93E-03	2.93E-03	2.93E-03	0.034	0.034	0.034
number of repeats (n)	3	3	3	3	3	3	4	4	4	4	3	3	3

The dead-volume could be reduced by various approaches such as precise drilling [184] or molding the capillary port [185], or by tapering the capillary to fit directly in an in-plane microchannel [94], [186].The geometry issue could also be addressed by integration of the separation channel directly into the chip (instead of using a capillary); this would eliminate the junctions altogether and simplify the overall setup, enabling a single integrated microfluidic device for injection, separation, and detection. Separation in PDMS channels has been reported by several groups [187], [188], though some have reported challenges in maintaining stable surface conditioning [189], [190]. An alternative may be to perform separation using an embedded capillary [191], [192]. With an optimized chip, one could expect the total plate height *H* to be similar to the 0-junction case. Indeed, the elimination of 1 junction shows significant improvement in separation (**Figure 3-7B**), and elimination of both junctions shows further improvement (**Figure 3-7A**), achieving baseline separation of FLT and five impurities. An optimized hybrid (2-junction) MCE system with improved capillary junction is therefore expected to be capable of similar baseline separation.

In addition to addressing the dead-volume at the capillary junctions in this manner, optimization of other parameters could also be explored to maximize separation efficiency. For example, applied electrical field can be increased to increase the velocity of analytes, which would reduce diffusive broadening, and either allow reduced separation times or enable the use of increased separation length.

3.6 Conclusions

The use of miniaturization to reduce the equipment size and shielding needed for the chemical purity analysis of PET tracers is expected to be a key part of streamlining the QC testing process, and ultimately the overall tracer production process. In this work, we have demonstrated the first proof-of-concept experiments to show the feasibility of microfluidic implementation of chemical identity and purity tests of radiopharmaceuticals.

The novel hybrid MCE device consists of a PDMS injection chip, a silica capillary, and a PDMS detection chip. Sample injection was based on hydrodynamic injection using microvalves to achieve satisfactory reproducibility while avoiding the known injection bias of conventional electrokinetic injection. The detection chip enabled adjustment of the optical path length to tune the limit of detection. Though an extended path length of 500 µm resulted in LOD comparable to HPLC when the higher performance light source/detector pair was used, we showed that further extension of the optical path (e.g. OPL ~2500 µm) could enable similar sensitivity even with the lower performance light source and detector, without significantly compromising the separation performance. In the integrated hybrid device, mixtures of FLT and impurities were successfully injected, separated, and detected. Even though FLT was successfully separated from all impurities, several impurity peaks were not fully resolved with baseline resolution. While the separation performance of the integrated device was lower than desired, a detailed analysis identified the capillary-chip junctions as the problem. Extrapolating from the performance when junctions are eliminated, we argue that a device with optimized junctions [94] could achieve the requisite performance. Furthermore, the optimized MCE device would be very much smaller than an HPLC system.

Unlike simple colorimetric tests that have been developed for determination of certain individual impurities (e.g. Kryptofix 2.2.2, a phase transfer catalyst frequently used in the synthesis of ^{18}F-labeled PET tracers), MCE-based testing provides a flexible way to assess different and multiple impurities, possibly by tuning separation conditions and/or adding detectors (e.g. electrochemical, pulsed amperometric, etc.) for detection of species with low UV absorbance. Furthermore, separation prior to detection greatly reduces the chance of false negatives or positives due to non-specific interactions that can occur in colorimetric tests. Due to the flexibility of a chromatographic approach, it is expected that this device could easily be applied to the evaluation of PET tracers other than FLT. Furthermore, integration of a radiation detector would enable assessment of radiochemical identity and purity in the same device.

In the long term, this device and other microfluidic QC tests could be combined in a unified lab-on-a-chip device for performing fully-automated QC testing of radiopharmaceuticals. In addition to alleviating the burden of performing and documenting QC tests, such a system would reduce the amount of sample consumed for analysis, reduce the radiation exposure to personnel, and potentially reduce the time needed to complete all QC tests.

4. Chapter 4: Novel volumetric method for highly repeatable injection in microchip electrophoresis

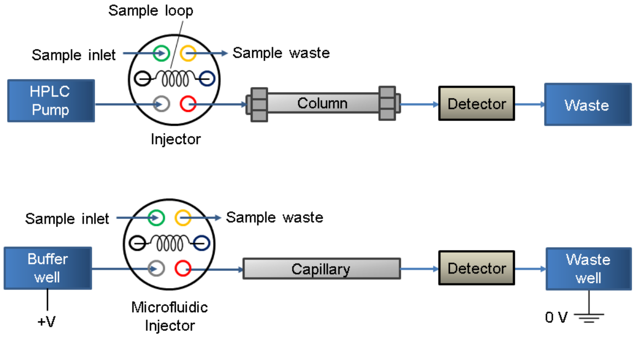

Volumetric injection (bottom) provides reliable injections for CE and MCE using the same concept as an HPLC injection valve (top)

4.1 Overview

We have previously explored the feasibility of using CE as a replacement for HPLC during quality control (QC) testing of batches of PET tracers. With CE, comparable separation performance and limit of detection could be achieved, while analysis times could be shortened in some cases. This is part of a larger effort to miniaturize all stages of tracer production to reduce costs of radiation shielding, equipment, and overall production, which could increase access to diverse PET tracers [23], [48], [193], [194].

4.1.1 **Motivation: Need of high injection repeatability in CE**

However, CE has often been considered to have inferior reproducibility compared to other separation techniques such as HPLC or gas chromatography (GC) due to sample injection bias, sample leakage and other factors inherently induced by current sample injection methods, and thus has not been as widely used in quantitative analysis [195]–[197]. Numerous advances have largely eliminated this concern in recent years [96], [156], though achieving the desired degree of reproducibility (e.g. peak area

RSD < 2% [182]) remains a challenge in many cases. In HPLC, highly repeatable sample volumes are achieved by using “injection valves”. In the “load” state of these specialized two-state valves, a “loop” of well-defined volume is filled with the sample, and, when switched to the “inject” state, this sample is injected directly into the separation pathway. Such method has not been directly applicable to CE due to the much smaller sample volume requirements of CE as well as issues arising from the use of high voltages. However, by developing an electrical decoupler, a similar approach has been shown in conventional, macroscale, CE systems [195], [198]. Sample was loaded into a nanoliter-scale injection valve, then pushed via a syringe pump through the electrical decoupler into the separation channel, after which the CE voltage can be applied. Combining this approach with low temperature operation, peak area RSD was reported to be 0.5 – 2.7%.

In microchip electrophoresis (MCE), however, it is generally preferable that the injection method be integrated directly into the microfluidic chip rather than relying on external systems. Though a wide variety of methods have been explored to increase the reliability of sample injection in MCE [168], [199], [200], to the best of our knowledge, there has not been a fixed loop injector as in HPLC that allows the same quantity of sample to be introduced per injection [197]. Typically in MCE devices, injection of sample into a separation channel occurs at the intersection point between a sample channel and the separation channel. The intersection may be a “T”, a cross, a “double T”. With a T junction, the sample flows directly into the separation channel and control of timing or the sample flow determines the injection volume. With a cross or double-T injection, the sample flow crosses the separation channel and flows toward a (sample) waste outlet; the detailed geometry of the junction and operation sequence/timing generally determines the injection volume.

4.1.2 **Various sample injection methods in MCE**

A common way to induce the sample flow is by applying a potential between the sample and a waste well (electrokinetic injection). While very simple and offering the possibility to perform integrated sample concentration (i.e. stacking) [95], this method suffers from injection bias in which solutes with higher electrophoretic mobilities are preferentially introduced, resulting in a difference between the compositions of the original and injected samples [167], [168]. The problem is exacerbated with repeated injections, though several groups have developed methods to replenish the sample to mitigate long-term changes in sample composition [201], [202]. The electrokinetic injection method is also sensitive to the voltage and to many properties of the sample (e.g. conductivity, pH, possibility of complex formation, electrolysis) [168].

To overcome these drawbacks, pressure-driven injection is becoming more widely used [168]. It is often performed in a cross or double-T geometry by applying a pressure difference between two points to drive sample into the separation channel, and then separation voltage is applied. The resulting sample plug is free of injection bias (thus representative of the original sample). The sample can be driven by hydrostatic pressure [203], with a syringe pump [204], or by applying positive or negative pressure to the sample well [192], [205]. A variety of other “plug shaping” techniques have been developed to reduce the sample volume and/or avoid sample “leakage” [188], [204], or to improve control of the sample volume [206], but they tend to add complexity and sometimes introduce injection biases.

Despite the advantages of these pressure-driven injection methods, injection reproducibility remains too low in many cases. Rather than rely on geometry to control the injection volume, several methods rely on internal pumps and valves to exert more precise control over the amount of sample injected. One approach is to use microvalve-based chips [207], typically made from poly(dimethylsiloxane) (PDMS). The basic concept is to apply constant pressure to the sample and use a computer-controlled microvalve that can be momentarily opened to inject the sample into the separation channel [188], [205]. Such valve-based approaches exhibit repeatable sample injection, yielding RSD of the peak area in the range of 1.76 to 5% [169], [200], [208]. Though pressure-driven injection eliminates analyte-dependent electrokinetic bias, it could still suffer from other types of variations due to its dependence on flow rate of the sample and microvalve timing to determine the volume injected and could be influenced by the sample properties such as viscosity, which can vary significantly with temperature.

In addition to timing-based valves, other approaches have been developed in an attempt to improve repeatability and reduce dependence on sample properties. Bowen and Martin reported controlling the actuation time and frequency of an on-chip peristaltic pump, rather than timing and pressure, to achieve consistent injection volume [103]. Karlinsey *et al.* reported a similar approach with a CV of peak area of ~5% [209]. There also has been an attempt to combine the on-chip pump with a valve-enclosed sample loading area; however, it would be challenging to achieve injection repeatability due to problems associated with the large dead volume [187]. Solignac and Gijs reported a different method in which an elastomeric membrane is actuated with an electromagnet to generate a pressure pulse to inject a controllable amount of sample [210]. Though most of these reports did not include reproducibility data, it is expected that all of these methods would still depend on fluid properties similarly to hydrodynamic injection.

4.1.3 **Our approach: Volumetric sample injection**

We have developed a valve-based microchip injection method that eliminates all of these biases and is similar in operation to an HPLC injection valve. Using PDMS microvalves placed around the separation channel, a well-defined fixed volume can be confined within the separation channel in a loading step [211]. Due to the volumetric metering approach, this method eliminates the injection bias found in electrokinetic injection and eliminates the influence of several variables in valve-based injection such as driving pressure, valve response times, or properties of the sample (e.g. viscosity). Furthermore, unlike previously reported methods to meter accurate volumes in an external injection loop, this method is directly integrated into the chip, avoids the need for an electrical decoupler, and avoids dispersion and mixing because the sample does not need to be moved before separation can begin. Thus substantially improved injection repeatability can be expected. We characterize the performance, compare to conventional hydrodynamic injection and electrokinetic injection, and demonstrate the independence from fluid properties such as viscosity.

4.2 Materials and methods

4.2.1 **Reagents and solutions**

Sodium phosphate monobasic (NaH_2PO_4), sodium phosphate dibasic dihydrate (Na_2HPO_4), sodium dodecyl sulfate (SDS), sodium hydroxide (NaOH), 3’-deoxy-3’-fluorothymidine (FLT), thymidine, 2´,3´-didehydro-3´-deoxythymidine (Stavudine) and zidovudine impurity B (chloro-L-thymidine; CLT) were purchased from Sigma Aldrich (Milwaukee, WI, USA). Glycerol (AR® ACS) was purchased from Avantor Performance Materials, Inc. (Center Valley, PA, USA). All chemicals were of analytical grade and were used as received without further purification. Deionized water (18 MΩ) was obtained using a Milli-Q® Integral Water Purification system (EMD Millipore, Billerica, MA, USA).

4.2.2 Microfluidic chip design and fabrication

The microfluidic injector chip and details of the channel design are shown in **Figure 4-1.** To achieve a well-controlled injection volume, sample is loaded into a fixed-volume chamber within the chip. The chamber is formed from a segment of a microchannel bounded by closed microvalves. The geometry and positioning of the microvalves are designed to minimize the dead volume. Inlets and outlet are connected to the sides of the chamber via microvalves to enable sample loading and washing. Once the chamber has been filled, microvalves at the ends of the chamber are opened, allowing the contents to be injected into the separation channel.

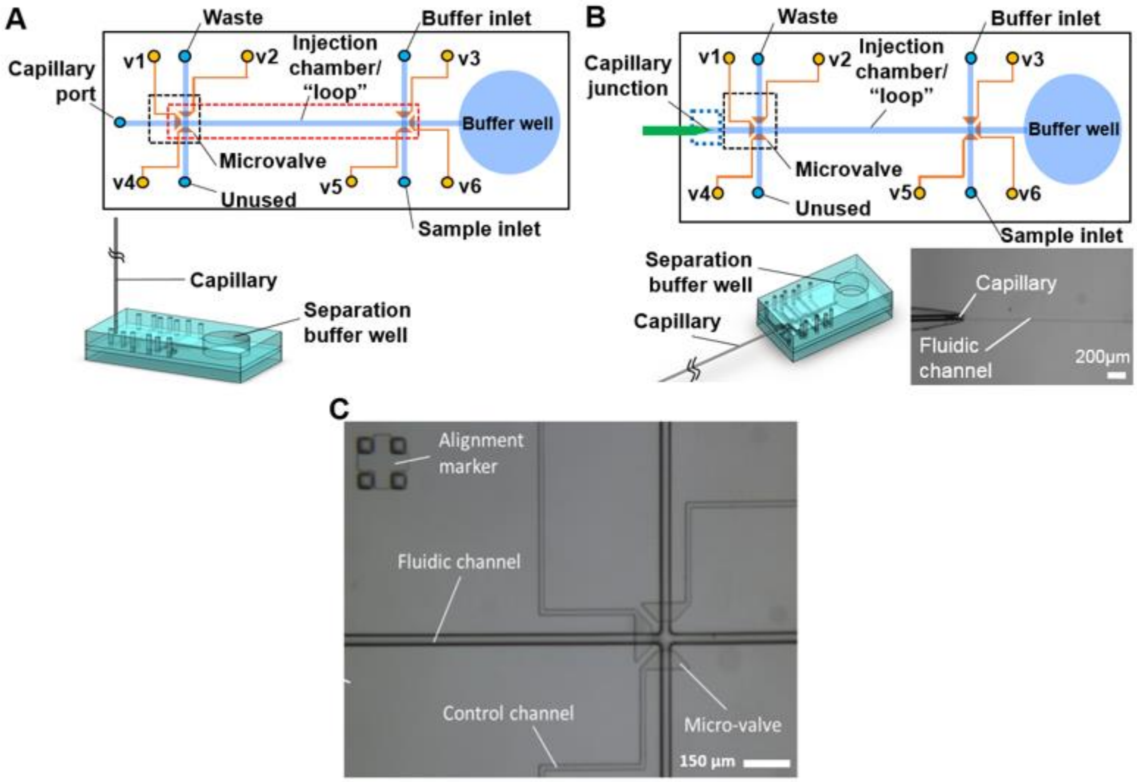

Figure 4-1. 3D representation and detailed channel design of the PDMS microfluidic chip.

Microfluidic injection chip connected to a capillary with (A) perpendicular junction geometry and (B) collinear junction geometry. Valve control channels are shown in orange and fluid handling channels are shown in blue. Micrograph of the collinear junction (blue dashed box) is shown in the inset in B. The injection chamber is outlined in a red dashed box. vx = valve control port. (C) Micrograph of the region in the black dashed box.

The chip was fabricated in the UCLA Integrated Systems Nanofabrication Cleanroom (ISNC) from poly(dimethylsiloxane) (PDMS) using multilayer soft lithography [207]. The chip consisted of two layers of PDMS bonded to a bottom PDMS substrate layer. Integrated microvalves were formed via a "push-up" valve architecture [170], with valve control channels (15 µm deep x 75 µm wide) molded in the thin PDMS layer closest to the substrate, and fluid-carrying ("flow") channels (20 µm deep x 75 µm wide) molded in a thicker layer above. The flow channel layers had a rounded cross section to enable complete channel sealing when underlying control channels were actuated. To minimize dead volumes, microvalves were placed as close as possible to the edge of the channel they were blocking. Details of the fabrication of molds and microfluidic chips are described previously [33].

Separation was performed in a 20 cm long, Teflon-coated fused silica capillary (75 µm I.D., 375 µm O.D; Polymicro, Phoenix, AZ, USA) connected to the PDMS chip. In initial experiments, the capillary was connected via a port perpendicular to the channel (“perpendicular junction”). While suitable for characterizing volume repeatability, the dead volume inherent in this design led to non-optimal separation. Thus, in later experiments, the capillary was connected by insertion directly into the microchannel through the side of the microfluidic chip (“collinear junction”) as mentioned in 3.5.3 (‘Separation of samples’). The two chip-to-capillary junctions are illustrated in **Figure 4-15**. For the chips with the capillary connected via the “collinear junction”, this port for the capillary was not punched. After three layers were assembled and completely cured, the chip was cut vertically from the top surface with a razor blade near the end of fluidic channel, such that the channel was accessible from the side of the chip. One end of the capillary was tapered by polishing with micro-grit sand papers (grit sizes of 600, 1200 and 2500 in sequence; 2 min each) on the spin-coater (Model PWM32, Headway Research, Inc., Garland, TX). At the end of this procedure, the capillary was tapered down to an outer diameter of close to 75 µm. With the aid of a stereomicroscope (Stemi SV 11, Zeiss, Oberkochen, Germany) and portable microscope (Dino-lite Plus AM311S, AnMo Electronics, Taipei), the tapered capillary was horizontally inserted about ~1mm deep into the exposed end of the fluidic channel.

To provide mechanical stabilization and provide an air-tight seal, additional PDMS pre-polymer mixture was poured near the interface and cured in the oven at 80°C for 2 h.

4.2.3 Microchip and capillary conditioning

The chip was hydrated prior to conditioning by filling the chip and capillary with water via the buffer inlet port. Water was loaded at 10 psi for 30 min to ensure all air was purged from the device. The chip was placed in a Petri dish containing a damp Kimwipe and wrapped with parafilm and the other end of the capillary was inserted into a septum-sealed vial containing DI water. Conditioning, to form hydroxyl groups [177] was performed by following this same procedure using 1M NaOH instead of water. Just prior to use, the NaOH was flushed first with water and then the separation buffer, i.e., 30 mM sodium phosphate buffer with 100 mM SDS.

4.2.4 Capillary electrophoresis setup

The overall setup to evaluate the PDMS injector chip is shown in **Figure 4-2**. The capillary extending out of the hybrid chip runs through a detection cell and the other end is placed in a PDMS waste well. The waste well is fabricated from two 1”x1/2” PDMS slabs (~5 mm thick). A well is created by punching a 4.75mm ID hole through the top slab prior to corona discharge bonding of the two slabs together.

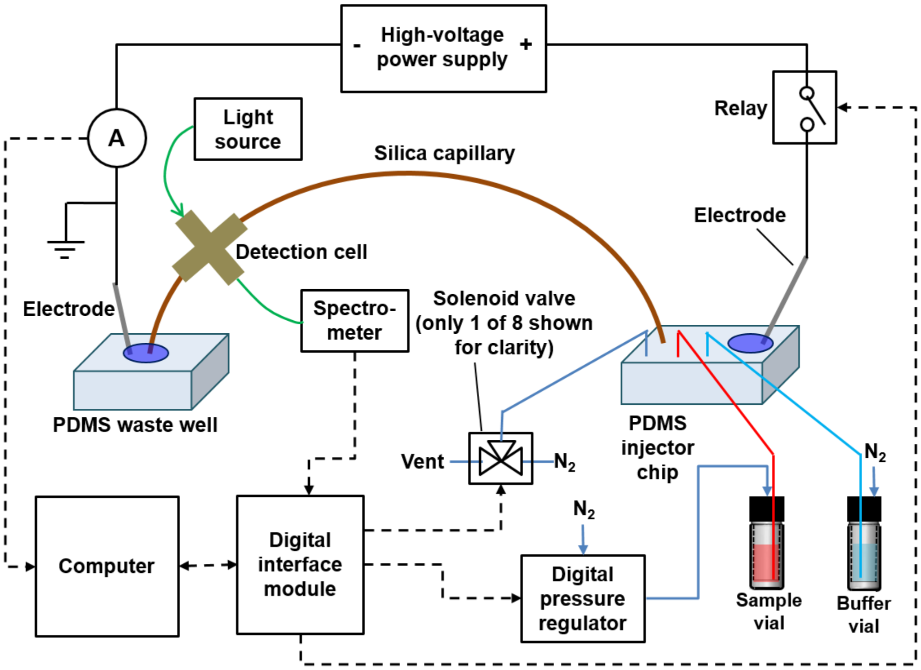

Figure 4-2. Experimental setup for evaluation of micro-injector chip.

The sample (~1 mL) was contained in a 2 mL septum-sealed vial (Fisherbrand™ 2 mL screw thread autosampler vial, Thermo Fisher Scientific, Waltham, MA, USA). Pressurized nitrogen gas was supplied to the vial through an electronic pressure regulator (ITV0010-3BL, SMC Corporation of America, Noblesville, IN, USA) set to a pressure of 1.5 psi. The vial also contained an outlet tubing (#30 PTFE tubing) connected to the sample inlet port of the injector chip. The buffer was contained in an identical vial, supplied with 6.0 psi nitrogen pressure, and with the outlet tubing connected to the buffer inlet of the injector chip. On-chip microvalves were each controlled by the common port of an external solenoid valve (S070B-5DG, SMC Corporation), connected to the chip via #30 PTFE tubing. The solenoid valves switched between two states: (i) supplying pressurized nitrogen (35 psi) to close the on-chip microvalve, and (ii) venting to atmosphere to allow the on-chip microvalve to open via elastic restoration of the PDMS. To avoid the generation of air bubbles inside the sample-containing channels of the chip, the valve control channels were filled with water. To achieve this, the end of each PTFE tubing was immersed in DI water and a ~1” water plug aspirated into the tubing prior to connection to the chip. By then supplying 35 psi pressure to each tubing for a few minutes, the small amount of air trapped in the corresponding channel was eliminated prior to operation.

Injected samples were separated via micellular electrokinetic chromatography (MEKC). The separation voltage was provided by a 0-30 kV high voltage DC power supply (HV350, Information Unlimited, Amherst, NH, USA). The tip of the high voltage electrode wire was submerged in the separation buffer well of the injector chip and that of the ground electrode wire was submerged in the PDMS waste well. Electrodes were held in place by electrically-insulated clamps mounted on a retort stand. 4kV was supplied to achieve a field of 190 V/cm across the separation channel (~1 cm long channel in chip plus 20 cm long capillary). CE voltage was turned on or off using a solid-state relay in series with the high-voltage side of the circuit. During operation, DC current was monitored in real-time via a digital multimeter (Model 2831E, BK precision, Yorba Linda, CA, USA) to detect any abnormal behavior of the chip such as air bubble formation followed by electrical arcing. The typical current was ~0.6 mA. If arcing occurred, the high voltage was immediately interrupted and the channel and capillary were flushed with buffer for 2 min to purge any bubbles and re-equilibrate the inner surfaces.

The detection cell was located 16 cm from the inlet of the capillary, i.e. 17 cm from the point of injection. It consisted of a 4-way junction (PEEK Cross, P-729, Idex Health & Science, Oak Harbor, WA, USA) for aligning the illumination and detection optical fibers with the capillary to perform UV absorbance measurements. Illumination was provided by a deuterium continuous light source (DH2000-DUV, Ocean Optics, Inc, Dunedin, FL, USA) and detection was performed via a spectrometer (USB4000, Ocean Optics, Inc, Dunedin, FL, USA). UV absorbance was measured at 262 nm, corresponding to the wavelength of maximum absorbance for the model compounds used (**Figure 4-3**).

The solenoid valves, digital pressure regulator and spectrometer were connected to a digital acquisition (DAQ) module (USB 6211, National Instruments Corporation, Austin, TX, USA). A custom-written LabVIEW program (National Instruments Corporation, Austin, TX, USA) was used to coordinate the timing of all functions.

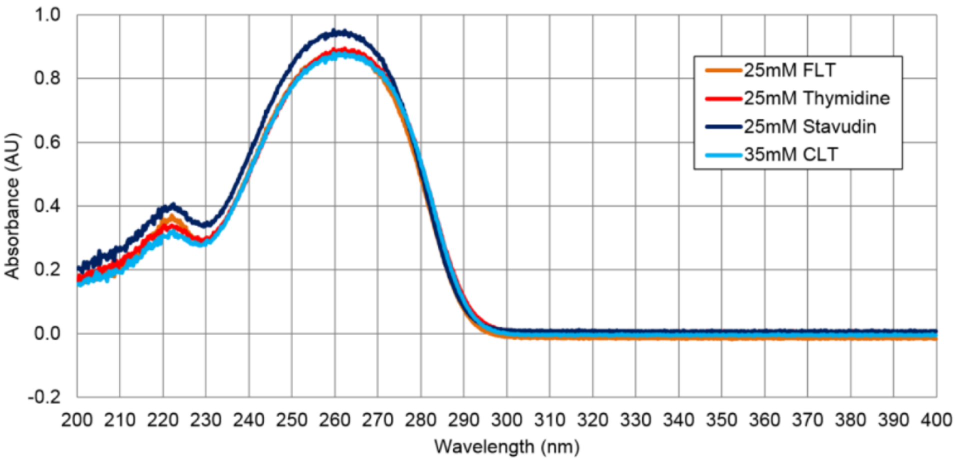

Figure 4-3. Absorbance of thymidine, stavudine, FLT and CLT as a function of wavelength.

4.2.5 **UV absorbance measurements**

Spectrometer output was recorded at a rate of 10 samples/s since the time of injection to create an electropherogram. The transmitted light intensity across the buffer-filled capillary, I_B, was measured by the spectrometer prior to sample injection and used as a reference. Then, the absorbance of the sample (A_S) was calculated as $A_S = \log_{10}(I_S / I_B)$, where I_S is the transmitted light intensity across the capillary containing the sample as measured by the spectrometer.

4.2.6 **Chip operation**

4.2.6.1 Volumetric injection

The detailed steps involved in operation of the chip to perform volumetric injection are shown in **Figure 4-4**. The basic approach is to prefill a fixed chamber (to volumetrically measure the sample), then open valves to fluidically connect this chamber to the separation channel, and finally apply the electric potential.

The chamber was a channel of length 4 mm (75 µm wide, 20 µm deep). Due to the rounded profile the nominal volume is approximately 4 nL. In our chip design, a valve (v7) was also included in the middle of this chamber, enabling switching to a chamber of only half the volume (i.e. ~2 nL). This valve is not shown in **Figure 4-4A**, but is shown in **Figure 4-6**. Valve v4 was not used and was kept closed at all times. Before operation, the chip was first primed with buffer (Step 1) to ensure that the tubing from the buffer vial and all channels are filled with buffer. This was accomplished by pressurizing the buffer vial (6 psi) and opening valves v1, v3, and v6 until the entire channel and capillary were filled with buffer, and the buffer started flowing out of all the ports and buffer well. Next (Step 2), the sample inlet was primed to ensure that the tubing from the sample vial as well as the sample inlet channel were completely filled with sample. This could be accomplished in two ways. In the first method (shown in the **Figure 4-4**), the sample vial could be temporarily pressurized to a higher pressure (e.g. ~10 psi) causing the air ahead of the sample to permeate out through the PDMS until the sample inlet was completely filled with sample up to the valve v5 (blind filling). A faster method is to purge the air by applying the normal sample pressure and opening both v2 and v5 until all of the air has passed through v5, the sample chamber, and past v2.

After priming, the sample chamber is loaded by pressurizing the sample to 1.5 psi and opening valves v2 and v5 (Step 3). Once the sample has started exiting the chamber through the waste, v5 is closed first, followed by closure of v2 after a ~2s delay (Step 4). The delay is included so that the sample pressure (1.5 psi) is not “trapped” in the sample chamber, which could distort the PDMS and change its volume [212]. The sample is then injected by opening valves v1 and v6 (Step 5), allowing a brief delay (150 ms) to ensure the valves are fully open, then then applying the electrophoretic potential (Step 6).

Though completion of chamber loading was monitored by observing liquid emerging out of the waste port, which could consume a relatively large amount of sample, it is conceivable to use other means such as on-chip peristaltic pumping for a certain number of cycles [103] to minimize sample consumption associated with each injection.

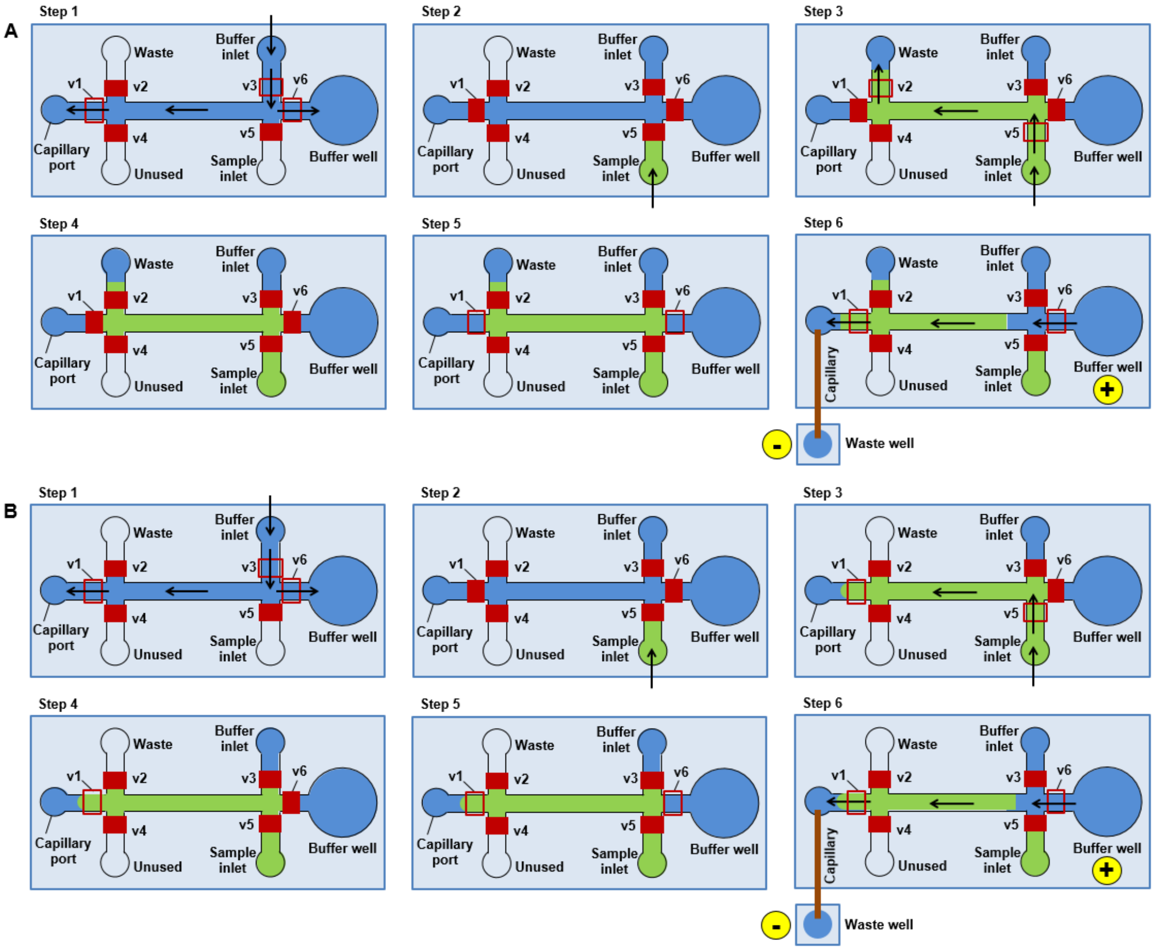

Figure 4-4. Schematic view of injector chip operation for volumetric injection (A) and timed injection (B).

Solid red boxes indicate closed microvalves and hollow red boxes indicate open microvalves. Arrows indicate direction of fluid flow. Channels filled with buffer are shown in blue while those filled with sample are shown in green. The capillary and waste well are connected for all steps but for clarity are only depicted in the final step when the separation voltage is applied. Diagrams not to scale.

4.2.6.2 Timed hydrodynamic injection

Using the same chip, it is also possible to perform conventional hydrodynamic sample injection, providing an ideal benchmark for comparison of the performance of the two injection methods. Basically, the sample is pressurized and a microvalve is momentarily opened to admit a small amount of sample into the separation channel. The detailed operation of the chip to perform “timed injection” is shown in **Figure 4-4B**.

Before use, the chip is first primed with buffer (Step 1) by pressurizing the buffer vial and opening valves v1, v3, and v6 until buffer started flow out of all the ports and buffer well. Next, the sample inlet is primed (Step 2) using either of the two methods described in the previous section. If the “purging” method is used, it it necessary to flush the sample out of the separation channel by flowing buffer through v3 and v2.

To load the sample, valve v1 is opened, and then valve v5 is momentarily opened for a fixed time to allow sample to fill part of the main channel in the chip (Steps 3-4). The opening time (600 ms) was chosen to achieve a comparable injection volume as the volumetric injection method (see **Figure 4-5**). The peak area resulting from volumetric injection was measured to be 3.5 AU-sec and 6.3 AU-sec for the timed injection.To inject the sample, v1 and v6 were opened (Step 5), followed by a brief delay (150 ms), and then electrophoretic potential was applied (Step 6).

It should be noted that in many reports of timed injection, there is no valve interrupting the separation channel. Since the sample flow is less constrained in that case (i.e. it flows both upstream and downstream into the separation channel), we believe such form of timed injection would have comparable or inferior performance to that reported here.

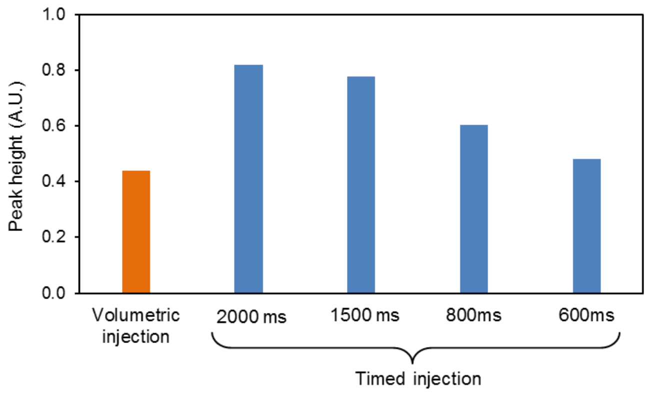

Figure 4-5. Determination of valve actuation time for hydrodynamic injection
Peak height of the timed injection as a function of valve opening time (n=1), and comparison to volumetric injection. Injected sample was 50mM FLT.

4.2.6.3 Controlling the injected volume: "Half" volume injection

We included a microvalve in the middle of the sample chamber to allow loading of two different sample volumes, i.e. a full chamber volume (~4 nL) or a half chamber volume (~2 nL). Chip operation to inject the full volume is shown in **Figure 4-4**. **Figure 4-6** shows the procedure to load a half chamber volume.

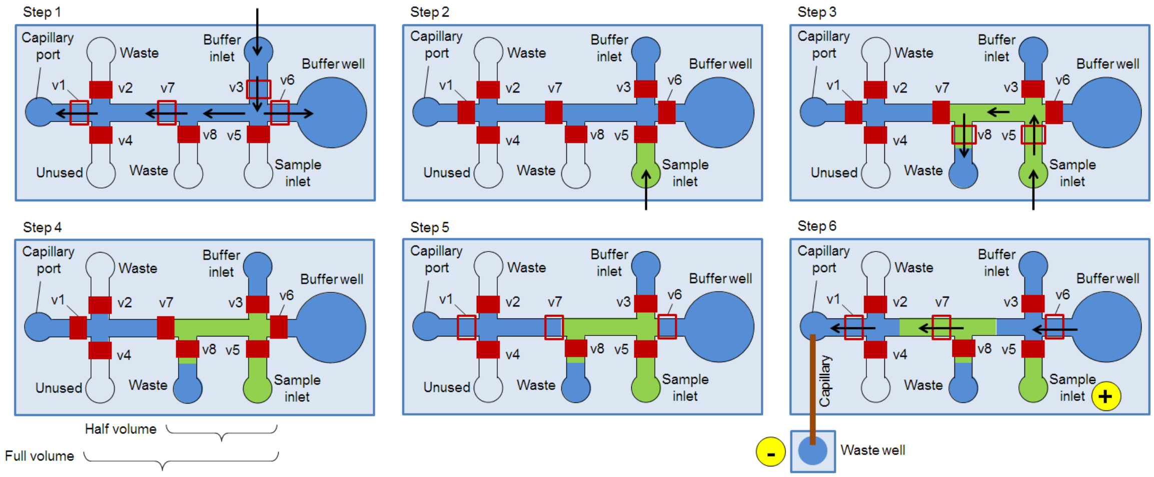

Figure 4-6. Sequence of operations to perform injection of a half chamber volume (2 nL).
The microfluidic chip used in this work contained an additional valve and waste port in the middle of the sample chamber that can be used to subdivide the sample chamber and thus provide some control over the sample volume. A full volume (4 nL) can be injected by keeping v7 open and v8 closed and performing the steps in **Figure 4-4**.

4.2.7 Injection performance characterization

Using the same chip design, comparisons were made among volumetric injection and timed hydrodynamic injection, as well as electrokinetic injection (see 4.2.8).

Injections were performed with single compounds initially, and then mixtures of multiple compounds. The single-compound samples comprised thymidine in DI water or FLT in 95:5 water:acetonitrile (v/v). The mixture sample contained thymidine, stavudine, FLT, and CLT in water. These represent the product and structurally-similar side products in the synthesis of the positron emission tomography (PET) tracer [^{18}F]FLT [102], [179]. Each injection resulted in an electropherogram. The detected UV absorbance peaks (at 262 nm) were fit to a Gaussian profile to determine the peak area and migration time (t_m; peak center) from each injection. Injection repeatability was measured by performing multiple injections in the same chip and calculating the RSD of peak areas. Sets of injections were performed in different chips to determine consistency.

Since peak symmetry can affect the resolution for mixture samples, we also characterized the peak symmetry by computing the U.S. Pharmacopeia (USP) tailing factor for each peak: $T_f = w_{ac} / 2w_{ab}$, where w_{ac} is the peak width at 5% of the peak height, and w_{ab} is the front half-width measured from the leading edge to a perpendicular dropped from the peak apex at 5% of the peak height. Tailing factor close to 1 is desired. The number of theoretical plates was also calculated for each peak: $N=16 \times (t_m/W)^2$, where t_m is the migration time and W is the baseline peak width determined via the tangent method (**Figure 4-7**). For mixture samples, the peak resolution between pairs of neighboring peaks was calculated: R= $(t_{m2}-t_{m1})/0.5*(W_1+W_2)$, where t_{mi} is migration time and W_i is the peak width at baseline (tangent method) for each peak (i = 1,2).

To avoid effects of buffer depletion, which can affect the migration speed and hence the peak area, the fluidic channels were flushed with fresh buffer solution after each individual injection. In addition, the buffer well and waste well were replenished with ~120 µL each of fresh buffer solution. It may be possible to avoid the need for manual buffer exchange by implmenting wells for buffer and waste that have larger volume. Alternatively, a more sophisticated microfluidic chip could be designed that includes additional valves and pumps to perform automated buffer exchange.

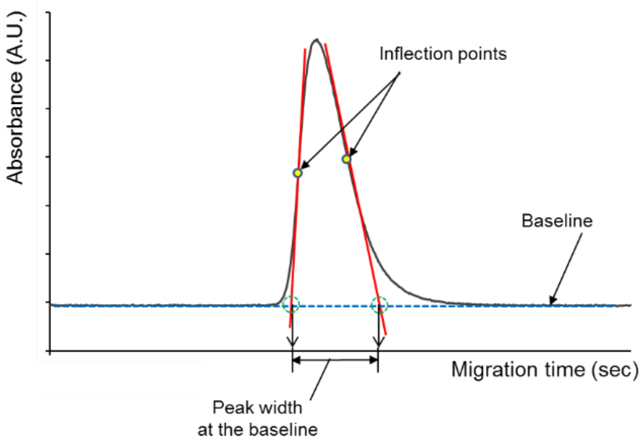

Figure 4-7. Method for determination of peak width
Baseline peak widths were measured using the tangent methods. Tangents were drawn from the inflection points on each side of the peak and intersection with the baseline determined. The distance between these intersection points was the peak width

4.2.8 Method of Electrokinetic injection

Electrokinetic injection (EK) was performed using the same chip to avoid the introduction of additional variables. Injection was performed by the series of steps in **Figure 4-8**. The chip is first filled with buffer (**Step 1**). During the sample loading step, v5 remains closed and sample reservoir is filled with the sample solution (**Step 2**). For sample injection, the same field strength as separation, 200 V/cm, was applied between sample reservoir and sample waste. Because the distance was 1.5 cm, a potential of 300 V was applied. Potential was applied for 3.0 s to inject sample in the sample reservoir toward sample waste (**Step 3**). This time was chosen to achieve a similar injection amount to the other approaches. Finally, the sample was injected into the capillary by applying separation voltage between the buffer well and waste well (**Step 4**). The injection electrodes submerged in the sample inlet and sample waste were physically removed from the wells 1 s prior to applying separation voltage to avoid any backflow or other undesired fluid movement. The channel was flushed with fresh buffer solution between injections with v5 closed to avoid any change in sample composition during the rinsing step.

To verify the comparable injection volume in EK injection and volumetric injection, we compared the peak area of each peak in multiple-compound electropherograms. For 20 mM thymidine, the peak area for volumetric injection was 1.21±0.01 AU-sec (n=4) and that for EK injection was 1.26±0.06 AU-sec (n=3). For 13.6 mM Stavudine, the peak areas of both volumetric and EK injections were 0.91 AU-sec (n=4 and 3, respectively).

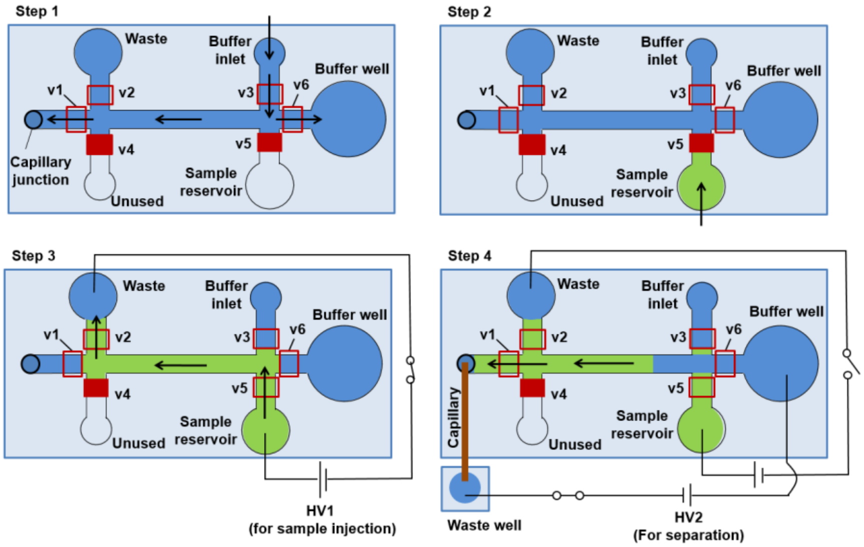

Figure 4-8. Schematic view of injector chip operation for EK injection.
Solid red boxes indicate closed microvalves and hollow red boxes indicate open microvalves. Arrows indicate direction of fluid flow. Channels filled with buffer are shown in blue while those filled with sample are shown in green. The capillary and waste well are connected for all steps but for clarity are only depicted in the final step when the separation voltage is applied. The same field strength (200 V/cm) was used for both sample injection (HV1) and sample separation (HV2).

4.2.9 **Measurement of microvalve response times**

To explore possible sources of variation in injected volumes for the timed injection method, we explored the consistency of response times of the on-chip microvalves. The experimental setup is shown in **Figure 4-2**. The positive terminal of a 5 VDC power supply was connected to the buffer well, and the ground terminal was connected to a series resistor, Rm = 8 MΩ, which was connected to the waste well. The potential causes a current to flow through the separation channel and capillary and through Rm. The voltage across this resistor, Vm, was measured over time while momentarily opening (for 600 ms) a microvalve positioned along the separation channel. When the valve was open, current could flow and Vm had a non-zero value. When the valve was closed, current could not flow and Vm was 0. The time period that the valve was open was determined from graphs of voltage versus time. Consistency of the total open time was compared for different valves on the same chip, different chips, and valves with different amount of hydraulic fluid (water) in the valve control lines.

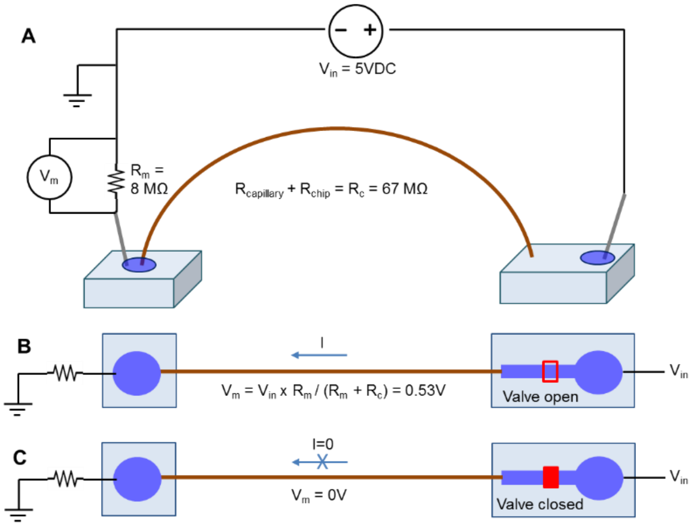

Figure 4-9. Experimental setup for electronically measuring the response time of microvalves.
(A)Experimental setup. V_m is recorded as a function of time by a computer as a valve is momentarily opened. The resulting plots are analyzed to determine the total time that the valve is open (i.e. non-zero V_m due to non-zero current through the fluidic circuit). (B) Illustration of current flow when microvalve is open. (C) Current is blocked when microvalve is closed.

4.3 Results and Discussion

4.3.1 Comparison of injection performance

In volumetric mode, the microfluidic chip with perpendicular chip-to-capillary junction was used to inject successive ~4 nL samples of single compounds. For each run, the electropherogram showed a flat baseline with a sharp single peak (**Figure 4-10A,B**). The migration time for thymidine was 207±2 s (n=11), and that for FLT was 221±6 s (n=11). Examples of the UV absorbance peaks from 11 successive injections in the same chip are shown in **Figure 4-10C** for 50 mM thymidine, and **Figure 4-10D** for 50 mM FLT. **Table 4-1** compares the peak area RSD values. As summarized in **Table**

4-1, the peak area RSD values for 3 trials (of 11 injections each) were 1.34%, 1.04%, and 1.47% for thymidine, and 1.79%, 1.55%, and 1.74% for FLT.

The small RSD values are comparable to or better than literature reports. To the best of our knowledge, the best reported peak area RSD was 1.77% (n=15) using a PDMS chip with integrated microvalves for timed hydrodynamic injection [169]. Since there are many factors of the setup that could affect the apparent consistency of the results (e.g., optical setup, light source stability, detector performance), our results likely cannot be directly compared to those of Li *et al*.

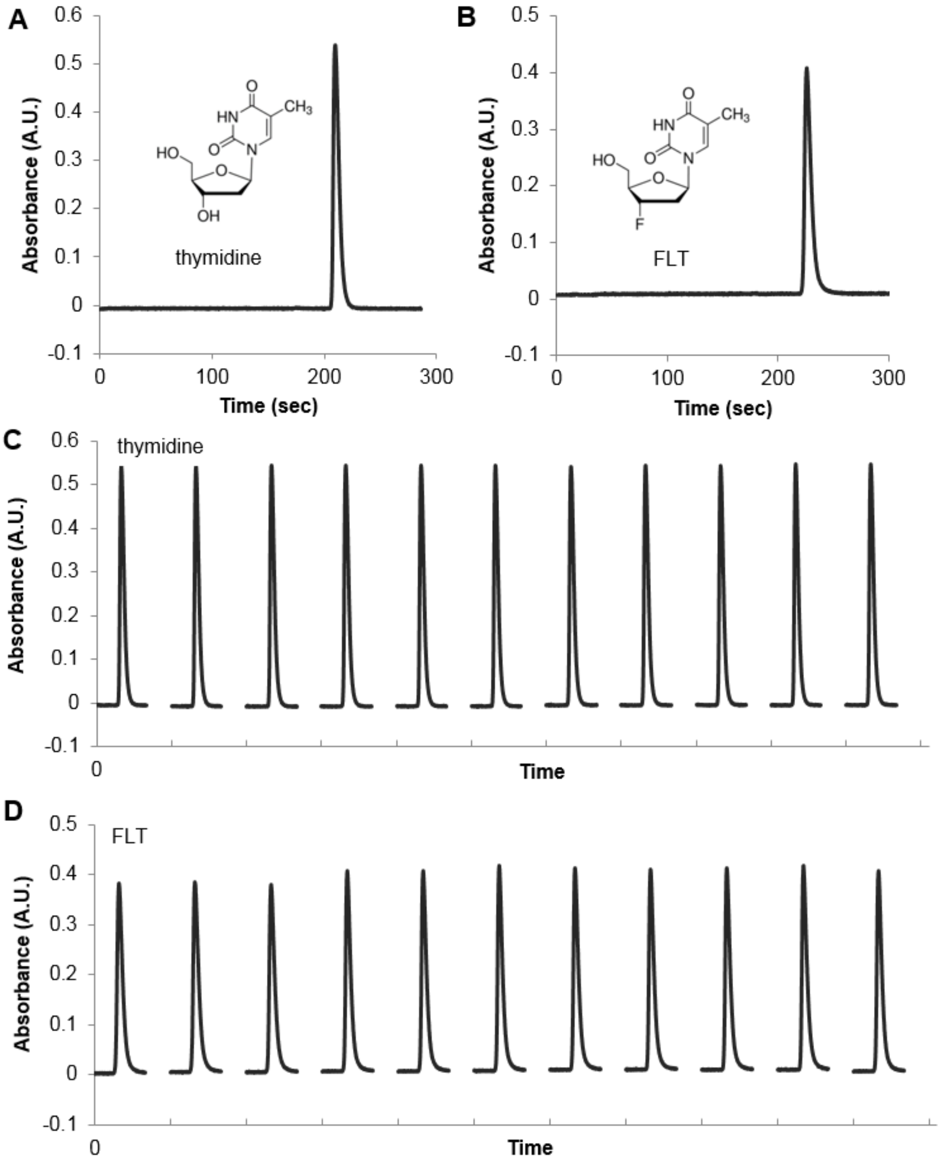

Figure 4-10. Electropherogram of single analyte injection.
(A) Example electropherogram of single injection of 50 mM thymidine using the microfluidic volumetric injector chip. (B) Example electropherogram for sample of 50 mM FLT. (C) Assembled electropherograms of successive injections (n=11) for 50 mM thymidine. Peak area RSD was 1.04%. There is a gap between peaks because the wells were replenished between runs to avoid effects of buffer depletion. (D) Assembled electropherograms for 50 mM FLT. Peak area RSD was 1.55%.

To better gauge the enhanced performance of volumetric injection, we also performed timed hydrodynamic injection in the same chip to eliminate potential variables. As expected, operation in time-dependent injection mode resulted in higher peak area RSD compared to volumetric injection. For thymidine, we observed peak area RSD values of 2.04%, 3.37% and 4.59% in three chips (11 injections per chip), and for FLT we observed values of 1.86%, 3.65% and 7.16%. Clearly, using the same chip and CE setup, volumetric injection shows significantly improved performance over timed injection.

Table 4-1. Summary of RSD values.
RSD values for single-compound injections using volumetric injection and timed injection in the same PDMS chip design. Each RSD value is computed from n=11 individual injections. A fresh microfluidic chip was used for each trial and for each compound.

Injection method	Injection parameters	Trial	Peak area RSD (%)	
			thymidine	FLT
Volumetric injection	Sample volume = 4 nL	1	1.34	1.79
		2	1.04	1.55
		3	1.47	1.74
Timed injection	Injection time = 600 ms	1	3.37	7.16
		2	4.59	1.86
		3	2.04	3.65

4.3.2 Sources of variation in timed injection

We investigated some factors that affect only the timed injection method to see if they could potentially explain the different performance (peak area RSD) between the two injection methods.

One consideration is the stability and repeatability of the pressure source. The flow rate of the sample would be expected to change linearly with any pressure changes. Some reports have controlled pressure via fluid height (hydrostatic pressure) [203], [213], [214] or external syringe pump [204], [215], while we used an electronic pressure regulator. The regulator is reported to have a stability of ±0.2% of full-scale value (i.e. ±0.06 psi). Since the sample pressure was nominally 1.5 psi, it is possible that pressure fluctuations could be responsible for at least some of the observed variation.

4.3.3 Measurement of microvalve response times

Another consideration is the consistency of microvalve operation: any variation in the opening or closing time could potentially affect the total amount of time the sample is flowing into the separation channel, and thus the volume that is loaded. The actual time the microvalve is open is the programmed opening time minus the opening response time plus the closing response time. The response times depend on several parameters: (i) the pressure of the gas used to control the valves (which may be subject to some fluctuation), (ii) the electromechanical response time of the external solenoid valve that switches between pressurized and vented state, (iii) the fluidic delay due to movement of pneumatic/hydraulic fluid within the valve control channel and valve control line (which would vary based on the amount of hydraulic fluid in the lines), and (iv) the mechanical deflection of the microvalve membrane (which would vary depending on the thickness of the micromachined valve membrane and the elastic properties of the PDMS). By monitoring the electrical current through a microchannel, we found in some cases significant variation (up to several %) in the total open time for a single valve (**Figure 4-11**) or for different valves (**Figure 4-12**) in the same chip. Variations in amount of hydraulic fluid in the valve control lines seem to have negligible effect on the total open time of the valves (**Figure 4-13**).

Volumetric injection, on the other hand, provides a way to use similar technology for injection (i.e. microvalves), but eliminate the effect of any variability in driving pressure, valve response times, etc.

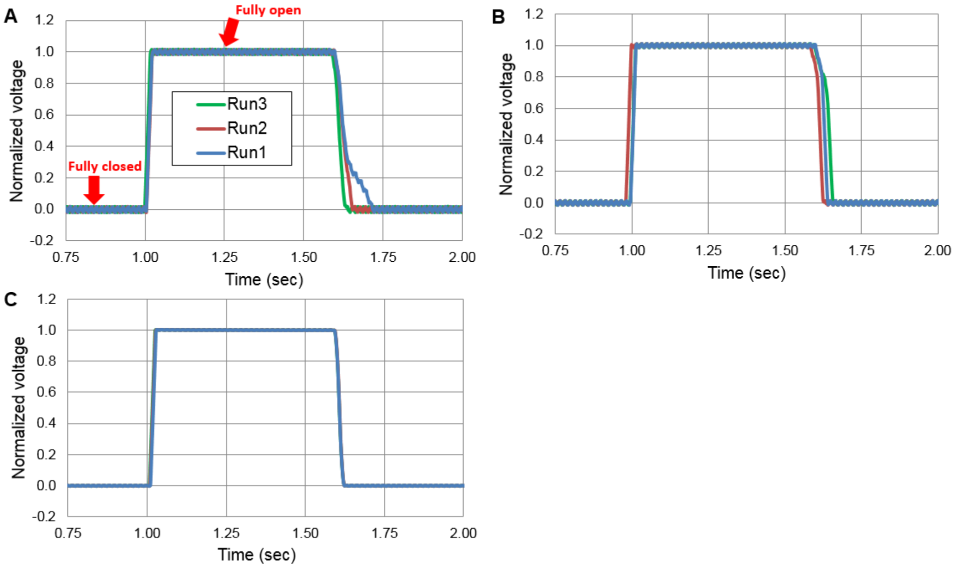

Figure 4-11. Repeatability of response time of the same microvalve in the same chip.
Graphs show normalized measurement of Vm, which is proportional to electrical current through the channel, as the valve was momentarily opened for 600 ms. (A) Valve in Chip 1, (B) Valve in Chip 2, (C) Valve in Chip 3. The same legend applies to all graphs. In chip 1, the valve had an open time RSD of 5.3% (n=3 runs), potentially contributing significant variation in injected volume and thus peak area. In chips 2 and 3, the valves had open time RSDs of 2.6% (n=3 runs) and 0.6% (n=3 runs), respectively.

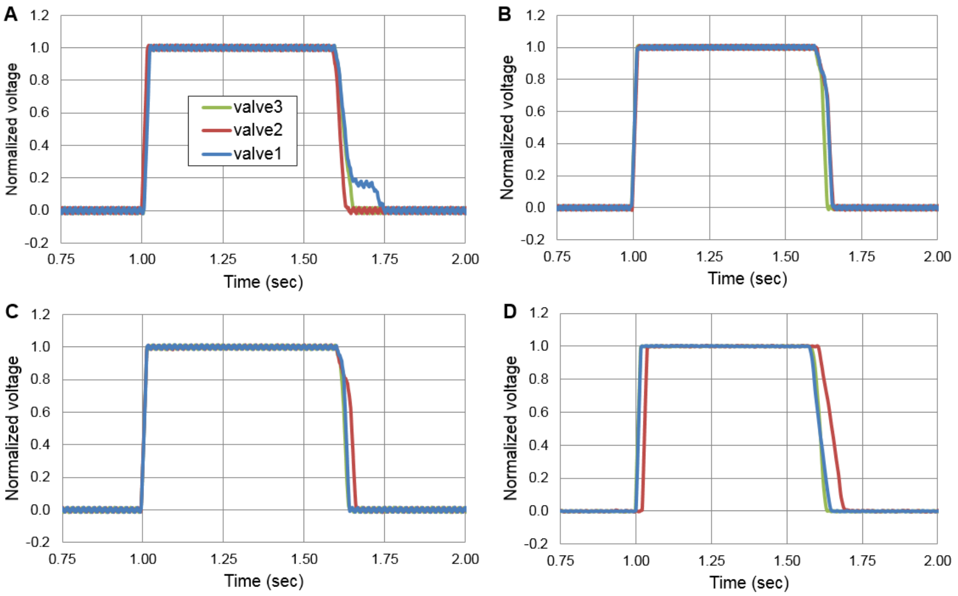

Figure 4-12. Repeatability of response time of different microvalves within the same chip.
Graphs show normalized measurement of V_m, which is proportional to electrical current through the channel, as the valves were momentarily opened for 600 ms. (A) Chip 1, (B) Chip 2, (C) Chip 3, and (D) Chip 4. The same legend applies to all graphs. The RSDs of the total open time were 7.9% (n=3 valves), 5.8 (n=3 valves), 1.8 (n=3 valves), and 0.9 (n=3 valves), respectively, for Chips 1-4.

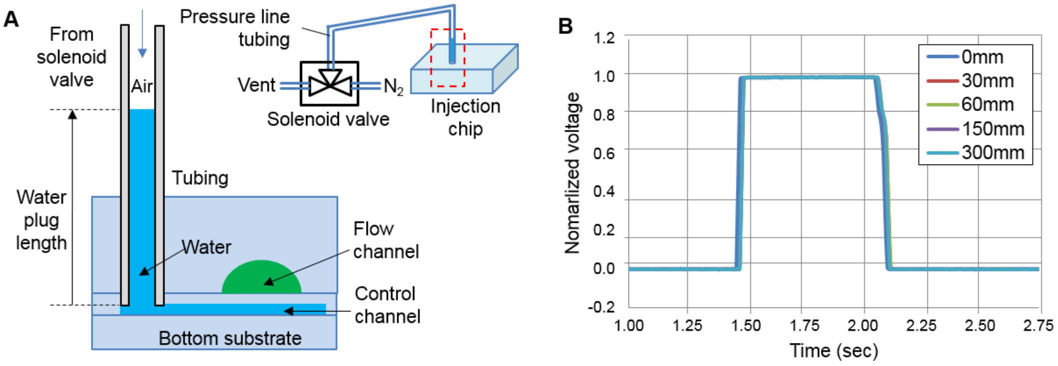

Figure 4-13. Effect of the amount of hydraulic fluid on the microvalve response time.
(A) Schematic showing the tubing connecting the solenoid valves to the control channel inlet ports on the microfluidic chip. The distal portion of the tubing (i.e. closest to the chip) is typically filled with hydraulic fluid (e.g., water) to avoid injection of pressurized gas into the other device channels by permeation through PDMS. (B) Normalized voltage profile of a single valve actuation with varying amounts of hydraulic fluid (water).

4.3.4 Effect of sample viscosity on injection repeatability

The volumetric flow rate, $Q = \Delta p/R$, can be affected by the stability of the driving pressure Δp or by the fluid resistance, *R*, which is highly dependent on the geometry of the channel as well as fluid properties (i.e., proportional to sample viscosity). A higher viscosity sample will flow more slowly than a low one, so any inconsistencies in sample concentrations, sample buffer composition, or temperature (e.g. Joule heating over time) can lead to poor reproducibility. The latter can be a significant issue as viscosity of aqueous solutions can exhibit significant temperature dependence (e.g., at room temperature, the viscosity of water or saline solution can vary ~2%/°C [216], [217]). One of the expected advantages of volumetric injection is that the loaded volume should be independent of the fluid properties. We compared the effect of viscosity on the quantity of sample injected for the two injection methods (**Figure 4-14**). Samples consisted of 50 mM thymidine dissolved in DI water or dissolved in 30% glycerol/water (v/v), with expected dynamic viscosities of 0.893 mPa-s and 2.57 mPa-s, respectively, at room temperature [218], [219].

For timed injection, the higher viscosity sample showed significantly lower peak area compared to non-viscous sample ($p = 8\text{x}10^{-8} << 0.05$, two-tailed T-test). The peak area was 3.58±0.10 AU-sec (n=6) for the low viscosity sample and 2.84±0.09 AU-sec (n=6) for the high viscosity sample. Based on the Hagen-Poiseuille equation, the flow rate is expected to be inversely related to the dynamic viscosity, and so a nearly 3-fold reduction in injected volume would be expected based on the viscosity differences (for the same driving pressure and valve opening time). A smaller reduction was seen, perhaps due in part to the elastic nature of the PDMS which may expand slightly and tend to reduce the fluidic resistance, counteracting the effect of increased viscosity.

In contrast, with volumetric injection, the peak areas of the low and higher viscosity samples were not significantly different (p = 0.20). The lower viscosity sample had peak area of 3.05±0.08 AU-sec (n=6), while the higher viscosity sample had peak area of 3.10±0.05 AU-sec (n=6). Thus the volumetric injection technique is expected to prevent differences in injection amounts for different samples, or for the same sample at different temperatures. This could enhance quantitative performance in situations where a variety of different samples (or sample buffers) may be injected in sequence.

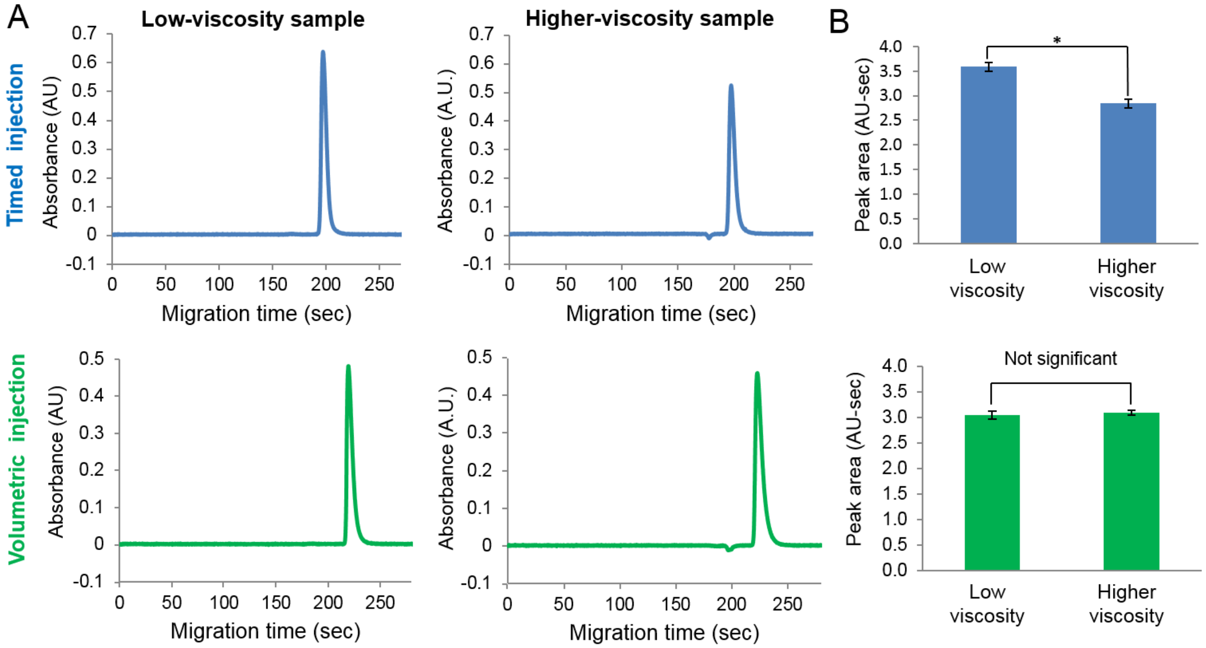

Figure 4-14. Effect of sample viscosity.
(**A**) Representative electropherograms of thymidine samples with different viscosities injected via timed injection (hydrodynamic injection) and volumetric injection. Note that the small negative peak in the eletropherograms for the higher viscosity samples likely represents the glycerol that is present in these samples. (**B**) Averaged peak area (n=6 each) observed at detector after separation voltage applied. The use of timed injection results in variation in peak area (i.e. amount injected) depending on viscosity. For volumetric injection, the peak area is independent of viscosity.

4.3.5 Other comparisons between injection methods

An advantage of timed injection is that different injection volumes can easily be achieved via control of the valve opening time. This flexibility can be used to accommodate different length capillaries or other variations in CE method that might require different sample amounts. In the volumetric approach, the volume too can be adjusted, but requires redesign of the chip to implement a chamber of different volume. Alternatively, modest changes in volume could be achieved by filling the chamber under pressurized conditions, which leads to a predictable expansion of the chamber volume [212]. (The loading process would need to be slightly modified to ensure that the sample chamber is closed while still under pressurized conditions.) Another possible approach to add volume flexibility is to introduce several microvalves along the sample chamber to allow the length of the chamber to be dynamically adjusted (in discrete steps) [220], as was done in the chip designed in this study (i.e. either ~2 or ~4 nL injection volume).

Another difference between the two injection methods is the flow profile. The hydrodynamic flow associated with timed injection has a parabolic velocity profile (i.e. faster flow in middle of channel compared to flow near the walls), which could lead to a small amount of dispersion in the sample plug as it is loaded from the inlet into the separation channel. In contrast, in volumetric injection, the injection chamber is part of the separation pathway and the sample does not undergo this dispersive flow prior to experiencing the separation potential.

4.3.6 Improvement of peak symmetry via colinear junction configuration

It was evident from the electropherograms (e.g. **Figure 4-10**) that there was significant peak tailing for both the volumetric and timed injection approaches. For samples of 50 mM FLT, the tailing factors were 1.78±0.2 (n=8; volumetric injection) and 1.80±0.19 (n=8; timed injection), and for 50 mM thymidine, the tailing factors were 1.62±0.14 (n=8; volumetric injection) and 1.85±0.05 (n=8; timed injection).

We suspected the tailing was largely due to the chip-to-capillary junction. The “perpendicular” junction used in initial studies has significant dead volume (**Figure 4-15**), which is known to be a cause of dispersion and potentially peak asymmetry as the sample plug is flowing through that region [184], [185]. To attempt to resolve the issue of peak shape, we implemented an improved chip-to-capillary junction with minimal dead volume. Indeed, when switching to a “collinear” junction geometry, we observed that absorbance peaks were significantly narrower and more symmetric (**Figure 4-16**). For samples of 50 mM thymidine, the tailing factor was within the acceptable range (i.e., 1.15±0.01, n=8) with the collinear junction compared to 1.62±0.14 (n=8) with the perpendicular junction and this was comparable to the tailing factor of electrokinetic injection with the collinear junction, 1.18±0.21 (n=8).

In addition, the number of theoretical plates increased from 7770±730 (n=8) to 9130±710 (n=8) with use of the collinear junction compared to the perpendicular junction. For a trial of successive injections, the peak area RSD was found to be 1.56% (n=10), which is in the same range as results with the perpendicular junction chips.

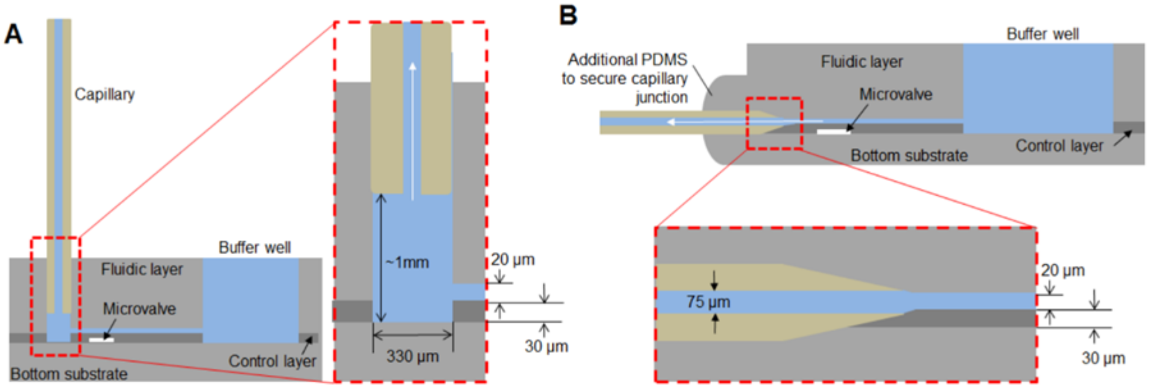

Figure 4-15. Schematic of chip-to-capillary junction geometry.
(A) Perpendicular junction; (B) collinear junction. Diagrams not to scale.

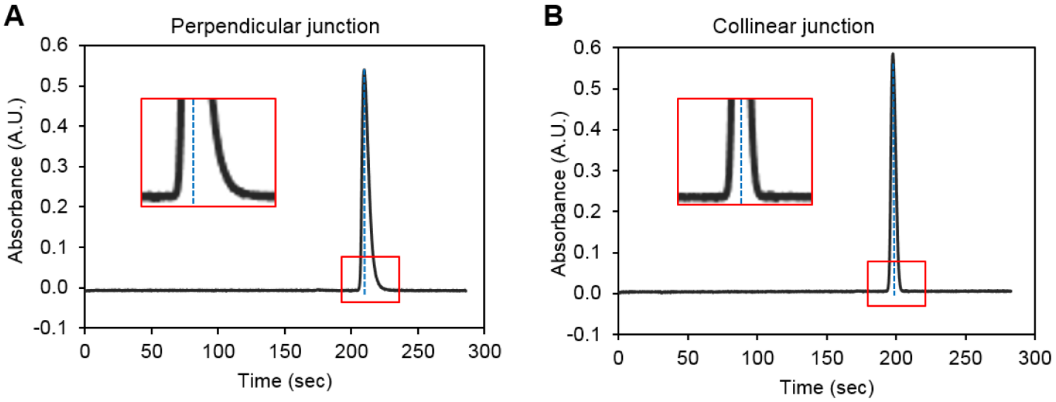

Figure 4-16. Peak symmetry comparison between two junction configurations.
Electropherograms of injected via the volumetric injector chip with the perpendicular chip-to-capillary junction (A) and the collinear junction (B). Inset shows zoomed in peak shape in the region of red box.

4.3.7 Separation of 4-compound mixtures

We then examined the ability to separate multiple compounds, and compared results of volumetric injection (with two different junction geometries) as well as the widely-used approach of electrokinetic injection. To avoid introducing additional variables, similar injection volume was used in all three different injection modes. Baseline separation of a mixture of 4 compounds was achieved using the microfluidic volumetric injector chip with the collinear junction (**Figure 4-17**). Separation using the perpendicular junction is shown in the , and separation using electrokinetic injection is shown in the **Figure 4-19.**

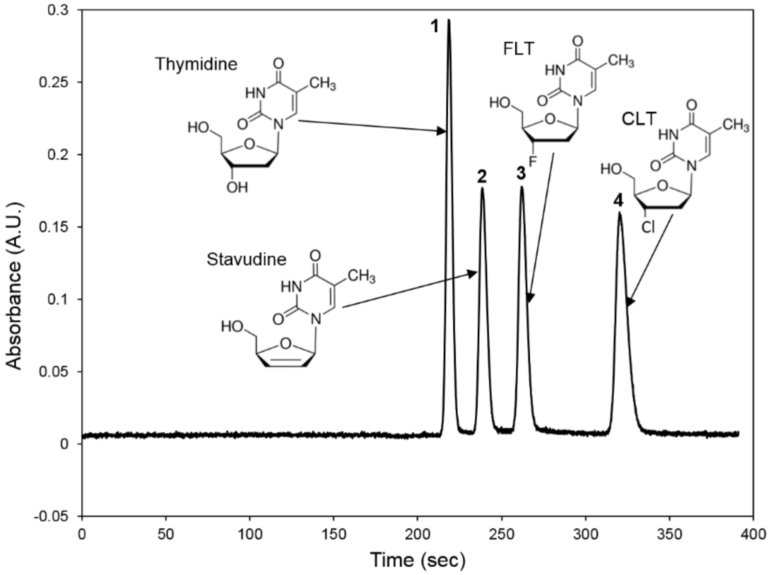

Figure 4-17. CE electropherogram showing baseline separation of a mixture of 4 compounds.
Using the microfluidic volumetric injector chip and 20 cm capillary connected via collinear junction. Injected sample contained: 20 mM thymidine (peak 1), 13.6mM Stavudine (peak 2), 16mM FLT (peak 3) and 14mM CLT (peak 4).

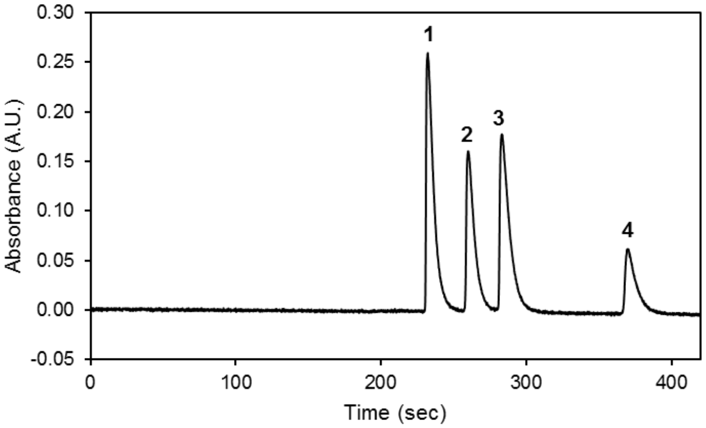

Figure 4-18. Electropherogram of four compound mixture injected via the volumetric injector chip with the perpendicular junction geometry
The sample contained: 20mM thymidine (peak 1), 14mM Stavudine (peak 2), 16mM FLT (peak 3) and 6mM CLT (peak 4).

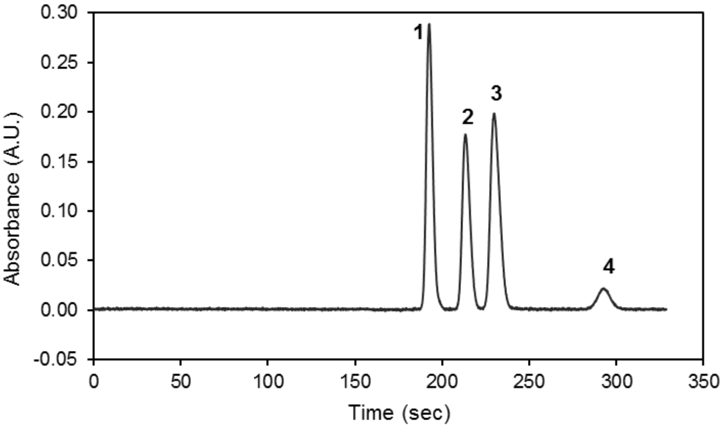

Figure 4-19. Electropherogram of four compound mixture injected electrokinetically in the volumetric injector chip with the collinear chip-to-capillary geometry
The sample contained: 20mM thymidine (peak 1), 13.6mM Stavudine (peak 2), 17mM FLT (peak 3) and 4mM CLT (peak 4).

Peak area RSD values for the 4 compounds and various injection methods are summarized in **Table 4-2**. It implies that the capillary-to-chip junction geometry does not significantly affect the sample injection repeatability. This is expected because the injected sample amount is physically metered within the injection chamber before even seeing the junction. For volumetric injection, the peak area RSD was always < 2.0% and values as low as 0.55% were observed. When electrokinetic injection was performed in the same chip with the same injection volume (as verified by comparing peak areas), the peak area RSD was found to be substantially higher, indicating less consistent sample injection. From these results and the comparison of volumetric and timed injection presented earlier, it appears that sample injection repeatability is mainly influenced by the injection method.

Table 4-2. Summary of peak area RSD (%) for mixture samples.

	Volumetric injection		**Electrokinetic injection**
	Perpendicular junction (n=4)	**Collinear junction (n=3)**	**Collinear junction (n=3)**
thymidine	0.40	0.55	7.13
stavudine	1.59	1.70	7.86
FLT	1.78	0.65	7.79
CLT	1.93	1.69	5.78

The number of theoretical plates, N, was also calculated for each peak for each junction geometry (**Table 4-3**). As expected, we observed N to be significantly higher for all compounds for injection using the collinear junction compared to the perpendicular junction ($p<0.05$). In addition, N was significantly higher using volumetric injection than electrokinetic injection in the same chip ($p<0.05$). The peak resolution, R, was also calculated between pairs of adjacent peaks (**Table 4-3**). Peak resolution between the thymidine and Stavudine peaks was significantly higher for volumetric injection using the collinear capillary-to-chip junction compared to the perpendicular junction; however, the difference in resolution for Stavudine and FLT peaks, and for FLT and CLT peaks, was not statistically significant. Interestingly, R was significantly higher for volumetric injection than for electrokinetic injection in the same chip. These results illustrate that the improved injection repeatability does not come at the expense of sacrificed performance elsewhere.

Table 4-3. Summary of the number of theoretical plates and the peak resolution for mixture samples.

	Peak(s)	**Volumetric injection**		**Electrokinetic injection**
		Perpendicular junction (n=4)	**Collinear junction (n=3)**	**Collinear junction (n=3)**
Number of theoretical plates, N	thymidine	12090 ± 1600	21910 ± 1100	12440 ± 860
	Stavudine	12130 ± 660	18190 ± 550	10720 ± 940
	FLT	10190 ± 750	15390 ± 770	8800 ± 1400
	CLT	14400 ± 1300	17570 ± 1030	8040 ± 530
Peak resolution, R	thymidine-Stavudine	3.18 ± 0.22	3.60 ± 0.19	2.65 ± 0.10
	Stavudine-FLT	2.28 ± 0.09	2.34 ± 0.07	1.77 ± 0.12
	FTL-CLT	7.77 ± 0.44	8.10 ± 0.19	5.32 ± 0.30

4.4 Conclusions

A novel type of volumetric microfluidic injector for CE was developed to eliminate variations in injection volume and thereby increase repeatability for quantitative analysis. With this injection method, substantially improved repeatability of sample injection was achieved compared to hydrodynamic injection. Volumetric injection showed relative standard deviation (RSD) of peak area as low as 1.04% (n=11) for single-compound injections and as low as 0.40% (n=4) for multiple compound injections, both of which are lower than the best RSD values reported in the literature for hydrodynamic microvalve-based injection. Furthermore, in contrast to hydrodynamic injection, volumetric injection was found not to depend on sample viscosity, which might be beneficial in situations where diverse samples are studied, or where sample temperature is not well controlled.

As a demonstration of the performance of the volumetric injection approach, we showed successful baseline separation of a 4-compound mixture with high injection repeatability. The set of compounds represents a positron emission tomography tracer and synthesis byproducts, illustrating how rapid CE analysis could be used in the QC testing process of radiopharmaceuticals to ensure that levels of impurities are below acceptable limits. In previous work we showed that adequate limit of detection could be achieved for this application [102].

We also made comparisons of injection repeatability, peak symmetry, and separation efficiency for different chip-to-capillary junction geometries between the PDMS injection chip and separation capillary. Injection repeatability was not influenced by the junction geometry, but number of theoretical plates and peak symmetry were all higher in the collinear junction (with very small dead volume) compared to the perpendicular junction (with significant dead volume). Compared to electrokinetic injection (performed in the same chip to avoid introducing additional variables), we found volumetric injection to have significantly higher separation efficiency, resolution, and injection repeatability.

The injector is straightforward to implement with standard PDMS microfluidic fabrication techniques. To increase volume flexibility, valve-based approaches where the volume or length of the chamber is dynamically adjusted can be readily incorporated [212], [220]. The separation channel can be incorporated in a hybrid fashion as was done here (i.e. with capillary), or could be integrated directly into the microfluidic chip. This injector would be useful in a wide range of applications where an accurate and/or consistent injection amount is needed.

5. Chapter 5: Integration of high-resolution radiation detector for microchip electrophoresis

5.1 Introduction

Capillary electrophoresis (CE) has been used in a variety of fields such as separation of biomolecules [92], [93], [147], environmental monitoring [150], [151], food analysis [152], [221], and explosive forensics [222]. Typically compounds are detected via UV absorbance [REF], and additional modes of detection can be implemented such as pulsed amperometric detection [103], capacitively coupled contactless conductivity detection (C4D) [104]–[106], refractive index detection [107], or mass spectrometry [108], [109]. Using a radiation detector, CE has also been used for separation of radioactive compounds, in applications such as assessing the purity of radiotracers labeled with positron-emitting isotopes for positron emission tomography (PET) or labeled with gamma-emitting isotopes for single photon emission computed tomography (SPECT) [99], [101], as well as the analysis of radioisotopes in nuclear fuel development [223], [224].

Analysis of radiopharmaceuticals is performed to satisfy quality control (QC) testing requirements after preparation of each batch of these compounds to ensure safety prior to use in patients [34], [36], [225]. Unlike ordinary pharmaceuticals, the short lifetime of radiopharmaceuticals due to radioactive decay requires fast analysis before injection. In addition, it requires high separation power to accurately determine the radiochemical purity and high sensitivity to quantify a variety of potential non-radioactive impurities. Though the analysis is typically performed with HPLC, the requirements align well with the general capabilities CE including rapid, high-resolution separation, sensitive detection, and small sample volume. In fact, these features of CE can be further improved by miniaturization of CE, i.e. microchip electrophoresis (MCE), which reduces reagent and sample consumption, reduces separation time, improves repeatability and can lower the overall cost via miniaturization and automation [88], [165]. An MCE setup is expected to have similar separating power as HPLC, but significantly smaller footprint – an important criteria in radiochemistry applications where radiation-shielded laboratory space is at a premium.

MCE has not yet been used for radiochemical analysis of radiopharmaceuticals, but we have previously demonstrated, using a “hybrid” MCE device, the successful separation and detection of non-radioactive impurities that arise during the synthesis of the PET tracer 3’-deoxy-3’-[^{18}F]fluorothymidine ([18F]FLT) [33], [94]. To perform radiochemical analysis, it would be necessary to add a radiation detector to this system. Radiation detection is challenging in MCE in general due to the tiny (nanoliter range) sample volume, which contains very little radioactivity and therefore requires a high-sensitivity detector to ensure individual analytes can be reliably detected with high temporal resolution. Furthermore, the spatial resolution of the radiation detector must be high to distinguish among closely spaced radioactive analytes. So far, most works involving radiation detection in radio-CE have used a scintillator combined with photomultiplier tube (PMT) as the detection method, which has reasonable sensitivity [99], [223], [224], [226]–[228]. However, these systems are bulky, and will require significant radiation shielding for the scintillator if not detecting specifically for positrons.

Measuring radioactivity, particularly for PET, in a microscale environment is tricky, since there are both the gamma rays (from positron-electron annihilation can come from further distance leading to a poor spatial resolution) and the positrons which only travel shorter distances (i.e., a few mm). A few groups have reported the microscale radiation detection methods for non-CE applications. When evaluating each of these approaches for potential use in our MCE device, it is important to note that radiation detection method must have both high sensitivity as well as high spatial resolution [229]. Taggart *et al*. used an array of silicon photomultipliers (SiPM) to measure radioactivity in a microchip for PET and SPECT tracers. However, gamma ray detection and the SiPM's intrinsic high background noise as well as low signal response led to low sensitivity [125]. They also required an entire array of detectors to gain high spatial resolution and account for gamma rays from other areas of their chip. Cho *et al.* described a system using a plastic scintillator and CCD camera to image a microchip used in PET tracer synthesis, though their spatial resolution and sensitivity come at the cost of long imaging times, and it requires complete dark conditions to reduce noise and sample to be stationary [129]. Dooraghi *et al.* also developed an imaging device for microchips, but using an avalanche photodiode (APD) as the radiation detector which shows near perfect sensitivity to the positrons and very low sensitivity to the gamma rays, with the limit of detection in the nano-Curie levels [133]. The analog signal response and internal gain makes the detector a good choice, though imaging requires a larger detector and long acquisition time that is too slow for a flowing sample. Tarn *et al.* was one of the few groups to demonstrate single-point detection, using a machined plastic scintillator microcell as a microscale HPLC radiation detector. Even though they showed excellent spatial resolution, the sensitivity was compromised due to its use of SiPM as mentioned above [230]. Use of an SiPM in this context would require either collimation, which increases the size of detector and reduces the sensitivity, or scintillation, which reduces spatial resolution and requires more comprehensive optical shielding.

The ideal low-activity radiation detector for MCE would be a positron/charged-particle-focused detector, since they interact strongly over a small range and therefore allow for a miniaturized sensitive device. From this information, the APD was chosen as the radiation detection method for our MCE system based on the inherent sensitivity of the device to charged particles, as well as the relative ease of integration into a microfluidic environment due to its small size. The typical radioactivity concentration in an injectable PET tracer ranges from 37 - 370 MBq/mL (1-10 mCi/mL), which leads to very low signal available due to small sample volume used in microfluidic devices. Since the APD can detect nearly all of the potential positron events, it can work in the low-activity regimes, and focusing on positrons can substantially improve the separation resolution. Since the positrons from most PET-relevant isotopes travel in the mm range before annihilating, this is particularly important [231], [232, p. 68], [233]. With its very low sensitivity to far-reaching gamma rays along with fast acquisition time, the APD is the ideal radiation detector for the MCE device.

Based on this approach, we develop here the first, to our knowledge, MCE system with integrated radiation detector. Into a microfluidic detection chip containing a Z-shaped cell for UV absorbance detection, we added a radiation detection region comprising a thin-walled segment of a microchannel against which a small APD could be mounted. The detection chip was coupled to a fused-silica capillary and PDMS injection chip in a “hybrid” radio-MCE device. We present a detailed characterization of this system and a demonstration of the ability to simultaneously perform chemical purity analysis and radiochemical identity analysis using the PET tracer [^{18}F]FLT as a model compound.

5.2 Materials and methods

5.2.1 Reagents

Sodium phosphate monobasic (NaH_2PO_4), sodium phosphate dibasic dihydrate (Na2HPO4, ≥99.0%), sodium dodecyl sulfate (SDS, ≥98.5), potassium phosphate monobasic (KH_2PO_4, ≥99.0%),), sodium hydroxide (NaOH), thymidine (≥99%), 2′,3′-didehydro-3′-deoxythymidine (stavudine, ≥98%), and nosyl chloride (97%) were purchased from Sigma–Aldrich (Milwaukee, WI, USA). Zidovudine impurity B (chlorothymidine, CLT, European Pharmacopoeia (EP) reference standard) was purchased from LGC Standards (Wesel, Germany). 3′-deoxy-3′-fluorothymidine (FLT reference standard, >95%), was purchased from ABX (Radeberg, Germany). SDS (100 mM) in 30 mM phosphate buffer was prepared by dissolving SDS in 30 mM PB. All samples were prepared with 18 MΩ deionized water using a Milli-Q® Integral Water Purification system (EMD Millipore, Billerica, MA, USA). All chemicals were of analytical grade and were used as received without further purification.

5.2.2 Preparation of radioactive sample, [^{18}F]FLT

The synthesis of [^{18}F]FLT was performed using an automated radiosynthesizer (ELIXYS, Sofie, Culver City, CA, USA) as previously described [234], with slight modification to reduce impurities. The synthesis scheme with all potential impurities is described in Figure 5-1.

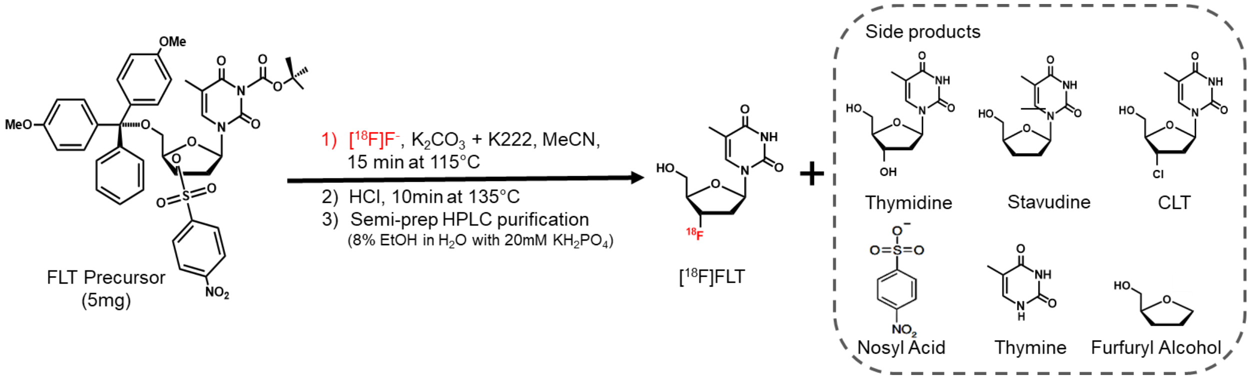

Figure 5-1. Synthesis of [^{18}F]FLT showing both product and side.

5.2.2.1 Reagents for [^{18}F]FLT synthesis

Anhydrous-grade acetonitrile (MeCN), ethanol, 2,3-dimethyl-2-butanol (thexyl alcohol), hydrochloric acid (HCl), sodium hydroxide (NaOH), were purchased from Sigma–Aldrich (Milwaukee, WI, USA). Kryptofix 2.2.2 (K222), 3-N-Boc-5′-O-dimethoxytrityl-3′-O-nosyl-thymidine (FLT precursor) were purchased from ABX (Radeburg, Germany). No-carrier-added [^{18}F]fluoride was produced by the ^{18}O(p,n)^{18}F reaction of [^{18}O]H_2O (84% isotopic purity, Zevacor Pharma, Noblesville, IN, USA) in an RDS-112 cyclotron (Siemens; Knoxville, TN, USA) at 11 MeV using a 1 mL tantalum target with havar foil. Unless otherwise specified, all reagents were analytical grade and used as received.

5.2.2.2 [^{18}F]FLT Synthesis details

The one-pot synthesis of [^{18}F]FLT was adapted from literature [235] and performed on the ELIXYS radiosynthesiszer (Sofie, Inc., Culver City, CA, USA). Briefly,

[^{18}F]fluoride in [^{18}O]H_2O (14.8 GBq [400 mCi]) was trapped on a pre-conditioned QMA cartridge and eluted with 1.38 mL of a 32% v/v H2O:MeCN mixture containing 0.59 mg K_2CO_3 and 15 mg K222 into the reaction vial. This solution was then dried at 110°C under nitrogen (8 psi) and vacuum. The cartridge was eluted twice more with 1 mL MeCN each and then further evaporated to dryness. 5 mg FLT precursor dissolved in 700 mL thexyl alcohol and 300mL H2O was added to the vial and reacted at 115°C for 15 min. After cooling, the solution was evaporated at 105°C until dryness, and then 2 mL 1N HCl was added to the vial and reacted at 135°C for 10 min. After cooling the vessel, the solution was neutralized with 1 mL of 2M NaOH, and then diluted with 2 mL of HPLC mobile phase (8% v/v EtOH in 20 mM phosphate buffer).

The sample was purified via reversed-phase semi-preparative HPLC with a WellChrom K-501 HPLC pump (Knauer; Berlin, Germany), C18 Luna column (250 x 10 mm, 5 µm particle size; Phenomenex, Torrance, CA, USA), WellChrom K250 spectrophotometer UV absorbance detector (254 nm; Knauer) and B-FC-3300 and B-FC-1000 radiation detector and counter (Bioscan Inc., Washington, DC, USA). At a flow rate of 4.0 mL/min, the retention time of FLT was 19-21 min. Since the mobile phase is suitable for injection, no additional formulation was performed. Identity and purity of the sample collected were confirmed via analytical radio-HPLC. The Smartline HPLC system (Knauer, Berlin, Germany) was equipped with a pump (Model 1000), degasser (Model 5050), UV detector (Model 2500) and a radiometric detector (B-FC-4000, Bioscan Inc., Washington DC, USA). Separation was performed using a C18 column (Luna, 250 mm x 4.6 mm, 5 µm particle size; Phenomenex, Torrance, CA, USA) with 10

% (v/v) EtOH in 20 mM phosphate buffer mobile phase at 1.5 mL/min. Retention time of FLT was 5.5 min.

To test the system at a range of radioactivity concentration, some collected [18F]FLT samples were concentrated by evaporation at 95 °C with a nitrogen stream (3-5 psi) to reduce the typical ~7 mL collected volume to <1 mL. After concentration, radioactivity concentration of 0.74 – 3.7 GBq/mL [20 – 100 mCi/mL] could be achieved.

5.2.3 Hybrid MCE device

The hybrid MCE device (**Figure 5-2**) comprised a PDMS sample injection chip, a 20 cm fused-silica capillary, and a PDMS detection chip. The two PDMS chips have been slightly modified from previous designs [94], [236].

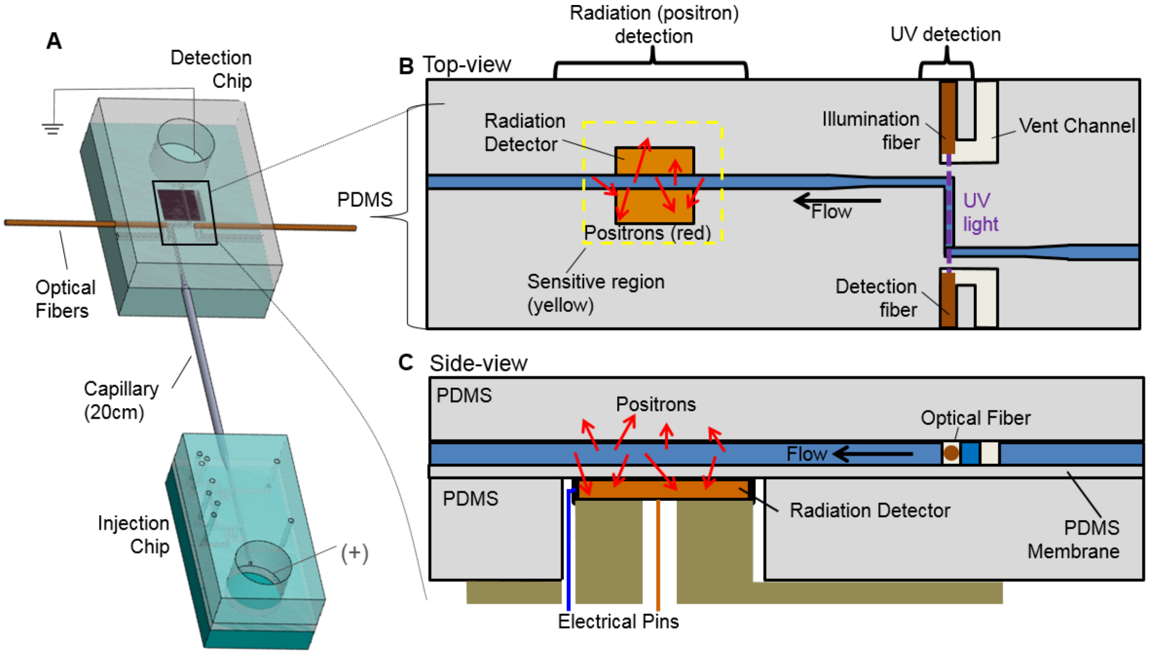

Figure 5-2. Schematic of the microchip design.
A) A 3D rendering of the injection and detection chips, capillary, and optical fibers. B) A top-view of the detection chip geometry, showing both UV and radiation detection systems. The sensitive region is all areas up to 1mm beyond detector edge. C) A side-view of the same geometry, showing the detector and substrate "tower." Side-view, top-view, and capillary are not to scale.

5.2.3.1 Injection chip

The injection chip was fabricated as reported previously [94] with several modifications of the channel design as shown in **Figure 5-3**. First, the number of inlets/outlets connected to the main separation channel to perform loading of buffer, loading of sample, and cleaning was reduced from 5 to 2.

Second, on these connections, we implemented “triple” microvalves instead of single microvalves to improve electrical isolation when activating the separation voltage. With a single microvalve to separate the side channels from the main channel, breakdown occurred frequently when operating at +12 kV (for separation in 60 cm capillary) and occasionally when operating at +4 kV (for separation in 20 cm capillary). We suspect that buffer, sample, or waste reservoirs fluidically connected to the chip act as local grounds, causing a large potential drop across the closed valve. Each valve provides only 30 μm (=2 x 15 μm) of PDMS as electrical insulation, where 15 μm is the thickness of the microvalve membrane. With typical breakdown strength in the range 19 - 133 V/ μm [237], the valve can withstand 0.6 – 4.0 kV, which is insufficient to prevent dielectric breakdown. In contrast, the triple valves can withstand 1.8 – 12 kV.

In all respects besides the simplification of the design, sample injection and valve actuation were performed in the same manner as previous work.[33]

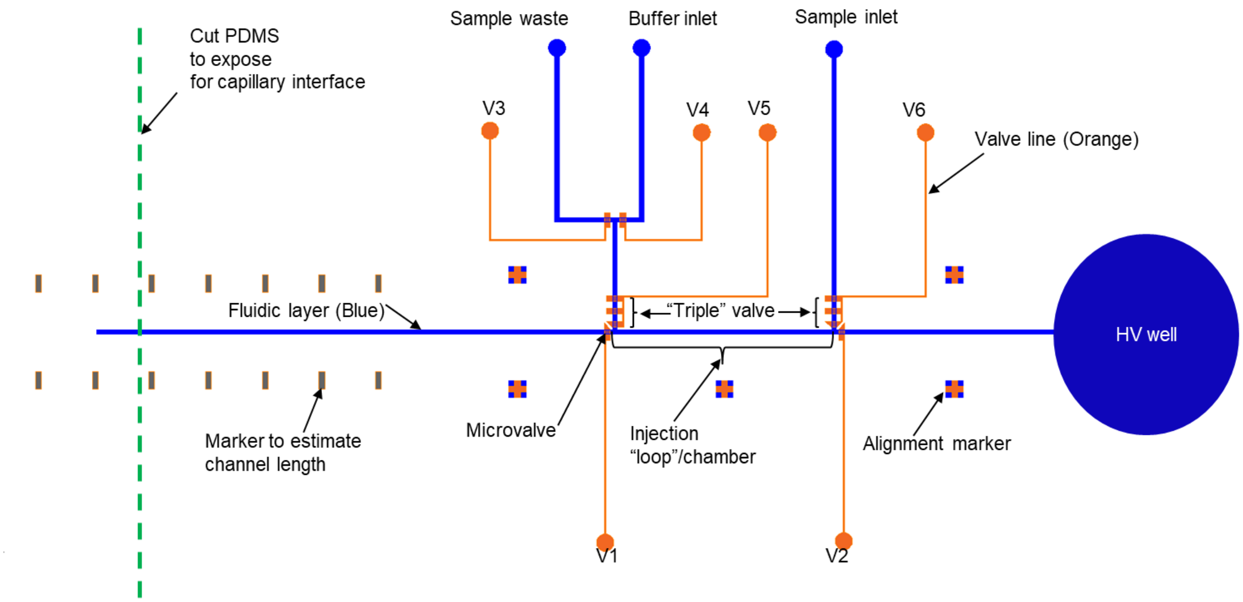

Figure 5-3. **Volumetric injection chip channel design.**
Fluidic layer is shown in blue. Valve control layer is shown in orange for control of flow using the microvalves. Tri-leaflet ("triple") valves are added near the side channel to avoid undesired current leakage from the main separation channel towards the side channels. Chip is cut vertically to expose the flow channel for interface with glass capillary.

5.2.3.2 Detection chip

The previous design of the PDMS detection chip [33] was modified to improve the performance in several ways.

The optical path length of the Z-shaped UV absorbance detection cell [33] was extended from 0.5 to 2.0 mm to enhance absorption sensitivity. The height of channels was 125 µm to enable inclusion of alignment channels to ensure optical fibers (125 µm outer diameter; ThorLabs, Newton, NJ, USA) were well aligned with the optical path of the cell. The optical fibers were connected to a light source and spectrophotometer as previously described [33]. In the initial version of the detection chip, the width of all channels, include the optical path, was 125 µm. However, to improve separation resolution, we explored a design with decreased volume of the UV absorbance cell, achieved by shrinking the channel width within the optical path from 125 to 45 µm while maintaining the same channel height (**Figure 5-4**). This change reduces the mismatch in cross-sectional area between the capillary and the rest of the chip that can lead to dispersion and increased peak widths (due to the lower flow velocity in the chip compared to the capillary) as described in **Figure 5-5**.

The UV signal was collected as previously described [33].

In addition, a radiation detector was integrated into the detection chip. Downstream of the UV absorbance cell, the detection channel crosses over a region with thin substrate (100 µm) where the 2 mm x 2 mm radiation detector is mounted, before terminating in the waste well. Fabrication of the detection chip was described previously [33], except that the bottom PDMS was created with a 3 mm x 3 mm square cavity that was aligned with the radiation detection region such that the sample was separated from the detector by only a 100 µm PDMS membrane. To create this substrate, a mold was machined from acrylic having a 25 mm square cavity with 1.01 cm depth and a 1.0 cm tall, 3 mm x 3 mm square pillar in the middle. After filling with degassed PDMS (10:1 mass ratio A:B, RTV615, Momentive, New Smyrna Beach, FL, USA), a final flat piece of acrylic was pressed on top of the mold and the PDMS cured at 80°C for at least 2 h. The layers were bonded by exposing each piece to air plasma for 2 min (Dyne-a-Mite LM4816; Enercon Industries Corp., Menomonee Falls, WV, USA), and then carefully aligning and pressing together and baking at 80°C for 10 min. The 1 cm thickness provides mechanical stability while the cavity allows the radiation detector to be positioned only 100 µm below the channel.

Finally, to improve separation resolution, the capillary-to-chip junction dead volume was reduced by implementing a collinear junction [94], [184], [185] as used in the injection chip, by tapering the capillary and inserting into end the detection channel via the side of the chip. To stabilize the connection, freshly-prepared and degassed liquid PDMS (10: 1 mass ratio A:B, RTV615, Momentive, New Smyrna Beach, FL, USA) was added and then cured at 80°C for at least 1 h. Prior to this step, the chip was filled with water to avoid clogging of channels by the liquid PDMS.

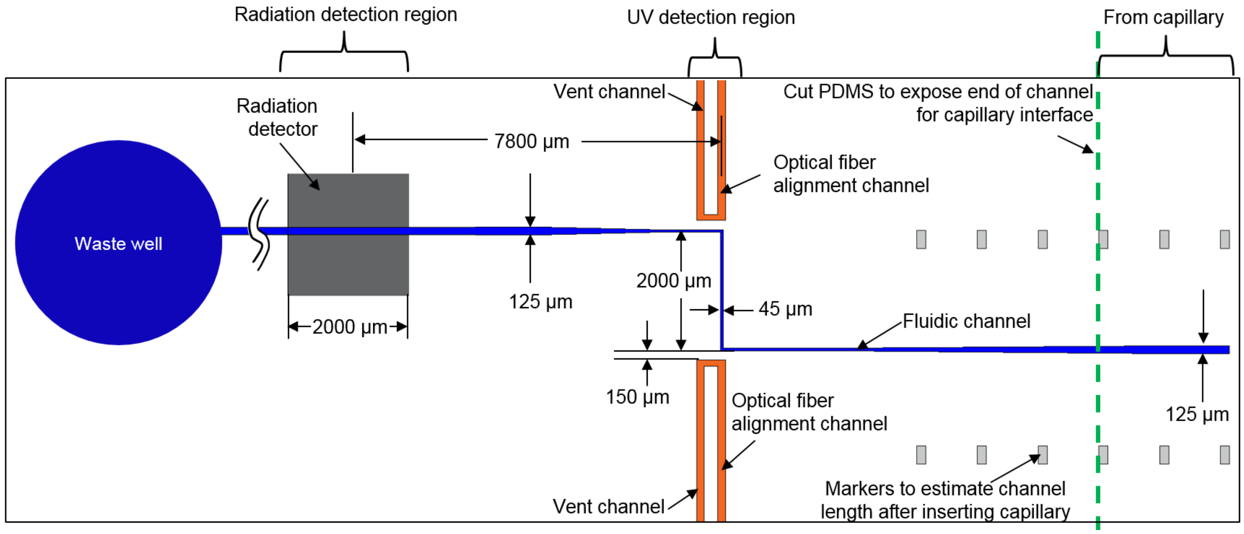

Figure 5-4. Detection chip channel design
Gradual tapering of fluidic channel from 125um to 45um, and narrower channel (45um wide) near the OPL to improve separation efficiency. The channel height is 125um everywhere. Chip is cut vertically to expose the flow channel for interface with glass capillary.

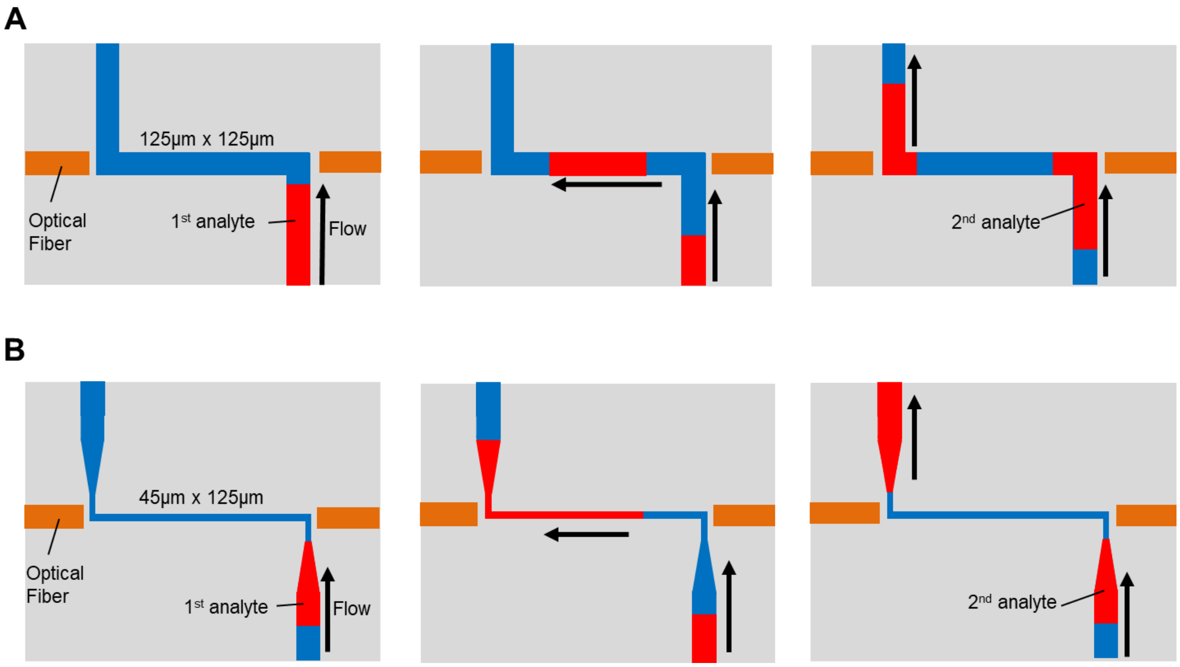

Figure 5-5. The influence of UB absorbance detector volume on separation resolution

Time sequence of multiple-analyte detection in the chip with (A) 125 µm wide detection region and (B) 45 µm wide detection region. The lower volume cell reduces the likelihood that adjacent peaks will overlap.

5.2.4 Radiation detector

Radiation detection was performed using an avalanche photodiode (APD; Radiation Monitoring Devices Inc., Watertown, MA, USA) with a 2 mm x 2 mm active area biased at 1750 V using a high-voltage power supply (TC952; Tennelec, Oak Ridge, TN, USA).

A thin opaque coating was deposited on the detector to prevent optical photons from triggering the detector while minimizing attenuation of positrons. The device was first coated with 2 µm of parylene C (Specialty Coating Systems Inc., Indianapolis, IN, USA) using a parylene deposition machine (PDS 2010, Specialty Coating Systems Inc.), followed by 350 nm of gold deposited by sputtering (Desk V, Denton Vacuum, Moorestown, NJ, USA), and finally followed by an additional 2 µm of parylene C. The gold layer also served as a Faraday cage, providing electrical shielding of the detector. A thin nichrome wire was attached to the detector substrate via silver epoxy (MG Chemicals, Burlington, Ontario, Canada) before the gold coating, and later soldered to circuit ground.

To discriminate electronic and heat-related noise and fluctuations from positron events, it is necessary to amplify and “shape” the signal, as the noise pulses have much lower amplitude than the desired signal. The current change in the APD when energy was deposited was too low to be directly measured, and is therefore passed through a trans-impedance amplifier, capacitively coupled to the detector to protect from the high bias voltage, as described by Dooraghi *et al*. [238]. This signal is then further processed by a pair of two passive filters, a CR filter of time constant 100 ns and a RC filter of time constant 200 ns, to shape the pulses to a sharp peak with a 200 ns width. Each filter is followed by a non-inverting amplifier to both increase the signal and stop each filter from interfering with the others. Once filtered and amplified, the signals were compared against an empirically-chosen threshold, and those above the threshold were counted as digital pulses by a data acquisition (DAQ) module (USB-6501, National Instruments, Austin TX, USA). A program written in LabVIEW (National Instruments, Austin, TX, USA) records the number of counts every 0.5 s, and the value is multiplied by 2.0 to determine an instantaneous value in units of cps. A detailed schematic of the process can be seen in **Figure 5-6**.

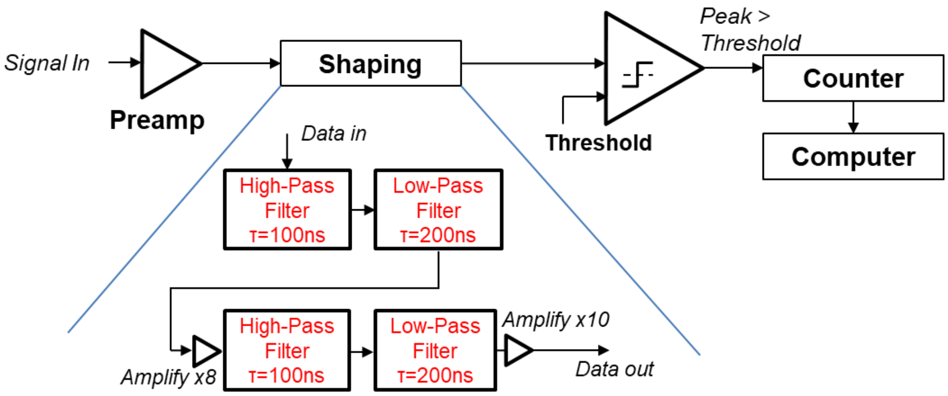

Figure 5-6. ***Schematic diagram of the signal shaping process.***
The preamplifier, a transimpedance amplifier, changed the small current into a voltage peak. The high-pass filters create a sharp leading edge on the peaks, for temporal resolution, and the low-pass filters smooth out any noise in the peaks. The asymmetry in the filter times was chosen as reducing noise/lengthening peaks was more beneficial to us than increasing peak shape-related SNR. The comparator is set to reject all peaks that fall below a certain value, which is all electronic noise-caused peaks.

5.2.5 **Characterization of radiation detector**

The dark noise of the radiation detector was measured by collecting data for 6 h, and then calculating the average and standard deviation of the data. During this time, the chip was empty, and no radioactive sources were located near the detector (i.e. exposed only to natural radiation background). The limit of detection (LOD) and limit of quantitation (LOQ) were computed as 3x and 10x the standard deviation, respectively. The average value of the dark noise, which was recalculated for each experiment, was subtracted from all data, and the standard deviation of the noise was used to determine the limits of detection for the day of experiment.

To investigate the linear range, a detection chip was filled with known concentrations of aqueous [18F]fluoride (11-1600 MBq/mL [0.3-42 mCi/mL]) and the resulting APD signal measured over 5 min for each sample. All measurements were performed with a single chip on a single day. Between each run, the chip was cleaned with DI water (1.0 mL) and dried with compressed nitrogen. Additionally, the dark noise was re-measured before each run to enable accurate subtraction of any background radioactivity that might be present due to contamination of the chip from the previous run. The 600 datapoints collected over each 5 min interval were averaged and plotted as a function of the radioactivity concentration. To estimate the LOD and LOQ for this setup (detection chip only), the dark noise from the lowest-concentration sample was used, and LOD and LOQ were computed as mentioned above.

5.2.5.1 Simulations of radiation detector

To estimate the size of the sensitive region of the detector, Monte Carlo simulations (PET specific extension of the Geant4 Monte Carlo environment) were performed to ascertain the total number of particles interacting with the detector, or events, by filling a channel of varying widths and heights with homogenous radioactivity concentration for 60s (see **Figure 5-7)**.

We modeled a microfluidic channel over a radiation detector to determine the number of particles hitting detector. The channel was filled with a uniform distribution of fluorine-18 solution (37 MBq/mL [1 mCi/mL]) embedded within a PDMS slab. The channel had a length of 2 cm (well beyond the expected sensitive area of the detector). The detector was modeled as a 200 µm thick piece of silicon. And different channel widths (100 – 2000 µm) and heights (100 – 2000 µm) were explored.

Both the width response (shown as total counts over 60s in **Figure 5-7**) and the height response (not shown) increase with size, up to 1mm away from the edge of the detector, where it drops off to almost flat. From this data, we observed that a channel width of 4 mm results in >95% of the maximum count rate value (for a channel much wider than the radiation detector, 2 mm), suggesting that the sensitive region can be considered to be a 4 mm segment of the channel for all experiments.

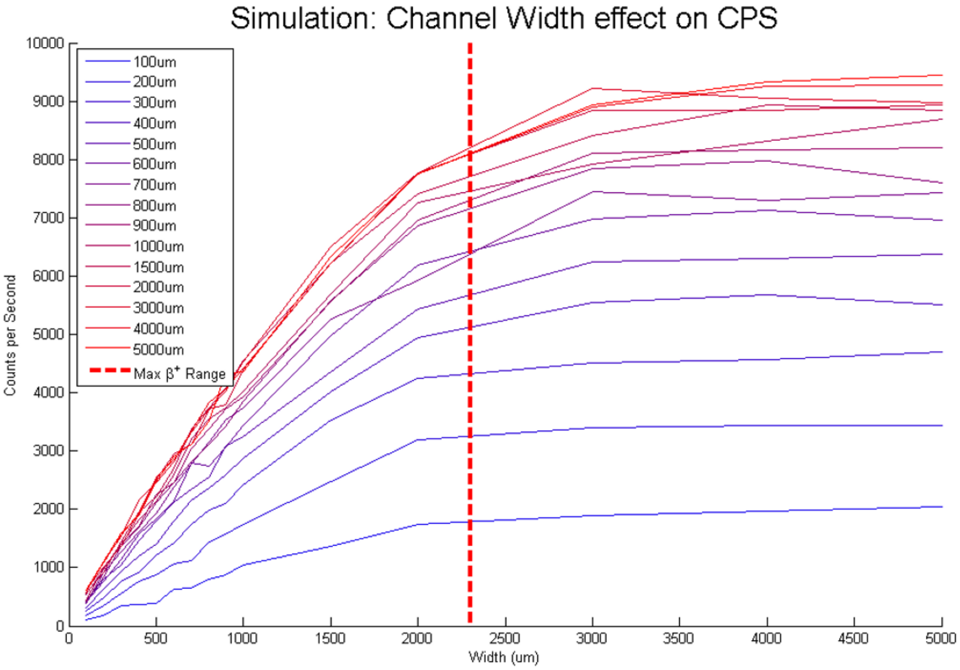

Figure 5-7. A graphical representation of the increasing signal with respect to channel width(centered on detector) for varying channel heights.
Each point was simulated using 37MBq/mL (1mCi/mL) radioactivity concentration, over a detection period of 1 minute. The data are grouped into lines based on the channel height (100 µm to 5mm). A distinct plateau can be seen in each line after the 4mm mark, with slowing before that, suggesting that no benefit is gained from activity beyond 1mm from the detector edge.

5.2.6 Performing microchip electrophoresis (MCE)

The detection and separation of samples was performed on the MCE chip via micellar electrokinetic chromatography (MEKC) as described previously [33], [94]. The buffer consists of 30 mM sodium phosphate buffer and 100 mM SDS in DI water. The sample was loaded into the injection chamber (~4 nL) inside the PDMS volumetric injection chip, and then injected into the separation channel (capillary) by applying ~4 kV between the buffer well in the injection chip and the waste well of the detection chip (field strength 200V/cm). For all radioactivity measurements, the bias voltage of the APD was turned on for 1 hour before injection to allow it to stabilize.

To demonstrate the utility for assessment of chemical purity, samples of purified PET tracer ([^{18}F]FLT) were injected. Demonstration of radiochemical identity testing was performed by co-injection of purified [^{18}F]FLT with FLT reference standard. To compare the MCE results to HPLC, samples were analyzed using the analytical HPLC conditions mentioned in '**[^{18}F]FLT Synthesis details**'.

In order to better align the UV and radiation peaks, the time signal of the radiation detection data was shifted by a calculated factor based on the geometry of the device and the migration time of the UV peak.

To estimate the sensitivity to radioactivity of the overall system, samples with different concentrations of [^{18}F]FLT (59 - 500 MBq/mL [=1.6 -1 3 mCi/mL] at time of injection) were injected. Radiation background was also measured for 5 min at the beginning of the experiment, and the average and standard deviation were calculated for use in limits of detection estimation. Data was collected for at least 30 s beyond the visual end of the radioactive peak, and resulting peaks analyzed to determine the peak area. The results were plotted against initial radioactivity concentration. All concentrations were tested using the same chip on a single day.

To estimate the LOD for this experimental setup, we ran a CE run with no sample injected as a blank. As no radioactive materials were present, no peak was available to measure. To determine an equivalent peak area for this blank, the LOD and LOQ values from the noise based on the peak height (standard deviation x3 and x10 respectively) were multiplied by the average FWHM of our samples after analysis.

5.2.7 **Data Analysis**

5.2.7.1 UV absorbance signal

Each UV electropherogram was analyzed as described previously [33], [94] to determine peak migration times (t_m, taken at peak center), peak widths (W_{FWHM}; full width at half maximum), number of theoretical plate (N), theoretical plate height (H), peak area (Gaussian fit), and separation resolution. Briefly, for each peak in the resulting electropherogram, the number of theoretical plates, *N*, was calculated as $N = 5.54 \times (t_m / W_{FWHM})^2$. The plate height, H, was calculated as H = L / N, where L is the effective separation length (21 cm). For mixture samples, the peak resolution, R, between pairs of peaks was computed as $R = 1.18 \times (t_{m2} - t_{m1}) / (W_{FWHM,1} – W_{FWHM,2})$, where t_{m1} and t_{m2} are the migration times of the two peaks and $W_{FWHM,1}$ and $W_{FWHM,2}$ are the peak widths (FWHM).

Peaks were identified based on migration times determined by injecting reference standards for each compound individually.

5.2.7.2 Radiation detector signal

After subtracting the average dark noise (measured on the day of the experiment), electropherograms were analyzed in a similar manner.

Because the migration time can vary from run to run and because the migration speed affects the apparent peak area, a time-correction is needed for any quantitative peak analysis. The differences might arise from inconsistency or deterioration in surface chemistry from run to run that could affect the magnitude of the electroosmotic flow, or from small temperature differences due to heating. This might be affected more severely in the PDMS channel as previously known [239] compared to glass capillary

[240]. Co-injection with non-radioactive reference standard was performed to confirm peak identity. In addition, the co-injection could be used to determine, and correct, the delay between UV absorbance and radiation detector signals provided the radiochemical identity was first verified with an independent method (e.g. radio-HPLC).

5.3 Results

5.3.1 Separation efficiency

The modified MCE setup included several improvements (lower dead volume chip-to-capillary junctions, and increased optical path length) to address limitations in separation efficiency and UV detection sensitivity observed in our previous work [33]. To assess the separation performance of the modified setup, non-radioactive samples were injected into the MCE device. For a 20 cm capillary length, the separation of a mixture of 4 compounds using the 125 µm wide optical flow cell is shown in **Figure 5-8A**. It is apparent that numerous peaks are overlapping and baseline separation has not been achieved. We performed the separation of a similar mixture with 5 compounds in a device with a modified UV detection cell (45 µm width instead of 125 µm to reduce the volume of the optical flow cell while maintaining the same optical path length) and achieved baseline separation of all species (**Figure 5-8B**). A more detailed comparison is included in **Table 5-1**. Notably, with the improved flow cell design, the resolution between the FLT and the closest impurity (stavudine) improved from 0.68 to 1.85 ± 0.17.

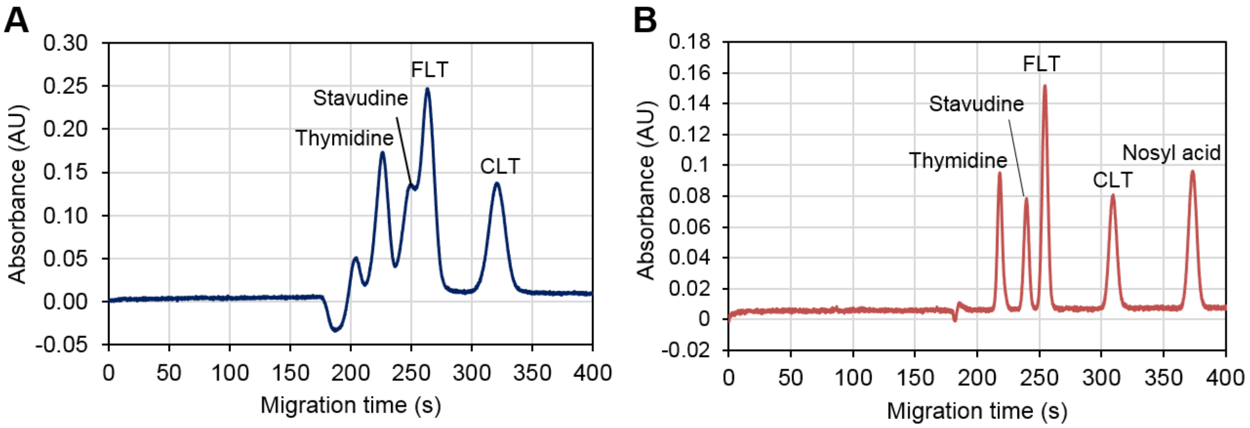

Figure 5-8. Separation of multiple compounds.
(A) Separation of 4 compound-mixture in 125 µm wide optical cell: thymidine 100 µM; stavudine 100 µM; FLT 100 µM; CLT 95 µM in DI water (B) Successful separation of FLT from 5 known impurities in 45 µm wide optical cell. Non-radioactive sample was used for this measurement: thymidine 250 µM; stavudine 250 µM; FLT 250 µM; CLT 237.5 µM; nosyl acid 250 µM in DI water. Non-radioactive samples were used.

Table 5-1. Summary of peaks observed after MCE separation of mixtures of non-radioactive compounds.
Peak area, migration time (tm), peak full width at half maximum (w1/2), number of theoretical plates (N), plate height (H), peak resolution (R) are shown for each. Peak resolutions between FLT and its nearest peak (stavudine) were calculated.

	125 µm optical detection cell (n=1)				**45 µm optical detection cell (n=3)**				
	Thymidine	**Stavudine**	**FLT**	**CLT**	**Thymidine**	**Stavudine**	**FLT**	**CLT**	**Nosyl acid**
Peak rea (AU*s)	2.17	1.83	3.10	2.26	0.42 ± 0.01	0.36 ± 0.01	0.80 ± 0.03	0.56 ± 0.02	0.74 ± 0.02
Migration time (s)	225.9	248.7	263.8	321.0	221.3 ± 12.9	243 ± 14.8	258.7 ± 16.3	315.2 ± 21.9	382.1 ± 28.5
FWHM (s)	12.6	13.7	12.5	16.5	4.5 ± 0	4.7 ± 0.1	5.1 ± 0.1	7.2 ± 0.1	7.7 ± 0.2
Number of theoretical plates, N	1783	1815	2474	2106	13482 ± 1277	14953 ± 1524	14116 ± 1471	10539 ± 1137	13488 ± 1165
Theoretical plate height (µm)	117.8	115.7	84.9	99.7	15.67 ± 1.45	14.14 ± 1.43	14.98 ± 1.51	20.07 ± 2.07	15.65 ± 1.33
Peak resolution (Stavudine-FLT)	0.68				1.85 ± 0.17				

5.3.2 **Characterization of radiation detector**

The dark noise (measured over 6 h), was found to be 0.01 ± 0.16 counts/s (cps). This corresponds to a LOD count rate of 0.48 cps, and a LOQ count rate of 1.6 cps. Repeat measurements showed that the noise level and thus ideal detection limits were consistent from day to day.

To investigate the linear range, a detection chip was filled with known concentrations of aqueous [^{18}F]fluoride (11-1600 MBq/mL [0.3-42 mCi/mL]) and the resulting APD signal measured over 5 min for each sample. **Figure 5-9** shows the signal as a function of radioactivity concentration. The resulting data is strongly linear (R2=0.994) and To estimate the limit of detection for this setup, the dark noise from the lowest-concentration sample led to LOD and LOQ count rate values of 3.7 and 12 cps, which corresponded to radioactivity concentrations of 592 kBq/mL and 2.0 MBq/mL (16 µCi/mL and 54 µCi/ml) respectively, which is very low by QC standards. However, since this data is from a fully filled 62.5 nL channel as opposed to a typical 4 nL injection, all it can tell us is that the data is linear over a wider range than the 37-370 MBq/mL (1-10 mCi/mL) range expected.

Next, we used the whole MCE setup and performed injections of different radioactivity concentrations of [^{18}F]FLT. Samples of 7 different radioactivity concentrations were injected. The radiation detector signal was plotted versus total injected activity in **Figure 5-10**. Additionally, detailed peak analysis including the number or theoretical plates and the theoretical plate height can be found in **Table 5-2**. Analysis of the peak shapes for the radioactivity measurements showed that the theoretical number of plates was around 5000, which was approximately half of the number of plates for the UV detection. This suggests that the radiation peaks are wider than the UV, and would have worse separation efficiency.

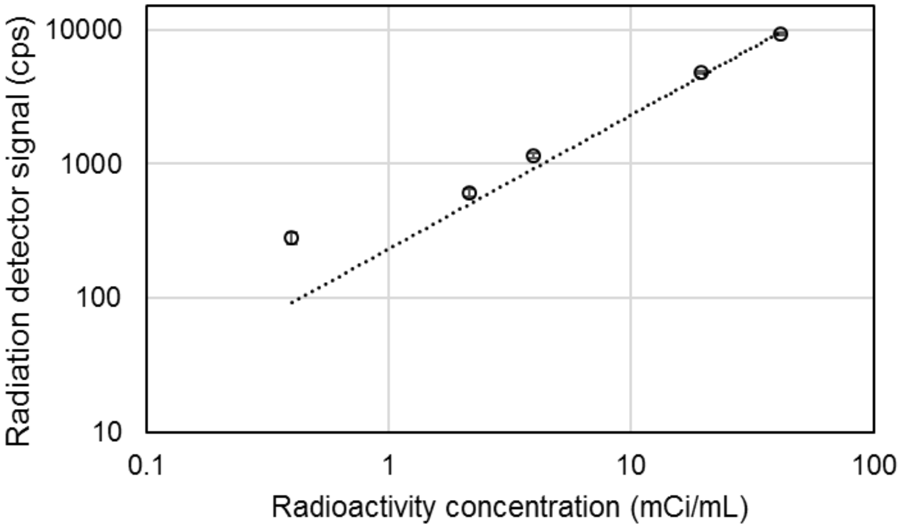

Figure 5-9. Radiation detector signal when detection channel is uniformly filled with aqueous [^{18}F]fluoride solution of different concentrations.
The dark noise has been subtracted from all values. Error bars represent the standard deviation of the 600 detector readings over the entire 5 min acquisition. The dashed line represents a linear fit with intercept of zero ($R^2 = 0.997$).

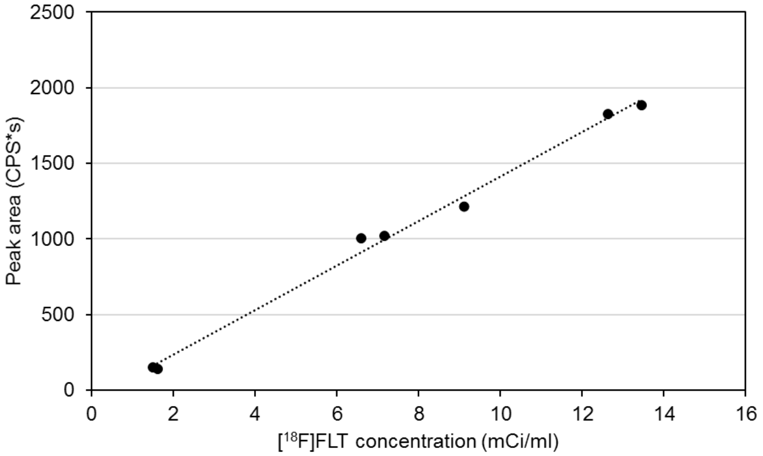

Figure 5-10. Calibration of radiation detector signal: peak area (CPS*s) vs [^{18}F]FLT concentration.
Peak area was computed based on a Gaussian fit to peak. Dashed line shows a linear least square fit ($y= 147x – 59$; $R^2 = 0.994$).

Table 5-2. Analysis of electropherogram of [^{18}F]FLT peak.
Summary of figures of merit for analysis of various concentration of [^{18}F]FLT. Migration time (tm), peak full width at half maximum (FWHM), number of theoretical plates (N), plate height (H), are shown for each concentration.

Activity Conc. (mCi/ml)	Peak Area (CPS*s)	Migration time (s)	FWHM (s)	Number of theoretical plates, N	Theoretical plate height (µm)
13.5	1884.8	208.5	7.71	4057	51.8
12.6	1828.1	207.1	7.77	3935	53.4
9.1	1214.5	198.1	7.25	4137	50.8
7.2	1019.6	210.0	7.60	4228	49.7
6.6	1005.7	211.2	7.99	3869	54.3
1.6	139.5	204.3	7.01	4703	44.7
1.5	152.4	199.5	7.22	4232	49.6

5.3.3 Demonstration of radio-MCE

A sample of purified and formulated [^{18}F]FLT was analyzed. With a concentration of 703 MBq/mL (19 mCi/mL), the total injected radioactivity in the 4 nL sample plug is estimated to be 2.8 kBq (76 nCi). A single peak was observed in the radioactivity electropherogram (**Figure 5-11A**), and a corresponding small peak was observed in the UV electropherogram. There were no UV impurity peaks observed at the expected relative migration times. To verify radiochemical identity, the same [^{18}F]FLT sample was spiked with the FLT reference standard (~500 uM final concentration) leading to a radioactivity concentration of 630 MBq/ml (17 mCi/mL). Once more, a single peak was observed in the radioactivity electropherogram **Figure 5-11B**, and a single large peak was observed in the UV electropherogram. To corroborate this result, 25 µL of the same sample was injected into analytical HPLC, and a similar single UV and radiation peak was observed at a retention time of 5.5 minutes, with the co-injection strengthening the same UV peak. From this, we know that the single radiation peak is indeed the

[18F]FLT. After determining the peak identity, the radiation peak data was shifted in time by the difference between the UV and radiation peak centers for visual clarity.

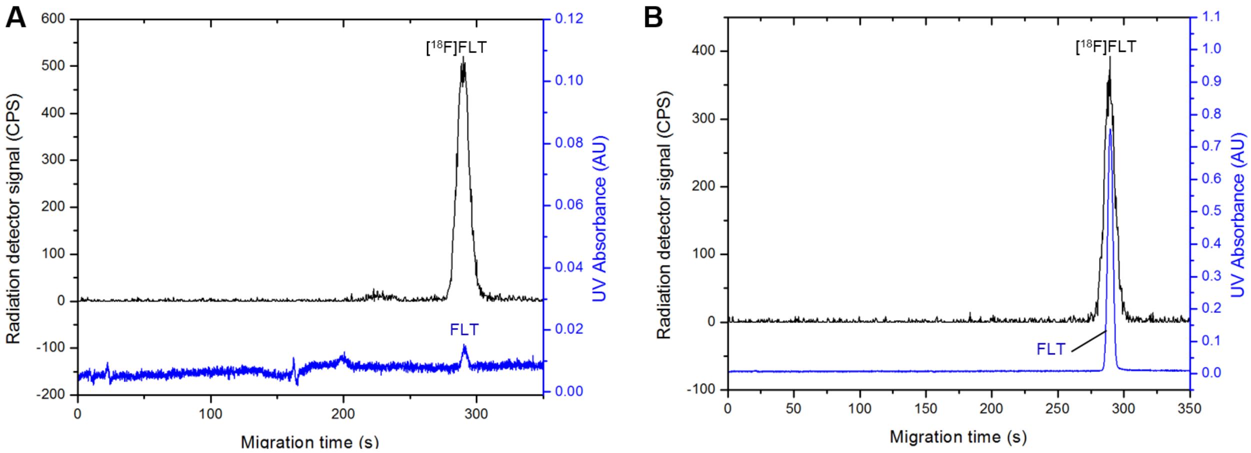

Figure 5-11. Example dual-modality electropherogram of radioactive sample
(A) purified/formulated [18F]FLT, and (B) the same sample co-injected with 500 µM FLT (reference standard). UV absorbance signal is shown in blue, and radiation detector signal is shown in black. The migration times of the radiation peaks were corrected according to the estimated delay between the two detectors.

Additionally, a “mock crude” sample was prepared by adding impurities into the [18F]FLT sample. The concentrations of the impurities were 250 µM thymidine, 250 µM stavudine, 450 µM FLT, 238 µM CLT, and 300 µM nosyl acid. As seen in **Figure 5-13**, all 5 peaks were discernable though baseline resolution was not quite achieved for thymidine, stavudine, and FLT.

A sample of crude [18F]FLT (before purification) was also analyzed (**Figure 5-13**). From the UV electropherogram, the major side products stavudine, thymidine, and CLT could be observed, as well as a significant peak not described in previous literature [179]. This impurity has been observed by other investigators but not identified [235]. Here we observe that the impurity appears to coincide with the migration time of nosyl acid, the by-product resulting from removal of the leaving group when the precursor is fluorinated. During purification, we collected the fraction corresponding to this peak and also confirmed its identity via analytical HPLC. The retention of the unknown impurity matched that of nosyl chloride (dissolved in DI water), and the peak size was confirmed to increase when the unknown impurity was coinjected with nosyl chloride.

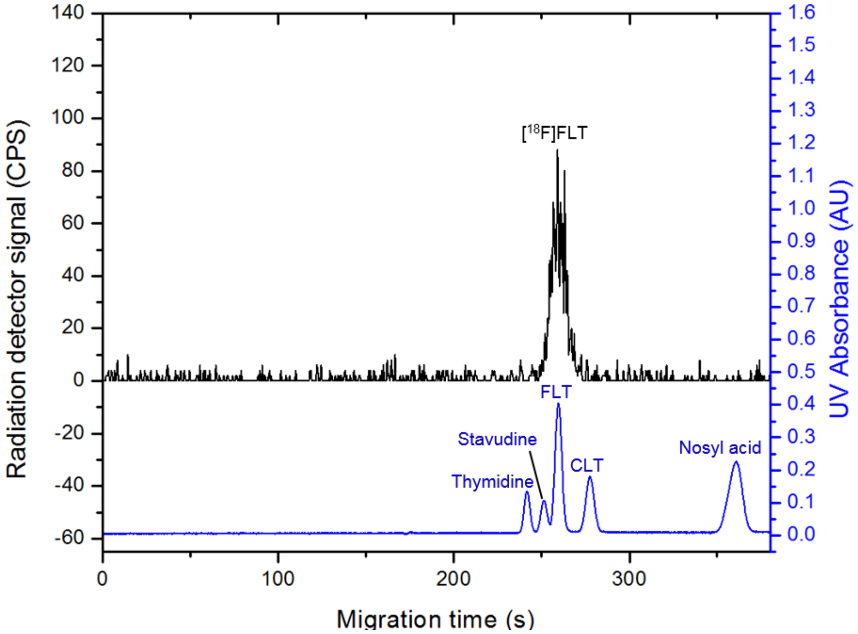

Figure 5-12. Separation of [^{18}F]FLT from 4 added impurities.
Radiation peak (in black) and UV absorbance peaks of added 4 known impurities (in blue). The concentrations of added impurities are estimated to be thymidine 250 µM; stavudine 250 µM; FLT 450 µM; CLT 237.5 µM; nosyl acid 300 µM. Note that migration time of radiation peak was shifted according to the estimated delay between two detectors.

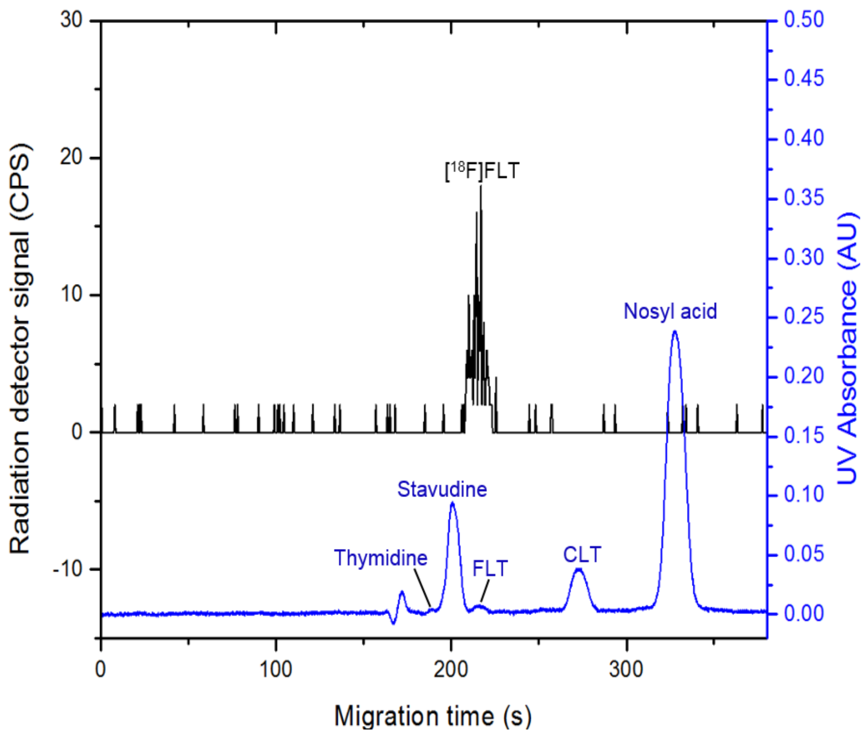

Figure 5-13. Superimposed electropherograms of crude [^{18}F]FLT product (non-purified sample).
Detection with a 125 µm wide optical flow cell was used. Note that migration time of radiation peak was corrected according to the estimated delay between two detectors.

5.3.4 UV absorbance peak calibration: Conc vs peak area

The calibration curve of UV absorbance peak area versus sample concentration was generated (**Figure 5-14**). The tested concentration ranges from 10 – 400 µM, and the linear relationship was observed with the R^2 value of 0.9987. And it becomes non-linear for the concentration higher than 700 µM and gradually plateaued. The typical concentration of PET tracer (including [^{18}F]FLT) lies within this range.

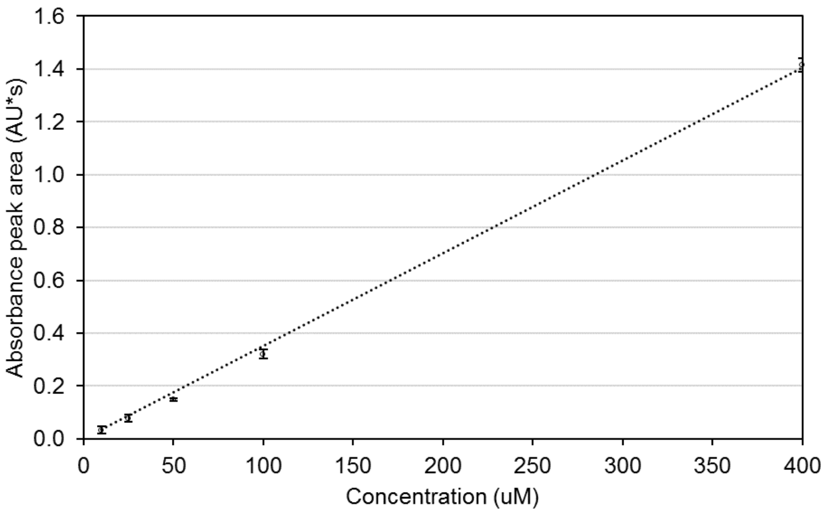

Figure 5-14. Calibration of UV absorbance peak area (AU*s) vs FLT concentration. Each concentration of FLT reference standard was analyzed in the MCE device, and the peak area was computed. Error bar shows the standard deviation of 3 repeats. Linear fit: y = 0.0035x, R^2= 0.9997.

5.4 Discussion

The use of the triple valve structure, shown in **Figure 5-3** was significant in a number of ways. First, from our previous work [33], we found that on some chips, particularly those utilizing longer (60cm) capillaries and therefore higher voltages, the sample vial and buffer vial, along with their side-channels would often form bubbles if not physically disconnected before applying the high voltage. We suspected this was from the stray current, and therefore requires a larger amount of PDMS blocking the channel to electrically isolate the wells from the CE supply. With the new triple valve structure, we have yet to see a single failure of this type, or any suspected bubbling in side-channels. The second benefit is the increase in the fluidic isolation of the side-channels from the main channel. This reduces the chances for a poor localized sealing of the channel that can lead to sample leakage into the channel during CE.

The APD had very low noise, with the all remaining noise pulses suspected as cosmic rays striking the device [133], or strong current changes from the APD itself which we have not investigated at this time. Small improvements could be made to the device by reducing distances between various components and reducing any detector movement with respect to the preamp circuit, though it is likely that the remaining noise is inherent to the fabrication method of our devices and will not be easily removed.

For the linearity testing, it was shown that the response of the device is linear with regards to radioactivity within the sensitive area well beyond the radioactivity range we would encounter from a QC sample with current injection volume (4 nL), 1.5 GBq/mL (40 mCi/mL) compared to the typical maximum 370 MBq/mL (10 mCi/mL). The calibration curve generated from actual injection resulted in a good curve, though this curve was not tested against an unknown concentration in this work. This would be an important next step, as it would be necessary to measure the precise amount of the analyte in unknown sample.

We have noticed a chip-to-chip variation of migration time for FLT. We believe the major culprit for this is variation in the capillary length caused during fabrication; a longer capillary leads to a longer migration time for the same field. Also, the alignment of chip-to-capillary junctions, temperature inside the chips, and the stability of the channel surface chemistry as well as the stability of power supply (separation voltage) could contribute to this variation. To resolve this, each chip could be referenced to previous data where the other chip was used, likely by a single injection of a known concentration standard before the main run. Also, improved fabrication consistency reduces the variation.

The sensitivity of the radiation detector is expected to vary for other isotopes, depending on the positron branching ratio and the positron range (related to the positron energy). Furthermore, the APD is expected to be sensitive to electrons (beta particles) and thus this approach could also be used for analysis of molecules containing beta-emitting therapeutic radioisotopes (e.g. Lu-177). For isotopes that emit predominantly gamma rays, another method of radiation detection may be needed as the APD has low sensitivity to gamma rays due to its thin dimensions. It may be possible to detect alpha particles, though the thickness of PDMS between the liquid in the channel and the detector would likely need to be reduced as alpha particle range is typically <100-200 μm.

Focusing on ^{18}F-labeled tracers, the typical concentration of the formulated tracer is in the range 37-370 MBq/mL (1-10 mCi/mL). Though we were able to obtain clear peaks for samples with concentration in this range, it would be challenging to detect low-abundance impurities. Typically, the passing criteria for the radiochemical purity test of a radiopharmaceutical is that the compound is >95% radiochemically pure. Thus, at minimum, the sensitivity should be able to quantify the amount of an impurity down to 5% abundance, or 1.85-18.5 MBq/mL (0.05-0.5 mCi/mL) radioactivity concentration in the original sample.

We can consider several potential approaches to improve sensitivity. One approach would be to add a second radiation detector on the other side of the channel, increasing the effective signal by nearly 100%; however, implementing such a configuration would be extremely challenging from a microfabrication point of view as well as developing appropriately shielded electronics. Reduction of the thickness of material between the liquid sample and detector would also increase the sensitivity. Dooraghi et al. [133] measured the effect of different thicknesses of low-density polyethylene (LDPE) material thicknesses on the signal detected from a Tl-204 sources (beta-emitter with beta energies only slightly higher than the positron decays from F-18). A 200 μm LDPE layer resulted in 60% signal attenuation and 100 μm resulted in 38% reduction. 100 μm of PDMS would be expected to have a similar attenuation as LDPE. Reduction in layer thickness is possible, but if the layer becomes too thin, it may suffer dielectric breakdown between the local separation voltage within the channel and the ground of the APD. Given that PDMS manufacturers quote the dielectric strength of PDMS as 10-15 V/μm, and the potential in the channel at the radiation detector would be around 200V (1cm away from the waste well), at least 40μm of PDMS would be required to protect the detector from breakdown.

Another approach to increase the signal would be to increase the sample volume, but this would likely require an increase in separation length (and thus separation time) to achieve the same resolution. Alternatively, signal can be increased by slowing down the sample such that it spends more time within the detection region. Though reducing the separation voltage is not desirable as it would slow down the analysis and reduce resolution, increased interaction between the sample and detector could be accomplished using a serpentine channel pattern above the radiation detector.

We have shown that the narrower optical flow cell (inside detection chip) substantially improves the separation efficiency even with the presence of two chip-to-capillary junctions. Further decrease in cross-sectional area of entire detection chip channel would further enhance the separation power of our system, though it would lead to reduced optical absorption signal unless smaller size optical fibers are utilized.

Additionally, longer separation channel (e.g., longer capillary) would help improving the separation efficiency as we have observed a better separation when the 60cm capillary was used [33]. However, when the longer capillary is utilized, in addition to the longer analysis time, a higher voltage is needed to maintain the same separation field strength. These higher voltages are more dangerous and difficult to work with, and the increase in voltage could result in the higher chance of breakdown of microvalves. Longer capillaries also lead to higher temperatures at steady state in both the capillary as well as the PDMS chips.

Currently our MCE system can be used for radiochemical identity analysis as well as chemical purity and identity tests, and could be used as a PET tracer QC device once able to perform radiochemical purity analysis. On top of that, our microfluidic radiation detection system could potentially be applied to applications other than MCE that involve radiolabeled compounds or radiolabeled cells, where high-sensitivity and relatively fine spatial resolution would be needed, particularly those involving real-time detection[130], [241]. With reductions in membrane thickness, the system could easily be used for QC of beta-emitting compounds (e.g. ^{177}Lu) and even alpha emitting compounds. Changes in the detection circuitry could even allow for online energy spectrum analysis, which would perhaps be beneficial for alpha isotopes that can have many side-particles.

5.5 Conclusions

A novel MCE device with a miniaturized positron detector (“radio-MCE”) was developed to analyze radioactive compounds following electrophoretic separation. The radioactive PET tracer [^{18}F]FLT of clinical concentration was successfully detected by the positron detector along with the UV absorbance detector. We demonstrated a successful separation of [^{18}F]FLT from all added impurities.

The detection system is capable of detecting radioactivity concentrations at the lowest end of PET tracer QC testing levels, though our quantitation limits are not low enough yet. We have shown that this system is capable of quantifying radioactivity concentrations down to 7 mCi/mL, though quantitating impurity peaks is currently limited to 20% or higher. These detection limits could be further lowered by improving electronics or reducing the distance between sample and detector, though the former has diminishing returns and the latter could become hazardous to the detector from the CE current.

The fast acquisition time of our system allows for a real-time detection method, which can identify and quantify radioactive compounds without compromising separation efficiency. In fact, the radioactivity peak was the stronger indicator of identifying FLT in our samples than the UV peak when the sample concentration was in the sub-nanomolar range.

Though further development and optimization is needed, the successful separation of FLT from its impurities and successful determination of radiochemical identity suggests that MCE has the potential to perform QC tests traditionally performed using HPLC. The sensitivity of the radiation detector was found to be sufficiently high for the expected clinical sample concentrations that would be analyzed by this system. We are investigating whether a similar device could be used to determine radiochemical purity, molar activity and half-life in a short timeframe.

6. Chapter 6: Microscale radiolabeling of Biomolecules

Summary

Radiolabeled peptides and antibody fragments provide a means to image disease-specific targets with extremely high specificity. However, many proteins including antibodies and antibody fragments can usually not be labeled directly with [^{18}F]fluoride due to required harsh reaction conditions like elevated temperatures and the use of organic solvents and incompatible pH conditions [242]. Thus, to preserve the function of proteins, the radioisotope fluorine-18 can initially be incorporated into an ^{18}F-labeled prosthetic group which is then conjugated to the biomolecule under mild conditions. However, these mild conditions often lead to slow rates of conjugation reaction, unless a large excess of the biomolecule is used. Typically, 100-500 µg of peptide or protein is used in conventional “macroscale” approaches [243]. To reduce the high cost of labeling, efficient techniques with lower biomolecule consumption are necessary. Previously, using a droplet-based microfluidic chip, it has been shown that reagent consumption for small-molecule tracers can be reduced 2-3 orders of magnitude compared to conventional approaches [27]. Here, the feasibility of using this microfluidic chip approach to reduce precursor consumption in radiolabeling of biomolecules is investigated. As an example, a thiol-containing RGD peptide was labeled with fluorine-18 in a site-specific manner via the maleimide-based prosthetic group, N-2-(4-[^{18}F]fluorobenzamido)ethylmaleimide ([^{18}F]FBEM). Furthermore, the site-specific labeling method was extended to the radiolabeling of antibody fragments (cys-diabodies).

6.1 Biomolecules as PET probes

Over the past few decades, radiolabeled biomolecular agents have evolved from large proteins (e.g. intact polyclonal antibodies with low specificity) to monoclonal antibodies and fragments with relatively higher specificity, to even smaller molecular recognition units such as single-chain antigen-binding domain fragments, and finally to receptor-specific peptides [244], [245]. Biomolecular PET imaging probes such as radiolabeled peptides, proteins and antibodies provide a means to target specific biological targets with exceptional specificity, such as tumor-specific targets in cancer diagnostics. These probes also play an increasing role in drug discovery to test the efficacy of a new drug by imaging before and after treatment [246].

Various methods have been reported for radiolabeling of biomolecules including indirect radiolabeling that generally employs a bifunctional linker containing a radionuclide or chelating group for attachment of radiometals and a reactive group that can react with functional groups on biomolecules [247], [248]. This chelation approach typically requires use of radionuclides (radiometals) with long half-life, such as the positron-emitting radionuclides iodine-124 (100.2 hr) and zirconium-89 (78.4 hr), copper-64 (12.7 hr) and yttrium-86 (14.7 hr). Even though theses half-lives match well with the long biological half-life of intact antibodies, different radionuclides are desired for smaller antibody fragments that have much shorter biological half-life, e.g. a few hours at most [246].

It would be ideal to match the physical half-life of the radionuclide with the biological half-life of the antibody or fragments. Fluorine-18 is of great interest for same-day imaging due to its wide availability and favorable short half-life (109.8 min), which matches the fast clearance of smaller antibody fragments such as scFvs, nanobodies, affibodies, and diabodies [249], [250]. Furthermore, fluorine-18 has almost ideal imaging properties, with a high positron yield (97%), low mean positron range (0.5 mm) and no simultaneous gamma ray emission that would increase background.

6.1.1 **Conventional approaches for protein/peptide radiolabeling with fluorine-18**

An ideal radiofluorination method for biomolecules requires (1) a short reaction time with high RCY and specific activity (2) reaction conditions (i.e., room temperature, pH 7, and aqueous medium) to prevent the denaturation of the biomolecules [251]. Peptides and other biomolecules can usually not be labeled directly with [^{18}F]fluoride due to required harsh reaction conditions like elevated temperatures and the use of organic solvents and incompatible pH conditions. Therefore, the synthesis of ^{18}F-labeled peptides and proteins often requires first synthesizing ^{18}F-containing “prosthetic groups”, small intermediate molecules which can be subsequently conjugated to biomolecules (**Figure 6-1**).

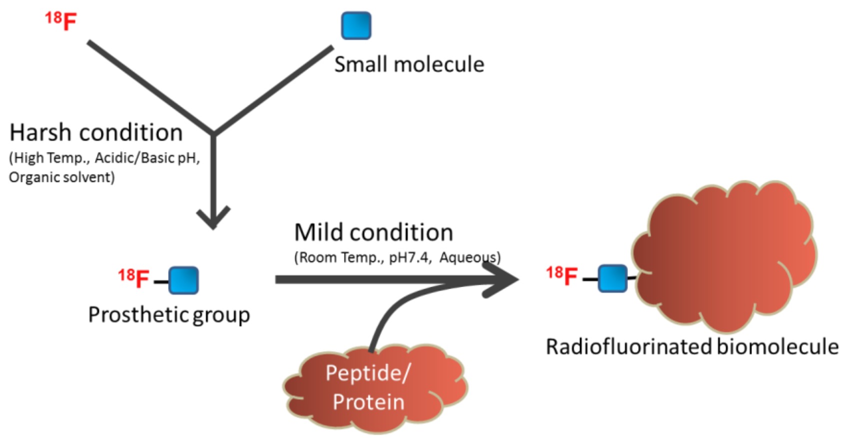

Figure 6-1. Fluorine-18 labeling of biomolecules.
Typical radiofluorination of biomolecules requires synthesis of intermediate molecule, “prosthetic group”, to gently introduce fluorine19 onto biomolecules.

Among many prosthetic groups, N-succinimidyl 4-[^{18}F]fluorobenzoate ([^{18}F]SFB) is the most widely used [252], [253]. The active ester group in [^{18}F]SFB can react with amine groups of protein and peptide **Figure 6-2**. However, [^{18}F]SFB is labile in the basic aqueous conditions generally required for efficient amino reactions, providing limited yield. Furthermore, [^{18}F]SFB often impairs the biological activity of the resulting conjugate which may result from the non-specific modification of amino groups near the binding region. Cai *et al.* reported that ^{18}F-labeled anti-carcinoembryonic agent (CEA) diabody was produced with compromised immunoreactivity (57%) when labeled with [^{18}F]SFB compared to other reported site-specific prosthetic groups such as [^{18}F]FBEM and [^{18}F]FPEGMA [254]–[256]. Labeling with [^{18}F]SFB often requires fairly large amounts of peptide or protein to achieve sufficient radiochemical yield. [^{18}F]FDG also has been used as a prosthetic group via oxime formation between aminooxy-functionalized peptide and [^{18}F]FDG [257]. The major limitations of FDG for protein labeling are the relatively high reaction temperature (100 °C or higher) and acidic pH required. High temperature and acidic pH are tolerated for many small unprotected peptides but might not be suitable for larger peptides and proteins [258].

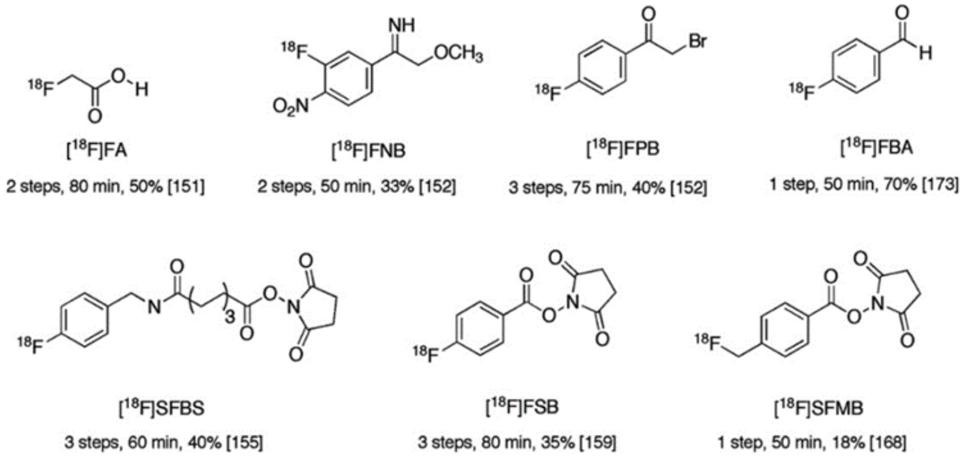

Figure 6-2. Examples of amine-reactive ^{18}F-labelled prosthetic groups used in protein labeling.
Adapted with permission from [247] Copyright © 2010 Elsevier.

6.1.2 Desired conditions for radiolabeling of biomolecules

Direct or indirect conjugation chemistries that react with random surface amino acid residues on biomolecules can compromise the binding affinity of antibodies and derivatives, especially those with critical tyrosine or lysine residues in the complementarity determining regions [246].

The ideal prosthetic group reacts at physiological pH and room temperature in less than 30 min. And the reaction does not require any organic solvent. More importantly, the conjugation occurs in a site-specific manner where the exact site of labeling can be predicted (**Figure 6-3**). A number of site-specific indirect conjugation methods have been reported that can specifically target cysteine residues in antibodies and antibody fragments after reduction of disulfide bridges [255], [259]. Conjugation and radiolabeling using thiol-reactive chemistries targeting reduced cysteines (either native or introduced via protein engineering) reduce the probability of adversely affecting the immunoreactivity of the antibody [246].

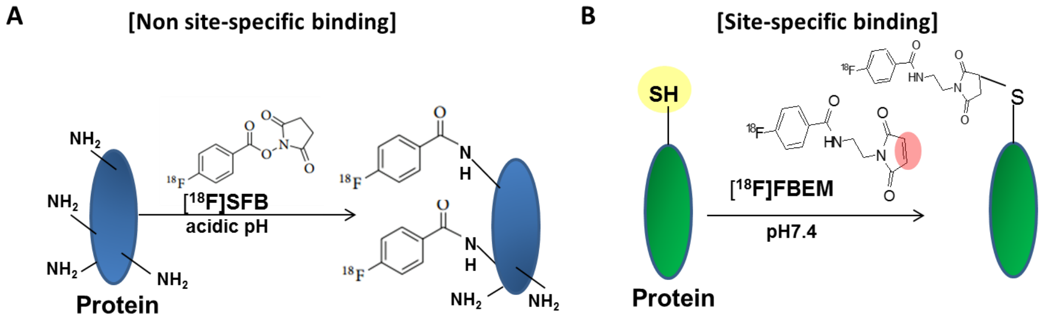

Figure 6-3. Types of radiofluorination of biomolecules.
(A) Non site-specific (random) labeling; (B) Site-specific labeling.

Michael-addition of a thiol (of cysteine) to a maleimide is commonly used for bioconjugation of drugs to macromolecules. The free thiol functional group is not very common in most peptides and proteins and is only present in cysteine residues. Thiol-reactive agents have therefore been used to modify peptides and proteins at specific sites. Several ^{18}F labeled thiol-reactive reagents have been reported in the literature including 1-(4-^{18}F-fluorophenyl) pyrrole-2,5-dione ([^{18}F]FPPD), 1-[3-(2-(^{18}F-fluoropyridin-3-yloxy)propyl]pyrrole-2,5-dione ([^{18}F]FPyME), N-[4-[(4-^{18}F-fluorobenzylidene) aminooxyl] butyl]maleimide ([^{18}F]FBABM) and N-[2-(4-^{18}F-fluorobenzamido)ethyl]maleimide ([^{18}F]FBEM) [260] (**Figure 6-4, Table 6-1**). More recently, “click” chemistry-based prosthetic groups have been introduced. In particular, the Cu(I)-catalyzed variant of the Huisgen 1,3-dipolar cycloaddition of terminal alkynes and azides offers a very powerful reaction with high specificity and excellent yields under mild conditions for ^{18}F-labeling of small molecules and peptides [251], [261], [262].

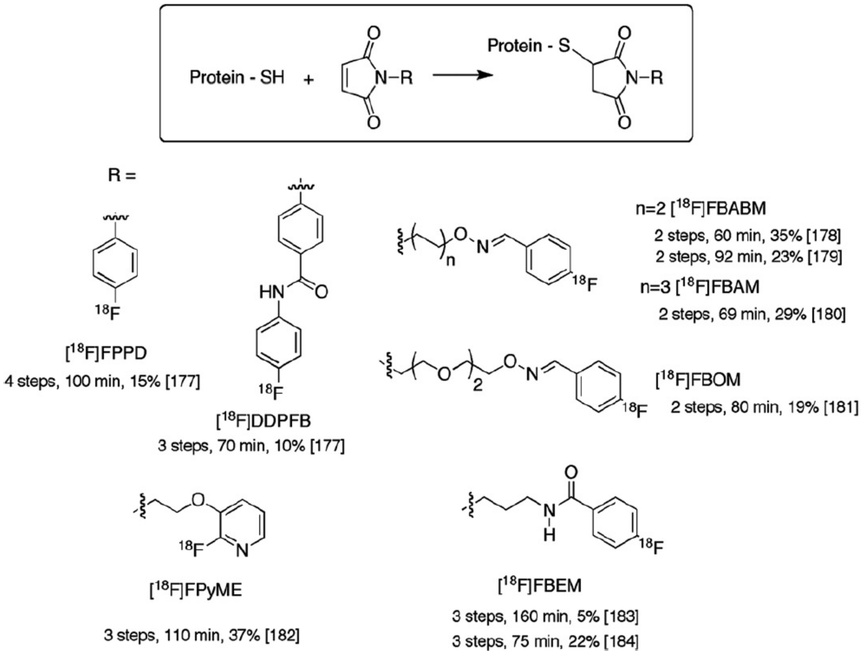

Fig. 7. Thiol-reactive ^{18}F-labelled maleimide-based prosthetic groups used in protein labellings.

Figure 6-4. Thiol-reactive ^{18}F-labelled prosthetic groups used in protein labeling. Adapted with permission from [247] Copyright © 2010 Elsevier.

Table 6-1. Examples of thiol-reactive maleimide-containing prosthetic groups.

Prosthetic group			Labelled Peptides/Proteins	Radiolabeling condition	Coupling yield (%)	Ref.
Type	**Radiochemical yield (%)**	**Synthesis time (min) / #steps**				
[^{18}F]FNEM	4	75 min from EOB/ 2 steps in 1 pot	GLP-1 analogue:[Cys40]-exendin-4	30min, RT, pH 7.4	36 - 48	[263]
[^{18}F]FBOM	19	80 min / 2 steps	LDL apoB-100	20min, RT, pH7.2	5	[257]
[^{18}F]FBABM	23	92min / 2 steps in 1 pot	Annexin V-128	15min, RT, pH 7.4, periodic gentle agitation	37	[264]
[^{18}F]FDG-MHO	45-69	45 min / 3 steps	Annexin A5	30min, RT, pH 7.4(Tris-HCL), FDG-MHO in ethanol	44-58	[265]

[^{18}F]FBAM	29	69 min / 2 steps	LDL apoB-100	20min, RT, pH7.2	20	[266]
[^{18}F]FBEM	13 -44	100-150 min / 3 steps in 2 pots	RGD-SH	20 min, RT, pH 7.4	96	[260]
[^{18}F]FPyMe	34 – 4-	110min / 3 steps	Hexapeptide & Proteins (c-AFIM-0 & c-STxB)	15-30 min, RT, pH 8, 10% DMSO	33 - 85	[244]
[^{18}F]FPPD & [^{18}F]DDPFB	15 (FPPD),10 (DDPFB)	FPPD: 100 min / 4 steps; DDPFB: 70 min / 3 steps	Fab' from rabbit IgG	Not described	50	[267]

6.1.3 Application of Microfluidic Technology for ^{18}F-Labeling of Peptides

Biomolecules are usually labeled with a ^{18}F-labeled prosthetic group under mild conditions. These mild conditions often lead to slow rates of the conjugation reaction and therefore a large excess of the biomolecule precursor is often needed to promote efficient labeling. Typically, 100-500 µg of peptide or protein is used for radiolabeling [243]. Furthermore, the production of custom engineered antibody and antibody fragments is a very time-consuming process taking weeks to produce small amount of proteins. ^{18}F-labeling of peptides using novel techniques such as microfluidic technology offers several advantages over conventional radiolabeling methods, including shorter reaction times, more efficient radiochemistry and more economical use of starting material [268].

Microfluidic radio-synthesizers are emerging as useful platforms for PET probe synthesis due to their rapid reaction kinetics and exquisite reaction selectivity. Batch microfluidic platforms, in contrast to flow-through platforms, provide additional advantages such as the ability to work at extremely low volumes (nL–µL), thus having the potential to increase the fluorination kinetics by achieving higher concentration of

[^{18}F]fluoride ions or ^{18}F-labeled prosthetic groups in a batch reaction. Similarly, although yet to be investigated, the reduced reagent consumption in batch microdevices has the potential to reduce cost, to simplify the downstream purification process, and to produce PET probes with higher specific activity [269].

Biomolecules are often labeled by hand (manual pipetting) as commercial radiosynthesizers are not designed to operate at the small reagent volumes (e.g. 10-100 µL) that radiochemists prefer in order to minimize reagent consumption. Droplet microreactors, with typical work volume of 1 - 20 µL are ideally suited to automate this labeling, with potential for further reduction in reagent consumption.

Several microfluidic platforms have been explored to harness the advantages of droplet reactions in radiochemistry. Keng *et al.* demonstrated the successful radiosynthesis of several ^{18}F-labeled compound using an electrowetting-on-dielectric chip, droplet-based digital microfluidic chip. The electrowetting-on-dielectric (EWOD) system, a promising digital microfluidic device, uses electric potentials to manipulate liquids without mechanical valves, pumps, or channels. It has shown that reagent consumption for small-molecule tracers can be reduced 2-3 orders of magnitude compared to conventional approaches [20]. Despite the widespread use of EWOD-based systems, there have been many challenges due to the high cost of prototype chips, frequent failure of the dielectric coating and the operating complexity. To address these issues, Wang *et al.* recently reported a simpler microfluidic device based on passive droplet transport using based on passive droplet transport using patterned wettability for multi-step radiochemical reactions and demonstrated production of [^{18}F]fallypride and [^{18}F]FDG [22]. Microfluidic radiosynthesis can significantly reduce the amount of radiation shielding necessary for safety and the amount of precursor and other reagents needed for the synthesis. Furthermore, significant improvements in the molar activity of the tracers have been observed.

Based on these recent successful and promising results of radiosynthesis in microfluidic platforms [22], [270], [271], we expect the same advantages to be applied to the production of biomolecular PET probes, where the cost of starting material is particularly high.

6.2 Microfluidic radiolabeling of peptide

Here, the feasibility of using this microfluidic chip approach to reduce precursor (biomolecule) consumption in radiolabeling is investigated. As an example, a thiol-containing RGD peptide was labeled with fluorine-18 in a site-specific manner via the maleimide-based prosthetic group, N-2-(4-[^{18}F]fluorobenzamido)ethylmaleimide ([^{18}F]FBEM) (see **Figure 6-5**).

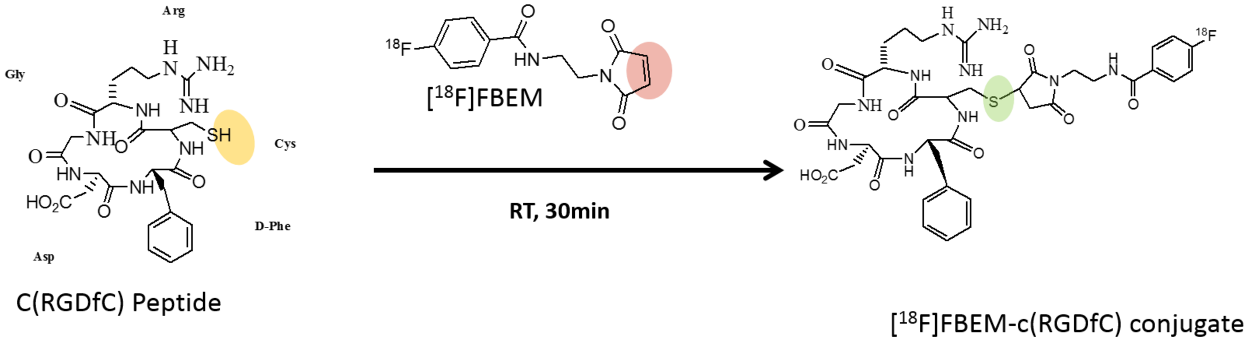

Figure 6-5. Site-specific radiolabeling of peptide.
As an example, c(RGDfC) peptide was labeled with [^{18}F]FBEM.

6.2.1 Selection of prosthetic group: [^{18}F]FBEM

Among several thiol-reactive maleimide prosthetic groups (shown in **Table 6-1**), [^{18}F]FBEM was chosen for this study since it has been reported in multiple studies with relatively high radiochemical yield (RCY), and successful preclinical imaging has been demonstrated [272], [273]. Additionally, [^{18}F]FBEM reacts with biomolecules very quickly in a site-specific manner at physiological pH without requiring organic solvents. Furthermore, the precursor for this prosthetic groups is commercially available.

A cysteine-containing RGD peptide was selected as model for the microscale radiolabeling. The RGD peptide targets integrin $\alpha_v\beta_3$ that plays a key role in tumor angiogenesis and metastasis [260].

Table 6-2. Examples of [^{18}F]FBEM-labeled biomolecules

Year	**Biomolecules (proteins or peptides)**				**Prosthetic group: [^{18}F]FBEM**				**Radiolabeling yield (%)**	**Ref.**
	Type	**Size (kDa)**	**Amount (µg)**	**Solvent**	**Molar activity (Ci/µmol)**	**Radiochemical yield (%)**	**Amount (mCi)**	**Solvent**		
2006	c(RGDyK) & E[c(RGDyK)]2	> 620	200	50 µl DMSO, 1mg TCEPHCL in 100µl Water	4 - 5.4	5 (non-corrected)	5 (non-corrected)	600 µl MeCN	80% non-corrected based on starting [^{18}F]FBEM	[260]
2008	Affibodies (ZHER2:2395-cys & ZHER2:342-cys)	7 & 8	100	250µl PBS	NA	22.4 (non-corrected)	2.7 - 10	10 µl MeCN	10 .5 & 11.6 (decay non-corrected)	[274]

2011	Glucagon-like peptide-1 (GLP-1)	> 3.3-4	115 - 135	100 µl of DMF:DMS:PBS(=10:45:45)	3-Feb	24.8 (non-corrected)	1.9 - 3	10 µl EtOH	24.9 (decay non-corrected)	[275]
2012	Single-chain (sc)-VEGF with a Cys-tag	28	100-200	100µl PBS	1.58	20.6 (non-corrected)	15-37	10µl EtOH	20.6 (decay non-corrected) based on starting [^{18}F]FBEM	[276]
2014	Glutathione (GSH)	0.31	1000	1mL of PBS buffer	1.2-1.8	15-20	20	NA	99 (decay corrected)	[277]
2015	Wild-type annexin V	36	100	100 µl PBS	NA	NA	5.4	Dried FBEM	4 ± 2 % (n = 5) based on starting [^{18}F]FBEM) (decay corrected)	[278]
2015	Cys-Annexin V with a cysteine-tag	36	50-100	100µl PBS	4	5.4	11.5	10µl EtOH	71.5% ± 2.0% (decay non-corrected)	[272]

6.2.2 **Materials and Methods**

6.2.2.1 Synthesis of N-[2-(4-**[^{18}F]fluorobenzamido)ethyl]maleimide, [^{18}F]FBEM**

[^{18}F]FBEM was synthesized on an automated radiochemistry synthesizer (ELIXYS, Sofie Biosicences, Inc.) in high radiochemical yield (35±8% *(n=7)*, decay-corrected) in 100 min following a previously reported method [234].

The automated synthesis of [^{18}F]FBEM was adapted from Kiesewetter *et al.* [256] and Ackermann *et al.* [277] with slight modifications. The fluorobenzoic acid precursor used for FBEM synthesis (5 mg in 0.5 mL MeCN) was added to the activated [^{18}F]fluoride residue in reaction vessel 1. The contents of the vessel were heated for 10 min at 120 °C. Following the reaction, diethyl ether (2 mL) was added and the contents were transferred directly through a silica cartridge and delivered into reaction vessel 2. The ether was completely evaporated using 4psi of N2 pressure at 35°C. Additional ether (2 mL) was added to reactor 1, and then transferred through the silica cartridge to reaction vessel 2, followed by evaporation at 35°C. Next, TFA (300 μL) was added to the vessel and heated for 2 min at 30°C. The TFA was then evaporated slowly at 30°C for 6 min.

After TFA was removed, the FBEM maleimide precursor (2.3mg in 300μL of MeCN, mixed with 5.8mg of DCNP in 300μL of MeCN), was added to the reactor. A solution of DIEA (30 μL) in MeCN (300 μL) was also added. The mixture was heated for 7 min at 75°C. Following the reaction, the solvent was evaporated at 75°C to dryness (~2 min). A solution of 5% MeCN in 50mM NH4OAc (2 mL) was then added and the diluted crude mixture was transferred to the HPLC injection loop for semipreparative HPLC purification. The purified [^{18}F]FBEM was formulated manually using an Oasis Plus WCX cartridge preconditioned with 5mL of EtOH and 10mL of water. The collected HPLC fraction was diluted with water (30 mL), and then pushed through the cartridge to trap the product. After trapping, the cartridge was rinsed with water (5 mL) and then dried with a stream of nitrogen. The product was then eluted from the cartridge with DCM (2 mL). Finally, the solution was concentrated by evaporating the solvent with a gentle stream of nitrogen at room temperature and subsequently used in the labeling of thiolated peptides and proteins.

6.2.2.2 Microfluidic chip fabrication

To fabricate the Teflon-coated glass chip (**Figure 6-6A**), a glass slide was cleaned thoroughly with MeOH and acetone, 5 min each in an ultrasonic cleaner, followed by Piranha cleaning (3:1 H_2SO_4:H_2O_2, 20 min at 120°C). After rinsing with DI water, the clean glass slide was treated with trichloro(1H,1H,2H,2H-perfluorooctyl)silane (97% purity, Sigma-Aldrich, Milwaukee, WI, USA) as an adhesion promoter inside a desiccator overnight. It was then spin-coated at 1000 rpm for 30 s with a 1% solution of Teflon AF 2400 (Chemours, Wilmington, Delaware, USA) to create a 100 nm thick hydrophobic surface. The teflon-coated glass chip was heated at 160°C for 10 min and at 245°C for 10 min. It was further annealed at 340°C for 3.5 hr in the Carbolite oven to achieve smooth surface.

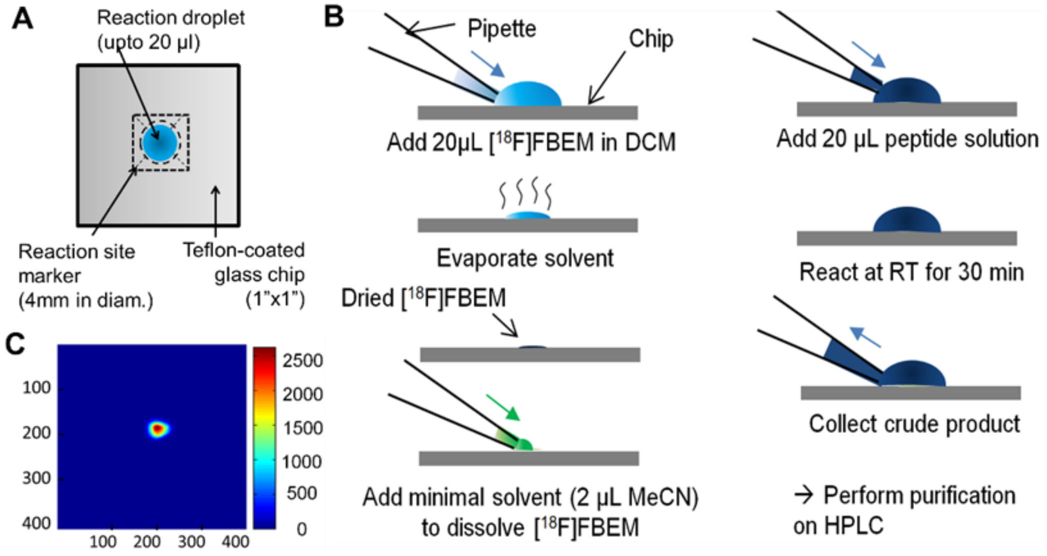

Figure 6-6. On-chip radiolabeling of biomolecules

(A) Schematic representation of Teflon-coated glass chip (top view). Reaction site marker is on the back side of the chip. (B) Step-by-step process for on-chip peptide labeling with [^{18}F]FBEM. Note that the amount of [^{18}F]FBEM radioactivity can be increased by repeating the first 3 steps more than once. DCM=dichloromethane, MeCN=acetonitrile (C) Cerenkov image confirms the successful concentration of [^{18}F]FBEM at the reaction region.

6.2.2.3 Microscale site-specific labeling of RGD peptide

Firstly, to perform the microscale labeling (**Figure 6-6B**), a 20 µl droplet of [^{18}F]FBEM dissolved in dichloromethane (DCM) was concentrated (by rapidly evaporating solvent) onto a small part of the reaction site of the chip, and the distribution of radioactivity on chip was visualized via Cerenkov imaging (**Figure 6-6C**). This concentration step was repeated a few times to achieve desired radioactivity concentration (e.g., ~ 1mCi = 37 MBq). Dried FBEM was re-dissolved by adding a 2 µl droplet of MeCN and waiting for 1min. Then, 20 µL peptide solution (in PBS, pH 7.4) was added for the room temperature conjugation reaction. After 30min reaction, 50 µl PBS was added to quench the reaction. The crude product was extracted from the chip an analyzed via analytical HPLC. The effect of peptide concentration was explored by using peptide solution droplets containing different amounts of peptide (0.2 to 100 µg).

6.2.2.4 Data analysis (Estimation of radiolabeling efficiency)

The crude reaction product was collected for analysis via analytical HPLC (Smartline HPLC system, Knauer, Berlin, Germany). Analytical HPLC employed a C18 Luna reverse phase column (4.6 mm × 250 mm, 5 µm; Phenomenex, Torrance, CA, USA) and a gradient eluant of 5% A, 80% B from 0 - 2 min to 35% A, 75% B from 2- 32 min, then 95% A, 75% B from 32 – 40 min . Solvent A was 0.1% TFA in acetonitrile. Solvent B was 0.1% TFA in DI water. The flow rate was 1mL/min.

The radiochemical conversion was estimated based on the area under curve (AUC) of radio HPLC peak of the conjugate, [^{18}F]FBEM-c(RGDfC), relative to the sum of all AUCs detected (Figure 6-7). The sample collection efficiency (%) was calculated by measuring the remaining radioactivity on chip after sample was collected, then comparing it to the radioactivity on chip before the collection (after reaction is completed). The crude radiolabeling yield (an estimate of isolated yield) was estimated by multiplying the conjugation efficiency by the sample collection efficiency to estimate the expected amount of product if it was purified ("crude RCY").

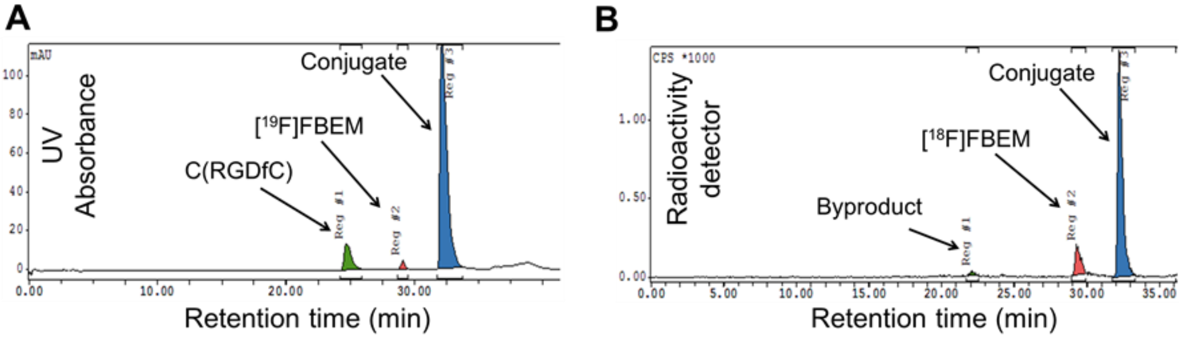

Figure 6-7. Preparative HPLC chromatogram
(A) "cold" (non-radioactive reaction for peak identification purpose) and (B) "hot" (radioactive) crude reaction mixture. Performed on analytical-scale HPLC.

6.2.3 **Results**

Labeling efficiency was investigated as a function of the amount of peptide precursor participating in the reaction. On-chip [^{18}F]FBEM conjugation of c(RGDfC) resulted in high labeling efficiency: 96.7, 94.8, 84.7% for 100, 20 and 6.7 μg of peptide precursor, respectively (**Figure 6-8A**). Even with 2 μg peptide, it exhibited practical conjugation efficiency (26.6%). The collection efficiency of sample from the chip was over 90%. The crude radiochemical yield was found be very high: 84.1, 83.9, 70.2% for 100, 20 and 6.7 µg peptide, respectively (**Figure 6-8B**).

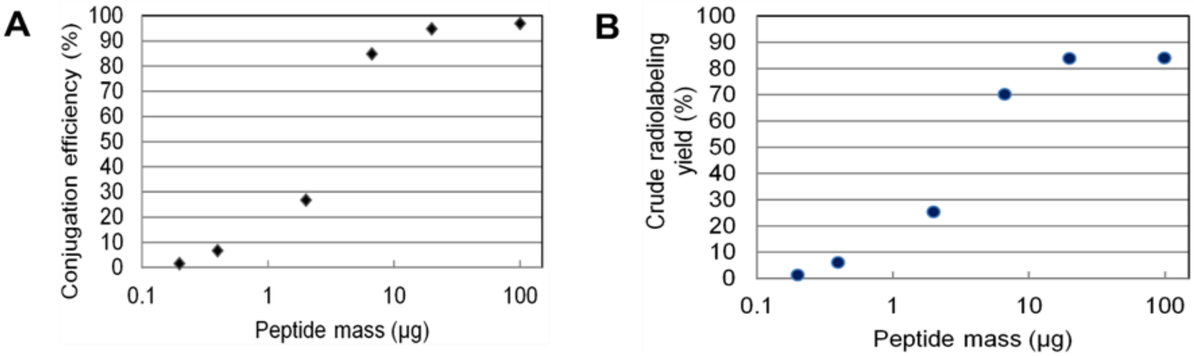

Figure 6-8. Labeling efficiency as a function of peptide mass
(A) Conjugation efficiency of [^{18}F]FBEM to labeled peptide based on the percent peak area corresponding to conjugate in the HPLC chromatogram. (B) Estimate of radiolabeling yield. Crude radiolabeling yield corresponds to the conjugation efficiency multiplied by the collection efficiency from the chip. Note that efficient conjugation is possible on chip with as little as a few µg of peptide.

6.2.4 **Conclusion**

We have demonstrated that microscale radiolabeling of peptides using low amount of peptide is feasible using droplet microfluidics. Peptide consumption was reduced 50-250 times compared to conventional methods where 100 - 500 µg of peptide is typically required. Although the current study used ~1mCi of [^{18}F]FBEM per experiment, the activity could be easily scaled up for clinical & pre-clinical imaging by repeated [^{18}F]FBEM loading, or by pre-concentrating [^{18}F]FBEM using a method like microfluidic membrane distillation as our group demonstrated previously [43].

We envision that this small volume reaction approach could potentially be applied to the development of antibody-based imaging probes and radiotherapeutics with reduced precursor consumption and could possibly increase the effective molar activity (radioactivity per protein mass).

6.3 Radiolabeling of protein: Labeling engineered antibody fragments

6.3.1 Introduction

To extend our findings from peptide labeling to protein labeling, we explored the radiolabeling of engineered antibody fragment (cys-diabody) used in immunoPET. ImmunoPET, utilizing the specificity of antibodies, could provide additional phenotypic information regarding the presence or modulation of a lymphocyte-specific target, and has the potential to improve diagnosis, therapy selection, and patient stratification [279].

CD20 antigen expression on B-cell malignancies is an important biomarker and therapy target, as evidenced by the clinical success of anti-CD20 monoclonal antibodies (mAbs) such as rituximab and obinutuzumab [280]. While radiolabeled full-length antibodies have been successfully used for PET imaging, their long plasma half-life and their therapeutic activity are disadvantageous for both prompt and repeated imaging. Zettlitz *et al.* previously developed CD20-specific immunoPET tracers using obinutuzumab (GA101) based antibody fragments radiolabeled with zirconium-89 (^{89}Zr) or iodine-124 (^{124}I) and showed antigen specific targeting of malignant and endogenous B cells in vivo [19].

The smallest bivalent fragment, the cys-diabody (GAcDb, 55 kDa), presents a suitable compromise between tumor uptake (peak uptake 1-2 hr) and blood clearance ($t_{1/2}$ = 2-5 hr) that aligns with the half-life of fluorine-18. ^{18}F-radiolabeling of GAcDb could enable same-day imaging and lower the patient's radiation exposure compared with the longer-lived ^{124}I and ^{89}Zr. Here, we are exploring the site-specific conjugation of [^{18}F]FBEM to GAcDb.

6.3.2 Site-specific radio-fluorination of diabody (GAcDb) with [^{18}F]FBEM

For site-specific radiolabeling, [^{18}F]FBEM (330 MBq in 30 µL PBS) was incubated with reduced (10-fold TCEP, 2 h, 22°C) GAcDb (100 µg in 30 µL PBS) for 15 min at 22°C. Excess prosthetic groups were separated from the conjugate using Micro Bio-Spin size exclusion columns (Bio-Rad) pre-blocked with PBS, 1%FBS. Labelling efficiency and radiochemical purity were analyzed using ITLC strips (for monoclonal antibody preparation, Biodex Medical Systems) with saline as solvent (Wizard 3' 1480 Automatic Gamma Counter, Perkin Elmer).

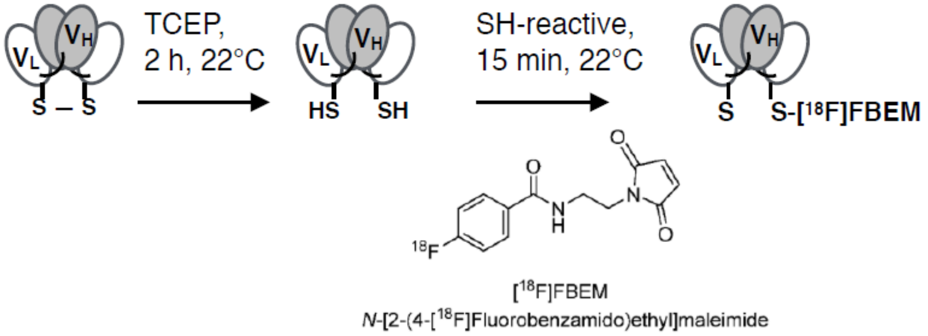

Figure 6-9. Schematic of site-specific conjugation using [^{18}F]FBEM to the Cterminal cysteine residues (after mild reduction using TCEP) resulting in [^{18}F]FBEM-GAcDb.

SDS-PAGE analysis shows the unconjugated GAcDb migrating with an apparent molecular weight of approximately 55 kDa corresponding to the covalent homodimer (**Figure 6-10**, lane 1). Incubation with TCEP results in complete reduction of the solvent exposed C-terminal disulfide bond and the visible band corresponds to the scFv monomer (M_W 27.3 kDa) (**Figure 6-10**, lane 2). After TCEP removal (by size exclusion spin column) the GAcDb reoxidizes to its dimeric conformation within 24 hr (**Figure 6-10**, lane 3). Incubation of the reduced GAcDb with [^{18}F]FBEM and with TCEP present or with TCEP removed, leads to site-specific conjugation, blocks reoxidation of the cys-tag and [^{18}F]FBEM-GAcDb migrates as a monomer **(Figure 6-10**, lane 4, 5).

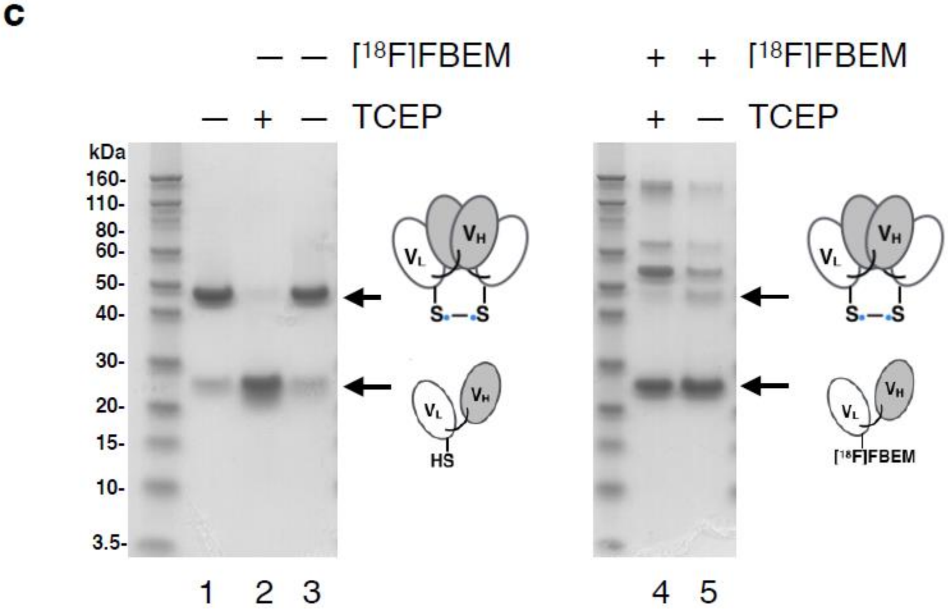

Figure 6-10. SDS-PAGE analysis of site-specific conjugation (non-reducing conditions).
GAcDb (lane 1), with TCEP (lane 2), reoxidized after TCEP removal (lane 3), conjugated with [^{18}F]FBEM in the presence of TCEP (lane 4) or after TCEP removal (lane 5).

6.3.3 Microscale radiolabeling of diabody with [^{18}F]FBEM

As a proof-of-concept, microscale labeling of diabody was performed on the chip as shown earlier in **Figure 6-6** with minor modification. First, [^{18}F]FBEM was concentrated on the chip. Then, dried [^{18}F]FBEM was re-dissolved by adding a 2 µl droplet of PBS (1x, pH 7.4) and incubating for 1min. Then, 10 µL diabody solution (20 µg in 10 µL, reduced with TCEP) was added for the room temperature conjugation. After 30min reaction, 50 µl PBS was added to quench the reaction. The crude product was extracted from the chip an analyzed via iTLC. Detailed reaction conditions and results are summarized in **Table 6-3**. From the iTLC results, we confirmed that successful conjugation occurs in the on-chip reaction as observed in conventional scale method where 100 µg diabody was used. However, large variation between chips was observed.

In the future, we will systematically characterize this microscale radiolabeling, and potentially optimize the reaction conditions (e.g., reaction time, reaction volume, molar ratio of prosthetic group to protein, mixing parameters) to achieve higher and more repeatable labeling yield.

Table 6-3. On-chip radiolabeling of GAcDb

Chip	Starting activity of [^{18}F]FBEM (mCi)	Protein volume (µl)	Absolute protein amount (µg)	Sample collection efficiency (% recovery from chip to collection vial)	Crude labeling yield (%, based on iTLC)
1	1.30	10	20 (0.37nmol)	84.07	5.47
2	0.87			75.12	17.11
3	0.16			84.79	12.28
4	0.17			100.00	37.75

6.3.4 Preclinical imaging: ImmunoPET/CT imaging, ROI analysis and biodistribution

To investigate properties of this new diabody-based probe, PET imaging (Inveon, Siemens) was performed under 2% isoflurane anaesthesia followed by a CT scan (MicroCAT, Siemens). For immunoPET imaging, mice were injected with 15 to 20 µg (3.7-7.4 MBq) of [^{18}F]FBEM-GAcDb. 1-2 hour dynamic PET acquisitions were followed by ten minute static scans at 2, 4 and 6 h post injection (p.i.). PET images were reconstructed using maximum a posteriori (OSEM MAP) algorithm and PET and CT images are presented as maximum intensity projection (MIP) overlays. As a comparison, the diabody conjugated to the most common prosthetic group, [^{18}F]SFB, to form [^{18}F]FB-GAcDB, was injected for imaging.

For quantitation of the PET signal in specific organs, 3D regions of interest (ROI) were drawn and the mean voxel value was converted to %ID/cc ROI using the decay corrected injected dose and an empirically determined cylinder factor for F-18. [^{18}F]FBEM-GAcDb (**Figure 6-11**) showed earlier (5 min p.i.) and higher target specific accumulation in the spleen peaking at 30 min p.i. followed by a steady decrease of the radioactivity signal compared to [^{18}F]FB-GAcDB. The signal in the heart (estimating the activity in the blood pool) decreased visibly from 10 min p.i. on, indicating a more rapid blood clearance compared with [^{18}F]FB-GAcDb. Similar to [^{18}F]FB-GAcDb, the site-specifically conjugated [^{18}F]FBEM-GAcDb showed primarily renal clearance with activity visible in the kidneys after 10 min and in the bladder at 30 min p.i. (**Figure 6-12**). Approximately 60 min p.i. activity started to become visible in the gastrointestinal (GI) tract and 2 hr p.i. accumulation of radiometabolites in the gall bladder (GB) suggest a secondary hepatobiliary clearance route. It indicates that the [^{18}F]FBEM-GAcDb is not fully stable in vivo and its metabolites have distinctive excretion route.

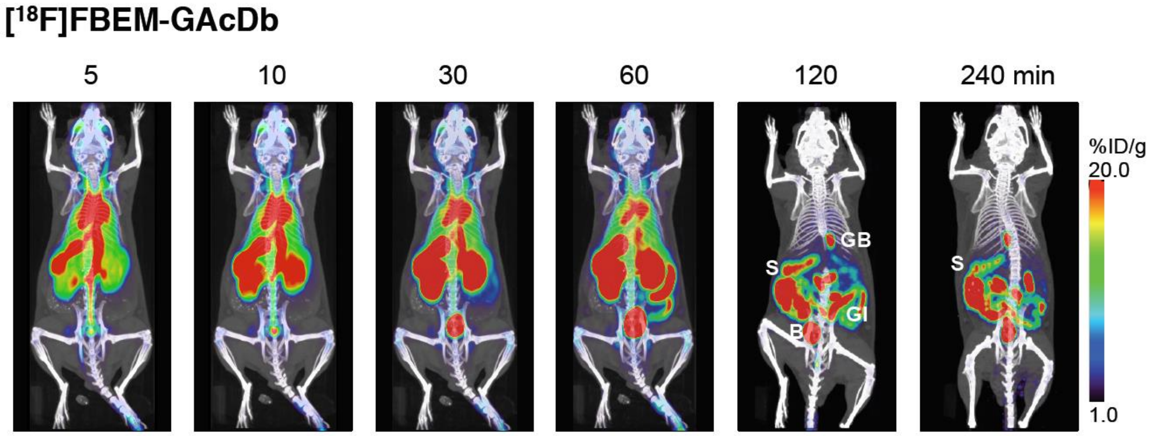

Figure 6-11. ImmunoPET imaging of hCD20 transgenic mice shows antigen specific retention in the spleen
[^{18}F]FBEM-GAcDb immunoPET, 4.3 MBq/12 μg. Primarily renal clearance (kidneys, K) and excretion into urine (bladder, B) is visible. Increased gallbladder (GB) and GI tract activity suggests secondary excretion of radiometabolites through the hepatobiliary system.

Anti-CD20 immunoPET tracer, [^{18}F]FBEM-GAcDb, successfully visualized the normal tissue distribution of hCD20 in spleen and lymph nodes (rescaled images in **Figure 6-12**). Notably, the smallest (popliteal) lymph nodes visible in the immunoPET scans, are only about 1 mm^3 in size. Although the signal in the spleen at 4 hr p.i. is comparable between the two tracers, the remaining activity in the intestines for [^{18}F]FBEM-GAcDb obstructs the view of the abdominal area.

In conclusion, we have confirmed that [^{18}F]FBEM-GAcDb shows specific targeting of hCD20 B cells and optimized pharmacokinetics to enable same-day imaging.

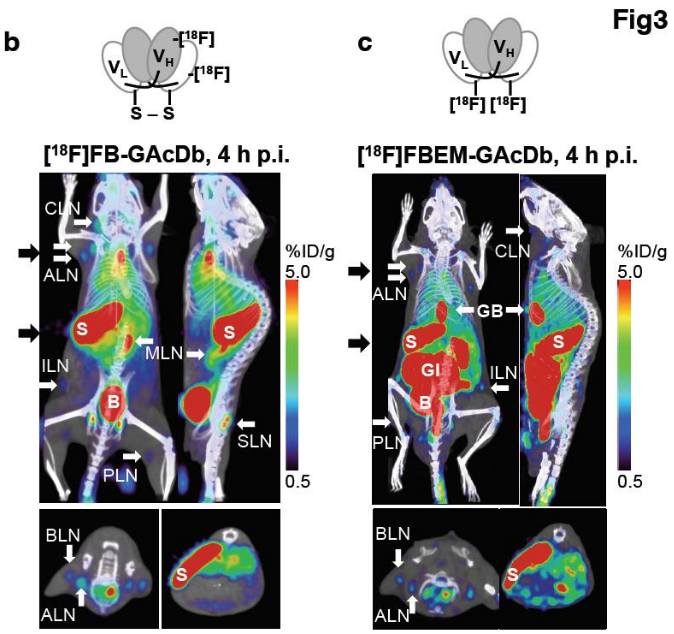

Figure 6-12. ImmunoPET imaging using [^{18}F]FBGAcDb and [^{18}F]FBEM-GAcDb, 4 h p.i.

Specific spleen and lymph node uptake are visible. The secondary secretion route of radiometabolites through the hepatobiliary system is indicated by the high signal in the gallbladder (GB) and the intestines (GI) and excretion of radioactivity with feces. Scans are depicted as microPET/CT overlay, whole body MIP. Black arrows indicate the location of the 2 mm transverse section shown in the lower panel.

6.4 Future directions

As we successfully demonstrated the site-specific radiolabeling of a peptide and a protein, we can now explore the use of microscale reactions to minimize the precursor (biomolecule) consumption while also maximizing labeling yield.

Additionally, we will investigate the effective molar activity of labeled proteins in microscale radiolabeling. As the isolation of labelled protein molecules from the non-labeled proteins is usually not feasible due to the chemical similarity of the labeled and non-labeled proteins, the effective molar activity is defined as the ratio of the mass (or molar quantity) of a single species radiotracer to the total of the radiotracer and non-radioactive compound that have similar biochemical properties. It is expected that the effective molar activity of labeled proteins would increase in our microfluidic approach if the amount of protein can be reduced compared to conventional methods. Radiolabeled protein probes with higher effective molar activity are expected to show better visualization of targets *in vivo*, especially for saturable binding sites.

One potential problem of on-chip conjugation that might be encountered is adhesion of proteins to the chip surface that could make the protein unavailable for reaction, or could make it difficult to remove labeled proteins from the surface. If needed, surface passivation techniques, or alternative surface materials will be considered.

In the future, in addition to the thiol-maleimide site-specific reaction, we will explore other bio-orthogonal labeling methods such as “Click” chemistry for on-chip radiolabeling. One potential candidate is an aromatic ^{18}F -PEG-Azide compound. Sachine *et al.* have explored the copper-free strain-promoted alkyne azide cycloaddition (SPAAC) click reaction and shown highly efficient labeling yield of RGD peptide, 92% (decay-corrected), and the reaction was performed in aqueous solvent for 20 min reaction at room temperature [281]. Furthermore, more recently introduced sydnone cycloadditions can also be explored [282], [283].

If a robust radiolabeling platform is established, the next step is to automate the system. A fully automated microfluidic radiolabeling system for biomolecules would significantly lower the radiation exposure to operators, lower the degree of skill needed to perform labeling, and substantially lower the labeling cost making it more accessible to investigators.

7. Chapter 7: Electrodewetting microfluidic droplet manipulation

Summary:

The ability to manipulate liquid droplets on substrate with only electric signals [284]gave birth to digital microfluidics, which has found applications from optical [285], [286] and biomedical [270], [287] to thermal [288] and electronic [289], including commercial [290]–[292]. For many such electrical actuations, especially electrowetting-on-dielectric (EWOD)[293], [294], a liquid drop is attracted towards and spread on a conductive substrate covered with a dielectric layer and a hydrophobic topcoat. While credited to make electrowetting practical, these added layers are responsible for the relatively high actuation voltage (20-200 V) and reliability issues such as dielectric breakdown [295], electric charging [296], and biofouling [297]. Here we report "electro-dewetting" that acts in an opposite manner to electrowetting, i.e., electrically repels a droplet on substrate effectively enough to support digital microfluidics. This surfactant-mediated mechanism uses a hydrophilic surface, eliminating the issues originating from the added layers. This study investigates the underlying mechanism and operating characteristics of nd to manipulate droplets on substrate in air. Using only ±2.5 V and a few µA, electrodewetting is demonstrated to generate, move, split, and merge water droplets on silicon in open air. The compatibility is further validated with a variety of liquids, including common buffers and organic solvents. Despite the required use of surfactant, electrodewetting shows a great promise for microscale liquid handling platform that is extremely simple and highly reliable.

7.1 Introduction: Electrowetting and EWOD vs. Electro-dewetting

As an elegantly simple platform technology for microfluidics, electrowetting (more specifically electrowetting-on-dielectric (EWOD) [293], [294]) has enjoyed exponential advancement during the past 15 years and has culminated in many commercial applications [290]–[292]. Despite the success, however, EWOD devices are well known to suffer from reliability problems, which are predominantly associated with the dielectric layer and hydrophobic topcoat [295]–[297]. First, since the electric double layer (EDL) can sustain only a small voltage (e.g., < ~1V) between the liquid and substrate and the electrowetting force generated by the small voltage is too weak for most applications, a dielectric layer is added on the substrate (hence the term EWOD [294], [298], [299]). Since the voltage applicable on a given dielectric material is proportional to the thickness and the electrowetting force is proportional to the voltage squared [294], [299], one would prefer a reasonably thick dielectric to make the EWOD devices more robust (especially important for commercial product) despite a relatively high voltage required. However, since deposition of a defect-free thin film is challenging, especially across the relatively large area of some devices, the dielectric layer often experiences electric leakage or even breakdown [295], resulting in the notoriously well-known device failure by electrolysis27. Second, the top surface needs to be hydrophobic so that a droplet is naturally dewetted on it and has a sufficient room for significant induced wetting by electrowetting. However, since most materials, including the added dielectric layer, are hydrophilic, a low-energy material is coated on top to render the final surface hydrophobic. Unfortunately, this hydrophobic topcoat, e.g., polytetrafluoroethylene (PTFE), is susceptible to charging under electric field[296] and prone to protein fouling[297], not to mention its material and deposition costs. Despite the associated problems, the dielectric layer and hydrophobic topcoat (i.e., EWOD) were the critical advances that made the once-obscure concept of electrowetting practical for applications, leading to the digital microfluidics of today.

Here, we expect electrodewetting to be a mirror opposite of the well-known electrowetting with comparable effectiveness. While most of the electrically-induced dewetting phenomena were not effective for common microfluidics because they are based on irreversible processes [300], [301] or special conditions [302], studies involving surfactants have shown that reversibility may be possible. For example, electrically-initiated dewetting of an aqueous film on derivatized gold electrodes has been demonstrated using redox-active surfactants [303]. Recently, by using ionic surfactants, the coefficient of a lubricated friction was switched in a solid-liquid-solid configuration [304], and boiling bubble nucleation was modulated in a liquid-vapor-solid system [305]. Furthermore, an organic droplet was translated on a conjugated polymer electrode in an aqueous electrolyte [306]. However, they have not led to a microfluidic platform technology, which would require an electric actuation that is reversible, repeatable, strong, and easily applicable to a liquid-fluid-solid system [298]. In fact, we could not obtain electrodewetting with aqueous droplets containing ionic surfactants on either bare metal electrodes [304], [305] or the dielectric-coated conductive substrate of EWOD.

Instead, we have discovered that a bare silicon wafer does the trick by letting its native oxide resistively pass the electric current as well as providing a very hydrophilic surface. An expected consequence for this electrodewetting is that, with neither the added dielectric layer nor the hydrophobic topcoat, the reliability problems of EWOD can be avoided, not to mention the device simplification and cost reduction.

7.2 Electrodewetting: Novel droplet actuation

The electrodewetting mechanism would be impactful for microfluidic applications only if the wetting and dewetting states have a significant difference to induce a strong actuation, the transition between the two states is reversible, and the mechanism is realized in a simple device configuration. The electrodewetting was found to induce the contact angle difference between the two states that is large enough (e.g., > 20°, the contact angle hysteresis on common materials) to incite strong-enough fluidic actuations; reversibly switches over 10,000 cycles with no apparent degradation; and demonstrated in an extremely simple configuration.

When an electrodewetting test similar to this study was tried with water on a gold surface, we did not observe the appreciable contact angle change found on the silicon surface. We believe water, which has 60-65° of contact angle on gold surface [307] is not hydrophilic enough for effective electrodewetting. As matter of fact, gold was used as a hydrophobic metal when electrowetting was explored for microfluidics before EWOD took its place [299]. After testing many surfaces, our experience indicated that a hydrophilic surface with contact angle < 25° is desired to perform effective electrodewetting on. This is a stark contrast to electrowetting and EWOD, which requires a hydrophobic surface with contact angle typically > ~100°. While electrodewetting uses an electric field formed inside a droplet to manipulate the adsorption of ionic surfactant molecules on the solid surface, electrowetting (i.e., EWOC) and EWOD use an electric field formed across EDL and the dielectric layer, respectively.

Some other approaches: There have been interesting advances in recent years to achieve effective electrowetting without the dielectric and hydrophobic layer. One approach is to use special surfaces (e.g., the basal plane of highly oriented pyrolytic graphite) with an extremely low contact-angle hysteresis. One can achieve a large contact-angle change on such a pinning-free surface using the conventional electrowetting [308]. Often called electrowetting-on-electrode (EWOC) to distinguish it from EWOD, this approach is attractive for its use of low voltages (~1 V). However, the actual electrowetting force is likely too small to overcome disturbances, such as gravity, vibration, and imperfections, which are bound to be encountered in realistic conditions. Another approach is to immerse the droplet in a second liquid and thus dramatically reduce the contact-angle hysteresis. Applicable to both EWOC and EWOD, this approach uses a much voltage than EWOD in air. With this two-liquids approach, one can further utilize surfactants to decrease the contact angle of the filler liquid, thus increasing the contact angle of the droplet and enhancing electrowetting effect35 and facilitate specific applications[309]. A related approach is to replace the dielectric coating with the native oxide of a liquid-metal electrode [310], making the device robust both for fabrication and usage. However, this approach also works in a two-liquid system, as it needs a low hysteresis and the help of oil-based surfactant. It is to be seen if any of the new approaches will show the level of effectiveness EWOD has enjoyed despite the reliability issues.

7.3 Mechanism of electrodewetting

To study the electrodewetting mechanism and characterize its behavior, we adopted the configuration popular for electrowetting studies, as shown in **Figure 7-1**. An elaborate setup was developed for accurate experimentation, as detailed in **Figure 7-3**. The droplet contains an ionic surfactant, which consists of a charged hydrophilic “head” group and a neutral hydrophobic “tail” region. Depending on the polarity applied and the type of surfactant, the electric field inside the conductive (resistive) liquid drives the ionic surfactant molecules towards or away from the liquid-solid interface, making the drop dewet the surface (**Figure 7-1a**) or wet it again (**Figure 7-1b**). An exemplary result shown **Figure 7-1c&d** used a decyltrimethylammonium bromide (DTAB) solution on a highly doped (i.e., conductive) silicon wafer, chosen for its smooth surface and native oxide (2-10 Å thick) that is highly hydrophilic (water contact angle < 10°). To assess the proposed mechanism, we have performed a separate experiment using a droplet containing a fluorescent cationic surfactant, as detailed in **7.5.3**. The fluorescent intensity on two surface regions – region I (always inside droplet) and region II (outside droplet during electrodewetting but inside during wetting) – are overlaid on **Figure 7-1c &d**. The higher fluorescent level on I.C than I.D supports the illustration of **Figure 7-1a&b** for region I. For region II, the much higher fluorescent level on II.C than II.D confirms that the retraction of the contact line by electrodewetting leaves a significant amount of surfactant on the substrate right outside the droplet. It also shows that these adsorbed surfactant molecules are removed from the surface as the contact line advances during wetting, further corroborating the proposed mechanism and explaining its reversibility.

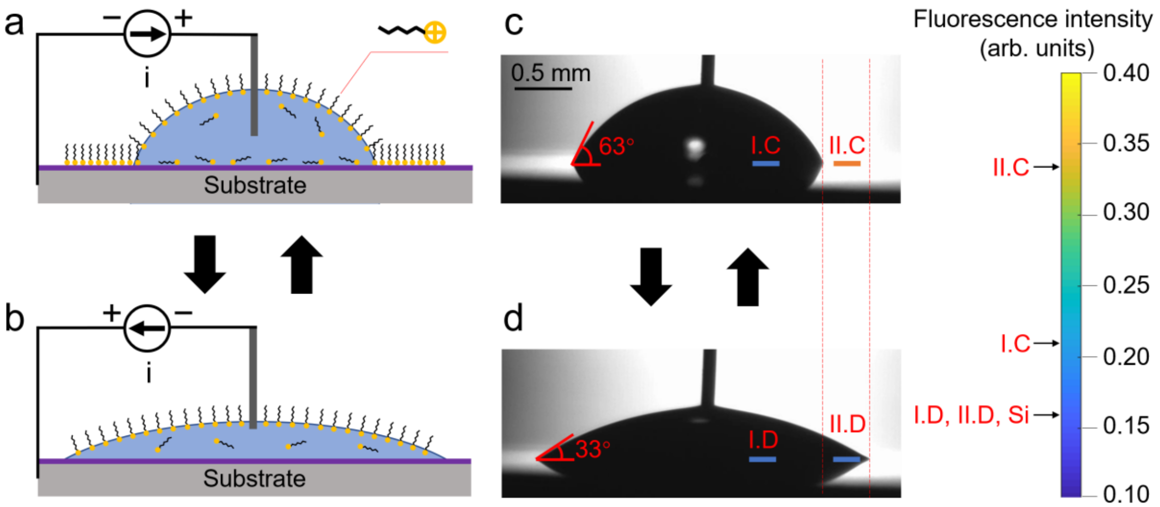

Figure 7-1. The surfactant-mediated electrodewetting mechanism proposed and studied with a wire-inserted sessile drop on a conductive, hydrophilic substrate.

a, For electrodewetting, the electric field inside the liquid between the substrate and wire, established by the small current across a thin oxide (purple line) and through the liquid (blue), draws the ionic surfactant molecules (cationic surfactant is shown) onto the liquid-solid interface, making the droplet dewet (bead up on) the substrate. b, For wetting by active recovery, the opposite electric field by the reverse current removes the ionic surfactant away from the surface, making the droplet wet (spread on) the substrate. For most cases, wetting is also possible by passive recovery, i.e., simply removing the electric signal. c, d, Electrodewetting experiment corresponding to (a) and (b), respectively, with a DTAB-containing aqueous droplet (~3 µL, pH ~7) on bare silicon (with native oxide) using ±3 V with ±3 µA. The surfactant concentrations on two different regions (I, II) of the substrate surface, obtained in a similar but separate test using a fluorescent cationic surfactant, corroborate the proposed mechanism.

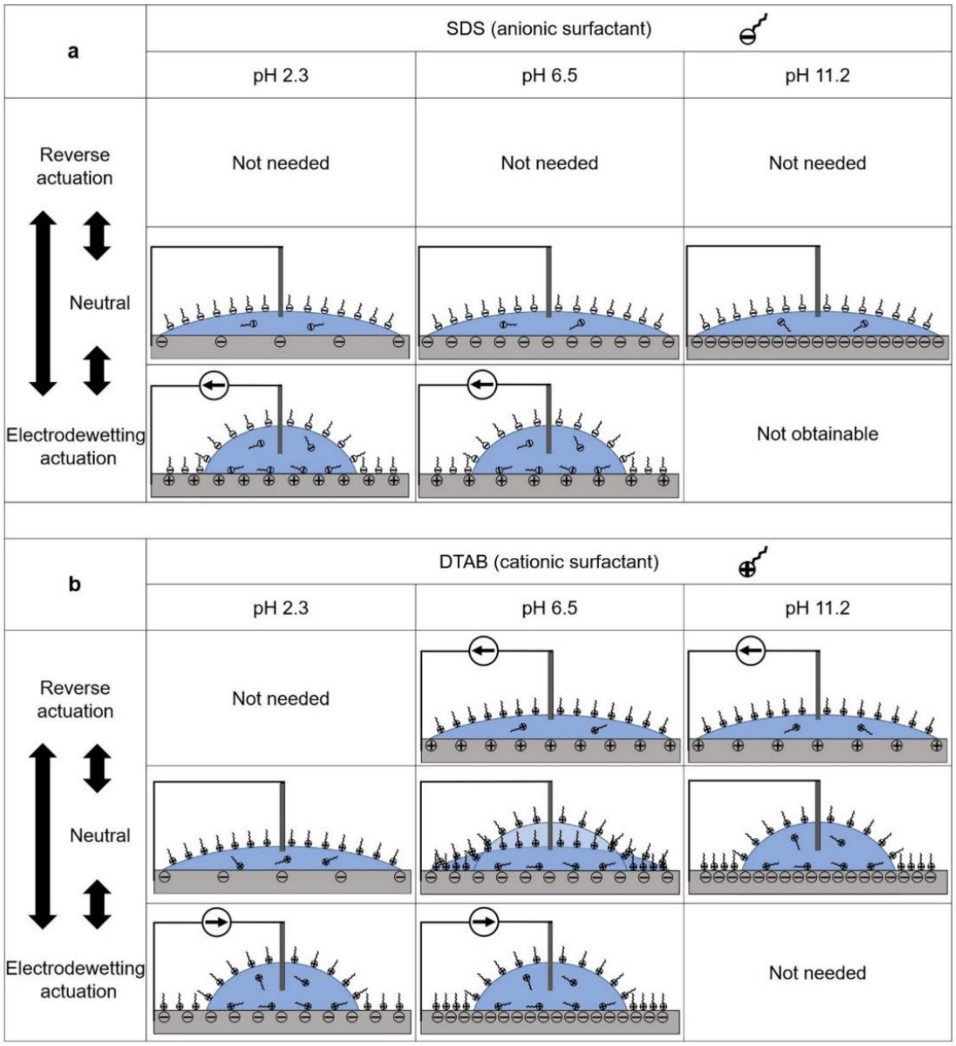

Figure 7-2. Switching between electrodewetting, neutral, and actively-recovered wetting state experimentally confirmed for droplets containing DTAB (cationic surfactant) and SDS (anionic surfactant) on a bare silicon wafer.
The working mechanisms are proposed by schematically illustrating surfactant molecules and surface charges.

Based on our current finding, current is essential and electrodewetting depends on the current. We reason that ionic surfactant requires electric field across the droplet to be migrated onto the surface and the migration of charged particles results in current. If we assume 3 µA of current, which would consume 1.12x10^{-7} mole electrons per hour, it would take ~150 hours to consume 10% of a 3 µL droplet. Considering EWOD actuation duration in typical tasks take less than an hour in most microfluidic applications, we expect the Faradaic reaction to be negligible for most cases. We have performed experiment using thicker (100 nm, thermally grown) oxide. 0-100 V were applied while monitoring the current. We did not observe electrodewetting effect before the 100 nm oxide broke down at ~100 V but observed electrodewetting after the break down. This result experimentally supports the currently understood mechanism.

7.4 Methods

7.4.1 Silicon wafer preparation

For the electrodewetting characterization in this study, we prepared bare silicon wafer in the following manner: piranha clean with 3 parts of 98% sulfuric acid and 1 part of 30% hydrogen peroxide at 110 °C for over 10 min; DI water rinse for 10 min; spin dry; bake on a hot plate at ~450 °C for 15 min to remove excess water and OH- groups40 for a consistent hydrophilicity. This process was used for all wafers including new wafers, i.e., directly out of a factory-sealed package, to ensure all characterization experiments are done on bare silicon of an identical surface condition.

7.4.2 Contact angle measurement

The test setup with the accuracy and repeatability needed to study and characterize electrodewetting is schematically shown in **Figure 7-3**. To induce electrodewetting, a platinum (to avoid oxidation and reduction) wire (100 μm diameter) was inserted vertically into a sessile drop on a conductive (p^{++}, resistivity < 0.005 ohm-cm) silicon wafer (4 inch diameter). Two cameras (Point Grey FL3-U3-13Y3M-C CCD with GO® Edmund VZM™ 200i Zoom Imaging Lens), each mounted on an independent XYZ stage, were used to record the droplet side views, from which contact angles were obtained using ImageJ with DropSnake plugin[38] or an in-house code to assist measuring very low contact angles (< 10°). The wafer was placed on an XY stage, and the wire was attached to a separate Z stage. Before each test, the wire was rinsed in DI water to remove the surfactant left from the previous test. After pipetting a droplet (~3 μL) of surfactant solution onto a fresh wafer, we adjusted the XY stage to center the droplet right below the wire. We then lowered the Z stage to insert the wire into the droplet until the tip of the wire was ~85 μm above the substrate for all tests. The orthogonal views of the droplet by the two cameras were used to assist the user positioning the droplet and wire and later measuring the contact angles. A source measure unit (Keithley 2425 SourceMeter®) was used to apply voltage and monitor the current between the wire and substrate. All the stages were fixed on a vibration-isolation plate to obtain stable images, and all experiments were performed in a Class 1000 modular cleanroom (Terra Universal 12’x8’ Class 1000 Modular Clean Room) to minimize contamination of the fresh silicon surface by the ambient air.

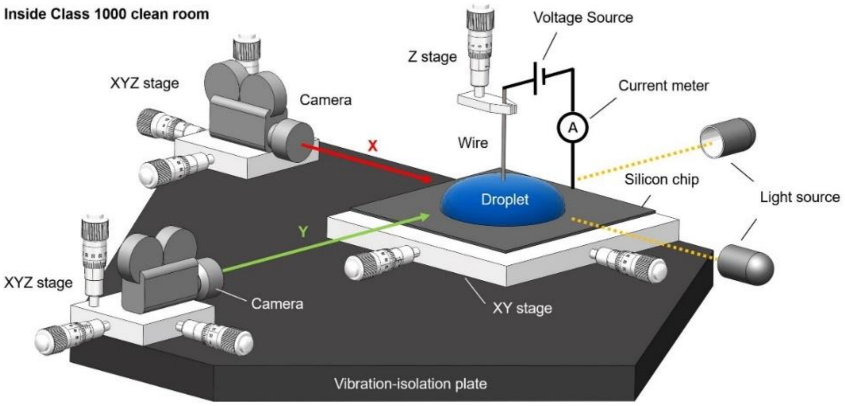

Figure 7-3. Contact angle measurement setup with a wire-droplet system for the current study.
The silicon substrate sits on an XY positioning stage; the wire electrode is attached to a Z positioning stage; and two cameras, each mounted on their own XYZ stage, view two orthogonal sides of the droplet. Drawn not to scale for clarity. All the stages are fixed on a vibration-isolation plate inside a Class 1000 modular clean room.

7.5 Characterization

7.5.1 Avoiding the autophobing effect

The degree of observed electrodewetting may be complicated by the "autophobing" effect [311], which refers to the spontaneous dewetting of a sessile droplet as a result of electrostatic attraction of ionic surfactant to the intrinsic surface charge [312]. Studies showed that adsorption of ionic surfactants on solids can be altered by controlling pH [312]–[314]. On the bare silica surface, increasing pH leads to deprotonation of silanol groups and increase negative surface charge. Under these conditions, cationic surfactants (e.g. CTAB) are increasingly attracted to the surface the higher the pH, resulting in increased amount of autophobing. To reduce autophobing to enable study of the electrodewetting effect in isolation, the pH can be lowered. There is little surface charge below pH ~6, and negligible charge below pH 2. For anionic surfactants, e.g. SDS, there can be some intrinsic adsorption due to hydrophobic interactions, but this can be minimized via increase in pH which leads to electrostatic repulsion. Autophobing was absent at pH 2.3, and the contact-angle change (purely by electrodewetting actuation) at pH 2.3 was smaller than those at pH 11.2 and 6.5, where autophobing effect exists. The use of a low-pH solution enabled us to study electrodewetting with minimal interference by autophobing.

7.5.2 **Electrodewetting of various liquids**

The above fundamental study and microfluidics demonstration were performed using well-controlled water (i.e., low salt concentration) solutions on identically-prepared bare silicon surfaces for scientific rigor. Next, we have explored the validity of electrodewetting for a variety of liquids: two buffer solutions widely used for biological applications – phosphate-buffered saline (PBS) and 2-[4-(2-hydroxyethyl)piperazin-1-yl]ethanesulfonic acid (HEPES); two common organic solvents used in chemistry applications – acetonitrile and dimethyl sulfoxide (DMSO); and ethylene glycol. Although the degree of effectiveness varied as shown in **Figure 7-4**, electrodewetting was found to work for all the tested liquids. We adopted the working liquids in only their typically used conditions in order to assess the utility, leaving more complete characterization of each liquid for future studies. The successful results with these five additional liquids suggest the versatility of the proposed electrodewetting, opening the door for a wide range of application areas.

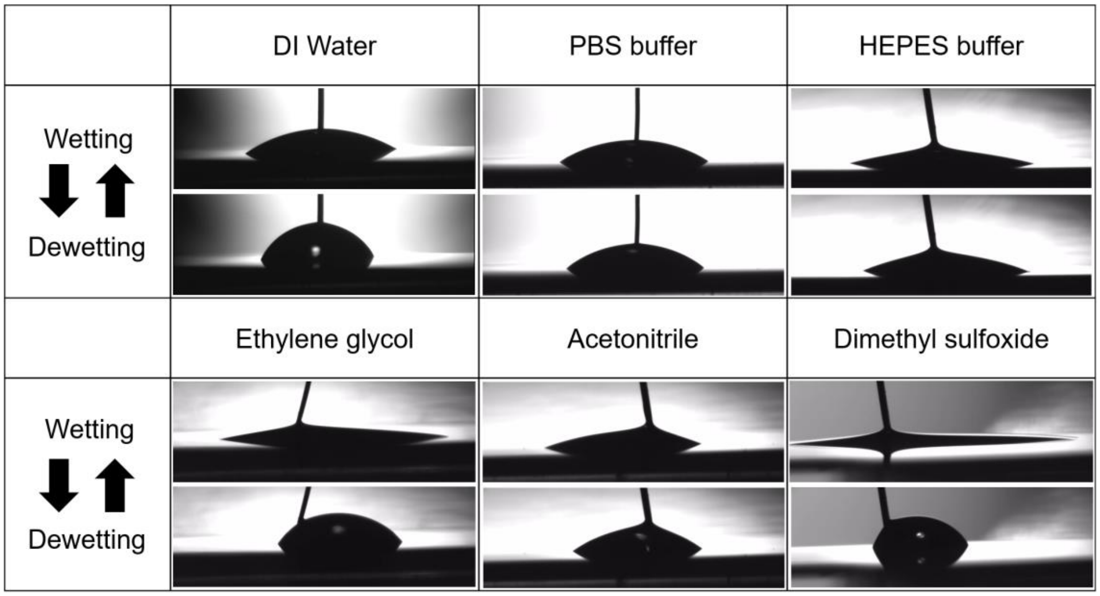

Figure 7-4. Electrodewetting confirmed for a variety of liquids on bare silicon. DI water (Fig. 1) is included as a reference. For PBS and HEPES, we added DTAB to a concentration of 0.15 mM and obtained ~9° and ~6° of contact-angle changes, respectively, using ±5 V. In the cases of ethylene glycol, acetonitrile, and DMSO, we added DTAB to a concentration of 20 mM and obtained ~40°, ~15°, and ~60° of contact-angle changes, respectively, using ±3 V.

7.5.3 Better understanding of electrodewetting using fluorescent surfactant

To visualize the proposed underlying mechanism of the electrodewetting in **Figure 7-1**, we have performed a separate experiment using a droplet containing a fluorescent cationic surfactant found to exhibit electrodewetting behavior similar to (albeit less controllably than) other cationic surfactants used in this study. By blowing the droplet away during dewetting and wetting states (equivalent to **Figure 7-1c** and **d**, respectively) and imaging the resulting dry surface with a fluorescence microscope, we were able to compare the level of surfactant adsorption onto the substrate surface during the two states. The level of surfactant adsorption is expressed as the fluorescent intensity, following the color bar on the right end of **Figure 7-1**. The fluorescent cationic surfactant solution was prepared by dissolving 10 mg of R18 (octadecyl rhodamine B chloride, ThermoFisher Scientific, Waltham, MA, Figure 7-5) in 1 mL of dimethyl sulfoxide (DMSO, Sigma Aldrich) and further diluting with DI water to 0.2 mM. The result was an aqueous solution with ~1.5% DMSO v/v. The pH was adjusted to 2.3 by adding hydrochloric acid (37 wt%).

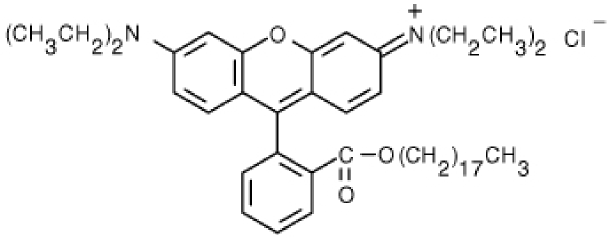

Figure 7-5. Structure of fluorescent surfactant, octadecyl rhodamine B chloride (R18).
Amphiphilic fatty acid contains hydrophobic “tail” and charged hydrophilic “head” with a fluorophore. Molecular formula: $C_{46}H_{67}ClN_2O_3$ (“R18”), Molecular weight: 731.5

A droplet containing R18 showed an apparent autophobing on the silicon surface: upon dispensing onto a fresh silicon substrate, the droplet moved around for a few seconds. To account for this, the wire was inserted into the droplet as soon as it stopped moving. For the color lines I.D and II.D in **Figure 7-1d**, we applied reverse electrodewetting (-5 V to the wire) for 10 seconds, and then the wetting droplet was physically blown away, using a compressed air duster, while the voltage was still on.

The air flow was roughly horizontal on the substrate from the duster tip positioned ~1 cm away from the droplet center. Immediately after blowing the droplet away, fluorescent images of the substrate surface were taken where the droplet had been located. For the color lines I.C and II.C in **Figure 7-1c**, we applied electrodewetting (5 V to the wire) for 10 seconds after reverse electrodewetting (-5 V to the wire) for 10 seconds and gently blew the dewetted droplet away while the electrodewetting (5 V to the wire) was on. We used an inverted fluorescent microscope (Zeiss Axio Observer Z1 with ORCA Flash 4.0 CCD camera, 20x magnification, 2 second exposure, DSRED filter) to acquire the fluorescent images on the substrate surface.

7.5.3.1 Reverse voltage for more repeatable and efficient actuation

Electrodewetting tests with a fluorescent amphiphilic fatty acid surfactant R18 (used in **Figure 7-1**) are elaborated to explain the surfactant clean-up process during a recovery-to-wetting step by reverse voltage after electrodewetting. Unlike a sessile droplet containing a regular ionic surfactant, a sessile droplet containing R18 electrodewetted and recovered to wetting with poor axisymmetry and repeatability. The droplet moved around despite the wire, and the contact line did not recede (dewet) and advance (wet) around a fixed central position on the surface when repeated. Thus, in **Figure 7-6** we show only three steps towards three states: reverse actuation (Step 1) actively recovered the droplet to a wetting state (State 1); electrodewetting actuation (Step 2) electrodewetted the droplet to a dewetting state (State 2); reverse actuation (Step 3) actively recovered the droplet to another wetting state (State 3). The droplet containing R18 exhibited severe autophobing compared with the droplets containing the other surfactants used in this study (DTAB, TTAB, CTAB, and SDS). The severe autophobing, which apparently caused the poor axisymmetry and repeatability above, might be explained by the high hydrophobicity and low solubility of R18, resulting from the hydrophobicity of both its hydrocarbon “tail” and the bulky fluorescent group near the “head” region. Therefore, even if there was not much electrostatic interaction between the substrate and the cationic “head” of R18 at pH 2.3, where autophobing was not found for the case of DTAB, there could be a tendency for excess R18 molecules at the interfaces (especially near the triple-contact line), “propelling” or pushing the droplet around. Despite the limitation, the fluorescent intensities shown at the bottom of **Figure 7-1** indicates the reverse actuation (Step 3) was effective in cleaning up the surfactant molecules left outside the droplet during the preceding dewetting (Step 2). Despite the poor electrodewetting performance with R18, this three-step exercise nevertheless helps explain how the reverse actuation assists returning an electrodewetted surface back to the natural, wetted state.

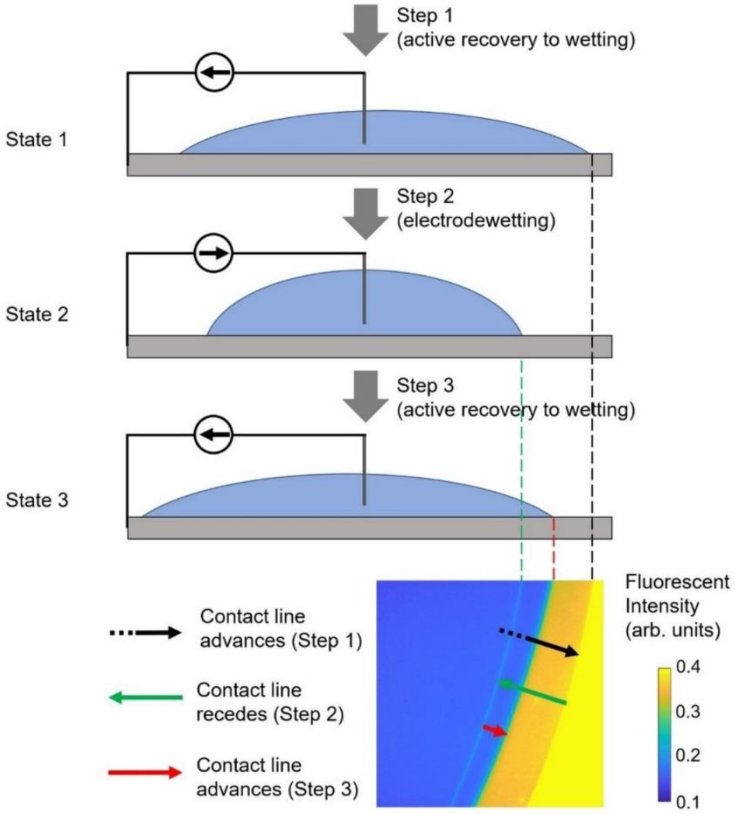

Figure 7-6. Surfactant concentration on substrate surface during electrodewetting and reverse electrodewetting revealed by a blow-off test.
A water droplet with ionic fluorescent surfactant was electrically actuated to wet, dewet, and wet the surface successively, as illustrated in the three sideview schematics (top portion of the figure). The top-view fluorescent image (bottom right) reveals the surfactant molecules left on the

substrate surface after the droplet was blown away while actuation was on. The fluorescent image is color-enhanced. The surface outside the droplet has a high concentration of surfactant due to autophobing after the droplet was initially placed on the fresh surface. Step 1 lets the droplet wet the surface, i.e., natural state, by applying reverse electrodewetting. The contact line advances to the black dashed line drawn in the sideview schematics, corresponding to the black arrow in the fluorescent image. Step 2 lets the droplet dewet the surface by applying electrodewetting. The contact line retreats to the green dashed line drawn in the sideview schematics, corresponding to the green arrow in the fluorescent image. Step 3 lets the droplet wet the surface again by applying reverse electrodewetting. The contact line advances to the red dashed line drawn in the sideview schematics, corresponding to the red arrow in the fluorescent image.

7.5.3.2 Confocal imaging

To better visualize the distribution of surfactant within the droplet under the influence of an applied electrical field, we also explored confocal fluorescence microscopy. 3 µl of 0.2 mM R18 (dissolved in DI water) was placed on Si wafer (**Figure 7-7A**). Using a X-Z scanning mode (line scanning along z-axis, optical sectioning thickness: 0.992 µm), images of the droplet were recorded with an inverted confocal microscope (SP8-SMD, Leica, Wetzlar, Germany). When there is no voltage applied, the majority of R18 molecules (i.e. brightest area in the image) was observed near the droplet-air interface (**Figure 7-7B**). When the voltage was applied, however, a higher intensity of fluorescent signal was observed near the droplet-substrate interface. This is consistent with the hypothesis that applied voltage leads to migration and adsorption of cationic surfactant to the surface, while removal or reversal of voltage allows the surfactant to diffuse away from the interface.

We noticed that continuous vertical movements of the microscope stage during the X-Z scanning mode caused significant vibration of the droplet, potentially leading to mixing in the droplet. Further study using 3D confocal microscopy and confocal microscopy over a larger fraction of the droplet in the future could lead to additional insight and clarification about the distribution of the surfactant, especially if such imaging could be performed in real-time as the droplet was actuated between wetting and dewetting states.

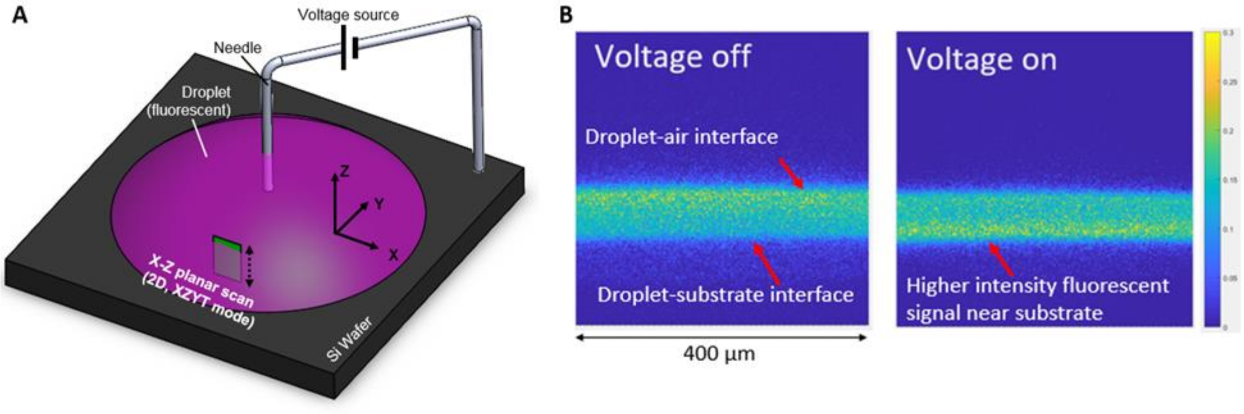

Figure 7-7. Confocal imaging of fluorescent droplet
(A) Chip setup for confocal imaging: 3 µL R18 droplet placed on Si wafer, (B) Snap shots of X-Z scanning (stacking) showing the distribution of surfactants with the presence of applied voltage.

7.6 Demonstration of droplet manipulation on digital microfluidic chip

7.6.1.1 To assess the potential for sophisticated digital microfluidic applications, we have developed an electrodewetting device. Using proper actuation sequences and 0.2 mM DTAB solution, we have achieved droplet generation, transportation, splitting, and merging. Although pH 2.3 solution was used for **Figure 7-8**, any pH level works for electrodewetting. Building blocks for more complex microfluidic protocols for applications, these basic droplet logic operations were successfully obtained in air, i.e., without the help of the commonly-used filler oil, on an open device, i.e., without using a cover plate. While in-air operations are more difficult than in-oil but still possible, open-device operations of generating or splitting droplets is not possible with EWOD. Furthermore, the droplets were transported (**Figure 7-8b**) in a speed comparable to EWOD despite the 10-100 times slower actuation observed during sessile drop tests. This unique performance of electrodewetting suggests its microfluidic operation comparable to EWOD in addition to the inherent reliability.

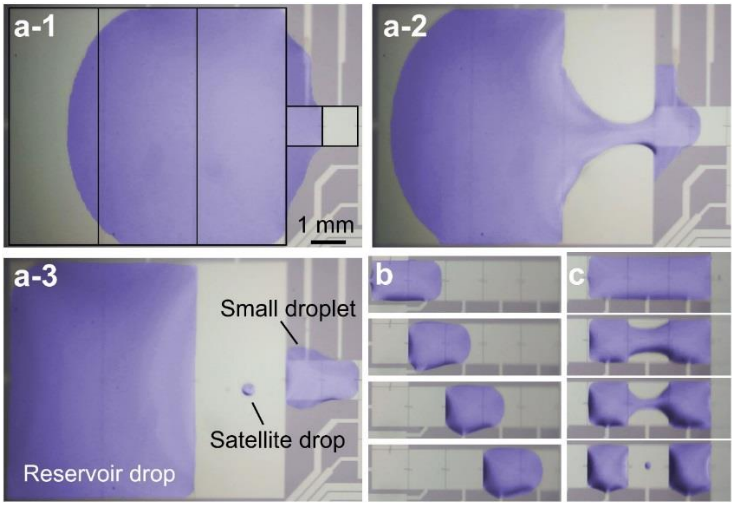

Figure 7-8. Droplet generation, transportation, and splitting realized by electrodewetting.
Water droplets are operated in air on a silicon device with no cover plate, using ±2.5 V (or 0 and 5 V). Images were captured from Video 4 and enhanced by coloring the liquid portions. **a,** Sequential images of a small (~0.2 µL) droplet generated from a reservoir droplet (~3 µL). **a-1,** The added black lines indicate the large electrodes underneath the reservoir. **a-2,** Dewetting the third reservoir electrode from left results in necking of the reservoir droplet. **a-3,** A droplet is generated on the two small electrodes to the right of the reservoir. **b, c,** Four sequential images showing droplet transportation and splitting. Along with **a** and merging (not shown), they establish the basis for digital microfluidics.

8. References

[1] G. Mariani *et al.*, “A review on the clinical uses of SPECT/CT,” *Eur J Nucl Med Mol Imaging*, vol. 37, no. 10, pp. 1959–1985, Oct. 2010.

[2] M. E. Phelps, *PET: Molecular Imaging and Its Biological Applications*, 1st ed. Berlin, Germany: Springer Science & Business Media, 2004.

[3] M. E. Phelps, “PET: The Merging of Biology and Imaging into Molecular Imaging,” *J Nucl Med*, vol. 41, no. 4, pp. 661–681, 2000.

[4] A. Bansal *et al.*, “Novel 89Zr cell labeling approach for PET-based cell trafficking studies,” *EJNMMI Research*, vol. 5, no. 1, p. 19, Mar. 2015.

[5] A. W. J. M. Glaudemans, E. F. J. de Vries, F. Galli, R. A. J. O. Dierckx, R. H. J. A. Slart, and A. Signore, “The Use of 18F-FDG-PET/CT for Diagnosis and Treatment Monitoring of Inflammatory and Infectious Diseases,” *Clinical and Developmental Immunology*, vol. 2013, pp. 1–14, Aug. 2013.

[6] F. Buckingham *et al.*, “Organomediated Enantioselective 18F Fluorination for PET Applications,” *Angew. Chem. Int. Ed.*, vol. 54, no. 45, pp. 13366–13369, Nov. 2015.

[7] D. L. Bailey and K. P. Willowson, “An Evidence-Based Review of Quantitative SPECT Imaging and Potential Clinical Applications,” *J Nucl Med*, vol. 54, no. 1, pp. 83–89, Jan. 2013.

[8] I. M. Jackson, P. J. H. Scott, and S. Thompson, “Clinical Applications of Radiolabeled Peptides for PET,” *Seminars in Nuclear Medicine*.

[9] M. M. Khalil, J. L. Tremoleda, T. B. Bayomy, and W. Gsell, “Molecular SPECT Imaging: An Overview,” *International Journal of Molecular Imaging*, 2011. [Online]. Available: https://www.hindawi.com/journals/ijmi/2011/796025/abs/. [Accessed: 19-Aug-2017].

[10] R. Bejot and V. Gouverneur, “18F-Radionuclide Chemistry,” in *Fluorine in Pharmaceutical and Medicinal Chemistry: From Biophysical Aspects to Clinical Applications*, V. Gouverneur and K. Muller, Eds. London: Imperial College Press, 2012, pp. 335–382.

[11] S. Banister, D. Roeda, F. Dolle, and M. Kassiou, “Fluorine-18 Chemistry for PET: A Concise Introduction,” *Current Radiopharmaceuticals*, vol. 3, no. 2, pp. 68–80, Apr. 2010.

[12] J. Czernin and M. E. Phelps, “Positron emission tomography scanning: current and future applications,” *Annu. Rev. Med.*, vol. 53, pp. 89–112, 2002.

[13] L. Cai, S. Lu, and V. W. Pike, “Chemistry with [18F]Fluoride Ion,” *European Journal of Organic Chemistry*, vol. 2008, no. 17, pp. 2853–2873, Jun. 2008.

[14] T. Ramenda, J. Steinbach, and F. Wuest, “4-[18F]Fluoro-N-methyl-N-(propyl-2-yn-1-yl)benzenesulfonamide ([18F]F-SA): a versatile building block for labeling of peptides, proteins and oligonucleotides with fluorine-18 via Cu(I)-mediated click chemistry,” *Amino Acids*, vol. 44, no. 4, pp. 1167–1180, Apr. 2013.

[15] W. A. Weber and R. Figlin, “Monitoring Cancer Treatment with PET/CT: Does It Make a Difference?,” *J Nucl Med*, vol. 48, no. 1_suppl, pp. 36S – 44, Jan. 2007.

[16] P. Marchand, V. Bekaert, A. Ouadi, P. Laquerriere, D. Brasse, and H. Curien, “Forty Years of 18F-Labeled Compound Development in an Open Access Database,” *J Nucl Med*, vol. 54, no. 1, pp. 15N-17N, Jan. 2013.

[17] “Radiosynthesis Database of PET Probes (RaDaP).” [Online]. Available: http://www.nirs.qst.go.jp/research/division/mic/db2/. [Accessed: 08-May-2017].

[18] P. D. Shreve, Y. Anzai, and R. L. Wahl, “Pitfalls in Oncologic Diagnosis with FDG PET Imaging: Physiologic and Benign Variants,” *RadioGraphics*, vol. 19, no. 1, pp. 61–77, Jan. 1999.

[19] K. A. Zettlitz, R. Tavaré, S. M. Knowles, K. K. Steward, J. M. Timmerman, and A. M. Wu, “ImmunoPET of Malignant and Normal B Cells with 89Zr- and 124I-Labeled

Obinutuzumab Antibody Fragments Reveals Differential CD20 Internalization In Vivo," *Clin Cancer Res*, vol. 23, no. 23, pp. 7242–7252, Dec. 2017.
[20] P. Y. Keng and R. M. van Dam, "Digital Microfluidics: A New Paradigm for Radiochemistry," *Mol. Imag.*, vol. 14, pp. 579–594, 2015.
[21] P. Y. Keng, M. Esterby, and R. M. van Dam, "Emerging Technologies for Decentralized Production of PET Tracers," in *Positron Emission Tomography - Current Clinical and Research Aspects*, C.-H. Hsieh, Ed. Rijeka, Croatia: InTech, 2012, pp. 153–182.
[22] J. Wang, P. H. Chao, S. Hanet, and R. M. van Dam, "Performing multi-step chemical reactions in microliter-sized droplets by leveraging a simple passive transport mechanism," *Lab Chip*, vol. 17, no. 24, pp. 4342–4355, Dec. 2017.
[23] P. Y. Keng, M. Sergeev, and R. M. van Dam, "Advantages of Radiochemistry in Microliter Volumes," in *Perspectives on Nuclear Medicine for Molecular Diagnosis and Integrated Therapy*, Y. Kuge, T. Shiga, and N. Tamaki, Eds. Springer Japan, 2016, pp. 93–111.
[24] G. Pascali, P. Watts, and P. Salvadori, "Microfluidics in radiopharmaceutical chemistry," *Nuclear Medicine and Biology*, vol. 40, no. 6, pp. 776–787, Aug. 2013.
[25] A. Lebedev, "Microfluidic devices for radio chemical synthesis," in *Microfluidic Devices for Biomedical Applications*, X. J. Li and Y. Zhou, Eds. Cambridge: Woodhead Publishing, 2013, pp. 594–633.
[26] P. W. Miller, A. J. deMello, and A. D. Gee, "Application of Microfluidics to the Ultra-Rapid Preparation of Fluorine-18 Labelled Compounds," *Current Radiopharmaceuticals*, vol. 3, pp. 254–262, 2010.
[27] P. Y. Keng *et al.*, "Optimization of radiosynthesis of molecular tracers in EWOD microfluidic chip," in *Proceedings of the Fourteenth International Conference on Miniaturized Systems for Chemistry and Life Sciences*, Groningen, The Netherlands, 2010, pp. 668–670.
[28] G. Pascali, G. Nannavecchia, S. Pitzianti, and P. A. Salvadori, "Dose-on-demand of diverse 18F-fluorocholine derivatives through a two-step microfluidic approach," *Nuclear Medicine and Biology*, vol. 38, no. 5, pp. 637–644, Jul. 2011.
[29] S. Archibald, N. Pamme, N. Brown, and M. Tarn, "Integrated microfluidic lab-on-a-chip systems for 18F radiotracer synthesis, purification and quality control," *J Nucl Med*, vol. 56, no. supplement 3, pp. 167–167, May 2015.
[30] K. Lisova *et al.*, "Microscale radiosynthesis, preclinical imaging and dosimetry study of [18F]AMBF3-TATE: A potential PET tracer for clinical imaging of somatostatin receptors," *Nuclear Medicine and Biology*, vol. 61, pp. 36–44, Jun. 2018.
[31] P. H. Chao, M. Lazari, S. Hanet, M. K. Narayanam, J. M. Murphy, and R. M. van Dam, "Automated concentration of [18F]fluoride into microliter volumes," *Applied Radiation and Isotopes*, vol. 141, pp. 138–148, Nov. 2018.
[32] P. H. Chao, J. Collins, J. P. Argus, W.-Y. Tseng, J. T. Lee, and R. M. van Dam, "Automatic concentration and reformulation of PET tracers via microfluidic membrane distillation," *Lab Chip*, vol. 17, no. 10, pp. 1802–1816, May 2017.
[33] J. Ly, N. S. Ha, S. Cheung, and R. M. van Dam, "Toward miniaturized analysis of chemical identity and purity of radiopharmaceuticals via microchip electrophoresis," *Anal Bioanal Chem*, vol. 410, no. 9, pp. 2423–2436, Mar. 2018.
[34] E. Fermi, "Quality Control of PET Radiopharmaceuticals," in *Molecular Imaging: Radiopharmaceuticals for PET and SPECT*, Springer Berlin Heidelberg, 2009, pp. 197–204.
[35] P. J. H. Scott and B. G. Hockley, *Radiochemical Syntheses, Radiopharmaceuticals for Positron Emission Tomography*. Hoboken, NJ, USA: John Wiley & Sons, 2011.
[36] U.S. Pharmacopeia (USP), "General Chapter <823>: Positron Emission Tomography Drugs for Compounding, Investigation, and Research Uses." USP: Rockville, MD, USA, Nov-2011.

[37] "CFR - Code of Federal Regulations Title 21." [Online]. Available: http://www.accessdata.fda.gov/scripts/cdrh/cfdocs/cfcfr/CFRSearch.cfm. [Accessed: 30-Jun-2013].

[38] European directorate for the quality of medicines & healthcare, "Technical guide for the elaboration of monographs on radiopharmaceutical preparations." European Pharmacopeia, Edition-2010.

[39] J. C. Hung, "Comparison of Various Requirements of the Quality Assurance Procedures for 18F-FDG Injection*," *Journal of Nuclear Medicine*, vol. 43, no. 11, pp. 1495–1506, Nov. 2002.

[40] S. Yu, "Review of 18F-FDG synthesis and quality control," *Biomed Imaging Interv J*, vol. 2, no. 4, p. e57, 2006.

[41] F. Lodi and S. Boschi, "Quality Control of PET Radiopharmaceuticals," in *Basic Science of PET Imaging*, Springer, Cham, 2017, pp. 105–126.

[42] D. Ferguson, S. McGrath, G. O'Hara, and C. Marshall, "Investigation of staff finger doses during quality control of FDG production," *Health Physics*, vol. 100, no. 5, pp. 523–529, May 2011.

[43] QC1, "Automatic quality control for PET and MI tracers," *http://www.qc1.com*. [Online]. Available: http://www.qc1.com/. [Accessed: 20-Nov-2017].

[44] "Trace-ability, Inc. - SBIR Source," *SBIRSource.com*. [Online]. Available: http://sbirsource.com/sbir/firms/26162-trace-ability-inc. [Accessed: 26-Dec-2015].

[45] A. I. Anzellotti, A. R. McFarland, D. Ferguson, and K. F. Olson, "Towards the Full Automation of QC Release Tests for [18F]fluoride-labeled Radiotracers," *Current Organic Chemistry*, vol. 17, no. 19, pp. 2153–2158, Oct. 2013.

[46] V. Awasthi *et al.*, "A 'dose on demand' Biomarker Generator for automated production of [18F]F− and [18F]FDG," *Applied Radiation and Isotopes*, vol. 89, pp. 167–175, Jul. 2014.

[47] A. M. Elizarov *et al.*, "Design and Optimization of Coin-Shaped Microreactor Chips for PET Radiopharmaceutical Synthesis," *J Nucl Med*, vol. 51, no. 2, pp. 282–287, Feb. 2010.

[48] C. Rensch *et al.*, "Microfluidics: A Groundbreaking Technology for PET Tracer Production?," *Molecules*, vol. 18, no. 7, pp. 7930–7956, Jul. 2013.

[49] G. M. Whitesides, "The origins and the future of microfluidics," *Nature*, vol. 442, no. 7101, pp. 368–373, Jul. 2006.

[50] O. H. Hansteen *et al.*, "Quality Control Devices and Methods for Radiopharmaceuticals," US9291606B2, 22-Mar-2016.

[51] M. D. Tarn, A. Isu, S. J. Archibald, and N. Pamme, "On-chip absorbance spectroscopy for the determination of optical clarity and pH for the quality control testing of [18F]FDG radiotracer," in *Proceedings of the 18th International Conference on Miniaturized Systems for Chemistry and Life Sciences*, San Antonio, TX, 2014, pp. 1077–1079.

[52] C. M. Rushworth, J. Davies, J. T. Cabral, P. R. Dolan, J. M. Smith, and C. Vallance, "Cavity-enhanced optical methods for online microfluidic analysis," *Chemical Physics Letters*, vol. 554, pp. 1–14, Dec. 2012.

[53] M. I. Khan, K. Mukherjee, R. Shoukat, and H. Dong, "A review on pH sensitive materials for sensors and detection methods," *Microsyst Technol*, vol. 23, no. 10, pp. 4391–4404, Oct. 2017.

[54] H. Maruyama, F. Arai, and T. Fukuda, "On-chip pH measurement using functionalized gel-microbeads positioned by optical tweezers," *Lab Chip*, vol. 8, no. 2, pp. 346–351, 2008.

[55] A. Q. Maclin, M. D. Kim, S. A. Dergunov, E. Pinkhassik, and E. Lindner, "Small-Volume pH Sensing with a Capillary Optode Utilizing Dye-Loaded Porous Nanocapsules in a Hydrogel Matrix," *Electroanalysis*, vol. 27, no. 3, pp. 733–744, Mar. 2015.

[56] P. Mela *et al.*, “Monolayer-functionalized microfluidics devices for optical sensing of acidity,” *Lab on a Chip*, vol. 5, no. 2, pp. 163–170, 2005.
[57] L. Florea *et al.*, “Dynamic pH mapping in microfluidic devices by integrating adaptive coatings based on polyaniline with colorimetric imaging techniques,” *Lab on a Chip*, vol. 13, no. 6, pp. 1079–1085, 2013.
[58] A. Richter, G. Paschew, S. Klatt, J. Lienig, K.-F. Arndt, and H.-J. P. Adler, “Review on Hydrogel-based pH Sensors and Microsensors,” *Sensors*, vol. 8, no. 1, pp. 561–581, Jan. 2008.
[59] Q. Thong Trinh, G. Gerlach, J. Sorber, and K.-F. Arndt, “Hydrogel-based piezoresistive pH sensors: Design, simulation and output characteristics,” *Sensors and Actuators B: Chemical*, vol. 117, no. 1, pp. 17–26, Sep. 2006.
[60] J. Z. Hilt, A. K. Gupta, R. Bashir, and N. A. Peppas, “Ultrasensitive Biomems Sensors Based on Microcantilevers Patterned with Environmentally Responsive Hydrogels,” *Biomedical Microdevices*, vol. 5, no. 3, pp. 177–184, Sep. 2003.
[61] C.-F. Lin, G.-B. Lee, C.-H. Wang, H.-H. Lee, W.-Y. Liao, and T.-C. Chou, “Microfluidic pH-sensing chips integrated with pneumatic fluid-control devices,” *Biosensors and Bioelectronics*, vol. 21, no. 8, pp. 1468–1475, Feb. 2006.
[62] A. Yamada and M. Suzuki, “A Microfluidic pH Measurement Device with a Flowing Liquid Junction,” *Sensors*, vol. 17, no. 7, p. 1563, Jul. 2017.
[63] Food and Drug Administration, HHS, “Current good manufacturing practice for positron emission tomography drugs,” *Fed Regist*, vol. 74, no. 236, pp. 65409–65436, Dec. 2009.
[64] U.S. Pharmacopeia (USP), “General Chapters: <71> Sterility Tests.” 2011.
[65] A. M. Foudeh, T. F. Didar, T. Veres, and M. Tabrizian, “Microfluidic designs and techniques using lab-on-a-chip devices for pathogen detection for point-of-care diagnostics,” *Lab Chip*, vol. 12, no. 18, pp. 3249–3266, Aug. 2012.
[66] H. Bridle, B. Miller, and M. P. Y. Desmulliez, “Application of microfluidics in waterborne pathogen monitoring: A review,” *Water Research*, vol. 55, no. Supplement C, pp. 256–271, May 2014.
[67] D. Brandão, S. Liébana, and M. I. Pividori, “Multiplexed detection of foodborne pathogens based on magnetic particles,” *New Biotechnology*, vol. 32, no. 5, pp. 511–520, Sep. 2015.
[68] J. Mairhofer, K. Roppert, and P. Ertl, “Microfluidic Systems for Pathogen Sensing: A Review,” *Sensors*, vol. 9, no. 6, pp. 4804–4823, Jun. 2009.
[69] J. H. Jung, G.-Y. Kim, and T. Seok Seo, “An integrated passive micromixer– magnetic separation – capillary electrophoresis microdevice for rapid and multiplex pathogen detection at the single-cell level,” *Lab on a Chip*, vol. 11, no. 20, pp. 3465–3470, 2011.
[70] A. W. Lantz, Y. Bao, and D. W. Armstrong, “Single-Cell Detection: Test of Microbial Contamination Using Capillary Electrophoresis,” *Anal. Chem.*, vol. 79, no. 4, pp. 1720–1724, Feb. 2007.
[71] T. Sun and H. Morgan, “Single-cell microfluidic impedance cytometry: a review,” *Microfluid Nanofluid*, vol. 8, no. 4, pp. 423–443, Apr. 2010.
[72] M. Varshney and Y. Li, “Interdigitated array microelectrodes based impedance biosensors for detection of bacterial cells,” *Biosensors and Bioelectronics*, vol. 24, no. 10, pp. 2951–2960, Jun. 2009.
[73] N. Haandbæk, O. With, S. C. Bürgel, F. Heer, and A. Hierlemann, “Resonance-enhanced microfluidic impedance cytometer for detection of single bacteria,” *Lab on a Chip*, vol. 14, no. 17, pp. 3313–3324, 2014.
[74] U.S. Pharmacopeia (USP), “General Chapters: <85> Bacterial Endotoxin Test.” .
[75] A. P. Das, P. S. Kumar, and S. Swain, “Recent advances in biosensor based endotoxin detection,” *Biosensors and Bioelectronics*, vol. 51, pp. 62–75, Jan. 2014.

[76] Charles River Laboratories, Inc., “Endotoxin Testing Systems.” [Online]. Available: http://www.criver.com/products-services/rapid-micro/endosafe/endotoxin-rapid-testing-systems. [Accessed: 16-Sep-2017].

[77] C. W. Suh *et al.*, “Feasibility of on-chip detection of endotoxin by LAL test,” *Biotechnol Bioproc E*, vol. 9, no. 2, pp. 132–136, Apr. 2004.

[78] P. Miao, K. Han, J. Qi, C. Zhang, and T. Liu, “Electrochemical investigation of endotoxin induced limulus amebocyte lysate gel-clot process,” *Electrochemistry Communications*, vol. 26, no. Supplement C, pp. 29–32, Jan. 2013.

[79] K. Noda, H. Goto, Y. Murakami, A. B. F. Ahmed, and A. Kuroda, “Endotoxin assay by bioluminescence using mutant firefly luciferase,” *Analytical Biochemistry*, vol. 397, no. 2, pp. 152–155, Feb. 2010.

[80] W. Su, M. Lin, H. Lee, M. Cho, W.-S. Choe, and Y. Lee, “Determination of endotoxin through an aptamer-based impedance biosensor,” *Biosensors and Bioelectronics*, vol. 32, no. 1, pp. 32–36, Feb. 2012.

[81] L. Makszin, A. Kilár, P. Felső, Z. Péterfi, B. Kocsis, and F. Kilár, “Quantitative microfluidic analysis of S- and R-type endotoxin components with chip capillary electrophoresis,” *ELECTROPHORESIS*, vol. 33, no. 22, pp. 3351–3360, Nov. 2012.

[82] D. Franck, H. Nann, P. Davi, P. A. Schubiger, and S. M. Ametamey, “Faster analysis of radiopharmaceuticals using ultra performance liquid chromatography (UPLC®) in combination with low volume radio flow cell,” *Applied Radiation and Isotopes*, vol. 67, no. 6, pp. 1068–1070, Jun. 2009.

[83] D. Kryza and M. Janier, “Radio-UHPLC: A tool for rapidly determining the radiochemical purity of technetium-99m radiopharmaceuticals?,” *Applied Radiation and Isotopes*, vol. 78, pp. 72–76, Aug. 2013.

[84] D. S. Reichmuth, T. J. Shepodd, and B. J. Kirby, “Microchip HPLC of Peptides and Proteins,” *Anal. Chem.*, vol. 77, no. 9, pp. 2997–3000, 2005.

[85] “Agilent | HPLC-Chip/MS System Solutions.” [Online]. Available: http://www.agilent.com/en-us/products/liquid-chromatography/low-flow-lc-systems/1260-infinity-hplc-chip-ms-system/gp42776. [Accessed: 18-Oct-2017].

[86] J. Šesták, D. Moravcová, and V. Kahle, “Instrument platforms for nano liquid chromatography,” *Journal of Chromatography A*, vol. 1421, no. Supplement C, pp. 2–17, Nov. 2015.

[87] H. Yin and K. Killeen, “The fundamental aspects and applications of Agilent HPLC-Chip,” *J. Sep. Science*, vol. 30, no. 10, pp. 1427–1434, Jul. 2007.

[88] E. R. Castro and A. Manz, “Present state of microchip electrophoresis: State of the art and routine applications,” *Journal of Chromatography A*, vol. 1382, pp. 66–85, Feb. 2015.

[89] A. P. Lewis *et al.*, “Review on the development of truly portable and in-situ capillary electrophoresis systems,” *Meas. Sci. Technol.*, vol. 24, no. 4, p. 042001, Apr. 2013.

[90] D. Janasek, J. Franzke, and A. Manz, “Scaling and the design of miniaturized chemical-analysis systems,” *Nature*, vol. 442, no. 7101, pp. 374–380, Jul. 2006.

[91] S. Ahuja and M. Jimidar, *Capillary Electrophoresis Methods for Pharmaceutical Analysis*. Amsterdam, The Netherlands: Elsevier, 2011.

[92] G. G. Mironov, C. M. Clouthier, A. Akbar, J. W. Keillor, and M. V. Berezovski, “Simultaneous analysis of enzyme structure and activity by kinetic capillary electrophoresis-MS,” *Nat Chem Biol*, vol. advance online publication, Sep. 2016.

[93] G. G. Morbioli, T. Mazzu-Nascimento, A. Aquino, C. Cervantes, and E. Carrilho, “Recombinant drugs-on-a-chip: The usage of capillary electrophoresis and trends in miniaturized systems – A review,” *Analytica Chimica Acta*, vol. 935, pp. 44–57, Sep. 2016.

[94] N. S. Ha, J. Ly, J. Jones, S. Cheung, and R. M. van Dam, “Novel volumetric method for highly repeatable injection in microchip electrophoresis,” *Analytica Chimica Acta*, vol. 985, pp. 129–140, Sep. 2017.

[95] M. C. Breadmore *et al.*, “Recent advances in enhancing the sensitivity of electrophoresis and electrochromatography in capillaries and microchips (2010–2012),” *ELECTROPHORESIS*, vol. 34, no. 1, pp. 29–54, Jan. 2013.

[96] U. Holzgrabe, D. Brinz, S. Kopec, C. Weber, and Y. Bitar, “Why not using capillary electrophoresis in drug analysis?,” *Electrophoresis*, vol. 27, no. 12, pp. 2283–2292, 2006.

[97] D. Kaniansky *et al.*, “On-column radiometric detector for capillary isotachophoresis,” *Journal of Radioanalytical and Nuclear Chemistry, Articles*, vol. 129, no. 2, pp. 305–325, Feb. 1989.

[98] D. Kaniansky, P. Rajec, A. Švec, P. Havaši, and F. Macášek, “On-line radiometric detection in capillary isotachophoresis,” *Journal of Chromatography A*, vol. 258, pp. 238–243, Jan. 1983.

[99] S. L. Pentoney, R. N. Zare, and J. F. Quint, “On-line radioisotope detection for capillary electrophoresis,” *Anal. Chem.*, vol. 61, no. 15, pp. 1642–1647, Aug. 1989.

[100] K. D. Altria, C. F. Simpson, A. K. Bharij, and A. E. Theobald, “A gamma-ray detector for capillary zone electrophoresis and its use in the analysis of some radiopharmaceuticals,” *Electrophoresis*, vol. 11, no. 9, pp. 732–734, Sep. 1990.

[101] R. Jankowsky, B. Noll, and B. Johannsen, “Capillary electrophoresis of 99mtechnetium radiopharmaceuticals,” *Journal of Chromatography B: Biomedical Sciences and Applications*, vol. 724, no. 2, pp. 365–371, Mar. 1999.

[102] S. Cheung, J. Ly, M. Lazari, S. Sadeghi, P. Y. Keng, and R. M. van Dam, “The separation and detection of PET tracers via capillary electrophoresis for chemical identity and purity analysis,” *Journal of Pharmaceutical and Biomedical Analysis*, vol. 94, pp. 12–18, Jun. 2014.

[103] A. L. Bowen and R. S. Martin, “Integration of on-chip peristaltic pumps and injection valves with microchip electrophoresis and electrochemical detection,” *Electrophoresis*, vol. 31, no. 15, pp. 2534–2540, Aug. 2010.

[104] P. Kubáň and P. C. Hauser, “Effects of the cell geometry and operating parameters on the performance of an external contactless conductivity detector for microchip electrophoresis,” *Lab on a Chip*, vol. 5, no. 4, pp. 407–415, 2005.

[105] P. Kubáň and P. C. Hauser, “A review of the recent achievements in capacitively coupled contactless conductivity detection,” *Analytica Chimica Acta*, vol. 607, no. 1, pp. 15–29, Jan. 2008.

[106] P. Kubáň and P. C. Hauser, “Ten years of axial capacitively coupled contactless conductivity detection for CZE - a review,” *ELECTROPHORESIS*, vol. 30, no. 1, pp. 176–188, 2009.

[107] A. E. Bruno, B. Krattiger, F. Maystre, and H. M. Widmer, “On-column laser-based refractive index detector for capillary electrophoresis,” *Analytical Chemistry*, vol. 63, no. 23, pp. 2689–2697, 1991.

[108] E. A. Redman, J. S. Mellors, J. A. Starkey, and J. M. Ramsey, “Characterization of Intact Antibody Drug Conjugate Variants Using Microfluidic Capillary Electrophoresis–Mass Spectrometry,” *Analytical Chemistry*, vol. 88, no. 4, pp. 2220–2226, Feb. 2016.

[109] X. Chen, K. Tang, M. Lee, and G. C. Flynn, “Microchip assays for screening monoclonal antibody product quality,” *ELECTROPHORESIS*, vol. 29, no. 24, pp. 4993–5002, Dec. 2008.

[110] T. Chaly and J. R. Dahl, “Thin layer chromatographic detection of Kryptofix 2.2.2 in the routine synthesis of [18F]2-fluoro-2-deoxy-d-glucose,” *International Journal of Radiation Applications and Instrumentation. Part B. Nuclear Medicine and Biology*, vol. 16, no. 4, pp. 385–387, 1989.

[111] B. H. Mock, W. Winkle, and M. T. Vavrek, “A color spot test for the detection of Kryptofix 2.2.2 in [18F]FDG preparations,” *Nuclear Medicine and Biology*, vol. 24, no. 2, pp. 193–195, Feb. 1997.

[112] R. A. Ferrieri, D. J. Schlyer, D. L. Alexoff, J. S. Fowler, and A. P. Wolf, “Direct analysis of Kryptofix 2.2.2 in 18FDG by gas chromatography using a nitrogen-selective detector,” *Nucl. Med. Biol.*, vol. 20, no. 3, pp. 367–369, Apr. 1993.

[113] Y. Lao, C. Yang, W. Zou, M. Gan, P. Chen, and W. Su, “Quantification of Kryptofix 2.2.2 in [18F]fluorine-labelled radiopharmaceuticals by rapid-resolution liquid chromatography:,” *Nuclear Medicine Communications*, vol. 33, no. 5, pp. 498–502, May 2012.

[114] Y. Ma, B. X. Huang, M. A. Channing, and W. C. Eckelman, “Quantification of Kryptofix 2.2.2 in 2-[18F]FDG and other radiopharmaceuticals by LC/MS/MS,” *Nuclear Medicine and Biology*, vol. 29, no. 1, pp. 125–129, Jan. 2002.

[115] X. Sun, H. Gan, J. Qiao, L. Zhu, Y. Liu, and J. Zhong, “Rapid Detection of the Residual Kryptofix 2.2.2 Levels in [18F]-Labeled Radiopharmaceuticals by Ultra-Performance Liquid Chromatography Tandem Mass Spectrometry,” *Analytical Letters*, vol. 44, no. 7, pp. 1197–1205, May 2011.

[116] R. Nakao, T. Ito, M. Yamaguchi, and K. Suzuki, “Simultaneous analysis of FDG, ClDG and Kryptofix 2.2.2 in [18F]FDG preparation by high-performance liquid chromatography with UV detection,” *Nucl. Med. Biol.*, vol. 35, no. 2, pp. 239–244, Feb. 2008.

[117] Onyije Chima Charles, “WITHDRAWN - Radioanalysis for PET imaging pharmaceuticals: On-chip Detection of Kryptofix 2.2.2,” *Int. J. Sci. Eng. Res.*, vol. 7, no. 9, pp. 478–494, Sep. 2016.

[118] A. I. Anzellotti, A. R. McFarland, and K. F. Olson, “A rapid and simple colorimetric test for 2,2,2-cryptand (Kryptofix 2.2.2.) in solution,” *Anal. Methods*, vol. 5, no. 17, pp. 4317–4320, Aug. 2013.

[119] “FDA Guidance for Industry Q3C Impurities: Residual Solvents.” FDA: Silver Springs, MD, USA, Dec-1997.

[120] J. Koziorowski, “A simple method for the quality control of [18F]FDG,” *Applied Radiation and Isotopes*, vol. 68, no. 9, pp. 1740–1742, Sep. 2010.

[121] A. D. Wilson and M. Baietto, “Applications and Advances in Electronic-Nose Technologies,” *Sensors*, vol. 9, no. 7, pp. 5099–5148, Jun. 2009.

[122] R. Nutt, A. M. Giamis, and A. Mcfarland, “Quality Control Module for Biomarker Generator System,” U.S. Patent Application 20110070158, 24-Mar-2011.

[123] A. Bhushan, D. Yemane, D. Trudell, E. B. Overton, and J. Goettert, “Fabrication of micro-gas chromatograph columns for fast chromatography,” *Microsyst Technol*, vol. 13, no. 3–4, pp. 361–368, Feb. 2007.

[124] T. H. Tzeng *et al.*, “A Portable Micro Gas Chromatography System for Lung Cancer Associated Volatile Organic Compound Detection,” *IEEE Journal of Solid-State Circuits*, vol. 51, no. 1, pp. 259–272, Jan. 2016.

[125] M. P. Taggart *et al.*, “Development of radiodetection systems towards miniaturised quality control of PET and SPECT radiopharmaceuticals,” *Lab Chip*, vol. 16, no. 9, pp. 1605–1616, Apr. 2016.

[126] L. Convert *et al.*, “Blood compatible microfluidic system for pharmacokinetic studies in small animals,” *Lab on a Chip*, vol. 12, no. 22, pp. 4683–4692, 2012.

[127] A. A. Dooraghi, L. Carroll, J. Collins, R. M. van Dam, and A. F. Chatziioannou, “ARAS: an automated radioactivity aliquoting system for dispensing solutions containing positron-emitting radioisotopes,” *EJNMMI Res*, vol. 6, no. 1, p. 22, Dec. 2016.

[128] J. S. Cho, N. T. Vu, Z. T. Yu, R. W. Silverman, H. R. Tseng, and A. F. Chatziioannou, “Optimization of design parameters of a prototype CCD-based lens-coupled imaging system for the detection of beta particles in a microfluidic chip,” in *2007 IEEE Nuclear Science Symposium Conference Record*, 2007, vol. 6, pp. 4615–4619.

[129] J. S. Cho *et al.*, “Detection of Beta Particles in a Microfluidic Chip Using a Scintillator and CCD,” in *2006 IEEE Nuclear Science Symposium Conference Record*, 2006, vol. 4, pp. 1977–1981.
[130] G. Pratx *et al.*, “Radioluminescence Microscopy: Measuring the Heterogeneous Uptake of Radiotracers in Single Living Cells,” *PLOS ONE*, vol. 7, no. 10, p. e46285, Oct. 2012.
[131] J. S. Cho *et al.*, “Cerenkov radiation imaging as a method for quantitative measurements of beta particles in a microfluidic chip,” *Physics in Medicine and Biology*, vol. 54, no. 22, pp. 6757–6771, 2009.
[132] A. A. Dooraghi *et al.*, “Optimization of microfluidic PET tracer synthesis with Cerenkov imaging,” *Analyst*, vol. 138, no. 19, pp. 5654–5664, Aug. 2013.
[133] A. A. Dooraghi *et al.*, “Betabox: a beta particle imaging system based on a position sensitive avalanche photodiode,” *Phys. Med. Biol.*, vol. 58, no. 11, p. 3739, 2013.
[134] Y. S. Shin *et al.*, “Quantitative assessments of glycolysis from single cells,” *Technology (Singap World Sci)*, vol. 3, no. 4, pp. 172–178, Jun. 2015.
[135] M. D. Tarn *et al.*, “Positron detection in silica monoliths for miniaturised quality control of PET radiotracers,” *Chemical Communications*, vol. 52, no. 45, pp. 7221–7224, 2016.
[136] D. Maneuski *et al.*, “On the use of positron counting for radio-Assay in nuclear pharmaceutical production,” *Applied Radiation and Isotopes*, vol. 125, no. Supplement C, pp. 9–14, Jul. 2017.
[137] A. Mapelli *et al.*, “Scintillation particle detection based on microfluidics,” *Sensors and Actuators A: Physical*, vol. 162, no. 2, pp. 272–275, Aug. 2010.
[138] P. Maoddi *et al.*, “Scintillation detectors based on silicon microfluidic channels,” *J. Inst.*, vol. 9, no. 01, p. C01019, 2014.
[139] M. Lavén *et al.*, “Imaging of peptide adsorption to microfluidic channels in a plastic compact disc using a positron emitting radionuclide,” *Lab Chip*, vol. 5, no. 7, pp. 756–763, Jun. 2005.
[140] S. Sadeghi *et al.*, “Reusable electrochemical cell for rapid separation of [18F]fluoride from [18O]water for flow-through synthesis of 18F-labeled tracers,” *Applied Radiation and Isotopes*, vol. 75, pp. 85–94, May 2013.
[141] D. Sengupta, S. Miller, Z. Marton, F. Chin, V. Nagarkar, and G. Pratx, “Bright Lu2O3:Eu Thin-Film Scintillators for High-Resolution Radioluminescence Microscopy,” *Adv. Healthcare Mater.*, vol. 4, no. 14, pp. 2064–2070, Oct. 2015.
[142] D. Ory *et al.*, “Retention of [18F]fluoride on reversed phase HPLC columns,” *Journal of Pharmaceutical and Biomedical Analysis*, vol. 111, pp. 209–214, Jul. 2015.
[143] G. Pascali and P. A. Salvadori, “Opportunities and challenges in the utilization of microfluidic technologies to the production of radiopharmaceuticals,” *Chimica Oggi - Chemistry Today*, vol. 34, no. 3, pp. 28–32, Jun. 2016.
[144] K. S. Shah *et al.*, “Position sensitive APDs for small animal PET imaging,” in *2002 IEEE Nuclear Science Symposium Conference Record*, 2002, vol. 3, pp. 1411–1415 vol.3.
[145] E. González-Peñas, C. Leache, A. López de Cerain, and E. Lizarraga, “Comparison between capillary electrophoresis and HPLC-FL for ochratoxin A quantification in wine,” *Food Chemistry*, vol. 97, no. 2, pp. 349–354, Jul. 2006.
[146] T. Faller and H. Engelhardt, “How to achieve higher repeatability and reproducibility in capillary electrophoresis,” *Journal of Chromatography A*, vol. 853, no. 1–2, pp. 83–94, Aug. 1999.
[147] B. C. Durney, C. L. Crihfield, and L. A. Holland, “Capillary electrophoresis applied to DNA: determining and harnessing sequence and structure to advance bioanalyses (2009–2014),” *Anal Bioanal Chem*, vol. 407, no. 23, pp. 6923–6938, May 2015.
[148] Z. Yang and J. V. Sweedler, “Application of capillary electrophoresis for the early diagnosis of cancer,” *Anal Bioanal Chem*, vol. 406, no. 17, pp. 4013–4031, Mar. 2014.

[149] A. N. de Macedo, M. Irfan Yasin Jiwa, J. Macri, V. Belostotsky, S. Hill, and P. Britz-McKibbin, “Strong Anion Determination in Biological Fluids by Capillary Electrophoresis for Clinical Diagnostics,” *Anal. Chem.*, vol. 85, no. 22, pp. 11112–11120, Nov. 2013.

[150] S.-K. Ruokonen, F. Duša, J. Lokajová, I. Kilpeläinen, A. W. T. King, and S. K. Wiedmer, “Effect of ionic liquids on the interaction between liposomes and common wastewater pollutants investigated by capillary electrophoresis,” *Journal of Chromatography A*, vol. 1405, pp. 178–187, Jul. 2015.

[151] A. M. Skelley *et al.*, “Development and evaluation of a microdevice for amino acid biomarker detection and analysis on Mars,” *PNAS*, vol. 102, no. 4, pp. 1041–1046, Jan. 2005.

[152] F. J. V. Gomez and M. F. Silva, “Microchip electrophoresis for wine analysis,” *Anal Bioanal Chem*, pp. 1–11, Aug. 2016.

[153] E. Tamizi and A. Jouyban, “The potential of the capillary electrophoresis techniques for quality control of biopharmaceuticals—A review,” *Electrophoresis*, vol. 36, no. 6, pp. 831–858, Mar. 2015.

[154] A. Lloyd, M. Russell, L. Blanes, R. Somerville, P. Doble, and C. Roux, “The application of portable microchip electrophoresis for the screening and comparative analysis of synthetic cathinone seizures,” *Forensic Science International*, vol. 242, pp. 16–23, Sep. 2014.

[155] L. Suntornsuk, “Recent advances of capillary electrophoresis in pharmaceutical analysis,” *Anal Bioanal Chem*, vol. 398, no. 1, pp. 29–52, Sep. 2010.

[156] M. C. Breadmore, “Capillary and microchip electrophoresis: Challenging the common conceptions,” *Journal of Chromatography A*, vol. 1221, pp. 42–55, Jan. 2012.

[157] J. V. Pagaduan, V. Sahore, and A. T. Woolley, “Applications of microfluidics and microchip electrophoresis for potential clinical biomarker analysis,” *Anal Bioanal Chem*, vol. 407, no. 23, pp. 6911–6922, Apr. 2015.

[158] F. Shang, E. Guihen, and J. D. Glennon, “Recent advances in miniaturisation--the role of microchip electrophoresis in clinical analysis,” *Electrophoresis*, vol. 33, no. 1, pp. 105–116, Jan. 2012.

[159] S. Ohla and D. Belder, “Chip-based separation devices coupled to mass spectrometry,” *Current Opinion in Chemical Biology*, vol. 16, no. 3–4, pp. 453–459, Aug. 2012.

[160] M. Ueland *et al.*, “Capillary-driven microfluidic paper-based analytical devices for lab on a chip screening of explosive residues in soil,” *Journal of Chromatography A*, vol. 1436, no. Supplement C, pp. 28–33, Mar. 2016.

[161] K. K. R. Tetala and M. A. Vijayalakshmi, “A review on recent developments for biomolecule separation at analytical scale using microfluidic devices,” *Analytica Chimica Acta*, vol. 906, pp. 7–21, Feb. 2016.

[162] S. Fanali, “An overview to nano-scale analytical techniques: Nano-liquid chromatography and capillary electrochromatography,” *ELECTROPHORESIS*, vol. 38, no. 15, pp. 1822–1829, Aug. 2017.

[163] M. V. D’Ambrosio *et al.*, “Point-of-care quantification of blood-borne filarial parasites with a mobile phone microscope,” *Science Translational Medicine*, vol. 7, no. 286, pp. 286re4-286re4, May 2015.

[164] D. E. Patabadige, S. Jia, J. Sibbitts, J. Sadeghi, K. Sellens, and C. T. Culbertson, “Micro Total Analysis Systems: Fundamental Advances and Applications,” *Analytical chemistry*, 2015.

[165] M. Dawod, N. E. Arvin, and R. T. Kennedy, “Recent advances in protein analysis by capillary and microchip electrophoresis,” *Analyst*, vol. 142, no. 11, pp. 1847–1866, May 2017.

[166] S. Cheung, J. Ly, M. Lazari, S. Sadeghi, P. Y. Keng, and R. M. van Dam, “The separation and detection of PET tracers via capillary electrophoresis for chemical identity and purity analysis,” *J Pharm Biomed Anal*, vol. 94, pp. 12–18, Jun. 2014.

[167] J. P. Landers, *Handbook of Capillary Electrophoresis, Second Edition*. CRC Press, 1996.

[168] R. M. Saito, W. K. T. Coltro, D. Jesus, and D. P, “Instrumentation design for hydrodynamic sample injection in microchip electrophoresis: A review,” *ELECTROPHORESIS*, vol. 33, no. 17, pp. 2614–2623, Sep. 2012.

[169] M. W. Li, B. H. Huynh, M. K. Hulvey, S. M. Lunte, and R. S. Martin, “Design and characterization of poly(dimethylsiloxane)-based valves for interfacing continuous-flow sampling to microchip electrophoresis,” *Anal. Chem.*, vol. 78, no. 4, pp. 1042–1051, Feb. 2006.

[170] V. Studer, G. Hang, A. Pandolfi, M. Ortiz, W. F. Anderson, and S. R. Quake, “Scaling properties of a low-actuation pressure microfluidic valve,” *Journal of Applied Physics*, vol. 95, no. 1, pp. 393–398, Jan. 2004.

[171] K. W. Ro, K. Lim, B. C. Shim, and J. H. Hahn, “Integrated Light Collimating System for Extended Optical-Path-Length Absorbance Detection in Microchip-Based Capillary Electrophoresis,” *Anal. Chem.*, vol. 77, no. 16, pp. 5160–5166, Aug. 2005.

[172] Z. Liang, N. Chiem, G. Ocvirk, T. Tang, K. Fluri, and D. J. Harrison, “Microfabrication of a Planar Absorbance and Fluorescence Cell for Integrated Capillary Electrophoresis Devices,” *Anal. Chem.*, vol. 68, no. 6, pp. 1040–1046, Jan. 1996.

[173] B. Ma, X. Zhou, G. Wang, Z. Dai, J. Qin, and B. Lin, “A hybrid microdevice with a thin PDMS membrane on the detection window for UV absorbance detection,” *ELECTROPHORESIS*, vol. 28, no. 14, pp. 2474–2477, Jul. 2007.

[174] Momentive, “Momentive RTV615 Data sheet.” Momentive.

[175] Ocean Optics, “PX2 Pulsed Xenon Lamp Stability.” ocean optics, 08-Jul-2002.

[176] Ocean Optics, “DH-2000-BAL,” *Ocean Optics*. [Online]. Available: http://oceanoptics.com/product/dh-2000-bal/. [Accessed: 28-Dec-2015].

[177] I. Hoek, F. Tho, and W. M. Arnold, “Sodium hydroxide treatment of PDMS based microfluidic devices,” *Lab on a Chip*, vol. 10, no. 17, p. 2283, 2010.

[178] S. Terabe, “Capillary Separation: Micellar Electrokinetic Chromatography,” *Annual Review of Analytical Chemistry*, vol. 2, no. 1, pp. 99–120, 2009.

[179] C. Pascali *et al.*, “Simple preparation and purification of ethanol-free solutions of 3′-deoxy-3′-[18F]fluorothymidine by means of disposable solid-phase extraction cartridges,” *Nuclear Medicine and Biology*, vol. 39, no. 4, pp. 540–550, May 2012.

[180] Council of Europe, “2.2.47. Capillary Electrophoresis,” *European Pharmacopoeia*. pp. 74–79, Jan-2005.

[181] J. C. Giddings, “Generation of Variance, ‘Theoretical Plates,’ Resolution, and Peak Capacity in Electrophoresis and Sedimentation,” *Separation Science*, vol. 4, no. 3, pp. 181–189, Jun. 1969.

[182] C. Cianciulli and H. Wätzig, “Analytical instrument qualification in capillary electrophoresis,” *Electrophoresis*, vol. 33, no. 11, pp. 1499–1508, Jun. 2012.

[183] S. C. Jacobson, R. Hergenroder, L. B. Koutny, R. J. Warmack, and J. M. Ramsey, “Effects of Injection Schemes and Column Geometry on the Performance of Microchip Electrophoresis Devices,” *Anal. Chem.*, vol. 66, no. 7, pp. 1107–1113, 1994.

[184] N. H. Bings, C. Wang, C. D. Skinner, C. L. Colyer, P. Thibault, and D. J. Harrison, “Microfluidic devices connected to fused-silica capillaries with minimal dead volume,” *Analytical chemistry*, vol. 71, no. 15, pp. 3292–3296, 1999.

[185] C.-H. Chiou and G.-B. Lee, “Minimal dead-volume connectors for microfluidics using PDMS casting techniques,” *Journal of Micromechanics and Microengineering*, vol. 14, no. 11, p. 1484, 2004.

[186] M. F. DeLaMarre and S. A. Shippy, “Development of a Simplified Microfluidic Injector for Analysis of Droplet Content via Capillary Electrophoresis,” *Anal. Chem.*, vol. 86, no. 20, pp. 10193–10200, Oct. 2014.

[187] V. Sahore, S. Kumar, C. I. Rogers, J. K. Jensen, M. Sonker, and A. T. Woolley, “Pressure-actuated microfluidic devices for electrophoretic separation of pre-term birth biomarkers,” *Anal Bioanal Chem*, vol. 408, no. 2, pp. 599–607, Nov. 2015.

[188] Y. Cong, S. Katipamula, T. Geng, S. A. Prost, K. Tang, and R. T. Kelly, “Electrokinetic sample preconcentration and hydrodynamic sample injection for microchip electrophoresis using a pneumatic microvalve,” *ELECTROPHORESIS*, vol. 37, no. 3, pp. 455–462, Feb. 2016.

[189] N. A. Lacher, N. F. de Rooij, E. Verpoorte, and S. M. Lunte, “Comparison of the performance characteristics of poly(dimethylsiloxane) and Pyrex microchip electrophoresis devices for peptide separations,” *Journal of Chromatography A*, vol. 1004, no. 1–2, pp. 225–235, Jul. 2003.

[190] J. A. Vickers, M. M. Caulum, and C. S. Henry, “Generation of Hydrophilic Poly(dimethylsiloxane) for High-Performance Microchip Electrophoresis,” *Anal. Chem.*, vol. 78, no. 21, pp. 7446–7452, Nov. 2006.

[191] L. C. Mecker and R. S. Martin, “Integration of Microdialysis Sampling and Microchip Electrophoresis with Electrochemical Detection,” *Anal. Chem.*, vol. 80, no. 23, pp. 9257–9264, Dec. 2008.

[192] X. Sun, R. T. Kelly, W. F. Danielson, N. Agrawal, K. Tang, and R. D. Smith, “Hydrodynamic injection with pneumatic valving for microchip electrophoresis with total analyte utilization,” *ELECTROPHORESIS*, vol. 32, no. 13, pp. 1610–1618, Jun. 2011.

[193] G. Pascali and L. Matesic, “How Far Are We from Dose On Demand of Short-Lived Radiopharmaceuticals?,” in *Perspectives on Nuclear Medicine for Molecular Diagnosis and Integrated Therapy*, Y. Kuge, T. Shiga, and N. Tamaki, Eds. Springer Japan, 2016, pp. 79–92.

[194] W.-Y. Tseng and R. M. van Dam, “Compact microfluidic device for rapid concentration of PET tracers,” *Lab Chip*, vol. 14, no. 13, p. 2293, 2014.

[195] Y. Xu *et al.*, “Development of fully automated quantitative capillary electrophoresis with high accuracy and repeatability,” *Biomed. Chromatogr.*, vol. 30, no. 3, pp. 390–395, Mar. 2016.

[196] B. X. Mayer, “How to increase precision in capillary electrophoresis,” *Journal of Chromatography A*, vol. 907, no. 1–2, pp. 21–37, Jan. 2001.

[197] J. P. Schaeper and M. J. Sepaniak, “Parameters affecting reproducibility in capillary electrophoresis,” *Electrophoresis*, vol. 21, no. 7, pp. 1421–1429, Apr. 2000.

[198] M. Li, J. Zhou, X. Gu, Y. Wang, X. Huang, and C. Yan, “Quantitative capillary electrophoresis and its application in analysis of alkaloids in tea, coffee, coca cola, and theophylline tablets,” *J. Sep. Science*, vol. 32, no. 2, pp. 267–274, Jan. 2009.

[199] B. W. Wenclawiak and R. J. Püschl, “Sample Injection for Capillary Electrophoresis on a Micro Fabricated Device/On Chip CE Injection,” *Analytical Letters*, vol. 39, no. 1, pp. 3–16, Jan. 2006.

[200] J. M. Karlinsey, “Sample introduction techniques for microchip electrophoresis: A review,” *Analytica Chimica Acta*, vol. 725, pp. 1–13, May 2012.

[201] Q. Fang, F.-R. Wang, S.-L. Wang, S.-S. Liu, S.-K. Xu, and Z.-L. Fang, “Sequential injection sample introduction microfluidic-chip based capillary electrophoresis system,” *Analytica Chimica Acta*, vol. 390, no. 1–3, pp. 27–37, May 1999.

[202] P. Kubáň, K. Tennberg, R. Tryzell, and B. Karlberg, “Calibration principles for flow injection analysis–capillary electrophoresis systems with electrokinetic injection,” *Journal of Chromatography A*, vol. 808, no. 1–2, pp. 219–227, May 1998.

[203] Y. Luo *et al.*, “Double-Cross Hydrostatic Pressure Sample Injection for Chip CE: Variable Sample Plug Volume and Minimum Number of Electrodes,” *Anal. Chem.*, vol. 78, no. 17, pp. 6074–6080, Sep. 2006.

[204] N. Dossi, R. Toniolo, S. Susmel, A. Pizzariello, and G. Bontempelli, “A simple approach to the hydrodynamic injection in microchip electrophoresis with electrochemical detection,” *ELECTROPHORESIS*, vol. 31, no. 15, pp. 2541–2547, Aug. 2010.

[205] R. T. Kelly, C. Wang, S. J. Rausch, C. S. Lee, and K. Tang, “Pneumatic Microvalve-Based Hydrodynamic Sample Injection for High-Throughput, Quantitative Zone Electrophoresis in Capillaries,” *Anal. Chem.*, vol. 86, no. 13, pp. 6723–6729, 2014.

[206] A. Gáspár, P. I. Koczka, H. Carmona, and F. A. Gomez, “Split injection: A simple introduction of subnanoliter sample volumes for chip electrophoresis,” *Microchemical Journal*, vol. 99, no. 2, pp. 180–185, Nov. 2011.

[207] M. A. Unger, H.-P. Chou, T. Thorsen, A. Scherer, and S. R. Quake, “Monolithic Microfabricated Valves and Pumps by Multilayer Soft Lithography,” *Science*, vol. 288, no. 5463, pp. 113–116, Apr. 2000.

[208] A. K. Price and C. T. Culbertson, “Generation of Nonbiased Hydrodynamic Injections on Microfluidic Devices Using Integrated Dielectric Elastomer Actuators,” *Anal. Chem.*, vol. 81, no. 21, pp. 8942–8948, Nov. 2009.

[209] J. M. Karlinsey, J. Monahan, D. J. Marchiarullo, J. P. Ferrance, and J. P. Landers, “Pressure Injection on a Valved Microdevice for Electrophoretic Analysis of Submicroliter Samples,” *Anal. Chem.*, vol. 77, no. 11, pp. 3637–3643, Jun. 2005.

[210] D. Solignac and M. A. M. Gijs, “Pressure Pulse Injection: a Powerful Alternative to Electrokinetic Sample Loading in Electrophoresis Microchips,” *Anal. Chem.*, vol. 75, no. 7, pp. 1652–1657, Apr. 2003.

[211] B. T. C. Lau, C. A. Baitz, X. P. Dong, and C. L. Hansen, “A Complete Microfluidic Screening Platform for Rational Protein Crystallization,” *Journal of the American Chemical Society*, vol. 129, no. 3, pp. 454–455, Jan. 2007.

[212] K. Liu, Y.-C. Chen, H.-R. Tseng, C. K.-F. Shen, and R. M. van Dam, “Microfluidic device for robust generation of two-component liquid-in-air slugs with individually controlled composition,” *Microfluid Nanofluid*, vol. 9, no. 4–5, pp. 933–943, Apr. 2010.

[213] H. Gai, L. Yu, Z. Dai, Y. Ma, and B. Lin, “Injection by hydrostatic pressure in conjunction with electrokinetic force on a microfluidic chip,” *Electrophoresis*, vol. 25, no. 12, pp. 1888–1894, Jun. 2004.

[214] X. Huang, M. J. Gordon, and R. N. Zare, “Bias in quantitative capillary zone electrophoresis caused by electrokinetic sample injection,” *Anal. Chem.*, vol. 60, no. 4, pp. 375–377, Feb. 1988.

[215] C.-C. Lin, C.-C. Chen, C.-E. Lin, and S.-H. Chen, “Microchip electrophoresis with hydrodynamic injection and waste-removing function for quantitative analysis,” *J Chromatogr A*, vol. 1051, no. 1–2, pp. 69–74, Oct. 2004.

[216] J. Kestin and I. R. Shankland, “Viscosity of aqueous NaCl solutions in the temperature range 25–200 °C and in the pressure range 0.1–30 MPa,” *Int J Thermophys*, vol. 5, no. 3, pp. 241–263.

[217] J. Kestin, M. Sokolov, and W. A. Wakeham, “Viscosity of liquid water in the range −8 °C to 150 °C,” *Journal of Physical and Chemical Reference Data*, vol. 7, no. 3, pp. 941–948, Jul. 1978.

[218] P. N. Shankar and M. Kumar, “Experimental Determination of the Kinematic Viscosity of Glycerol-Water Mixtures,” *Proceedings of the Royal Society of London A: Mathematical, Physical and Engineering Sciences*, vol. 444, no. 1922, pp. 573–581, Mar. 1994.

[219] N.-S. Cheng, “Formula for the Viscosity of a Glycerol−Water Mixture,” *Ind. Eng. Chem. Res.*, vol. 47, no. 9, pp. 3285–3288, May 2008.

[220] Y.-C. Chen, K. Liu, C. K.-F. Shen, and R. M. van Dam, “On-demand generation and mixing of liquid-in-gas slugs with digitally programmable composition and size,” *J. Micromech. Microeng.*, vol. 25, no. 8, p. 084006, Aug. 2015.

[221] D.-S. Lian and H.-S. Zeng, “Capillary Electrophoresis Based on Nucleic Acid Detection as Used in Food Analysis,” *Comprehensive Reviews in Food Science and Food Safety*, vol. 16, no. 6, pp. 1281–1295, Nov. 2017.

[222] M. Calcerrada, M. González-Herráez, and C. García-Ruiz, “Recent advances in capillary electrophoresis instrumentation for the analysis of explosives,” *TrAC Trends in Analytical Chemistry*, vol. 75, pp. 75–85, Jan. 2016.

[223] A. Pitois, L. A. de L. Heras, and M. Betti, “Determination of fission products in nuclear samples by capillary electrophoresis-inductively coupled plasma mass spectrometry (CE-ICP-MS),” *International Journal of Mass Spectrometry*, vol. 270, no. 3, pp. 118–126, Mar. 2008.

[224] B. Martelat *et al.*, “Precise U and Pu Isotope Ratio Measurements in Nuclear Samples by Hyphenating Capillary Electrophoresis and MC-ICPMS,” *Anal. Chem.*, vol. 90, no. 14, pp. 8622–8628, Jul. 2018.

[225] European Pharmacopeia (EP), “Technical guide for the elaboration of monographs on radiopharmaceutical preparations,” Strasbourg, France: European directorate for the quality of medicines & healthcare, 2010.

[226] D. Thonon, G. Kaisin, J. Henrottin, J. Aerts, H. Van Malderen, and A. Luxen, “Evaluation of an unshielded luminescence flow-through radio-HPLC detector for LC quality control and preparation of PET radiopharmaceuticals,” *Applied Radiation and Isotopes*, vol. 73, pp. 84–89, Mar. 2013.

[227] S. L. Pentoney, R. N. Zare, and J. F. Quint, “Semiconductor radioisotope detector for capillary electrophoresis,” *Journal of Chromatography A*, vol. 480, pp. 259–270, Jan. 1989.

[228] G. L. Klunder, J. E. Andrews, P. M. Grant, B. D. Andresen, and R. E. Russo, “Analysis of Fission Products Using Capillary Electrophoresis with On-Line Radioactivity Detection,” *Anal. Chem.*, vol. 69, no. 15, pp. 2988–2993, Aug. 1997.

[229] N. S. Ha, S. Sadeghi, and R. M. van Dam, “Recent Progress toward Microfluidic Quality Control Testing of Radiopharmaceuticals,” *Micromachines*, vol. 8, no. 11, p. 337, Nov. 2017.

[230] M. D. Tarn *et al.*, “Plastic Scintillator-Based Microfluidic Devices for Miniaturized Detection of Positron Emission Tomography Radiopharmaceuticals,” *Chemistry – A European Journal*, vol. 24, no. 52, pp. 13749–13753, Sep. 2018.

[231] A. Alessio and L. MacDonald, “Spatially variant positron range modeling derived from CT for PET image reconstruction,” in *2008 IEEE Nuclear Science Symposium Conference Record*, 2008, pp. 3637–3640.

[232] A. Sanchez-Crespo, “Comparison of Gallium-68 and Fluorine-18 imaging characteristics in positron emission tomography,” *Applied Radiation and Isotopes*, vol. 76, pp. 55–62, Jun. 2013.

[233] A. Sánchez-Crespo, P. Andreo, and S. A. Larsson, “Positron flight in human tissues and its influence on PET image spatial resolution,” *Eur J Nucl Med Mol Imaging*, vol. 31, no. 1, pp. 44–51, Jan. 2004.

[234] J. Collins *et al.*, “Production of diverse PET probes with limited resources: 24 ^{18}F-labeled compounds prepared with a single radiosynthesizer,” *PNAS*, vol. 114, no. 43, pp. 11309–11314, Oct. 2017.

[235] P. Marchand *et al.*, “Automated and efficient radiosynthesis of [18F]FLT using a low amount of precursor,” *Nuclear Medicine and Biology*, vol. 43, no. 8, pp. 520–527, Aug. 2016.

[236] J. Ly, “Chemical Purity Analysis of PET Radiotracers via Microchip Capillary Electrophoresis,” Ph.D., University of California, Los Angeles, 2016.

[237] A. P. Gerratt and S. Bergbreiter, “Dielectric breakdown of PDMS thin films,” *J. Micromech. Microeng.*, vol. 23, no. 6, p. 067001, 2013.

[238] A. A. Dooraghi, R. W. Silverman, D. L. Prout, R. Taschereau, N. T. Vu, and A. F. Chatziioannou, “Evaluation of transimpedance amplifiers for readout of a position sensitive avalanche photodiode,” in *2011 IEEE Nuclear Science Symposium Conference Record*, 2011, pp. 924–927.

[239] I. Hoek, F. Tho, and W. M. Arnold, “Sodium hydroxide treatment of PDMS based microfluidic devices,” *Lab Chip*, vol. 10, no. 17, pp. 2283–2285, Sep. 2010.

[240] W. K. T. Coltro, S. M. Lunte, and E. Carrilho, “Comparison of the analytical performance of electrophoresis microchannels fabricated in PDMS, glass, and polyester-toner,” *ELECTROPHORESIS*, vol. 29, no. 24, pp. 4928–4937, Dec. 2008.

[241] M. E. Gallina *et al.*, “Toward a Droplet-Based Single-Cell Radiometric Assay,” *Anal. Chem.*, vol. 89, no. 12, pp. 6472–6481, Jun. 2017.

[242] H. S. Krishnan, L. Ma, N. Vasdev, and S. H. Liang, “18F-Labeling of Sensitive Biomolecules for Positron Emission Tomography,” *Chem. Eur. J.*, vol. 23, no. 62, pp. 15553–15577, Nov. 2017.

[243] Z. Wu *et al.*, “Facile Preparation of a Thiol-Reactive 18F-Labeling Agent and Synthesis of 18F-DEG-VS-NT for PET Imaging of a Neurotensin Receptor-Positive Tumor,” *Journal of Nuclear Medicine*, vol. 55, no. 7, pp. 1178–1184, Jul. 2014.

[244] B. de Bruin *et al.*, “1-[3-(2-[^{18} F]Fluoropyridin-3-yloxy)propyl]pyrrole-2,5-dione: Design, Synthesis, and Radiosynthesis of a New [^{18} F]Fluoropyridine-Based Maleimide Reagent for the Labeling of Peptides and Proteins,” *Bioconjugate Chemistry*, vol. 16, no. 2, pp. 406–420, Mar. 2005.

[245] A. M. Scott, J. D. Wolchok, and L. J. Old, “Antibody therapy of cancer,” *Nature Reviews Cancer*, vol. 12, no. 4, pp. 278–287, Apr. 2012.

[246] S. M. Knowles and A. M. Wu, “Advances in Immuno–Positron Emission Tomography: Antibodies for Molecular Imaging in Oncology,” *JCO*, vol. 30, no. 31, pp. 3884–3892, Nov. 2012.

[247] V. Tolmachev and S. Stone-Elander, “Radiolabelled proteins for positron emission tomography: Pros and cons of labelling methods,” *Biochimica et Biophysica Acta (BBA) - General Subjects*, vol. 1800, no. 5, pp. 487–510, May 2010.

[248] C. A. Boswell and M. W. Brechbiel, “Development of radioimmunotherapeutic and diagnostic antibodies: an inside-out view,” *Nuclear Medicine and Biology*, vol. 34, no. 7, pp. 757–778, Oct. 2007.

[249] A. C. Freise and A. M. Wu, “In vivo imaging with antibodies and engineered fragments,” *Molecular Immunology*, vol. 67, no. 2, Part A, pp. 142–152, Oct. 2015.

[250] A. M. Wu, “Engineered antibodies for molecular imaging of cancer,” *Methods*, vol. 65, no. 1, pp. 139–147, Jan. 2014.

[251] M. Pretze, D. Pietzsch, and C. Mamat, “Recent trends in bioorthogonal click-radiolabeling reactions using fluorine-18,” *Molecules*, vol. 18, no. 7, pp. 8618–8665, 2013.

[252] G. Tang, X. Tang, and X. Wang, “A facile automated synthesis of N-succinimidyl 4-[18F]fluorobenzoate ([18F]SFB) for 18F-labeled cell-penetrating peptide as PET tracer,” *Journal of Labelled Compounds and Radiopharmaceuticals*, vol. 53, no. 8, pp. 543–547, 2010.

[253] M. Glaser, E. Årstad, S. K. Luthra, and E. G. Robins, “Two-step radiosynthesis of [18F]N-succinimidyl-4-fluorobenzoate ([18F]SFB),” *Journal of Labelled Compounds and Radiopharmaceuticals*, vol. 52, no. 8, pp. 327–330, 2009.

[254] W. Cai *et al.*, “PET Imaging of Colorectal Cancer in Xenograft-Bearing Mice by Use of an 18F-Labeled T84.66 Anti-Carcinoembryonic Antigen Diabody,” *J Nucl Med*, vol. 48, no. 2, pp. 304–310, Feb. 2007.

[255] H. S. Gill *et al.*, “A Modular Platform for the Rapid Site-Specific Radiolabeling of Proteins with 18F Exemplified by Quantitative Positron Emission Tomography of Human Epidermal Growth Factor Receptor 2,” *J. Med. Chem.*, vol. 52, no. 19, pp. 5816–5825, Oct. 2009.

[256] D. O. Kiesewetter, O. Jacobson, L. Lang, and X. Chen, “Automated radiochemical synthesis of [18F]FBEM: A thiol reactive synthon for radiofluorination of peptides and proteins,” *Applied Radiation and Isotopes*, vol. 69, no. 2, pp. 410–414, Feb. 2011.

[257] F. Wuest, L. Köhler, M. Berndt, and J. Pietzsch, “Systematic comparison of two novel, thiol-reactive prosthetic groups for 18F labeling of peptides and proteins with the acylation agent succinimidyl-4-[18F]fluorobenzoate ([18F]SFB),” *Amino Acids*, vol. 36, no. 2, pp. 283–295, Feb. 2009.

[258] M. Namavari *et al.*, “A Novel Method for Direct Site-Specific Radiolabeling of Peptides Using [^{18} F]FDG,” *Bioconjugate Chemistry*, vol. 20, no. 3, pp. 432–436, Mar. 2009.

[259] J. N. Tinianow *et al.*, “Site-specifically 89Zr-labeled monoclonal antibodies for ImmunoPET,” *Nuclear Medicine and Biology*, vol. 37, no. 3, pp. 289–297, Apr. 2010.

[260] W. Cai, X. Zhang, Y. Wu, and X. Chen, “A Thiol-Reactive 18F-Labeling Agent, N-[2-(4-18F-Fluorobenzamido)Ethyl]Maleimide, and Synthesis of RGD Peptide-Based Tracer for PET Imaging of αvβ3 Integrin Expression,” *J Nucl Med*, vol. 47, no. 7, pp. 1172–1180, Jul. 2006.

[261] L. Jia *et al.*, “Fluorine-18 labeling by click chemistry: Multiple probes in one pot,” *Applied Radiation and Isotopes*, vol. 75, pp. 64–70, May 2013.

[262] R. Schirrmacher, C. Wangler, and E. Schirrmacher, “Recent Developments and Trends in 18F-Radiochemistry: Syntheses and Applications,” *Mini-Reviews in Organic Chemistry*, vol. 4, pp. 317–329, Nov. 2007.

[263] X. Yue *et al.*, “One-pot two-step radiosynthesis of a new (18)F-labeled thiol reactive prosthetic group and its conjugate for insulinoma imaging,” *Mol. Pharm.*, vol. 11, no. 11, pp. 3875–3884, Nov. 2014.

[264] X. Li *et al.*, “Site-Specific Labeling of Annexin V with F-18 for Apoptosis Imaging,” *Bioconjugate Chem.*, vol. 19, no. 8, pp. 1684–1688, Aug. 2008.

[265] F. Wuest, L. Köhler, M. Berndt, and J. Pietzsch, “Systematic comparison of two novel, thiol-reactive prosthetic groups for 18F labeling of peptides and proteins with the acylation agent succinimidyl-4-[18F]fluorobenzoate ([18F]SFB),” *Amino Acids*, vol. 36, no. 2, p. 283, Apr. 2008.

[266] M. Berndt, J. Pietzsch, and F. Wuest, “Labeling of low-density lipoproteins using the 18F-labeled thiol-reactive reagent N-[6-(4-[18F]fluorobenzylidene)aminooxyhexyl]maleimide,” *Nuclear Medicine and Biology*, vol. 34, no. 1, pp. 5–15, Jan. 2007.

[267] C.-Y. Shiue, A. P. Wolf, and J. F. Hainfeld, “Synthesis of 18F-labelled N-(p-[18F]fluorophenyl)maleimide and its derivatives for labelling monoclonal antibody with 18F,” *Journal of Labelled Compounds and Radiopharmaceuticals*, vol. 26, no. 1–12, pp. 287–289, Jan. 1989.

[268] S. Richter and F. Wuest, “18F-Labeled Peptides: The Future Is Bright,” *Molecules*, vol. 19, no. 12, pp. 20536–20556, 2014.

[269] M. R. Javed *et al.*, “High yield and high specific activity synthesis of [18F]fallypride in a batch microfluidic reactor for micro-PET imaging,” *Chem. Commun.*, vol. 50, no. 10, pp. 1192–1194, 2014.

[270] P. Y. Keng *et al.*, “Micro-chemical synthesis of molecular probes on an electronic microfluidic device,” *PNAS*, vol. 109, no. 3, pp. 690–695, 2012.

[271] M. Sergeev *et al.*, "Performing radiosynthesis in microvolumes to maximize molar activity of tracers for positron emission tomography," *Communications Chemistry*, vol. 1, no. 1, p. 10, Mar. 2018.

[272] C. Lu, Q. Jiang, M. Hu, C. Tan, H. Yu, and Z. Hua, "Preliminary Biological Evaluation of 18F-FBEM-Cys-Annexin V a Novel Apoptosis Imaging Agent," *Molecules*, vol. 20, no. 3, pp. 4902–4914, Mar. 2015.

[273] G. Kramer-Marek, D. O. Kiesewetter, L. Martiniova, E. Jagoda, S. B. Lee, and J. Capala, "[18F]FBEM-ZHER2:342–Affibody molecule—a new molecular tracer for in vivo monitoring of HER2 expression by positron emission tomography," *Eur J Nucl Med Mol Imaging*, vol. 35, no. 5, pp. 1008–1018, Dec. 2007.

[274] D. O. Kiesewetter, G. Krämer-Marek, Y. Ma, and J. Capala, "Radiolabeling of HER2 specific Affibody(R) molecule with F-18," *J Fluor Chem*, vol. 129, no. 9, pp. 799–805, Sep. 2008.

[275] H. Gao *et al.*, "PET of Insulinoma Using 18F-FBEM-EM3106B, a New GLP-1 Analogue," *Mol. Pharmaceutics*, vol. 8, no. 5, pp. 1775–1782, Oct. 2011.

[276] H. Wang *et al.*, "Site-Specific Labeling of scVEGF with Fluorine-18 for Positron Emission Tomography Imaging," *Theranostics*, vol. 2, no. 6, pp. 607–617, 2012.

[277] U. Ackermann *et al.*, "Fully automated synthesis and coupling of [18F]FBEM to glutathione using the iPHASE FlexLab module," *J. Label Compd. Radiopharm*, vol. 57, no. 2, pp. 115–120, Feb. 2014.

[278] A. Perreault, J. C. Knight, M. Wang, J. Way, and F. Wuest, "18F-Labeled wild-type annexin V: comparison of random and site-selective radiolabeling methods," *Amino Acids*, vol. 48, no. 1, pp. 65–74, Aug. 2015.

[279] K. E. McCabe and A. M. Wu, "Positive Progress in ImmunoPET—Not Just a Coincidence," *Cancer Biotherapy and Radiopharmaceuticals*, vol. 25, no. 3, pp. 253–261, Jun. 2010.

[280] S. H. Lim, S. A. Beers, R. R. French, P. W. M. Johnson, M. J. Glennie, and M. S. Cragg, "Anti-CD20 monoclonal antibodies: historical and future perspectives," *Haematologica*, vol. 95, no. 1, pp. 135–143, Jan. 2010.

[281] K. Sachin *et al.*, "F-18 Labeling Protocol of Peptides Based on Chemically Orthogonal Strain-Promoted Cycloaddition under Physiologically Friendly Reaction Conditions," *Bioconjugate Chem.*, vol. 23, no. 8, pp. 1680–1686, Aug. 2012.

[282] E. Decuypère, L. Plougastel, D. Audisio, and F. Taran, "Sydnone–alkyne cycloaddition: applications in synthesis and bioconjugation," *Chem. Commun.*, vol. 53, no. 84, pp. 11515–11527, Oct. 2017.

[283] H. Tao *et al.*, "Origins of halogen effects in bioorthogonal sydnone cycloadditions," *Chem. Commun.*, vol. 54, no. 40, pp. 5082–5085, May 2018.

[284] S. K. Cho, H. Moon, and C.-J. Kim, "Creating, transporting, cutting, and merging liquid droplets by electrowetting-based actuation for digital microfluidic circuits," *J. MEMS*, vol. 12, no. 1, pp. 70–80, Feb. 2003.

[285] R. A. Hayes and B. J. Feenstra, "Video-speed electronic paper based on electrowetting," *Nature*, vol. 425, no. 6956, pp. 383–385, Sep. 2003.

[286] B. Berge and J. Peseux, "Variable focal lens controlled by an external voltage: An application of electrowetting," *Eur. Phys. J. E*, vol. 3, no. 2, pp. 159–163, Oct. 2000.

[287] V. Srinivasan, V. K. Pamula, and R. B. Fair, "An integrated digital microfluidic lab-on-a-chip for clinical diagnostics on human physiological fluids," *Lab Chip*, vol. 4, no. 4, pp. 310–315, 2004.

[288] J.-T. Cheng and C.-L. Chen, "Active thermal management of on-chip hot spots using EWOD-driven droplet microfluidics," *Exp Fluids*, vol. 49, no. 6, pp. 1349–1357, Apr. 2010.

[289] U. Diebold, "The surface science of titanium dioxide," *Surface Science Reports*, vol. 48, no. 5–8, pp. 53–229, Jan. 2003.

[290] Illumina, “NeoPrep Library Prep System,” 2015. [Online]. Available: https://www.illumina.com/company/news-center/press-releases/press-release-details.html?newsid=2018793. [Accessed: 27-Oct-2018].
[291] Corning, “Varioptic® Lenses,” 2018. [Online]. Available: https://www.corning.com/worldwide/en/innovation/corning-emerging-innovations/corning-varioptic-lenses.html. [Accessed: 27-Oct-2018].
[292] GenMark Diagnostics, “ePlex,” 2018. .
[293] M. G. Pollack, R. B. Fair, and A. D. Shenderov, “Electrowetting-based actuation of liquid droplets for microfluidic applications,” *Appl. Phys. Lett.*, vol. 77, no. 11, pp. 1725–1726, 2000.
[294] H. Moon, S. K. Cho, R. L. Garrell, and C.-J. Kim, “Low voltage electrowetting-on-dielectric,” *J. Appl. Phys.*, vol. 92, no. 7, p. 4080, 2002.
[295] B. Raj, M. Dhindsa, N. R. Smith, R. Laughlin, and J. Heikenfeld, “Ion and Liquid Dependent Dielectric Failure in Electrowetting Systems,” *Langmuir*, vol. 25, no. 20, pp. 12387–12392, Oct. 2009.
[296] H. J. J. Verheijen and M. W. J. Prins, “Reversible Electrowetting and Trapping of Charge: Model and Experiments,” *Langmuir*, vol. 15, no. 20, pp. 6616–6620, Sep. 1999.
[297] E. N. A. Latip *et al.*, “Protein droplet actuation on superhydrophobic surfaces: a new approach toward anti-biofouling electrowetting systems,” *RSC Adv.*, vol. 7, no. 78, pp. 49633–49648, Oct. 2017.
[298] W. C. Nelson and C.-J. ‘CJ’ Kim, “Droplet Actuation by Electrowetting-on-Dielectric (EWOD): A Review,” *Journal of Adhesion Science and Technology*, vol. 26, no. 12–17, pp. 1747–1771, 2012.
[299] J. Lee, H. Moon, J. Fowler, T. Schoellhammer, and C.-J. Kim, “Electrowetting and electrowetting-on-dielectric for microscale liquid handling,” *Sensors and Actuators A: Physical*, vol. 95, no. 2–3, pp. 259–268, Jan. 2002.
[300] M. I. Nave, Y. Gu, Y.-C. K. Chen-Wiegart, J. Wang, and K. G. Kornev, “Is an electric field always a promoter of wetting? Electro-dewetting of metals by electrolytes probed by in situ X-ray nanotomography,” *Faraday Discuss.*, vol. 199, no. 0, pp. 101–114, Jul. 2017.
[301] G.-H. Hu, A.-J. Xu, Z. Xu, and Z.-W. Zhou, “Dewetting of nanometer thin films under an electric field,” *Physics of Fluids*, vol. 20, no. 10, p. 102101, Oct. 2008.
[302] F. Lapierre, Y. Coffinier, R. Boukherroub, and V. Thomy, “Electro-(de)wetting on Superhydrophobic Surfaces,” *Langmuir*, vol. 29, no. 44, pp. 13346–13351, Nov. 2013.
[303] B. S. Gallardo *et al.*, “Electrochemical Principles for Active Control of Liquids on Submillimeter Scales,” *Science*, vol. 283, no. 5398, pp. 57–60, Jan. 1999.
[304] S. He, Y. Meng, and Y. Tian, “Correlation Between Adsorption/Desorption of Surfactant and Change in Friction of Stainless Steel in Aqueous Solutions Under Different Electrode Potentials,” *Tribol Lett*, vol. 41, no. 3, pp. 485–494, Mar. 2011.
[305] H. J. Cho, J. P. Mizerak, and E. N. Wang, “Turning bubbles on and off during boiling using charged surfactants,” *Nature Communications*, vol. 6, p. 8599, Oct. 2015.
[306] W. Xu, J. Xu, X. Li, Y. Tian, C.-H. Choi, and E.-H. Yang, “Lateral actuation of an organic droplet on conjugated polymer electrodes via imbalanced interfacial tensions,” *Soft Matter*, vol. 12, no. 33, pp. 6902–6909, 2016.
[307] R. A. Erb, “Wettability of gold,” *J. Phys. Chem.*, vol. 72, no. 7, pp. 2412–2417, Jul. 1968.
[308] D. J. Lomax *et al.*, “Ultra-low voltage electrowetting using graphite surfaces,” *Soft Matter*, vol. 12, no. 42, pp. 8798–8804, Oct. 2016.
[309] B. P. Chock, D. R. Harding, and T. B. Jones, “Using Digital Microfluidics to Dispense, Combine, and Transport Low-Surface-Energy Fluids,” *Fusion Science and Technology*, vol. 73, no. 2, pp. 237–247, Feb. 2018.

[310] C. B. Eaker, I. D. Joshipura, L. R. Maxwell, J. Heikenfeld, and M. D. Dickey, “Electrowetting without external voltage using paint-on electrodes,” *Lab Chip*, vol. 17, no. 6, pp. 1069–1075, Mar. 2017.

[311] E. F. Hare and W. A. Zisman, “Autophobic Liquids and the Properties of their Adsorbed Films,” *J. Phys. Chem.*, vol. 59, no. 4, pp. 335–340, Apr. 1955.

[312] P. Wängnerud and G. Olofsson, “Adsorption isotherms for cationic surfactants on silica determined by in situ ellipsometry,” *Journal of Colloid and Interface Science*, vol. 153, no. 2, pp. 392–398, Oct. 1992.

[313] T. P. Goloub, L. K. Koopal, B. H. Bijsterbosch, and M. P. Sidorova, “Adsorption of Cationic Surfactants on Silica. Surface Charge Effects,” *Langmuir*, vol. 12, no. 13, pp. 3188–3194, Jan. 1996.

[314] F. Mugele and J.-C. Baret, “Electrowetting: from basics to applications,” *Journal of Physics: Condensed Matter*, vol. 17, no. 28, pp. R705–R774, 2005.